



# Technische Universität München

Fakultät für Chemie

## **Current Challenges in Stability Assessment of Oxygen Evolution Reaction Catalysts for PEM Water Electrolyzer**

Alexandra Hartig-Weiß

Vollständiger Abdruck der von der Fakultät für Chemie der Technischen Universität  
München zur Erlangung des akademischen Grades einer

Doktorin der Naturwissenschaften (Dr. rer. nat.)

genehmigten Dissertation

Vorsitz:

Prof. Dr. Barbara Lechner

Prüfer der Dissertation:

1. Prof. Dr. Hubert A. Gasteiger

2. Prof. Dr.-Ing. Kai-Olaf Martin Hinrichsen

Diese Dissertation wurde am 17.05.2021 bei der Technischen Universität München eingereicht  
und durch die Fakultät für Chemie am 24.01.2022 angenommen.





„...And just like that, after a long wait, a day like any else, [...].  
I decided to see every problem as the opportunity to find a solution.”

*Walt Disney*



# Abstract

Hydrogen produced via the electrochemical splitting of water in a proton exchange membrane water electrolyzer (PEM-WE) is a promising alternative energy carrier to promote the transition to renewable energies. The PEM-WE system is technically already quite advanced, however, there are still some hurdles that have to be passed to enable a large-scale application. Although today's commonly used OER (oxygen evolution reaction) catalysts would be sufficiently active, the high iridium packing density hampers the fabrication of electrodes with sufficiently low iridium loadings. Lowering the iridium loading while still maintaining a high OER activity can e.g., be achieved by the dispersion of iridium-nanoparticles on electrically conductive antimony-doped tin oxide (ATO). The Ir/ATO catalyst not only exhibits a lower iridium packing density but also a significantly higher mass activity compared to commercially available catalysts. Beside the activity, the long-term stability is crucial. A method typically used to assess performance and durability of OER catalysts is the RDE (rotating disk electrode) method using aqueous electrolytes.

However, RDE cannot be used in the case of Ir based OER catalysts for OER, since the lifetimes obtained differ from lifetimes obtained from MEA (membrane electrode assembly) measurements by orders of magnitude. This is due to the extensive accumulation of oxygen bubbles and the accompanied shielding of active sites within the catalyst layer when using an RDE setup. The accumulation of oxygen bubbles results locally in high potentials and consequently rapid catalyst degradation. When additional ultra-sonication is applied during the measurement, the accumulation of oxygen bubbles and thus the accompanied degradation can be avoided. Comparing commonly applied stability protocols performed in either an RDE or an MEA setup reveals that none of them can be used with an RDE setup. Hence, an accelerated stress test (AST) for an MEA configuration is proposed, in which times of operation alternate with idle periods. Leaving the cell at open circuit voltage (OCV) during the idle period leads to the formation of a hydrous iridium oxide, which in combination with the passivation of the used Ti porous transport layer (PTL) results in an additional interfacial resistance. The latter is responsible for the gradual decrease in performance over the course of load/idle cycling. However, when polarizing the cell at 1.3 V during the idle periods, a stable performance can be maintained, as reduction of the iridium oxide surface can be prevented therewith. Applying a Pt-wire as a reference electrode, which is centrally laminated between two membranes,

unambiguously proves that an additional contact resistance at the OER electrode is responsible for the decaying performance during the OCV-AST.

# Kurzzusammenfassung

Wasserstoff, welcher durch die elektrolytische Spaltung von Wasser in einem Protonenaustauschmembran-Wasserelektrolyseur (PEM-WE) erzeugt wird, ist ein vielversprechender Energieträger für den Übergang von fossilen zu erneuerbaren Energien. Auch wenn die Technologie der sauren Wasserelektrolyse bereits weit vorangeschritten ist, so müssen dennoch einige Herausforderungen gemeistert werden, um einen großskaligen Einsatz zu ermöglichen. Zum Beispiel verhindert eine hohe Packungsdichte von Iridium die Herstellung homogener Katalysatorschichten bei niedrigen Iridium Beladungen, obwohl die Aktivität im Hinblick auf die Sauerstoffreaktion (OER) der gängigsten Katalysatoren eigentlich ausreichend wäre. Eine Möglichkeit zur Reduktion der Ir-Beladung bei gleichzeitig ausreichend hoher katalytischer Aktivität ist das Abscheiden von Iridium-Nanopartikeln auf einem elektrisch leitfähigem Antimon-dotierten Zinnoxid (ATO), wodurch eine hohe Iridium Dispersion erzielt werden kann. Der synthetisierte Ir/ATO Katalysator zeichnet sich nicht nur durch eine geringe Iridium Packungsdichte, sondern auch durch eine deutlich höhere OER Aktivität im Vergleich zu kommerziellen Katalysatoren aus.

Neben der OER Aktivität ist bei der Anwendung auch die Langzeitstabilität entscheidend, welche häufig mittels der rotierenden Scheibenelektroden (RDE) Methode ermittelt wird. Die damit bestimmte Lebensdauer ist jedoch um Größenordnungen kleiner, als jene, die in Messungen im Realsystem (d.h. in einem PEM-WE) ermittelt werden. Während einer RDE-Messung können sich Sauerstoffblasen innerhalb der Katalysatorschicht anreichern was dazu führt, dass ein Teil der Katalysatorschicht ionisch abgeschirmt wird. Dies führt zu einem signifikanten Potentialanstieg an den noch zugänglichen, aktiven Oberflächen, was wiederum zur Degradation des Katalysators führt. Eine Anreicherung von Sauerstoffblasen während der RDE Messung kann durch die Anwendung von Ultraschall verhindert werden, was allerdings im Fall von Nanopartikeln nicht praktikabel ist. Ein direkter Vergleich etablierter Stabilitätsprotokolle, gemessen sowohl mittels RDE als auch in einer Membranelektrodeneinheit (MEA) zeigt deutlich, dass die Stabilität gemessen mittels RDE um Größenordnungen kleiner ist und keines der Protokolle die Stabilität von OER Katalysatoren verlässlich wiedergibt. Aus diesem Grund wurde ein beschleunigter Alterungstest (AST) für die MEA-Konfiguration entwickelt, bei welchen zwischen Betrieb und Leerlaufphasen gezykelt wird. Während der Leerlaufphasen bildet sich ein Iridium-Hydroxid ( $\text{Ir}(\text{OH})_x$ ) aus, welches in Kombination mit der Passivierung des Ti-PTLs (poröse Transportschicht) zu einem

zusätzlichen Kontaktflächenwiderstand und damit einhergehend zu einer Verschlechterung der Leistung führt. Durch die Einführung einer Pt-Referenzelektrode konnte zweifelsfrei gezeigt werden, dass der zusätzliche Widerstand auf einen Kontaktflächenwiderstand auf der Anode zurückzuführen ist.

# Acknowledgements

First and foremost I would like to thank my supervisor

**Prof. Dr. Hubert A. Gasteiger.**

During the past years, he guided and supervised me, showing me how much fun and passion electrochemistry can be. I admire his enthusiasm and commitment for electrochemistry and his extensive expertise, always having an open ear for problems and time for discussions. He taught me to critically analyze one's own data to make sure one won't miss a tiny detail. The bike-trips to the summer seminar were definitely something I won't forget- especially the hilly detour to get to Lago di Caldaro. It remains only to extend a heartfelt thank you! I really enjoyed and appreciated working with you!

Another special thanks goes to **Dr. Thomas Mittermeier** for guiding my baby steps in electrochemistry and spreading his enthusiasm for electrochemistry. He supported me throughout all these years and always had an open ear! Thank you!

I also would like to thank **Dr. Maximilian Bernt** and **Dr. Armin Siebel** – the electrolysis team when I started – and **Dr. Hany El-Sayed** and **Mohammad Fathi Tovini** – the so-called *bubble team* - for helping and teaching me the principles and fundamentals of water electrolysis. It was a great time and I really enjoyed working with you. Additionally, I would like to thank the research students I had the opportunity to work with for their contributions to the single studies and especially **Carina Schramm** and **Konstantin Weber**. I'm happy that both decided to stay in the field of electrochemistry.

I further would like to thank **Anna T.S. Freiberg** for her great support and open ear throughout all these years, no matter how stupid the questions was. I'm happy to have the great pleasure of working with her!

Furthermore, I want to thank some colleagues, who helped me a lot to get familiar with reference electrode measurements and the complexity of impedance measurements: **Dr. Johannes Landesfeind**, **Robert Morasch**, **Prof. Dr. Bharat Suthar**, **Anna T.S. Freiberg**, and **Dr. Daniel Pritzl**. Thank you for your patience and help untangling the web around impedance measurements.

I would also like to thank **Anna T.S. Freiberg** and **Dr. Thomas Mittermeier** for proofreading my thesis. Special thanks goes to **Veronika Pichler** for all her help regarding administrative things and her patience, when once more something was filled in incorrectly.

Of course, I would like to thank all my colleagues at the Chair of Technical Electrochemistry for the great working atmosphere and their help. Specially I would like to thank **Anna T.S. Freiberg, Ana Marija Damjanovic, Dr. Burak Koyutürk, Ceren Tok, Davide Menga, Mohammad Fathi Tovini, Paulette Loichet, Veronika Pichler** and **Yan-Sheng Li**, who have grown to be really good friends! Thank you for your support and I will miss you! Moreover, I would like to say thank you to some former TEC members, who made my stay at TEC unforgettable: **Dr. Dominik Haering, Dr. Gregor Harzer, Johannes Sicklinger**, and **Michael Striednig**.

Finally, I would like to thank my family and especially my parents **Dieter** and **Rosemarie Weiß**, for their endless support and encouragement during all these years. Without them, I wouldn't have come so far. Thank you! I would also like to thank my sister **Bianca** for always supporting me no matter what!

Lastly, a special thanks goes to my husband **Markus**. He supported me throughout all these years, always had my back and showed me how proud he is of me. The last word goes to **Michel**, my baby boy, who is the sunshine of my life and who makes our life each day brighter.



# Contents

Abstract .....	v
Kurzzusammenfassung .....	vii
Contents .....	xi
List of Acronyms .....	xv
1 Introduction .....	1
2 Proton Exchange Membrane Water Electrolysis .....	3
2.1 Efficiency and Voltage Losses .....	4
2.1.1 Thermodynamics .....	4
2.1.2 Kinetic Losses .....	7
2.1.3 Ohmic Losses .....	10
2.1.4 Transport Losses .....	12
2.2 Electrochemical Impedance Spectroscopy .....	14
2.2.1 Complex Impedance .....	14
2.2.2 Equivalent Circuit Model for a PEM Water Electrolyzer .....	17
2.3 Materials and Components .....	21
2.3.1 Polymer Electrolyte Membrane .....	21
2.3.2 Hydrogen Evolution Catalyst .....	23
2.3.3 Oxygen Evolution Catalyst .....	23
2.3.4 Porous Transport Layers .....	24
2.3.5 Bipolar Plates .....	25
2.4 Operation Conditions .....	25
2.4.1 Temperature .....	25
2.4.2 Pressure .....	26
2.5 Degradation Phenomena .....	27
2.5.1 Membrane .....	27

2.5.2	Catalyst Layer .....	28
2.5.3	Porous Transport Layers and Bipolar Plates .....	30
2.6	Hydrogen as an Energy Carrier .....	31
3	Experimental Methods .....	33
3.1	Rotating Ring Disk Electrode .....	33
3.1.1	Electrode and Ink Preparation .....	35
3.1.2	Electrochemical Measurement Setup .....	36
3.2	Polymer Exchange Membrane Water Electrolyzer .....	37
3.2.1	Membrane Electrode Assembly .....	38
3.2.2	Electrochemical Characterization .....	39
3.2.3	Scanning Electron Microscopy .....	41
3.2.4	Electrical Conductivity Measurements – 4-Point Probe .....	41
3.2.5	Contact Resistance Measurements .....	42
4	Platinum Wire Reference Electrode .....	43
4.1	Pt-Wire Reference Electrode Setup .....	43
4.2	Reference Electrode MEA Fabrication.....	45
4.3	Electrochemical Characterization.....	46
4.4	Analysis of the Electrochemical Impedance Spectra.....	47
4.5	Analysis of the Inductive Loop at Low Frequencies .....	51
4.5.1	Electrical Circuit Setup – Cable Configuration.....	51
4.5.2	Influence of Membrane Thickness .....	53
4.5.3	Influence of the Applied Amplitude.....	56
4.5.4	Comparison with the Literature.....	57
4.6	Analysis of the Anode Impedance Spectra.....	58
5	Scientific Contributions .....	67
5.1	Current Challenges in Catalyst Development for PEM Water Electrolysis.....	68
5.2	Iridium Oxide Catalyst Supported on Antimony -Doped Tin Oxide for High Oxygen Evolution Reaction Activity in Acidic Media .....	80

5.3 OER Catalyst Stability Investigation Using RDE Technique: A Stability Measure or an Artifact? .....	94
5.4 OER Catalyst Durability Tests Using the Rotating Disk Electrode Technique - the Reason Why This Leads to Erroneous Results .....	104
5.5 The Discrepancy in Oxygen Evolution Reaction Catalyst Lifetime Explained: RDE vs MEA – Dynamicity within the Catalyst Layer Matters.....	112
5.6 Impact of Intermittent Operation on Lifetime and Performance of a PEM Water Electrolyzer.....	126
5.7 A Platinum Micro-Reference Electrode for Impedance Measurements in PEM Water Electrolysis .....	140
6 Conclusion.....	155
Bibliography.....	159



# List of Acronyms

AEL	Alkaline Electrolysis
AST	Accelerated Stress Test
ATO	Antimony-doped Tin Oxide
Au-WRE	Gold Wire Reference Electrode
BoP	Balance of Plant
BP	Bipolar Plates
CAPEX	Capital expenditure
CE	Counter Electrode
COR	Carbon Oxidation Reaction
DHE	Dynamic Hydrogen Electrode
ECM	Equivalent Circuit Model
ECSA	Electrochemically Active Surface Area
EIS	Electrochemical Impedance Spectroscopy
EW	Equivalent Weight
GDL	Gas Diffusion Layer
HER	Hydrogen Evolution Reaction
HOR	Hydrogen Oxidation Reaction
ICP-MS	Inductive Coupled Plasma Mass Spectrometry
LFR	Low Frequency Resistance
MEA	Membrane Electrode Assembly
OCP	Open Circuit Potential
OER	Oxygen Evolution Reaction
PEM-FC	Proton Exchange Membrane Fuel Cell

PEM-WE	Proton Exchange Membrane Water Electrolyzer
PFSA	Perfluorinated Sulfonic Acid
PGM	Platinum Group Metals
PTFE	Polytetrafluoroethylene
PTL	Porous Transport Layer
Pt-WRE	Platinum Wire Reference Electrode
RDE	Rotating Ring Disk
rds	Rate Determining Step
RE	Reference Electrode
rf	Roughness Factor
RH	Relative Humidity
RHE	Reversible Hydrogen Electrode
SEM	Scanning Electron Microscopy
SHE	Standard Hydrogen Electrode
SFC	Scanning Flow Cell
TLM	Transmission Line Model
TS	Tafel-Slope
WE	Working Electrode

# 1 Introduction

Nowadays the impact of greenhouse gas emissions on the climate change is undeniable. In Germany the average temperature increased by  $\approx 1.9\text{ }^{\circ}\text{C}^1$  within the last decade (2011 – July 2020) compared to a reference period between 1881-1910 and if no action is taken, it is expected to rise even further.<sup>2</sup> This would result in more frequent ecological disasters (e.g. droughts and flooding) and a rising sea level – just to mention some consequences of the climate change. Even though the overall greenhouse gas emission in Germany was reduced significantly from 1990 (1.249 Mt - eq. CO<sub>2</sub>) to 2019 (810 Mt - eq.CO<sub>2</sub>)<sup>3</sup>, the goal is to obtain a neutral greenhouse gas balance by 2050. The biggest share to the total emission arises from the energy sector and industry (437 Mt-eq.CO<sub>2</sub> in 2019)<sup>3</sup>, wherefore alternative process flows and energy carriers are needed. Hydrogen can make a major contribution with respect to the energy transition, since it is a versatile energy carrier. It can serve as a flexible and on-demand energy carrier or as raw material in industry (e.g. ammonia synthesis). Moreover, it can be used as a fuel for fuel cell driven vehicles in the mobility sector. Hence, hydrogen can serve as a sustainable energy storage and supply medium in the long-term. Therefore, the federal cabinet of Germany approved the national hydrogen strategy in 2020, promoting the opportunity to meet the climate protection goals for 2050, while providing a framework to establish and endorse reliable hydrogen technologies.<sup>4,5</sup> The CO<sub>2</sub>-emission free generation of hydrogen (green hydrogen) is an indispensable requirement to successfully accomplish the decarbonization of the energy demand. This will be achieved if the energy is provided by renewable energies exclusively. However, the share of renewable energies to the overall energy supply in 2019 in Germany was only 17.1%.<sup>6</sup> Bareiß et al.<sup>7</sup> showed that the CO<sub>2</sub>-balance (kg CO<sub>2</sub>-eq./ kg H<sub>2</sub>) is greatly influenced by the electricity mix and that with today's electricity mix in Germany, the global warming impact (kg CO<sub>2</sub>-eq./ kg H<sub>2</sub>) for hydrogen produced via water splitting in a PEM-WE (Proton Exchange Membrane Water Electrolyzer) is  $\approx 3$  times higher compared hydrogen produced via conventional steam reforming. Thus, the CO<sub>2</sub>-balance is affected adversely, as long as hydrogen is not produced by renewable energies exclusively.

Considering that hydrogen is already widely used in the chemical industry (e.g. ammonia synthesis) and that new process flows using hydrogen should be established (e.g. steel industry), the demand for hydrogen will increase significantly.<sup>5</sup> Hydrogen produced via the electrochemical splitting of water in a PEM-WE bears great potential due to its flexibility, high pressure and current density operation as well as the degree of purity of the produced hydrogen.<sup>8</sup>

Therefore, the installation of additional electrolyzer systems (targeting 5 GW) are aimed for and should be operated by 2030, resulting in an annual increase on the order of hundreds of MW to add up to 5 GW in 9 years.<sup>5</sup> Although the technology of a PEM-WE is already quite advanced and some companies already provide electrolyzers in the MW-range,<sup>9-10</sup> there are still some obstacles that have to be solved in order to provide a large-scale application of PEM-WEs. Due to the harsh environment during operation such as high anodic potentials and low pH, the choice of catalyst is limited to platinum group metals (PGM), mostly platinum and iridium. Besides the catalyst costs, the availability of iridium is a major concern when targeting GW-scale PEM-WE applications.<sup>11</sup> Hence, a reduction in iridium loading is a necessity, which is tackled by the development of new catalysts. One possibility is the deposition of iridium nanoparticles on a porous and highly conductive support material (e.g., antimony doped tin oxide).<sup>12</sup> The synthesis of new catalysts can be time-consuming and is often done on a laboratory scale, yielding only a few milligrams. Reliable screening tools, such as scanning flow cell measurements (SFC)<sup>13-15</sup> or rotating disk electrode (RDE)<sup>16</sup> measurements are often used to assess catalyst activity and stability, requiring only a small amount of catalyst. The lifetimes obtained from these measurements, however, are orders of magnitude lower than those measured in a PEM-WE system.<sup>17</sup> Therefore, the long-term stability has to be assessed in a PEM-WE system, which not only requires a larger amount of catalyst (on the orders of grams rather than milligrams) but also the development of meaningful accelerated stress tests (ASTs). Within this PhD-thesis, some of these challenges will be analyzed and tackled in more detail.



## 2 Proton Exchange Membrane Water Electrolysis

The proton exchange membrane water electrolyzer (PEM-WE) provides an efficient way to produce hydrogen via the electrochemical splitting of water. A schematic of a PEM-WE is depicted in Figure 2.1, where a polymer based proton exchange membrane serves as an ionic conductor between anode and cathode as well as an electrical insulation and a gas barrier. On each side of the membrane the respective catalyst layer is attached, which provides sufficiently high catalytic activity for the desired electrochemical reactions. Aside from a high catalytic activity, the catalyst should also constitute a high electrical conductivity as well as a high porosity for the transport of water and the removal of the generated gas. To ensure sufficient proton conductivity, an ionomer is usually added to the catalyst layer. This setup is often referred to as the membrane electrode assembly (MEA) and represents the core component of a PEM-WE. The MEA is sandwiched between a titanium based porous transport layer (PTL) on the anode and a carbon fiber based gas diffusion layer (GDL) on the cathode, maintaining a proper water and gas transport and distribution. At both ends, a bipolar plate (BP) is completing the cell setup, providing electrical and thermal conductivity.

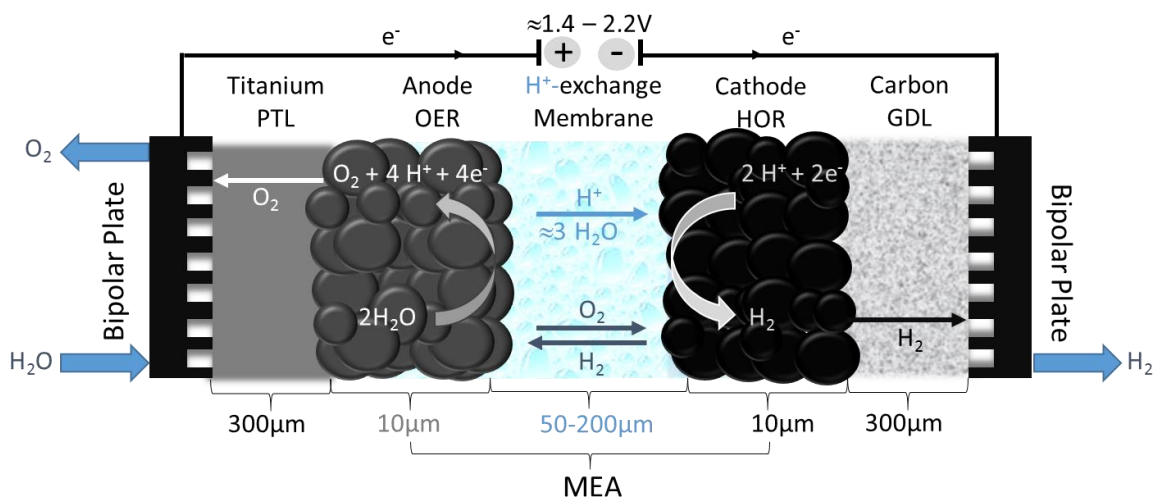


**Figure 2.1** Schematic of a proton exchange membrane water electrolyzer (PEM-WE) cell setup (the single components are not drawn to scale), depicting the MEA as the main component of the cell including the prevailing electrochemical reactions on each cathode and anode, as well as both diffusion media and the bipolar plates.

As depicted in Figure 2.1, the prevailing electrochemical reaction at the anode (positive electrode) is the electrochemical oxidation of water, namely the oxygen evolution reaction (OER; see equation 2.1) and the concomitant formation of protons ( $H^+$ ), electrons ( $e^-$ ) and oxygen ( $O_2$ ). While the protons driven by an electric field can move through the membrane to the cathode (negative electrode), the electrons are passed through an external electrical circuit

and are recombined with the protons to form hydrogen ( $H_2$ ) via the hydrogen evolution reaction (HER; see equation 2.2). The overall reaction in a PEM-WE is depicted in equation 2.3. Both gases ( $H_2$  and  $O_2$ ) are removed via the gas diffusion medium (cathode) or the porous transport layer (anode) to the gas outlets. Often water is only supplied to the anode side of the cell. Due to the electro-osmotic drag, however, water molecules will be transported through the membrane along with the protons during operation, thereby humidifying the cathode catalyst layer.



## 2.1 Efficiency and Voltage Losses

The production of hydrogen via the electrochemical splitting of water is one way to efficiently store energy, which is essential to use the full capabilities of renewable energies. Compared to the well-known alkaline water electrolysis, a PEM-WE bears the advantage to operate at high current densities ( $>2 \text{ Acm}^{-2}_{\text{geo}}$ ) and high pressures (up to  $\approx 165 \text{ bar}$ ),<sup>18-19</sup> while covering a wide power density window.<sup>20</sup> However, operating at higher pressures the overall efficiency will be reduced due to a cross-permeation of both oxygen and hydrogen. In the following section, the individual performance limiting losses are evaluated.

### 2.1.1 Thermodynamics

In order to electrochemically split water, both thermal as well as electrical energy input is required and is represented by the reaction enthalpy ( $\Delta H_R^0$ ) of the net water electrolysis reaction (see equation 2.3). Since the reaction enthalpy of both hydrogen and oxygen is  $0 \text{ kJ mol}^{-1}$  at standard conditions of  $298 \text{ K}$  and  $1 \text{ bar}$  partial pressure per definition, the reaction enthalpy can be represented by the formation enthalpy of liquid water ( $\Delta H_{l,H_2O}$ ), which is  $-286 \text{ kJmol}^{-1}$  at standard conditions (oxygen and hydrogen partial pressure of  $1 \text{ bar}$ ;  $T = 298 \text{ K}$ ).<sup>21</sup> The reaction enthalpy can be derived from the contributions of both the change in entropy ( $\Delta S_R$ ), representing the disorder of the system, as well as the change in Gibbs free energy ( $\Delta G_R^0 = 237 \text{ kJmol}^{-1}$  at standard conditions), the maximum work provided by the system as shown in equation 2.4.

$$\Delta H_R = \Delta G_R + T \cdot \Delta S_R \quad 2.4$$

If the system is operated at equilibrium and no additional losses occur, the reversible potential ( $E_{rev}^0$ ) will define the minimum electrical work that is required to allow the splitting of water. The reversible potential can be calculated by using the defined Gibbs free energy at standard conditions, the Faraday constant ( $F = 96485 \text{ Asmol}^{-1}$ ) and the number of electrons/charge transferred ( $z$ ) during the reaction (equation 2.5). By definition, the reversible potential for electrolytic cells is negative, however, in the electrolysis research community the absolute value is commonly used.

$$E_{rev}^0 = \left| -\frac{\Delta G_R^0}{z \cdot F} \right| = 1.229 \text{ V} \quad 2.5$$

If the thermal energy required is not provided externally, the system must provide enough energy ( $\Delta H_R^0$ ) to sustain the reaction and the so called thermoneutral potential ( $E_{th}^0$ ) can be calculated by equation 2.6.

$$E_{th}^0 = \left| -\frac{\Delta H_R^0}{z \cdot F} \right| = 1.481 \text{ V} \quad 2.6$$

When operated below  $E_{th}^0$ , the electrolyzer requires heat input from the environment in order to maintain the electrolyzer temperature. Moreover, the reversible potential ( $E_{rev}$ ) is also influenced by the temperature and activity of each individual species participating in the reaction ( $a_i$ ) and can be derived by the Nernst equation (equation 2.7), where  $R$  represents the ideal gas constant ( $8.314 \text{ Jmol}^{-1}\text{K}^{-1}$ ).

$$E_{rev} = E_{rev,T}^0 - \frac{R \cdot T}{2 \cdot F} \ln \left( \frac{a_{H_2O}}{a_{H_2} \cdot \sqrt{a_{O_2}}} \right) \quad 2.7$$

The activity of both hydrogen and oxygen can be approximated by the partial pressure normalized to the standard pressure (1 bar) and since the activity for liquid water is one, equation 2.7 can be simplified to equation 2.8.

$$E_{rev} = E_{rev,T}^0 - \frac{R \cdot T}{2 \cdot F} \ln \left( \frac{1}{\frac{p_{H_2}}{1bar} \cdot \sqrt{\frac{p_{O_2}}{1bar}}} \right) \quad 2.8$$

The reversible potential at different temperatures can be derived from equation 2.9.<sup>22</sup>

$$E_{rev,T}^0 = 1.2291 \text{ V} - 0.0008456 \text{ V} \cdot (T - 298.15 \text{ K}) \quad 2.9$$

Considering that commonly the operation temperature of an electrolyzer is around 80 °C and at atmospheric total pressure (1 bar), where the water vapor pressure is  $p_{H_2O} = 0.47$  bar, so that the oxygen and hydrogen partial pressures are 0.53 bar, e.g., equation 2.7 – 2.9 yield a reversible potential of  $E_{rev,80\text{ }^\circ\text{C}} = 1.168$  V.

Due to different losses, which will be explained in further detail within the next sections, the potential deviates from the ideally reversible potential, wherefore the cell efficiency ( $\varepsilon_{Cell}$ ) is one important parameter of the system. The cell efficiency represents the energy derived from a system (output) compared to the energy required to operate the system (input) and can be derived from equation 2.10, where  $\varepsilon_{Faradaic}$  represents the Faradaic efficiency and  $\varepsilon_{Voltage}$  represents the voltage efficiency.

$$\varepsilon_{Cell} = \varepsilon_{Voltage} \cdot \varepsilon_{Faradaic} \quad 2.10$$

As already mentioned, gas permeation through the membrane reduces the overall efficiency, which is captured by the Faradaic efficiency and depends on the materials used (membrane thickness and composition), the operation conditions (i.e., temperatures and pressure) as well as the current density applied. The Faradaic efficiency can be calculated by the actual amount of hydrogen produced ( $\dot{n}_{H_2,real}$ ), where crossover losses are accounted for versus the amount of hydrogen theoretically ( $\dot{n}_{H_2,theo}$ ) produced (equation 2.11).

$$\varepsilon_{Faradaic} = \frac{\dot{n}_{H_2,real}}{\dot{n}_{H_2,theo}} \quad 2.11$$

The voltage efficiency (see equation 2.12) can be calculated by the ratio of the amount of energy theoretically required ( $\Delta H_R^0$ ) and the actual energy provided by the system at a certain cell voltage.

$$\varepsilon_{Voltage} = \left| -\frac{\Delta H_R^0}{2 \cdot F \cdot E_{Cell}} \right| = \frac{E_{th}^0}{E_{Cell}} \quad 2.12$$

When liquid water is supplied to the cell, the voltage efficiency must be calculated based on the higher heating value (HHV), where the system must provide enough energy to evaporate water ( $\Delta H_{V,vap,H_2O}^0 = 44$  kJmol<sup>-1</sup>). If the efficiency of the individual steps is of interest or if the hydrogen is used in an application, where the condensation of water has no advantage, the lower heating value (LHV) will be used. In Table 2.1 both the enthalpies related to the HHV as well as the LHV are listed.

**Table 2.1** Enthalpy ( $\Delta H_{V,H_2O}^0$ ) of water splitting for both water being in the gaseous state (LHV) and water being in the liquid state (HHV) as well as the corresponding thermoneutral voltage ( $\Delta E_{th}^0$ ).

	$\Delta H_{V,H_2O}^0$ [kJmol <sup>-1</sup> ]	$\Delta E_{th}^0$ [V]
lower heating value (LHV)	242	1.25
higher heating value (HHV)	286	1.48

In a full electrolyzer plant, beside the stack efficiency itself, the whole balance of plant (BoP), amongst other compressor, heaters, etc. needs to be elaborated when calculating the system efficiency.

### 2.1.2 Kinetic Losses

Both electrochemical reactions, the OER (anode) as well as the HER (cathode), require a certain additional amount of energy for the reaction to occur at a given rate, expressed by the so-called activation overpotential ( $\eta_{act}$ ). The overpotential depends on the type of catalyst used as well as the operation pressure and temperature. The activation overpotential caused by the kinetics of the respective reaction leads to an increase in cell potential and thus to an irreversible loss in performance. The relationship between activation overpotential and current density can generally be described by the Butler-Volmer equation:

$$i_{cathodic/anodic} = i_o \cdot rf \cdot \left[ \exp\left(\frac{\alpha_a \cdot F \cdot \eta}{R \cdot T}\right) - \exp\left(\frac{\alpha_c \cdot F \cdot \eta}{R \cdot T}\right) \right] \quad 2.13$$

where  $i_{cathodic/anodic}$  describes the current for the forward and backward reaction in each half-cell and  $i_o$  is the exchange current density, which is a kinetic constant that describes the reaction rate at equilibrium and which depends on the electrocatalyst and electrolyte used. Note that here, for convenience  $\eta_{act}$  was simply expressed by  $\eta$ .  $rf$  is the roughness of the electrode, correlating the real surface area of the electrocatalyst with the geometric surface area of the electrode ( $\text{cm}_{\text{surface}}^2 / \text{cm}_{\text{electrode}}^2$ ).  $\alpha_a$  and  $\alpha_c$  describe the anodic and cathodic transfer coefficient and usually range between  $0 < \alpha_{a,c} < 1$ .  $\alpha$  represents the symmetry of the energy barrier for a redox process and the number of electrons involved in the rate determining step (rds). The difference between the applied potential and the reversible potential is the so-called overpotential ( $\eta$ ), being positive for a cathodic and negative for an anodic reaction.  $T$  is the temperature at which the system is operated,  $F$  the Faraday constant, and  $R$  is the ideal gas constant. In the following section, the overpotential of the HER and OER are analyzed individually.

### Kinetics of the hydrogen evolution reaction

The hydrogen evolution reaction on the cathode is commonly catalyzed by a platinum based electrocatalyst and it is well known that due to the fast kinetics of the HER on Pt the resulting overpotentials ( $\eta_{HER}$ ) are rather small,<sup>23-25</sup> wherefore equation 2.13 can be linearized to describe  $\eta_{HER}$ :

$$\eta_{HER} = i_{HER} \cdot \frac{R \cdot T}{(\alpha_a + \alpha_c) \cdot F \cdot i_{0,HER}} \cdot \frac{1}{L_{Pt} \cdot A_{Pt}} = i_{HER} \cdot \frac{R \cdot T}{(\alpha_a + \alpha_c) \cdot F \cdot i_{0,HER}} \cdot \frac{1}{rf} \quad 2.14$$

where  $\alpha_a$  and  $\alpha_c$  represent the symmetry coefficients of both the anodic (hydrogen oxidation) and the cathodic (hydrogen evolution) reaction. The exchange current density for the HER is represented by  $i_{0,HER}$  and is usually orders of magnitude larger ( $\approx 500 \text{ mA cm}^{-2}_{Pt}$ )<sup>23</sup> than for the oxygen reduction reaction ( $\approx 2.5 \cdot 10^{-5} \text{ mA cm}^{-2}_{Pt}$ )<sup>26</sup> wherefore the assumption of small overpotentials is valid.  $A_{Pt}$  is the electrochemically available Pt surface area in  $\text{cm}^2_{Pt} \text{ mg}^{-1}_{Pt}$  and  $L_{Pt}$  is the platinum loading in  $\text{mg}_{Pt} \text{ cm}^{-2}_{\text{electrode}}$ .

### Kinetics of the oxygen evolution reaction

The Butler-Volmer equation considers both the forward and backward reaction and shows an exponential increase in current with overpotential. At high overpotentials, however, the contribution of the reverse reaction becomes negligible, wherefore the Butler-Volmer equation can be simplified (see equation 2.15), as shown here for the OER at high overpotentials.

$$i_{OER} = i_o \cdot rf \cdot \left[ \exp\left(\frac{\alpha_a \cdot F \cdot \eta_{OER}}{R \cdot T}\right) \right] \quad 2.15$$

Rearranging equation 2.15, the direct relation between current and overpotential can be derived and is called the Tafel equation, where  $TS$  is the Tafel slope, representing the overpotential ( $\eta_{OER}$ ) required to increase the current by a factor of 10:

$$\eta_{OER} = \frac{2.303 \cdot R \cdot T}{\alpha_a \cdot F} \log\left(\frac{i_{OER}}{i_{0,OER} \cdot rf}\right) = TS \cdot \log\left(\frac{i_{OER}}{i_{0,OER} \cdot rf}\right) \quad 2.16$$

Plotting the  $iR$ -free (corrected for ohmic resistances, see chapter 2.1.3) cell voltage, measured against a stable reference potential (e.g., a reversible hydrogen reference electrode), versus the current on a logarithmic scale (Figure 2.2), the Tafel-slope ( $TS$ ) can be determined from the slope at low current densities (grey dashed line). The exchange current density can be

determined by extrapolating the fitted Tafel slope to the reversible cell voltage (i.e., to  $\eta_{OER} = 0$ ).

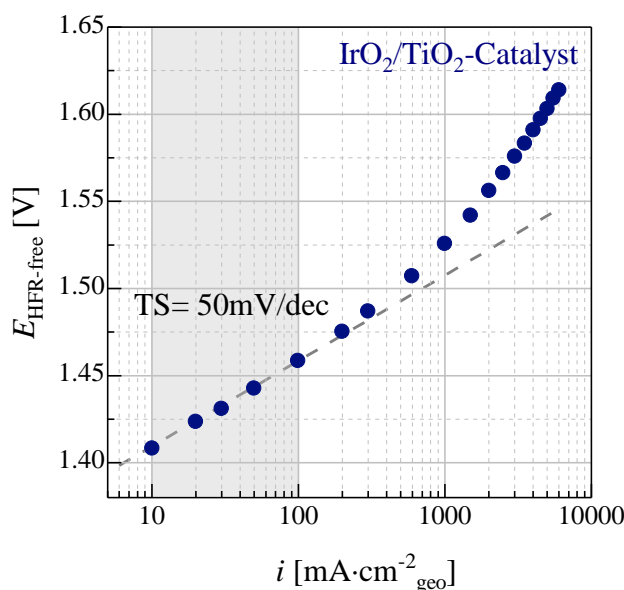


**Figure 2.2** Tafel plot of  $E_{\text{HFR-free}}$  vs  $\log(i)$  measured at 80 °C and ambient pressure in an MEA. An  $\text{IrO}_2/\text{TiO}_2$  (75 wt.-% Ir; Elyst Ir75 0480 from Umicore, Germany) catalyst was used on the anode ( $1.9 \text{ mg}_{\text{Ir}}\cdot\text{cm}^{-2}_{\text{geo}}$ ), while a Pt/C (45.8 wt.-% Pt; TEC10V50E from Tanaka, Japan) catalyst was used on the cathode ( $0.09 \text{ mg}_{\text{Pt}}\cdot\text{cm}^{-2}_{\text{geo}}$ ). The Tafel slope was determined between  $0.01 \text{ A cm}^{-2}_{\text{geo}}$  and  $0.1 \text{ A cm}^{-2}_{\text{geo}}$  (gray shaded region), where mass-transport losses can be neglected.

Choosing the right current range, where only the kinetic losses of the OER are dominant and where the HER kinetics and other losses such as proton transport within the electrodes or mass transport limitations are negligible, is crucial for a proper TS determination. At low current densities ( $10 - 100 \text{ mAcm}^{-2}_{\text{geo}}$ ) this criterion is fulfilled, yielding a TS of  $\approx 50 \text{ mVdec}^{-1}$ . The TS measured herein is in good agreement with the values reported by Bernt et al.,<sup>27</sup> where the TS for the same  $\text{IrO}_2/\text{TiO}_2$  based catalyst varies between  $45 - 50 \text{ mVdec}^{-1}$  and with the values reported by Matsumoto and Sato<sup>28</sup>, where the TS for a sputtered and thermally prepared  $\text{IrO}_2$  ranges between  $40 - 56 \text{ mVdec}^{-1}$ . Since there is a strong correlation between the hydration state and morphology of the iridium and its OER activity, the TS for crystalline  $\text{IrO}_2$  is usually higher than the one measured for amorphous  $\text{IrO}_x$  (see chapter 5.6), which is known to be more active towards the OER.<sup>29-30</sup> The TS can give an indication of the rate-determining step of the electrochemical reaction. While a TS of  $40 \text{ mVdec}^{-1}$  indicates that an electrochemical step is rate-determining (see equation 2.17), a TS closer to  $60 \text{ mVdec}^{-1}$  would indicate that a chemical step subsequent to the first electron transfer step is rate-determining (see equation 2.18).<sup>31-33</sup> Here, S illustrates a (active) surface site.



In order to extract the right kinetic information, a proper determination of TS is crucial. As can be seen in Figure 2.2, the iR-free cell voltage deviates from a linear behavior at higher currents ( $> 200 \text{ mAcm}^{-2}_{\text{geo}}$ ), which can be attributed to additional mass transport and proton conduction losses within the electrodes (see chapter 2.1.4).

### 2.1.3 Ohmic Losses

In addition to kinetic losses, the overall cell performance is also decreased by ohmic losses ( $R_{\Omega}$ ), originating from electrical contact resistances ( $R_{el}$ ) as well as proton transport resistances through the proton exchange membrane ( $R_{ionic}$ ):

$$R_{\Omega} = R_{el} + R_{ionic} \quad 2.19$$

The ohmic voltage losses can be represented by Ohm's law (see equation 2.20), whereby  $R_{\Omega}$  is often referred to as the high frequency resistance (HFR).

$$\eta_{\Omega} = i \cdot R_{\Omega} \quad 2.20$$

#### Electrical resistances

Electrical resistances are observed for the conduction of electrons through the cell components and their interfaces. Though highly conductive materials are used (i.e. carbon and titanium), an increased resistance at the interfaces is caused by geometrical junctions (i.e., low contact area) and possible resistive surface films as titanium oxide or hydrated iridium oxides. Depending on the applied pressure of the cell, Bernt et al.<sup>27</sup> showed that the contact resistance measured ex-situ (see chapter 3.2.5) for both the carbon as well as the Ti-PTL can vary between 5 – 10  $\text{m}\Omega\text{cm}^2$ . The contact resistance measured ex-situ, however, only accounts for the interface between the flow field (FF) and the carbon GDL as well as the interface between the FF and the Ti-PTL, wherefore the through-plane bulk resistivity of both materials needs to be considered as well. For Ti, the bulk resistivity is negligible, whereas the carbon bulk resistivity, according to the manufacturer, accounts for  $\approx 2 \text{ m}\Omega\text{cm}^2$ .<sup>27</sup> Summing these values up, the total electrical resistance at a pressure of 1.7 MPa on the lands of the FF would be  $\approx 12 \text{ m}\Omega\text{cm}^2$ .<sup>27</sup>



### Ionic resistances

The bigger contribution to the ohmic losses stems from the resistance of proton transport through the polymer electrolyte membrane ( $R_{ionic}$ ), which can be calculated via the thickness of the membrane ( $l_{membrane}$ ) as well as the conductivity of the membrane ( $\sigma_{membrane}$ ):<sup>20</sup>

$$\eta_{ionic} = i \cdot R_{ionic} = i \cdot \frac{l_{membrane}}{\sigma_{membrane}} \quad 2.21$$

Both the operating temperature as well as the water content in the membrane ( $\lambda \equiv \frac{mol_{H_2O}}{mol_{RSO_3H}}$ ) significantly influence the proton transport:<sup>34</sup>

$$\sigma_{membrane} = (0.005139 \cdot \lambda - 0.00326) \cdot \exp \left[ 1268 \cdot \left( \frac{1}{303} - \frac{1}{T} \right) \right] \quad 2.22$$

Here,  $\sigma_{membrane}$  is in units of  $\Omega \text{ cm}^{-1}$ , with T given in units of K. The water content of the membrane strongly depends on the pre-treatment and equivalent weight ( $EW \equiv \frac{g_{Polymer}}{mol_{RSO_3H}}$ ) of the membrane, the temperature as well as the relative humidity (RH).<sup>35</sup> Assuming that the membrane is always exposed to liquid water at a typical operating temperature of (80 °C), the water content at 80 °C would be  $\lambda \approx 21$ .<sup>36-38</sup> This would result in a membrane conductivity of  $\approx 190 \text{ mScm}^{-1}$  and is in good agreement with values reported experimentally.<sup>39</sup> Hence, this equation can be used to estimate the conductivity of a Nafion<sup>®</sup> membrane.

Since the membrane is exposed to liquid water, the wet thickness ( $l_{membrane,wet}$ ) needs to be considered when calculating the ionic resistance. In this case, only the through-plane expansion is considered, since little in-plane swelling is assumed due to the extreme aspect ratio of the membrane and the mechanical constraint at the edges of the membrane when compressed between the gaskets. Therefore, the increase in thickness ( $\Delta t_{membrane}$ ) can be estimated from the total increase in volume ( $\Delta V_{membrane}$ ):<sup>40</sup>

$$t_{membrane,wet} = t_{membrane,dry} \cdot \left( 1 + \frac{M_{H_2O} \cdot \rho_{membrane,dry} \cdot \lambda}{EW \cdot \rho_{H_2O}} \right) \quad 2.23$$

where  $\rho_{membrane,dry}$  is the density of the dry ionomer ( $\approx 2 \text{ gcm}^{-3}$  for Nafion<sup>®</sup>),  $\rho_{H_2O}$  the density of water,  $t_{membrane,dry}$  the dry film thickness of the membrane and  $M_{H_2O}$  the molar mass of water. For example, the film thickness of Nafion<sup>®</sup> 212 at 50%RH ( $\lambda = 3.7$ ) and 23 °C is  $\approx 50 \mu\text{m}$ ,<sup>41-42</sup> wherefore a dry film thickness of  $\approx 45 \mu\text{m}$  can be assumed. This would lead to an

increase in membrane thickness of  $\approx 50\%$  at  $80\text{ }^\circ\text{C}$  compared to the nominal thickness at  $23\text{ }^\circ\text{C}$  and when exposed to liquid water ( $\lambda \approx 21$ ).

#### 2.1.4 Transport Losses

##### Proton sheet resistance

Catalyst layers usually consists of the electrocatalyst as well as a proton conducting ionomer, whereby commonly perflourinated sulfonic acid based (PFSA) polymers are used (see chapter 2.3.1). Since the proton conduction mechanism within the catalyst layer is similar to the one in the membrane, this leads to an additional ionic resistance often referred to as the proton sheet resistance ( $R_{H^+,a/c}$ ). Contrary to the ionic resistance of the membrane, the effective proton sheet resistance ( $R_{H^+,c/a}^{eff}$ ) depends on the current density, even if the current distribution were uniform across the entire catalyst layer thickness. In this case the effective proton sheet resistance would equal 1/3 of the proton sheet resistance ( $R_{H^+,c/a}^{eff} = \frac{1}{3}R_{H^+,a/c}$ ). Since the through-plane electrical resistance of an electro-catalyst layer is usually significantly lower compared to its proton sheet resistance, the utilization and thus the local current density is highest at the membrane||electrode interface, except at very low current densities, where it is approximately uniform. Hence, the change in catalyst layer utilization across the electrode thickness needs to be considered or otherwise the voltage loss due to the proton conduction in the electrode would be overestimated.<sup>43</sup> Moreover, depending on the operation conditions (e.g., relative humidity) and the applied current density, the OER kinetics or the proton sheet resistance effect becomes dominating, thus influencing the current distribution within the electrode.<sup>44</sup>

The effective proton sheet resistance of the PEM-WE anode can be expressed by the following term:<sup>44-45</sup>

$$R_{H^+,a}^{eff} = \left( \frac{R_{H^+,a}}{\zeta + 3} \right) \quad 2.24$$

$$R_{H^+,a} = \frac{t_a}{\sigma \cdot V_{ion.wet} / \tau} \quad 2.25$$

where  $R_{H^+,a}$  depicts the area-based proton sheet resistance (see equation 2.25) within the whole catalyst layer and  $R_{H^+,a}^{eff}$  the effective proton sheet resistance responsible for the voltage loss during operation. In equation 2.25  $t_a$  is the anode electrode thickness,  $\sigma$  the conductivity of the ionomer,  $\tau$  the apparent tortuosity of the ionomer phase in the electrode and  $V_{ion.wet}$  the

ionomer volume fraction within the electrode when equilibrated with liquid water.<sup>27</sup>  $\zeta$  is a correction factor (see equation 2.26), accounting for the utilization of the electrode at different current densities, which can be described as a function of  $R_{H^+,a}$ ,  $i$  and the  $TS$ .<sup>46</sup>

$$\zeta = f\left(\frac{R_{H^+,a} \cdot i}{TS}\right) \quad 2.26$$

where  $i$  is the current density at which the system is operated and  $TS$  the Tafel slope. At low current densities ( $\zeta = 0$ ) equation 2.24 would result in the correlation derived from a transmission line model (TLM), which is often used to model the impedance spectra of porous electrodes (see chapter 2.2.2).

Commonly electrochemical impedance spectroscopy (EIS) is used to determine the proton sheet resistance within electrocatalyst layers. For this, the cell is usually operated with  $H_2/N_2$  on the counter/working electrode (often referred to as “blocking” conditions), so that the charge transfer kinetics of the working electrode become infinitely large and a simplified TLM can be applied to extract the proton sheet resistance.<sup>47-48</sup>

While the proton sheet resistance of the PEM-WE anode side can be derived from a Tafel kinetic approach, the proton sheet resistance on the PEM-WE cathode can be derived from the linear HER kinetics:<sup>43-44</sup>

$$\frac{R_{H^+,c}}{R_{H^+,c}^{eff}} = \frac{\beta}{\left(\frac{e^\beta + e^{-\beta}}{e^\beta - e^{-\beta}} - \frac{1}{\beta}\right)} \quad 2.27$$

with

$$\beta = \left(\frac{R_{H^+,c}}{R_{K,HER}}\right) \quad 2.28$$

where  $R_{H^+,c}$  is the area-based proton sheet resistance within the cathode and  $R_{H^+,c}^{eff}$  the effective proton sheet resistance responsible for the voltage loss due to proton conduction within the cathode catalyst layer.  $R_{K,HER}$  represents the charge transfer resistance of the HER on the cathode side:

$$R_{K,HER} = \frac{R \cdot T}{(\alpha_a + \alpha_c) \cdot F \cdot i_{0,HER}} \cdot \frac{1}{rf} \quad 2.29$$

### Mass transport losses

In order to run the electrochemical reaction, sufficient reactant, in this case water, needs to be supplied to the electrochemically active sites through both the porous transport layer as well as through the catalyst layer. At the same time, however, the produced gas needs to exit the cell in order to prevent any gas accumulation and thus blocking of active sites. One possible model to describe the transport losses in an electrolyzer is based on the assumption that the mass transport within the porous electrode is diffusion driven and can be described using Fick's law:<sup>20, 49</sup>

$$J = -D_{eff} \cdot \left( \frac{\delta C_i}{\delta x} \right) \quad 2.30$$

where  $D_{eff}$  is the effective diffusivity of the species  $i$ ,  $C_i$  is the molar concentration and  $J$  the diffusion flux. When the removal of produced gases is insufficient during operation, hydrogen and/or oxygen can accumulate within the electrode and lead to the blocking of active sites, thus slowing down the reaction. To account for these losses, Fick's law can be coupled with the Nernst equation:<sup>49</sup>

$$\eta_{diff} = \frac{R \cdot T}{z \cdot F} \ln \left( \frac{C_i}{C_{i,0}} \right) \quad 2.31$$

where  $C_i$  is the concentration of the active species at the membrane||electrode interface and  $C_{i,0}$  the concentration of the active species within the channels of the flow field.

## **2.2 Electrochemical Impedance Spectroscopy**

### **2.2.1 Complex Impedance**

To obtain a more detailed picture about the individual performance losses occurring during operation, one commonly applied in-situ technique is electrochemical impedance spectroscopy (EIS). Impedance spectroscopy is a non-destructive technique, which can be measured during operation without altering the working conditions. It represents the frequency-dependent resistance of an electrochemical system upon application of a sinusoidal potential ( $V_i$ ) or current ( $I_i$ ) perturbation (equation 2.32). The resistance ( $R$ ), measured in Ohm [ $\Omega$ ], of an ideal resistor is independent of the applied AC frequency and both the applied perturbation and the measured response are in phase. In case of capacitive or inductive elements the corresponding response in current ( $I(t)$ ) or potential ( $V(t)$ ) can be shifted in phase by  $\phi$  (equation 2.33).<sup>50</sup>

$$V_t = V_A \cdot \sin(\omega t) \quad 2.32$$

$$I(t) = I_A \cdot \sin(\omega t + \phi) \quad 2.33$$

where  $V_A$  and  $I_A$  are the individual amplitudes and  $\omega$  the angular frequency ( $2\pi f$ ).

Using Ohm's law (equation 2.34) the resistance can be determined by voltage over current. Based on this relationship the complex impedance  $\hat{Z}(\omega)$  is determined as the ratio of the complex voltage to the complex current (equation 2.35). From this the following expression for complex impedance (equation 2.36) can be derived, where  $\frac{V_A}{I_A(\omega)}$  is the  $\omega$ -dependent ratio of voltage to current amplitude.

$$R = \frac{V}{I} \quad 2.34$$

$$\hat{Z}(\omega) = \frac{\bar{E}(\omega)}{\bar{I}(\omega)} \quad 2.35$$

$$Z(\omega) = \frac{V_A}{I_A(\omega)} e^{j\phi(\omega)} \quad 2.36$$

with  $j \equiv \sqrt{-1}$ .

Applying Euler's formula the complex impedance can be transformed into a polar form (equation 2.37).<sup>51</sup>

$$Z(\omega) = |Z| \cdot \cos(\phi) + j \cdot |Z| \cdot \sin(\phi) = Re(Z) + j \cdot Im(Z) \quad 2.37$$

where  $Re(Z)$  represents the real part of the complex impedance and  $Im(Z)$  the imaginary part.

Nyquist plots are often used to depict the complex impedance (Figure 2.3).

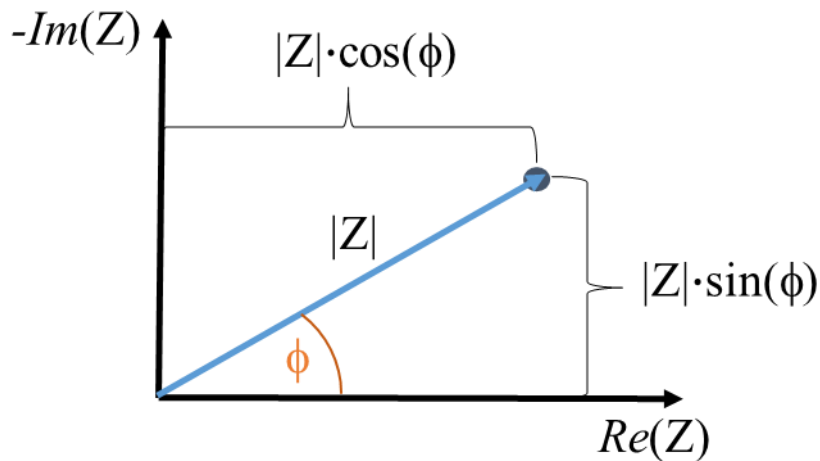


**Figure 2.3** Representation of a complex impedance (in a Nyquist Plot). Note that for electrochemical systems, it is common to plot  $-Im(Z)$  rather than  $Im(Z)$

By using equation 2.36 the complex impedance of circuit elements can be calculated. An overview of the resulting complex impedance of simple circuit elements is given in table 2.2.

**Table 2.2** Complex resistance of circuit elements, where  $L$  is the inductance [H] and  $C$  the capacitance [F].

	Resistor	Capacitor	Inductor
$Z(\omega)$	$R$	$\frac{1}{j\omega C}$	$j\omega L$

In an electrochemical system, multiple processes occur simultaneously during operation and hence, the recorded impedance is the sum of the impedances of the individual processes. Each process can be represented by an electrical circuit element using an equivalent circuit model (ECM), and by doing so the individual resistances can be extracted. The impedance in series (equation 2.38) and impedance in parallel rule both apply (equation 2.39).

$$Z^-(\omega) = \sum Z_k(\omega) \quad 2.38$$

$$Z^{||}(\omega) = \frac{1}{\sum Z_k(\omega)} \quad 2.39$$

Assuming a simple equivalent circuit model (Figure 2.4), the complex impedance can be calculated as followed:

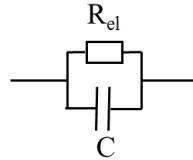


**Figure 2.4** Equivalent circuit model of an RC-element,  $Z_{el}||Z_C$

$$Z^{||}(\omega) = Z_{el}||Z_C = \frac{Z_{el} \cdot Z_C}{Z_{el} + Z_C} = \frac{-j \cdot R_{el}}{R_{el} \cdot C \cdot \omega - j} \quad 2.40$$

Equation 2.40 can be rewritten as

$$Z(\omega) = \frac{R_{el}}{1 + (R_{el} \cdot C \cdot \omega)^2} \cdot \{1 - j \cdot (R_{el} \cdot C \cdot \omega)\} \quad 2.41$$

which when plotted in a Nyquist plot corresponds to a semicircle with a diameter of  $R_{el}$ .

## 2.2.2 Equivalent Circuit Model for a PEM Water Electrolyzer

In an electrochemical PEM water electrolyzer cell multiple processes occur simultaneously and in order to capture all of the occurring processes and to obtain a proper determination of the single losses, the right choice for an equivalent circuit model is crucial. Overall one has to consider the contact resistances ( $R_{cont.}$ ), the charge transfer ( $R_{ct}$ ) and proton sheet ( $R_{H^+}$ ) resistances as well as the double layer capacitance ( $C$ ) for both anode and cathode. Additionally, the resistance of the membrane ( $R_{\Omega}$ ) has to be accounted for. Mass transport losses, represented by a Warburg diffusion element ( $Z_w$ ), are neglected since the cell is supplied with an excess of liquid water and far from the limiting current density. In Figure 2.5 a widely used equivalent circuit model representing the impedance of an electrolyzer cell is depicted.

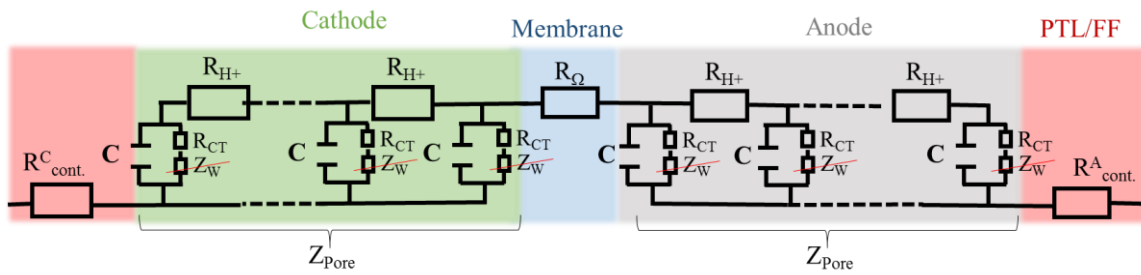


**Figure 2.5** Equivalent circuit model of a PEM water electrolyzer cell

The contact resistance along with the purely ohmic resistance of the membrane are current independent and can be represented by a simple resistor, often referred to as HFR (see equation 2.42).

$$HFR = R_{cont.} + R_{\Omega} = R_{cont.}^C + R_{cont.}^A + R_{\Omega} \quad 2.42$$

For each catalyst layer the double layer capacity ( $C$ ) as well as the Faradaic charge transfer resistance ( $R_{ct}$ ) need to be considered and are represented by one or several  $R||C$ -elements. Often a constant phase element (CPE) is used instead of a pure  $C$ -element in order to account for the inhomogeneous (non-ideal) catalyst surface.

Since both the OER as well as the HER are known to occur at the triple phase boundary (ionomer||catalyst||reactant-interface), the proton conduction within the catalyst layer needs to be considered and is represented by a resistor ( $R_{H^+}$ ). The model widely used as an approach to depict the electrical network within a porous electrode (i.e., represents the green shaded or the grey shaded regions in Figure 2.5) is called transmission-line model (TLM, see equation 2.43).<sup>40, 52-53</sup>

$$Z_{pore} = Z_{||} + Z^* \frac{1 + 2 \cdot p \cdot s [\sqrt{1 - \tanh(\nu)^2} - 1]}{\tanh(\nu)^2} \quad 2.43$$

with

$$Z_{||} = \frac{Z_p \cdot Z_s}{Z_p + Z_s} \quad 2.44$$

$$Z^* = \sqrt{(Z_p + Z_s) \cdot Z_Q} \quad 2.45$$

$$p = \frac{Z_p}{Z_p + Z_s} \quad 2.46$$

$$s = \frac{Z_s}{Z_p + Z_s} \quad 2.47$$

$$\nu = \sqrt{\frac{Z_p + Z_s}{Z_Q}} \quad 2.48$$

where  $Z_p$  is the impedance of the ionically conducting pore phase,  $Z_s$  is the impedance of the electron conducting solid phase, and  $Z_Q$  represents the impedance of the electrolyte||solid interface.<sup>53</sup> Here, a similar approach was used as in the study by Landesfeind et al.<sup>53</sup>  $Z_p$  describes the ionic resistance within the electrode ( $R_{pore}$ ),  $Z_s$  is defined by the electrical resistance within the electrode ( $R_{el}$ ), and  $Z_Q$  is described by an R||C-element (equation 2.49), representing the charge transfer resistance ( $R_{ct}$ ) and capacitive elements at the catalyst layer||electrolyte interface ( $Q$ ).

$$Z_Q = \frac{R_{ct}}{R_{ct} \cdot Q_{ct} \cdot (i\omega)^{\alpha_{ct}} + 1} \quad 2.49$$

In Figure 2.6 the impedance spectra of a 5 cm<sup>2</sup> PEM-WE cell using two Nafion<sup>®</sup> 212 membranes at two different current densities are depicted. At the cathode side, a Pt/C based catalyst is used for the HER. As shown in chapter 2.1.2, the kinetics of the HER on Pt/C is quite fast and therefore the associated charge transfer resistance assumed negligibly small. Hence, it is assumed that the ECM shown in Figure 2.5 can be simplified by removing the cathode circuit elements, and that the anode is dominating the impedance response. At high frequencies the impedance spectra exhibits a 45°-region (red dotted line) arising from the proton sheet resistance, with a subsequent semi-circle (green half-circle) representing the R||C-elements of the anode catalyst layer.

In the limit of  $f \rightarrow \infty$ , the capacitors in Figure 2.5 have zero resistance, hence the total impedance equals  $R_{cont.}^C + R_{cont.}^A + R_{\Omega} = \text{HFR}$ . Ideally, the HFR can be estimated from the



high-frequency intercept with the real axis of a Nyquist plot. Due to inductive effects at high frequencies, however, the HFR determined from the intercept is usually higher than the one obtained by using an ECM, where the inductance can be taken into account. Hence, one can use the intercept to estimate the HFR, for a precise determination however, the inductance needs to be considered. The contact resistances can be determined ex-situ (see chapter 3.2.5) and by subtracting the contact resistances in addition to the carbon-GDL bulk resistance ( $\approx 2 \text{ m}\Omega\text{cm}^2$ )<sup>27</sup> (the bulk resistance of the Ti-PTL is negligibly small), from the HFR, the membrane resistance can be determined. In a study by Bernt et al.,<sup>27</sup> the overall contact resistance (flow-field||Ti-PTL + flow-field||C-GDL) including the carbon-GDL bulk resistance was determined to be ( $\approx 12 \text{ m}\Omega\text{cm}^2$ ).<sup>27</sup> Assuming that the contact resistances account for  $\approx 12 \text{ m}\Omega\text{cm}^2$  and that both Nafion<sup>®</sup> 212 membranes behave equally, this would result in a membrane resistance of  $40 \text{ m}\Omega\text{cm}^2$  for the depicted measurement in Figure 2.6, being in good agreement with what can be calculated by equation 2.21.

A platinum-based catalyst is typically used for the HER, which exhibits fast kinetics towards the HER. As shown in chapter 2.1.2, the charge transfer kinetics can be estimated using a linearized Butler-Volmer approach (see equation 2.14). Assuming a typical Pt loading of  $L_{\text{Pt}} = 0.3 \text{ mg}_{\text{Pt}}\text{cm}^{-2}$  and an electrochemically available Pt-surface area of  $A_{\text{Pt}} = 60 \text{ m}^2_{\text{Pt}}\text{g}_{\text{Pt}}^{-1}$ ,<sup>44</sup> this would equate to a charge transfer resistance for the HER of  $\approx 0.3 \text{ m}\Omega\text{cm}^2$ . Compared to the overall resistance excluding the ohmic and the contact resistances (Figure 2.6;  $\Delta R \approx 110 \text{ m}\Omega\text{cm}^2$ ), the charge transfer resistance at the cathode accounts for only  $\approx 0.2\%$  and is hence often neglected. This might be valid for low current densities, where the charge transfer of the anode is dominant and the charge transfer from the cathode is comparably small. At higher current densities, however, the contribution from the cathode becomes more significant ( $\approx 1.8\%$ ) and hence the contributions arising from the cathode, including charge transfer and proton sheet resistance have to be accounted for. In their study Bernt et al.<sup>27</sup> also estimated the effective proton sheet resistance on the cathode and anode to be  $\approx 2.5 \text{ m}\Omega\text{cm}^2$  and  $14 - 30 \text{ m}\Omega\text{cm}^2$  respectively. As will be shown later (chapter 4.6), the proton sheet resistance estimated by Bernt et al.<sup>27</sup> for the anode matches quite well with the one measured in “blocking” conditions. Although the contribution of the proton sheet resistance within the cathode is smaller compared to the anode, one would need to determine the proton sheet resistance of the cathode and anode individually in order to justify any simplifications.

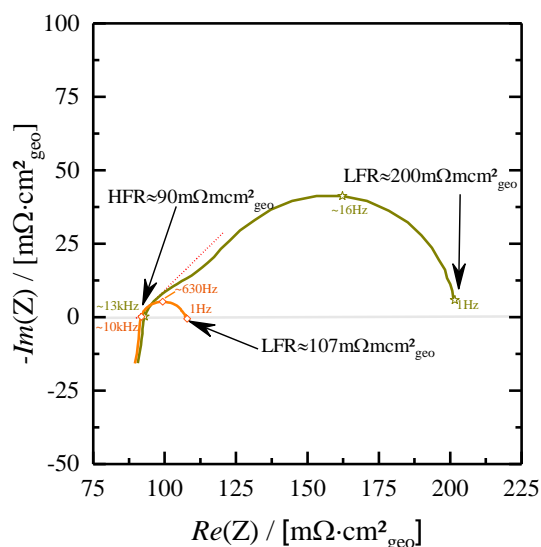


**Figure 2.6** Electrochemical impedance spectrum of a PEM-WE anode during a voltage hold at 1.5 V (green curve) and 1.9 V (orange curve) of a 5 cm<sup>2</sup> PEM water electrolysis cell recorded at 80 °C, 1 bar<sub>a,cathode</sub>, 1 bar<sub>a,anode</sub>, and 5 mL<sub>H<sub>2</sub>O</sub> min<sup>-1</sup>; MEA specifications: ≈2 mg<sub>Ir</sub> cm<sup>2</sup><sub>MEA</sub> anode and ≈0.3 mg<sub>Pt</sub> cm<sup>2</sup><sub>MEA</sub> cathode loading, using two Nafion® 212 (≈50 μm) membranes and a 50 μm Pt-wire with a 9 μm PTFE insulation as a reference electrode (see chapter 4).

Due to the sluggish reaction kinetics of the OER, the contribution arising from the charge transfer of the anode dominates the overall impedance. A more detailed analysis regarding the charge transfer kinetics for the OER as well as the proton sheet resistance of the anode is provided in chapter 4.6.

Overall, the ECM for a PEM-WE cell is quite complex and an unambiguous determination of the single losses is rather challenging. Properly defined ECMs as well as a-priori knowledge of the system under study are required to obtain meaningful information from the impedance measurement. Moreover, by adjusting the conditions during operation (e.g., blocking conditions)<sup>40, 47</sup> or using a reference electrode, the determination of individual parameters is possible.<sup>54-55</sup>

## 2.3 Materials and Components

### 2.3.1 Polymer Electrolyte Membrane

The most commonly used polymer electrolyte membrane is the Nafion<sup>®</sup> membrane from DuPont<sup>®</sup>, which is based on a perfluorosulfonic acid (PFSA) ionomer, comprising of a polytetrafluoroethylene (PTFE) backbone and sulfonic acid groups at the end of double ether perfluoro side chains (Figure 2.7).

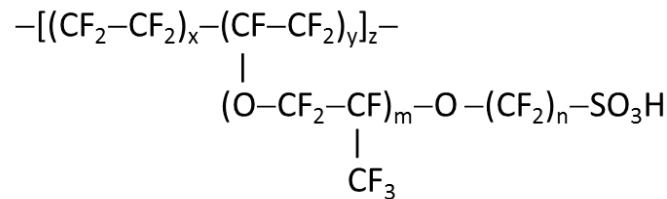


**Figure 2.7** Chemical Structure of perfluorosulfonate membrane; For Nafion<sup>®</sup>  $m \geq 1$ ,  $n=2$ ,  $x=5-13$ ,  $y=1000$ .<sup>33</sup>

PFSA based membranes offer a high thermal and chemical stability, along with a good mechanical strength, while still providing sufficiently high proton conductivity.<sup>42</sup> The proton conductivity of the membrane, however, strongly depends on the hydration state and thus the water uptake ( $\omega$ ) of the membrane:

$$\omega [\%] = \frac{\omega_{wet} - \omega_{dry}}{\omega_{dry}} \quad 2.50$$

where  $\omega_{dry}$  is the dry mass of the membrane and  $\omega_{wet}$  is the mass of the hydrated membrane. More commonly the water content ( $\lambda$ ) of the membrane in terms of molecules of water ( $mol_{H_2O}$ ) per sulfonic acid group ( $mol_{SO_3H}$ ) is used (see chapter 2.1.3):

$$\lambda = \frac{\omega \cdot EW}{M_{H_2O}} \quad 2.51$$

where EW is the equivalent weight ( $g_{ionomer} mol_{SO_3H}^{-1}$ ) of the ionomer and  $M_{H_2O}$  the molar mass of water ( $18 g mol^{-1}$ ). The water content of the membrane strongly depends on the activity of water and temperature. Usually, an electrolyzer is operated with liquid water, wherefore a change in water content during operation is highly unlikely and a fully humidified membrane, with sufficiently high proton conductivity can be assumed. One major drawback, however, is the decreasing proton conductivity due to the loss of water beyond  $100^\circ C$  under ambient pressure conditions, which limits the operation range of PFSA based membranes at ambient pressure. Higher temperatures, however, would be beneficial due to i) improved kinetics (lower overpotential), ii) a decreased membrane resistance and iii) a lower reversible potential (less

heat to radiate).<sup>56-57</sup> Operating the cell at temperatures beyond 100 °C while still maintaining the liquid state of water would be possible when operated at elevated pressures (e.g., 3 bar<sub>a</sub> and 120 °C).<sup>58</sup>

Another main task of the membrane is preventing gas crossover of both O<sub>2</sub> and H<sub>2</sub> during operation, which can lead to the formation of explosive mixtures (≥4% H<sub>2</sub> in O<sub>2</sub>), a more complex purification process for hydrogen in case a high purity is required (e.g., for use in a PEM fuel cell),<sup>59</sup> and a decrease in efficiency (see chapter 2.1). It was recently shown, that with increasing current density and increasing operation pressure hydrogen crossover increases.<sup>59-60</sup> In order to operate the system at ≥70%<sub>LHV</sub> and within non-explosive regime, only a small operation range (1 – 2 Acm<sup>-2</sup><sub>geo</sub>) is feasible for a Nafion<sup>®</sup> 117 (150 μm) at 30 bar<sub>cathode</sub>.<sup>60</sup> A smaller ohmic overpotential by decreasing the membrane thickness would be desirable, but since the gas crossover is inversely proportional to the thickness of the membrane (see equation 2.52), a safe operation (outside of the explosion limit) at ≥70%<sub>LHV</sub> could not be realized with a Nafion<sup>®</sup> 212 (50 μm) membrane at 30 bar<sub>cathode</sub>.<sup>60</sup> The permeation rate  $N_{gas}^{perm}$  can be estimated based on

$$N_{gas}^{perm} = K_{P,gas} \cdot \frac{\Delta p_{gas}}{\delta_{membrane}} \quad 2.52$$

where  $K_{P,gas}$  denotes the permeability coefficient,  $\delta_{membrane}$  the thickness of the membrane, and  $\Delta p_{gas}$  the partial pressure difference between anode and cathode of the individual gas.

One possible mitigation strategy is the incorporation of a recombination catalyst, into the membrane (i.e., Pt), catalyzing the recombination of hydrogen and oxygen would recombine to water, thus lowering the gas crossover and preventing the formation of an explosive mixture.<sup>61</sup>

Moreover, during electrolyzer operation water is dragged along with protons via the electro-osmotic drag ( $n_{drag}$ ) from the anode to the cathode side, depending on the temperature and water content of the membrane. It was shown that the electro-osmotic drag varies between 2.5 – 2.9 at 30 °C when operated with liquid water. At different temperatures, with liquid water  $n_{drag}$  can also be derived from the following correlation, yielding in a slightly higher drag coefficient of ≈4 at 30 °C:<sup>39, 62</sup>

$$n_{drag} = 0.0134 \cdot T + 0.03 \quad 2.53$$

Within equation 2.53 T is in the units of K.

The drag of water through the membrane is an important parameter when designing the balance of plant (BoP) for an electrolyzer (e.g., pumps, recirculation, hydrogen processing).

### 2.3.2 Hydrogen Evolution Catalyst

From fuel cell literature it is well known that the kinetics of the hydrogen evolution reaction on platinum in acidic media are fast, and therefore a reduction in loading (to as low as  $\approx 0.05 \text{ mg}_{\text{Pt}} \text{ cm}^{-2}_{\text{geo}}$ ) without any significant losses ( $< 3 \text{ mV}$ ) is possible.<sup>23, 25, 63</sup> While in the beginning Pt-black was applied as a HER catalyst, the support of Pt-nanoparticles on highly conductive and high surface area carbon ( $\approx 250 \text{ m}^2 \text{ g}^{-1}_{\text{Carbon}}$ )<sup>45</sup> allowed for a significant reduction in Pt-loading due to an improved utilization of the platinum. The spherical carbon particles (30 – 40 nm diameter) coalesced into highly structured primary agglomerates constitute a high-structured support material that lead to highly porous electrodes. Owing the high volume fraction of carbon within the catalyst layer for a typical 50 wt.-% Pt/C catalyst, 3 – 5  $\mu\text{m}$  thick catalyst layers with low Pt loadings can be prepared.<sup>64</sup> Based on both the fast HER kinetics and the possibility to reduce the Pt-loading (wt.-% Pt) by using a high surface area carbon support, Bernt et al.<sup>65</sup> showed that the Pt-loading on the cathode of a PEM-WE can be significantly reduced (to as low as  $\approx 0.025 \text{ mg}_{\text{Pt}} \text{ cm}^{-2}_{\text{geo}}$ ) without any significant losses in performance.

### 2.3.3 Oxygen Evolution Catalyst

According to previously established so-called Volcano plots, evaluating the activity of different catalysts, iridium and ruthenium provide the highest activity towards the oxygen evolution reaction;<sup>66</sup> however, due to the low stability of ruthenium at high potentials, iridium in the form of oxides is commonly the catalyst of choice.<sup>28, 66-67</sup> Owing the relatively low specific surface area of iridium in state-of-the-art commercial catalysts and the thus low utilization of iridium, relatively high iridium loadings ( $\approx 2 \text{ mg}_{\text{Ir}} \text{ cm}^{-2}_{\text{geo}}$ ) on the anode are used to ensure sufficiently high performance.<sup>20</sup> A lot of effort has been put in reducing the anode catalyst loading and hence the overall catalyst costs over the past years, focusing on either increasing the intrinsic activity by alloying<sup>68-69</sup> or increasing the specific surface area of iridium by, e.g., the use of support materials.<sup>12</sup>

Even though it was shown that the activity along with the stability could be improved by mixing  $\text{RuO}_2$  with  $\text{IrO}_2$ ,<sup>70-71</sup> still a rather high loading of noble metal would be necessary to ensure a good performance. Therefore, the more feasible approach is the reduction of the overall noble metal content by the use of a support material. One of the most commonly used OER catalysts is  $\text{IrO}_2$  supported on  $\text{TiO}_2$  (e.g.,  $\text{IrO}_2/\text{TiO}_2$  with 75 wt.-% iridium; Elyst Ir75 0480 from Umicore,

Germany), where the electrical conductivity is provided through the IrO<sub>2</sub> layer, since TiO<sub>2</sub> itself has a rather low conductivity.<sup>72</sup> Hence a high amount ( $\approx 75$  wt.-% Ir) of iridium is necessary to ensure a continuous layer of iridium covering the TiO<sub>2</sub>, wherefore low loadings cannot be realized with this type of catalyst due to its high packing density ( $\approx 2.3$  g<sub>Ir</sub>·cm<sup>-3</sup>) and the resulting very thin and inhomogeneous electrode layers at low loadings ( $< 0.05$  mg<sub>Ir</sub>·cm<sup>-2</sup><sub>geo</sub>).<sup>65</sup> In order to efficiently reduce the amount of iridium, a highly structured support material, that provides sufficiently high conductivity ( $> 0.01$  S·cm<sup>-1</sup>) and is stable at the PEM-WE operating conditions (high potentials and acidic environment) is necessary.<sup>33</sup> This approach would be similar to the design of the Pt/C catalyst used as an HOR catalyst and will be discussed in further detail in chapter 5.2 (“*Rational Design and Synthesis of Iridium Oxide Catalyst Supported on Antimony-Doped Tin Oxide for High Oxygen Evolution Reaction Activity in Acidic Media*”).

### 2.3.4 Porous Transport Layers

The two main tasks of the porous transport layer (PTL) in a PEM-WE are on the one hand the homogenous distribution of water (reactant) across the active area of the MEA, while at the same time efficiently removing the produced gases (hydrogen/oxygen) and ensuring good electrical connectivity between the electrode layer and the bipolar plates. A planar and smooth geometry with sufficiently high porosity and good electrical conductivity is needed to prevent any damage of the catalyst layer and the membrane (e.g., shorting, formation of hot-spots) and to ensure efficient mass transport of liquid water and gases. While on the cathode side carbon paper or carbon cloths are usually applied as gas diffusion layers (GDL), the high potentials which would lead to the oxidation and thus the corrosion of carbon (COR; see equation 2.54), excludes this type of material at the anode.



The state-of-the-art material for the PTL at the anode is titanium, due to its sufficiently good stability in the acidic environment and at high anodic potentials. However, one main disadvantage is the formation of a poorly conductive TiO<sub>2</sub> surface film due to the oxidation of titanium at high anodic potentials, leading to an increased ohmic contact resistance,<sup>73</sup> wherefore an additional coating is often used to prevent the passivation of the titanium.<sup>74-75</sup> Besides a good electrical conductivity, the morphology, especially the porosity of the PTL is extremely important. If the pores are too small, mass transport limitations can easily occur due to the trapping of oxygen and water within the PTL. On the other hand, a high porosity (large pores) would enhance the gas transport but also result in a decreased electrical contact area. Therefore, a balanced design of the PTL is one of the main challenges in the design of a PEM electrolyzer

to improve catalyst utilization, electrical contact resistances, and mass transport.<sup>76-77</sup> Commonly, sintered powder type materials or felts are used due to their adjustable porosity. While the porosity (50 – 80%) and pore sizes (20 – 200  $\mu\text{m}$ ) can be varied more freely for different felts, the sintered powder materials are more rigid, which is beneficial when operating at elevated pressures.<sup>33</sup>

### **2.3.5 Bipolar Plates**

The bipolar plates provide the framework for an electrolyzer cell as well as a separation of adjacent cells within a stack, which is why they are also often called separator plates. They provide electrical contact between adjacent cells, while at the same time separating the different gas environments. Usually deionized water ( $\text{pH} \approx 6 - 7$ ) is fed to the cells, wherefore the requirements for the materials of choice are less specific than for PTLs or catalyst support materials. Nevertheless, bipolar plates have to provide sufficiently high electrical and thermal conductivity, mechanical stability and need to be gas-tight to prevent any gas-leakage between the single cells. Since they connect adjacent cells electrically with each other, they have to be stable at both high anodic and cathodic potentials. Titanium is often used to manufacture PEM-WE bipolar plates, owing its excellent strength, high initial thermal and electrical conductivity. However, its surface passivation over time and the accompanied increase in electrical contact resistance leads to a decreasing performance over time,<sup>73</sup> and similar to the PTL, an additional protective coating would be necessary to maintain the initially high electrical conductivity over the required lifetime of the system (10 – 20 years).<sup>20</sup> Cheaper materials such as stainless steel are considered as an alternative; however, an additional coating to prevent corrosion is inevitable in this case. To prevent the formation of any potential weak spots, where corrosion might take place, a homogenous and continuous coating is essential. Contrary to the bipolar plates applied in fuel cells, the bipolar plates for electrolysis systems utilizing a small cell area do not necessarily require the implementation of a flow field.<sup>20</sup> Depending on the operation conditions, the cell design and morphology of the PTL, a flow field might not be necessary to handle the mass transport of both produced gas and liquid water.

## **2.4 Operation Conditions**

### **2.4.1 Temperature**

Commercial state-of-the-art PEM water electrolyzer operate at temperatures up to 60  $^{\circ}\text{C}$ ,<sup>78-79</sup> though a higher operating temperature would be desirable to improve the performance. At higher temperatures not only the activation losses ( $\eta_{\text{act}}$ ) as well as the ohmic losses arising from

the membrane would be lower, but also less electrical energy would be required due to a lower reversible potential at higher temperatures.<sup>11, 56</sup> Babic et al. showed the impact of temperature on cell performance, where a significant decrease in cell voltage as well as ohmic resistance was observed when increasing the temperature from 60 °C to 80 °C.<sup>11</sup> At elevated pressures (e.g., 3 bar<sub>a</sub>) the operation of a PEM-WE beyond 100 °C (e.g., 120 °C), while still sustaining the liquid state of water, would be possible, however, the increased gas crossover at higher temperatures and pressures as well as the durability of the membrane under such conditions may be challenging. While C. K. Mittelstaedt showed that the chemical stability of state-of-the-art membranes does not seem to limit the operation at elevated temperatures,<sup>56</sup> the mechanical stability of the polymer especially at high differential pressures could bear a safety risk. Recently, Garbe et al. showed that, increasing the temperature while decreasing the membrane thickness, the hydrogen permeation increases significantly and that, when considering a safety limit of 2% H<sub>2</sub> in O<sub>2</sub>, operating the cell at 120 °C and 3 bar<sub>a</sub> with a thin membrane (Nafion<sup>®</sup>212; 50 μm) at current densities <0.76 Acm<sup>-2</sup><sub>geo</sub> is not possible.<sup>58</sup> Short side-chain PFSA polymers might be a promising option when aiming for higher temperatures due to their higher crystallinity observed, when compared to a long side-chain PFSA polymer at the same equivalent weight.<sup>11, 80</sup> Although some promising material improvements were already established, the stability challenges for today's commonly used PFSA polymers along with the temperature limitations for the ion-exchanging resins, which are used to ensure a high purity of the feed water, still determine the operation temperature for state-of-the-art PEM-WE.<sup>11</sup>

## 2.4.2 Pressure

Desirably hydrogen is stored at elevated pressures and depending on the application up to 1000 bar (in case of a H<sub>2</sub> fueling station) are required,<sup>81</sup> while common state-of-the-art electrolyzers operate at a pressure up to 35 bar.<sup>78</sup> Pressurizing hydrogen electrochemically would spare additional mechanical pressurizing steps and hence lower the maintenance and investment costs. An electrolyzer can be operated at either balanced pressure, where anode and cathode are operated at the same pressure, or at differential pressure, where the cathode is usually operated at higher pressures. From a thermodynamic point of view operating at elevated pressures is disadvantageous, since the absolute value of the reversible cell voltage would increase:

$$\Delta E_{rev} = \frac{R \cdot T}{2 \cdot F} \ln \left( \frac{p_{H_2}}{p_{H_2}^\circ} \right) \quad 2.55$$



where  $p_{H_2}^\ominus$  is the pressure at standard conditions,  $p_{H_2}$  the applied pressure, and  $\Delta E_{rev}$  the shift of the absolute value of the reversible cell voltage when operated at elevated pressure. Exemplarily, increasing the  $H_2$  partial pressure from 1 to 30 bar while keeping the  $O_2$  partial pressure constant would lead to a positive shift in  $E_{rev}$  of  $\approx 50$  mV at  $80^\circ C$ . On the contrary, operating at higher pressures should be beneficial in terms of overpotentials caused by gas bubbles trapped within the catalyst layer, due to a decreased gas bubble size<sup>82-83</sup> and improved mass transport.<sup>84</sup> Bernt et al.<sup>27</sup> showed that operating a PEM-WE cell at a cathode pressure of 30 bar<sub>a</sub> the cell voltage beyond  $300 \text{ mAcm}^{-2}_{geo}$  is lower than what would have been expected from a thermodynamic point of view based on the performance data at 1 bar<sub>a</sub> cathode pressure. Since the oxygen side was operated at ambient pressure in their study, the improved performance was attributed to an increase in partial pressure of hydrogen within the catalyst layer and thus decreased mass transport resistances on the cathode side. However, they also showed that at lower current densities the hydrogen permeation through the membrane is similar to the oxygen production rate and hence an explosive mixture can be formed on the anode ( $>4\% H_2$  in  $O_2$ ).<sup>85</sup> Thus, operating at higher  $H_2$  pressures might be beneficial in terms of cost reduction, but the increased  $H_2$  permeation would lead to lower faradaic efficiencies and safety issues. Since the hydrogen crossover is not only a function of pressure but depends also on the thickness of the membrane,<sup>60</sup> in future scenarios where thinner membranes should be applied in order to decrease the ohmic losses particularly at the envisaged high current densities, the hydrogen crossover and the accompanied safety issue will become even more important. To circumvent the formation of an explosive gas mixture, platinized current collectors or recombination catalysts within the membrane are proposed.<sup>83, 86</sup> Nevertheless, reliable operation of a PEM water electrolyzer system for  $\approx 20.000$  h was shown by Ayers et al.,<sup>18</sup> where the cathode was operated at pressures up to 165 bar while the anode was operated at ambient pressure.

## 2.5 Degradation Phenomena

### 2.5.1 Membrane

One of the main degradation mechanisms observed for Nafion<sup>®</sup> based electrolytes is an increasing ohmic resistance<sup>11, 87</sup> due to the presence of cations through either improperly treated feed water or due to corrosion of the used materials.<sup>88-90</sup> By ion-exchanging the protons within the polymer electrolyte membrane as well as within the ionomer in both catalyst layers, the proton transport resistance increases, ultimately leading to the failure of the system. Sun et al.<sup>91</sup>

showed that after boiling a used membrane in sulfuric acid the initial performance can mostly be recovered and hence attributed the decreasing performance over time (7800 h) to cationic contamination. Commonly water purification ion-exchange (e.g., ion-exchange resins) and corrosion-resistant coatings<sup>92</sup> are applied to prevent cationic contaminations and quite recently Babic et al.<sup>93</sup> proposed a CO<sub>2</sub>-assisted regeneration method, where cationic contaminations can be removed during operation. In addition to an increase in ohmic resistance, Fenton's active cations (e.g., Fe, Ni) can promote the formation of radicals (e.g., OH•, H•) and thus the chemical degradation of the membrane through a peroxy attack of the ionomer endgroup, which can lead to the formation of pinholes and cracks.<sup>94</sup> Usually the extent of chemical degradation of the membrane is measured through the hydrofluoric acid (HF) release rate, a product which is formed during the radical attack of the endgroups. Since hydrogen terminating endgroups are assumed to be the preferred point of attack, modified Nafion<sup>®</sup> membranes are used nowadays, which show a significantly lower chemical degradation.<sup>95</sup> It was also shown that the degradation of the membrane strongly depends on the relative humidity during operation and that operation at low relative humidity accelerates membrane degradation.<sup>96</sup> This, however, seems to be less of an issue for PEM water electrolyzers, since they are commonly operated with liquid water.

Other than the mentioned chemical induced degradation, mechanical stressors resulting in the deterioration of the membrane cannot be neglected. The main failure mechanisms caused by mechanical stress are the penetration of the membrane through large protruding particles or fibers from either the catalyst layer or the PTL as well as tear formation induced by temperature and RH changes.<sup>97-98</sup> The Ti-based PTLs, which are commonly used at the anode side, are more stiff and rigid compared to the carbon GDL applied on the cathode. However, the risk of protruding fibers is quite high, especially when a fiber based PTL and thin membranes (< 50 μm) are used. Therefore, the fabrication of a smooth surface as well as a proper sealing within the cell is important.

### 2.5.2 Catalyst Layer

As already mentioned in chapter 2.3.3, IrO<sub>2</sub> is the catalyst of choice due to its superior stability compared to RuO<sub>2</sub>.<sup>99</sup> According to the Pourbaix diagram, depicting the thermodynamic stability of metals as a function of potential and pH, IrO<sub>2</sub> is stable at high potentials (>1.0 V) and over a wide pH-range.<sup>100</sup> The desired crystalline IrO<sub>2</sub> can be obtained through annealing, where a certain temperature (> 400 °C) is required to actually form a thick layer of crystalline IrO<sub>2</sub> at the surface,<sup>29</sup> while otherwise an amorphous hydrous Ir(OH)<sub>x</sub> will be formed. Even though the OER activity of an amorphous hydrous Ir(OH)<sub>x</sub> is higher than that of a crystalline IrO<sub>2</sub>,<sup>14-15</sup> its

stability is significantly lower. This was confirmed by recent studies, where a scanning flow-cell (SFC) coupled with an ICP-MS (inductive coupled plasma mass spectrometry) is used to measure the iridium release rate during a linear voltage scan (LSV) in the OER regime, revealing the lower stability of iridium metal compared to an iridium oxide, annealed at different temperatures.<sup>13</sup> Therefore, the hydration state along with the morphology of the iridium-oxide seems to be important regarding the lifetime and stability of the OER catalyst. Quite recently Kasian et al.<sup>101</sup> showed that a change in hydration state during the OER seems to trigger the dissolution of iridium and, depending on the surface species and the overpotential, the dissolution proceeds via different routes. Nevertheless, these findings have to be considered with caution, since they are based on scanning flow cell measurements and, so far, these findings have not been confirmed in MEA measurements. Geiger et al.<sup>17</sup> already showed that the lifetimes predicted based on SFC measurements differ quite significantly from the ones extracted from MEA measurements. This discrepancy is also reflected in the measurements carried out by Sun et al.,<sup>91</sup> where iridium black was used as an OER catalyst during a 7800 h stability test and no degradation of the anode catalyst layer was observed, while SFC measurements predict a rather high dissolution for iridium black. Up to now, MEA measurements are necessary to assess the stability and lifetime of individual catalysts. This issue will be discussed further in Chapter 5.1 (*Current Challenges in Catalyst Development for PEM Water Electrolyzers*).

Besides anode catalyst degradation, the carbon supported platinum cathode catalyst layer can degrade over time, where the following mechanisms are considered as the main cause for a loss in active surface area: i) dissolution and agglomeration of smaller Pt-particles, resulting in a lower electrochemically active surface area (Ostwald ripening);<sup>102-103</sup> ii) dissolution and reprecipitation of Pt-particles within the membrane;<sup>104</sup> iii) carbon support corrosion.<sup>105</sup> However the proposed degradation mechanisms usually occur at high potentials<sup>106-107</sup> or when the potential is cycled. Since the potential of the cathode is usually close to the H<sub>2</sub>/H<sup>+</sup> reversible potential ( $\approx 0$  V) during operation, a severe degradation of the cathode catalyst layer due to a loss in active surface area is not expected. Up to now, rather high Pt-loadings (0.1 – 0.5 mg<sub>Pt</sub>cm<sup>-2</sup><sub>geo</sub>) are commonly used<sup>20</sup> and due to the fast kinetics of the HOR only a very large loss in electrochemically active surface area would lead to a measurable performance loss. Cathode catalyst degradation, however, will become more important if lower loadings are to be realized.

### 2.5.3 Porous Transport Layers and Bipolar Plates

Often titanium based porous transport layers and bipolar plates are used and hence the passivation of titanium and the accompanied increase in contact resistance is one of the main issues. An additional coating might be applied to prevent the formation of a passivation layer.<sup>73</sup> The choice of material for a protective coating, however, is limited, since it has to withstand the harsh environment (low pH and high anodic potentials) without getting dissolved or passivated itself. At the same time, the material should be abundant and cheap in order to keep the additional costs at a minimum. The latter is hard to be satisfied, therefore, in consideration of all the aforementioned requirements, platinum is often used.<sup>73, 108</sup> The bipolar plate itself already contributes significantly to the costs of a PEM-WE stack<sup>7, 18</sup> and adding an additional layer of platinum would increase the costs even further. Just to give some numbers as a ballpark reference, the DOE (Department of Energy) target for the Pt-specific power density for PEM fuel cells in automotive applications in 2020 is  $\leq 0.1 \text{ g}_{\text{Pt}}\text{kW}^{-1}$ ,<sup>109</sup> wherefore the additional amount of Pt added as a protective layer in a PEM-WE should be very low. In case a Pt coating thickness of  $\approx 100 \text{ nm}$  were required in order to prevent the passivation of titanium, this would result in an additional platinum loading of  $\approx 0.5 \text{ mg}_{\text{Pt}}\text{cm}^{-2}$ . Operating the electrolyzer at a power density of  $\approx 5 \text{ Wcm}^{-2}$  ( $3 \text{ Acm}^{-2}$  at 1.75 V), this would result in a Pt-specific power density of  $0.1 \text{ g}_{\text{Pt}}\text{kW}^{-1}$  and hence additional  $\approx 2 \text{ €kW}^{-1}$ .<sup>110</sup> Considering that the average long-term cost targets for a PEM-WE are  $\approx 1000 \text{ €kW}^{-1}$ ,<sup>111</sup> the additional platinum coating would only constitute a share of 0.2% of the overall investment costs.

## 2.6 Hydrogen as an Energy Carrier

In a future energy scenario, where energy is mainly provided via renewable energies, hydrogen as an energy carrier produced through the electrochemical splitting of water can play an important role. Hydrogen bears the advantage to serve as an energy carrier, as fuel for fuel cell vehicles and as feedstock in the chemical industry (e.g., ammonia, methanol). However, in order to meet the aimed climate protection requirements, a MW-scale production of hydrogen via electrolysis is necessary ( $\approx 3800$  GW would already be needed just to replace the worldwide fossil energy demand for transportation<sup>65</sup>).

In consideration of both, the huge increase in capacity along with the inevitable coupling with renewable energies, the hydrogen production via polymer electrolyte membrane water electrolysis becomes the most promising technology. Even though the energy consumption nowadays is quite similar for both systems, PEM-WE and alkaline electrolyzer systems (AEL) ( $\approx 4.8$  kWh  $\text{m}_\text{N}^{-3}$ ) and is assumed to become even more similar until 2050, there is still a huge discrepancy in terms of capital expenditure (CAPEX).<sup>112</sup> The production costs normalized to the produced amount of hydrogen are almost twice as high for a PEM-WE system ( $\approx 7000$  €  $(\text{Nm}^3\text{h}^{-1})^{-1}$ ) compared to alkaline electrolysis ( $\approx 4000$  €  $(\text{Nm}^3\text{h}^{-1})^{-1}$ ).<sup>112</sup> Even though projections show that, the costs will eventually level out until 2050 due to the increased progress in PEM-WE technology development, an upscaling of the PEM-WE system is required for this cost reduction. Nevertheless, the PEM-WE technology bears the advantage of operating at high current densities (PEM-WE:  $1-2$   $\text{Acm}^{-2}_{\text{cell}}$  vs AEL:  $0.25-0.45$   $\text{Acm}^{-2}_{\text{cell}}$ ), enabling pressurized operation (PEM-WE:  $30-50$  bar vs AEL:  $10-30$  bar) and offers a higher load flexibility (PEM-WE:  $0-100\%$  vs AEL:  $20-100\%$ ).<sup>8</sup> Since the hydrogen production rate scales linearly with the current density (omitting loss of hydrogen by cross-over to the anode compartment), the PEM-WE technology ( $\approx 8.4$   $\text{Nm}^3/\text{m}^3_{\text{cell}}$ ) exhibits a roughly 4-times higher cell-area normalized hydrogen production rate compared to an AEL ( $\approx 1.9$   $\text{Nm}^3/\text{m}^3_{\text{cell}}$ )<sup>8</sup> and in combination with its high flexibility and fast response time promotes hydrogen as an alternative carrier, when coupled with renewable energies.

Up to now PEM-WE systems are often sold in small scales ( $\leq 1$  MW) and the required materials and components are often custom made, wherefore the production costs of the individual components are rather high. In light of the fact that an annual increase in capacity in the GW-range is necessary, the small-scale production of the individual components would turn into a large-scale production, thereby reducing the specific costs drastically. Nonetheless, this would

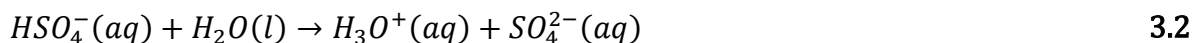
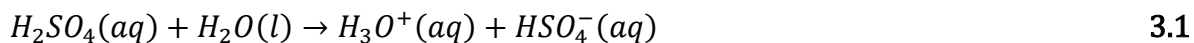
result in temporarily higher investment costs to provide the necessary infrastructure and production capacity until a certain threshold is reached.

The most critical PEM-WE stack components are the membrane/ionomer, the PTLs, the bipolar plates, and the catalysts, the latter being the most critical one. Due to the scarcity of iridium and the fact that it is only obtained as a byproduct during, e.g., Pt or Ni-mining, a significant reduction of the iridium-specific power density ( $\leq 0.05 \text{ g}_{\text{Ir}}\text{kW}^{-1}$ ) is necessary to realize a GW-scale installation.<sup>65, 112</sup> As an example, the total primary energy consumption of Germany in 2016 was 13.525 PJ,<sup>113</sup> which would correspond to an annual production of  $\approx 100 \text{ Mt}_{\text{H}_2}$  (based on the higher heating value of hydrogen  $\approx 285.8 \text{ kJmol}^{-1}$ ) if all energy sectors were to exclusively run on hydrogen gas as an energy carrier. The corresponding average electrical power needed to produce this hydrogen via PEM water electrolysis would be in the range of  $\approx 500 \text{ GW}$ . With state-of-the-art loadings ( $\approx 2 \text{ mg}_{\text{Ir}}\text{cm}^{-2}$ ) and an average power density of  $\approx 4 \text{ Wcm}^{-2}$ , an iridium-specific power density of  $\approx 0.5 \text{ g}_{\text{Ir}}\text{kW}^{-1}$  can be achieved. Considering the annual mining rate of iridium of  $\approx 7 \text{ t}_{\text{Ir}}$ <sup>112</sup> (recycling of iridium is not considered in this example) this entire amount of iridium would allow to replace PEM-WE with a total power of  $\approx 14 \text{ GW/year}$ , so that 50 years worth of iridium would be required just to produce  $\text{H}_2$  that would be needed for the energy supply of Germany. This example shows that a reduction of the iridium-specific power density of at least one order of magnitude is necessary to make hydrogen as an energy carrier competitive.

## 3 Experimental Methods

### 3.1 Rotating Ring Disk Electrode

Rotating ring disk electrode (RDE) measurements are often used as a screening tool to characterize the activity as well as stability of individual catalysts. Since only a small amount of catalyst (mg-range) is needed to characterize the catalyst, the RDE technique is favorable especially for the synthesis and screening of new catalyst materials. Usually a three-electrode electrochemical cell is used (Figure 3.1), where an interchangeable RDE PTFE or PEEK-holder (Pine Research Instrumentation, USA) with a 5 mm diameter polycrystalline Au-disk is used as a working electrode (WE), a reversible hydrogen electrode (RHE) as a reference electrode (RE), and a high-surface area Au-mesh as a counter electrode (CE). Commonly, the RE is separated from the main compartment via a closed electrolyte bridge (Luggin capillary). One issue that frequently occurs is the dissolution and redeposition of gold from the CE, wherefore an additional porous glass frit is applied to avoid the migration of dissolved gold into the main compartment. In order to minimize the overpotential of the CE, a high-surface area of the CE is required, wherefore meshes are commonly used. If one would manage to make the surface area large enough, then the current during the CV experiments may even be provided by the (pseudo-)capacitance of the CE and no dissolution would occur. As a reference electrode, a reversible hydrogen electrode was used, where a Pt-wire was exposed to a hydrogen atmosphere ( $\approx 1 \text{ bar}_a$ ) while being in contact with the electrolyte (0.1 M  $\text{H}_2\text{SO}_4$ ). While  $\text{H}_2\text{SO}_4$  can undergo two de-protonation steps (see equation 3.1 and 3.2), only the first de-protonation step ( $K_{a1} \approx 10^3$ ) is considered to be complete and the second to be incomplete ( $K_{a2} \approx 10^{-2}$ ), resulting in a proton concentration of roughly 0.11 M and thus a potential ( $E_{rev(\text{H}_2/\text{H}^+)}$ ) of  $\approx 57 \text{ mV}$  vs the standard hydrogen potential (SHE) should be established at the reference electrode (see equation 3.3).



$$E_{rev(\text{H}_2/\text{H}^+)} = E_{rev(\text{H}_2/\text{H}^+)}^0 - \frac{2.303 \cdot R \cdot T}{F} \cdot \text{pH} \quad 3.3$$

$$\text{pH} = -\log(c(\text{H}_3\text{O}^+)) \quad 3.4$$

$E_{rev(\text{H}_2/\text{H}^+)}^0$  is the standard reversible potential (0 V) of a standard hydrogen electrode at standard conditions (pH = 0; 25 °C, 1.013  $\text{bar}_{a,\text{H}_2}$ ), R the ideal gas constant ( $8.314 \text{ J mol}^{-1} \text{ K}^{-1}$ ), T the temperature and F the Faradays constant ( $96485 \text{ As mol}^{-1}$ ).

The pH can be calculated via the negative logarithm of the proton concentration ( $c(H_3O^+)$ ) (equation 3.4). However, prior to each measurement the potential of the RE was determined by applying a Pt-disk exposed to a hydrogen purged electrolyte serving as a reference electrode, while the reference compartment was operated as a working electrode. Beside a change of the pH, a change in gas composition can lead to a shift of the reference potential (see equation 3.5). Hence, a tight sealing of the Pt-wire within the reference compartment is necessary to prevent any gas leakage and thus, a continuous shift in potential due to a change in gas composition.

$$E_{rev(H_2/H^+)} = E_{rev(H_2/H^+)}^0 - \frac{2.303 \cdot R \cdot T}{2 \cdot F} \cdot \log(p_{H_2}/p_{H_2}^0) \quad 3.5$$

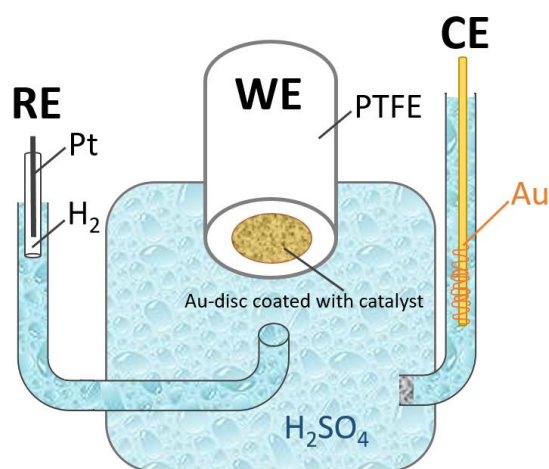


**Figure 3.1** Schematic setup of a standard three-compartment electrochemical cell used for rotating disk electrode measurements, where a interchangeable disk-electrode with a polycrystalline Au-disk serves as a working electrode (WE), a Pt-wire exposed to a hydrogen atmosphere as a reference electrode (RE) and a high-surface area Au-mesh as a counter electrode (CE).

Moreover, the right choice of the backing material used as a working electrode is important. Glassy carbon is unsuitable for OER measurements, since the carbon would corrode at high potentials<sup>106-107</sup> and an additional current stemming from the COR would be measured. Platinum itself is active towards the OER,<sup>31</sup> wherefore it would contribute to the measured current and should be excluded as disk material. Additionally, Geiger et al. recently showed that some disk electrode materials passivate over time, leading to an additional ohmic resistance that compromises stability tests.<sup>114</sup> They recommended to either use gold or boron-doped diamond as a disk electrode. Since gold does not exhibit an activity towards the OER in the potential range usually considered during OER measurements (see Figure 3.2),<sup>115</sup> an Au-disk was used throughout all measurements.



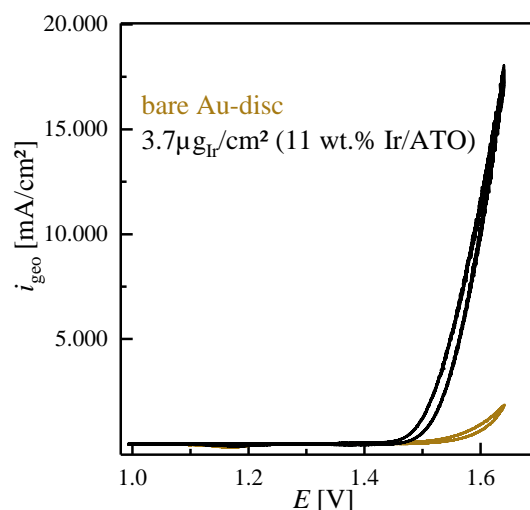


**Figure 3.2** Electrocatalytic OER polarization curves of a bare Au-disk and a 11 wt.-% Ir/ATO catalysts. All measurements were performed in O<sub>2</sub>-saturated 0.1 M H<sub>2</sub>SO<sub>4</sub>, 25 °C. Catalyst loading: 3.7 μg<sub>Ir</sub>/cm<sup>2</sup><sub>disk</sub>. Scan rate: 5 mV/s. 2500 RPM.

### 3.1.1 Electrode and Ink Preparation

Prior to each measurement, the polycrystalline Au disk has to be polished with a 0.3 μm Al<sub>2</sub>O<sub>3</sub> polishing suspension (Buehler Ltd.) on a water-wetted polishing cloth (Micro Cloth Buehler Ltd.) in an eight-shaped pattern for at least 3 minutes. Since iridium was found to be adhesive to the Au-disk, wiping off the previous catalyst coating with either water or 2-propanol was insufficient to remove the whole coating, wherefore polishing prior to each measurements was unavoidable. After polishing, the disk was rinsed and sonicated in deionized water for at least 3 times and 3 minutes. It is important to note that only the disk was sonicated, since interchangeable electrodes are not perfectly sealed and the electrical connections within the PTFE-holder corrode over time during sonication, resulting in a higher ohmic resistance. The whole electrode is handled carefully to avoid any contaminations, which would falsify the results. After reassembling the Au-disk into the holder, the catalyst ink is drop-casted onto the Au-disk and dried at atmospheric conditions. Catalyst inks were obtained by mixing the respective amount of catalyst (few milligrams) with either water or 2-propanol. No additional binder was usually added to the ink. The inks were sonicated at least 30 minutes before drop-casting and the sonication bath temperature was maintained below 35 °C to avoid evaporation of the solvent.

### 3.1.2 Electrochemical Measurement Setup

The used 0.1 M H<sub>2</sub>SO<sub>4</sub> electrolyte solutions were prepared from high purity H<sub>2</sub>SO<sub>4</sub> (Ultrapur, 96%, Merck Millipore KGaA) and ultrapure water (18.2 MΩcm at 20 °C Merck Millipore KGaA). The gases Ar, O<sub>2</sub>, and H<sub>2</sub> used for purging of the electrolyte were of high purity (6.0-grade, Westfalen AG). The whole cell setup was boiled for at least three times in ultrapure water to ensure its cleanliness. An Autolab potentiostat (PGSTAT302N, Metrohm AG, Switzerland) and a rotator (Pine Research Instrumentation, USA) with a polyether ether ketone shaft were used to perform the electrochemical measurements. In the beginning, the non-compensated electrolyte resistance was determined in an Ar-saturated electrolyte by electrochemical impedance spectroscopy (EIS) from 100 kHz to 100 Hz at open circuit potential (OCP) with an amplitude of 10 mV. Afterwards, cyclic voltammograms in a potential range of 0.05 and 1.45 V and a scan-rate of 100 mV/s were recorded in an Ar-saturated electrolyte to convert all metallic Ir (0) (blue CV in Figure 3.3) into hydrous Ir-oxide (red CV in Figure 3.3) when evaluating the Ir/ATO catalyst. Additional CVs were recorded within the same potential range using a smaller scan-rate of 20 mV/s, in order to compare the size of the mass-normalized CVs within different measurements. Finally, the electrolyte solution was purged for at least 10 min with O<sub>2</sub>, and polarization curves to determine the OER activity were recorded from 1.2 V<sub>RHE</sub> to 1.7 V<sub>RHE</sub> at 5 mV/s and 2500 rpm. Generally, these potential ranges were used, unless marked differently. Potentials are corrected for both the non-compensated electrolyte resistance and the potential of the reference electrode (vs RHE).

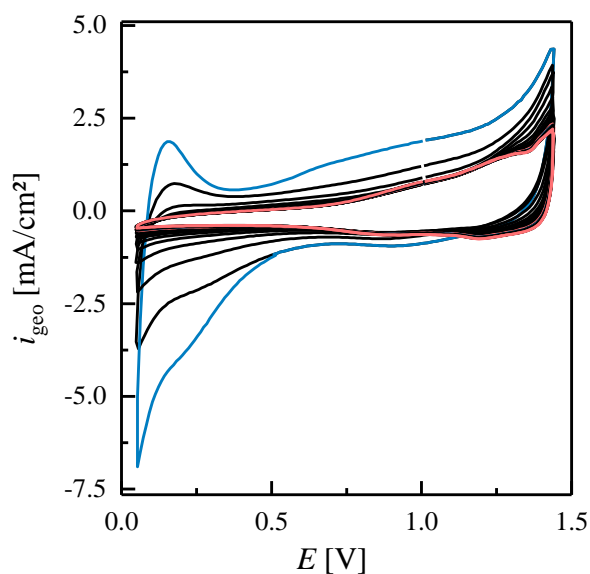


**Figure 3.3** Initial CV (blue) and after 30 cycles (red) of Ir/ATO (11 wt.-%) in Ar-saturated 0.1 M H<sub>2</sub>SO<sub>4</sub> at 100 mV/s and 25 °C. Catalyst loading is 44 μg<sub>Ir</sub>/cm<sup>2</sup><sub>disk</sub>.

## 3.2 Polymer Exchange Membrane Water Electrolyzer

Compared to an RDE measurement, where only a few milligrams of catalyst are required to determine the activity of a catalyst, MEA-based measurements require much more catalyst (few hundred mg) to fabricate proper catalyst layers. Hence, after a successful pre-screening of the OER activity, the next step is to obtain the performance of the respective catalyst in an MEA. The cell setup used throughout the study was developed and presented in the publication “*Influence of Ionomer Content in IrO<sub>2</sub>/TiO<sub>2</sub> Electrodes on PEM Water Electrolyzer Performance*” by M. Bernt and H.A. Gasteiger.<sup>27</sup> A schematic is shown in Figure 3.4.

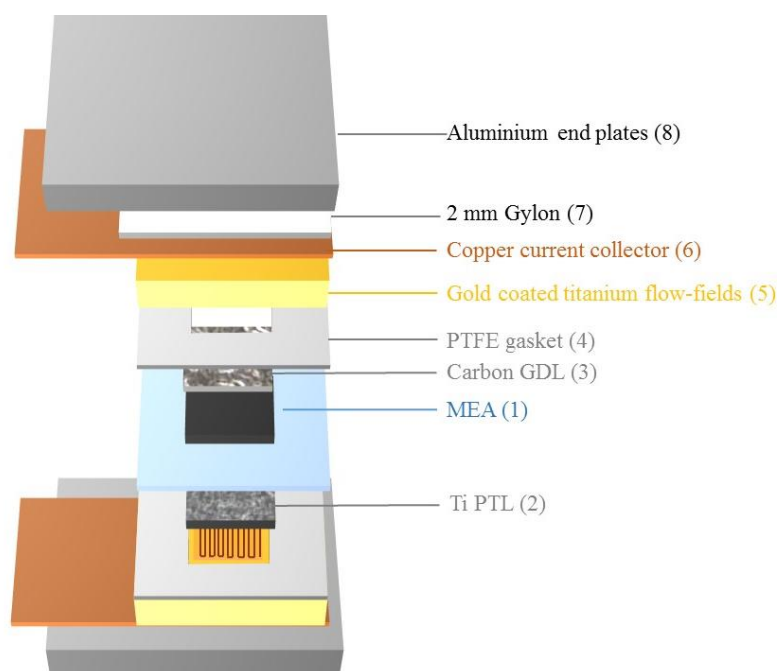


**Figure 3.4** Schematic cell setup of a 5 cm<sup>2</sup> cell.

The core of the single cell consists of an MEA ((1) in Figure 3.4) sandwiched between a  $\approx 280 \pm 10 \mu\text{m}$  thick carbon fiber GDL on the cathode (TGP-H-120T from Toray, no MPL, 20 wt.-% PTFE; cf. (3) in Figure 3.4) and a  $\approx 370 \pm 10 \mu\text{m}$  thick sintered titanium PTL on the anode (Mott Corporation, USA; cf. (2) in Figure 3.4). Two  $\approx 300 \mu\text{m}$  thick PTFE gaskets ((4) in Figure 3.4) frame the MEA setup to prevent any gas leakage, and an additional subgasket (thickness  $\approx 10 \mu\text{m}$ ) is used on the anode side to prevent an electrical shortening from protruding Ti-PTL fibers at the edges. The whole setup is placed between gold-coated titanium plates with

a single serpentine flow-field ( $5 \text{ cm}^2_{\text{geo}}$  active area; cf. (5) in Figure 3.4), which is again framed by the copper current collectors ((6) in Figure 3.4). On each side, a  $\approx 2 \text{ mm}$  thick Gylon sheet (Type 3545, Garlock® ENPRO Industries Inc., USA; cf. (7) in Figure 3.4) is used to provide a homogeneous pressure distribution along with an electrical insulation. Mechanical stability is ensured by the two  $\approx 25 \text{ mm}$  thick aluminum endplates ((8) in Figure 3.4), compressed by twelve M8 screws tightened with a force of 20 Nm. While the titanium PTL is assumed to be incompressible, the desired compression of the carbon GDL ( $\approx 25\%$ ) was achieved by choosing the thickness of the PTFE gaskets (compressibility  $\approx 3\%$ )<sup>116</sup> accordingly. Based on the different thicknesses and compressibility of the components used, a compression of  $\approx 1.7 \text{ MPa}$  over the entire land area within the active area of the cell should be achieved.<sup>27</sup> Further details about the cell setup and design are described in the publication and PhD thesis by Max Bernt.<sup>27, 116</sup>

### 3.2.1 Membrane Electrode Assembly

An  $\text{IrO}_2$  supported on  $\text{TiO}_2$  catalyst ( $\text{IrO}_2/\text{TiO}_2$  with 75 wt.-% iridium; Elyst Ir75 0480 from Umicore, Germany) as an anode catalyst and a platinum supported on Vulcan XC72 carbon (46.7 wt.-%Pt/C; TEC10V50E from Tanaka, Japan) as a cathode catalyst was used throughout the measurements. Catalyst inks were prepared by mixing the respective amount of catalyst with 2-propanol (purity  $\geq 99.9\%$ , from Sigma Aldrich) and Nafion® ionomer solution (20 wt.-% ionomer; D2021 from IonPower, USA). Due to their high surface area, both materials tend to ignite in contact with 2-propanol, wherefore the mixing was done in inert atmosphere ( $\text{N}_2$ ) using a small glovebox. An example for both an anode as well as cathode ink composition is shown in Table 3.1. Based on a study by Bernt et al.,<sup>27</sup> the ionomer content was adjusted to be  $\approx 11 \text{ wt.-%}$  for the anode catalyst layers.  $\text{ZrO}_2$  grinding beads (5 mm diameter) were added and the whole solution was mixed for at least 24 h using a roller mixer (Erichsen, RK K Control Coater) to obtain a homogeneous suspension. Using the Mayer-rod (K Bar, RK PrintCoat Instruments Ltd) technique, the catalyst suspension was coated onto an ETFE foil (25  $\mu\text{m}$  thick, FP361025 from Goodfellow, UK). The thickness of the electrode layers and thus the final loading ( $\text{mg}_{\text{Ir/Pt}}/\text{cm}^2$ ) was adjusted by using coating rods that yield different wet-film thicknesses.

**Table 3.1** Example for ink compositions for both anode and cathode electrode layers, resulting in an average loading of  $2.0 \text{ mg}_{\text{Ir}}\text{cm}^{-2}$  and  $0.2 \text{ mg}_{\text{Pt}}\text{cm}^{-2}$  respectively. 5 mm  $\text{ZrO}_2$  grinding beads were used and Mayer-rods with different sizes to adjust the wet-film thickness and thus the loading.

	Catalyst [mg]	2-propanol [mL]	Nafion <sup>®</sup> [ $\mu\text{L}$ ]	ZrO <sub>2</sub> -beads [g]	Coating rod [ $\mu\text{m}$ ]
IrO <sub>2</sub> /TiO <sub>2</sub>	942.3	1.01	582	6	60
Pt/C	325.1	4.41	510	8	120

After drying,  $5 \text{ cm}^2_{\text{geo}}$  electrode decals were cut at  $25 \text{ }^\circ\text{C}$  and 20 kN using an automated plate-press (Dr. Collin P 200 PM, Collin GmbH). A Nafion<sup>®</sup> 212 membrane (50  $\mu\text{m}$  thick; from Quintech, Germany) was placed between the respective electrodes and sandwiched between Kapton<sup>®</sup> and Gylon<sup>®</sup> sheets (Figure 3.5). These additional layers were added to avoid contamination and mechanical destruction of the membrane electrode assembly and to ensure a homogenous pressure distribution. The whole assembly was hot-pressed for 3 min at  $155 \text{ }^\circ\text{C}$ , applying a pressure of 2.5 MPa. Both electrode ETFE-decals were weighed before and after hot-pressing using a microbalance ( $\pm 1 \mu\text{g}$ ; from Mettler Toledo, Germany) to determine the final weight of the anode and cathode catalyst layer within the MEA setup.

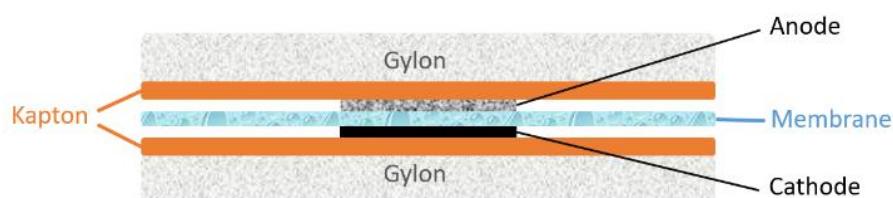


**Figure 3.5** Schematic Setup of a Membrane Electrode Assembly used for the Decal Transfer Step via Hot-Pressing

### 3.2.2 Electrochemical Characterization

In general, all electrochemical measurements of the MEAs were performed using an automated test station from Greenlight Innovation equipped with a Reference 3000 potentiostat and a 30 A booster from Gamry Instruments. The Emerald automation software was used to operate the test station. A BioLogic VSP 300 with a 20 A booster was used throughout the long-term study (see Chapter 5.6) as well as for all reference electrode measurements (see Chapter 4 and Chapter 5.7). Thermocouples placed within the flow-fields were used to control the temperature via the heating rods inserted in the aluminum end-plates and the fans externally placed on each side of the cell. The anode was continuously supplied with  $5 \text{ mL min}^{-1}$  deionized (DI) water that was pre-heated to  $80 \text{ }^\circ\text{C}$  throughout all the measurements. During the warm-up the cell was heated to  $80 \text{ }^\circ\text{C}$  under a nitrogen atmosphere and afterwards a current of  $1 \text{ A cm}^{-2}$  was applied

for 30 min to condition the cell. Subsequently, by flushing the cathode counter electrode with dry H<sub>2</sub> at 50 mL min<sup>-1</sup> to ensure a stable reference potential and by supplying the anode electrode with 5 mL min<sup>-1</sup> DI water, cyclic voltammograms (CVs) of the anode electrode were recorded. Usually, the CVs were recorded in a potential range of 0.05 V – 1.25 V at 20 mV s<sup>-1</sup> and 80 °C. For further evaluation, the second CV scan was used. A typical CV obtained for the used IrO<sub>2</sub>/TiO<sub>2</sub> catalyst is shown in Figure 3.6.

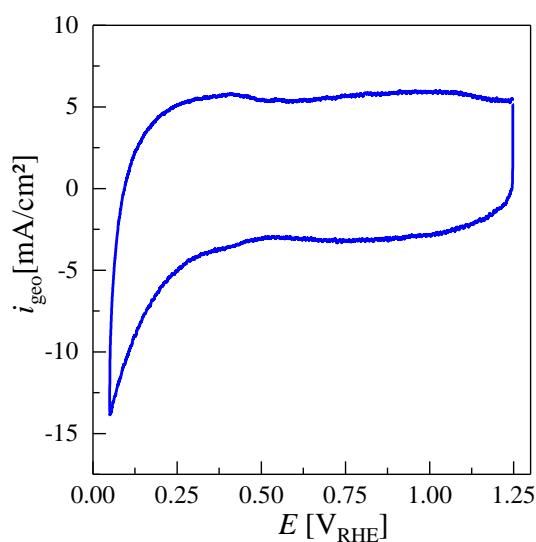


**Figure 3.6** Cyclic voltammograms (CVs) recorded at 20 mV/s, 80 °C, ambient pressure, and 5 mL<sub>H<sub>2</sub>O</sub> min<sup>-1</sup> (anode)/ 50 nccm H<sub>2</sub> (cathode). MEA specification: 5 cm<sup>2</sup> active-area with  $\approx 1.9$  mg<sub>Ir</sub>cm<sup>-2</sup><sub>geo</sub> anode and  $\approx 0.07$  mg<sub>Pt</sub>cm<sup>-2</sup><sub>geo</sub> cathode loading using a Nafion<sup>®</sup> 212 ( $\approx 50$   $\mu$ m thick) membrane.

Afterwards, by increasing the current density from 0.01 to 4 A cm<sup>-2</sup> stepwise with a hold time of 5 min at each current step to ensure a stable cell voltage, five consecutive polarization curves were taken at ambient pressure (1 bar<sub>a</sub>) and 80 °C. The last 10 s of the cell voltage at each current density were averaged and used for further evaluation (Figure 3.7 a). At each current density, additional AC impedance measurements were performed in a range from 100 kHz to 1 Hz. To fulfill the criteria of linearity, while still maintaining a sufficient signal to noise ratio, the current amplitude at each current density was adjusted to less than 20% of the applied current, except for a current density of 10 mAcm<sup>-2</sup><sub>geo</sub> where it was 40%. The high frequency resistance was determined via the high-frequency intercept with the real axis in a Nyquist plot. The HFR was used to correct for the ohmic and electrical resistance (hollow symbols in Figure 3.7 b). The described measurement procedure was used as a standard protocol to characterize the cell and additional measurements were adjusted individually according to the aim of the study and are described within the respective chapter.

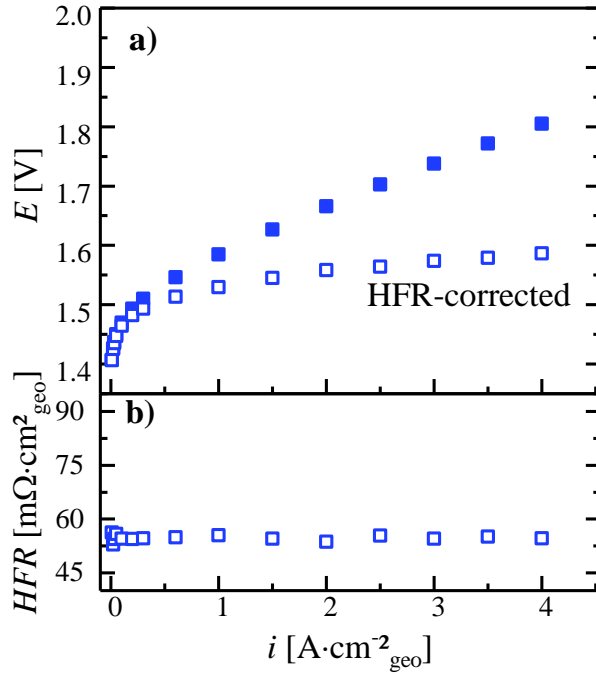


**Figure 3.7** PEM-WE performance data at 80 °C and ambient pressure **a)**  $E_{\text{cell}}$  vs  $i$  performance (filled symbols) and HFR-free performance data (hollow symbols) with an anode water-feed of  $5 \text{ mL}_{\text{H}_2\text{O}} \text{ min}^{-1}$ ; **b)** corresponding HFR values. MEA specification:  $5 \text{ cm}^2$  active-area with  $\approx 1.75 \text{ mg}_{\text{Ir}} \text{ cm}^{-2}_{\text{geo}}$  anode and  $\approx 0.2 \text{ mg}_{\text{Pt}} \text{ cm}^{-2}_{\text{geo}}$  cathode loading using a Nafion® 212 ( $\approx 50 \mu\text{m}$  thick) membrane.

### 3.2.3 Scanning Electron Microscopy

Cross-sectional scanning electron microscopy (SEM) measurements were performed by using a JEOL JCM6000Plus NeoScope scanning electron microscope at an accelerating voltage of 15 kV. Embedding the MEA in a room-temperature curing two-component epoxy (Epo Thin 2 resin and hardener; Buehler Ltd.) and drying over night at 80 °C, the SEM samples were prepared. Using a SiC paper, the sample surface was ground in two steps (grade P320 and P1200, from Buehler Ltd.) and subsequently polished on a microcloth using a 9  $\mu\text{m}$  diamond polishing agent.

### 3.2.4 Electrical Conductivity Measurements – 4-Point Probe

Using a 4-point-probe in-plane conductivity measurement (Lucas/Signatone Cooperation, USA) the electrical conductivities of catalyst layer decals were determined. By applying either different potentials or currents via the four collinearly aligned tungsten probes, the electrical resistance and thus the corresponding conductivity of the catalyst layer can be calculated.

### **3.2.5 Contact Resistance Measurements**

The contact resistances of the PTLs were measured with the test setup described by Bernt et al.<sup>27</sup> Therefore, the PTL was framed with an insulating Kapton<sup>®</sup> foil (25  $\mu\text{m}$ ) to ensure that the electrical resistance is only measured along the PTL and sandwiched between two gold coated titanium flow-fields. The whole setup was then placed between two copper plates, which were electrically insulated by an additional layer of Gylon<sup>®</sup> to any external components. To simulate the contact pressure during operation within the cell, a pressure of  $\approx 1.7$  MPa was applied to this stack. Different currents were applied via the copper plates and by measuring the associated voltage drop across the stack, the electrical resistance (essentially equating to the contact resistance) was quantified.



## 4 Platinum Wire Reference Electrode

### 4.1 Pt-Wire Reference Electrode Setup

Electrochemical impedance spectroscopy is a powerful tool to determine and analyze individual performance losses within an electrochemical cell. However, if solely the full-cell impedance spectra of a PEM-WE system is measured, the contribution of the cathode to the cell impedance will usually be assumed to be negligibly small.<sup>40, 47</sup> By applying a dynamic hydrogen electrode (DHE), where two Pt-wires are placed in proximity to the active electrode area, Li et al.<sup>117</sup> showed, that the impedance of the hydrogen electrode in a fuel cell (hydrogen side) is indeed smaller than that of the oxygen electrode, however, not negligible. Thus, in order to obtain an unbiased evaluation of the performance losses occurring during operation of each individual electrode, a determination of both half-cell spectra is necessary. A quite recent study by Sorsa et al.<sup>55</sup> used a Pt/C-ring (40 wt.-% Pt/C) sprayed equidistantly around the active area as a reference electrode using this to separate anode and cathode impedance. They showed that the anode impedance spectrum consists of two separate semi-circles, which they ascribed to mass-transport (high frequency arc) and charge transfer kinetics (low frequency arc). The interpretation of the cathode spectra, however, was more complicated. While the semi-circle at high frequencies was straightforwardly linked to the charge transfer kinetics, the interpretation of the inductive loop occurring at low frequencies was more challenging. Ultimately, they assigned the inductive loop to carbon corrosion of the cathode catalyst support, which they state has to be considered when fitting an equivalent circuit model (ECM) to the spectra.<sup>55</sup> Since a non-linear potential profile in close proximity to the active electrode area or a small misalignment of the active electrode can lead to erroneous impedance measurements, a proper positioning of the reference electrode is essential.<sup>118-119</sup>

Therefore, a similar approach, where the reference electrode is placed centrally between anode and cathode, and which is already applied successfully within lithium-ion batteries was considered.<sup>54</sup> In a previous study by our group, an Au-WRE (gold wire reference electrode) was introduced to determine individual half-cell spectra of a lithium-ion battery.<sup>54</sup> Herein, an insulated Au-wire was sandwiched between two separators and electrochemically alloyed with lithium in-situ to maintain a stable reference potential. Subsequent studies showed that with a proper design of experiments it is possible to separate and determine individual performance losses, such as the charge transfer resistance ( $R_{ct}$ ), the contact resistance ( $R_{cont.}$ ) or the pore

resistance ( $R_{pore}$ ) of the individual electrodes.<sup>53, 120</sup> Hence, an approach similar to the Au-WRE was adapted to the MEA of a PEM-WE. In this case, a 50  $\mu\text{m}$  thick Pt-wire with a 9  $\mu\text{m}$  PTFE insulation (Goodfellow, Great Britain) was placed centrally between two 50  $\mu\text{m}$  membranes, each coated with the respective catalyst layer. A schematic of the setup is depicted in Figure 4.1a along with an SEM cross-section of such an MEA (Figure 4.1b). As the Pt-WRE (wire reference electrode) is placed centrally within the cell, it is exposed to both  $\text{H}_2$  as well as protons ( $\text{H}^+$ ) during the measurement, wherefore its potential should be close to the reversible hydrogen potential ( $\approx 0 \text{ V}_{\text{RHE}}$ ). Upon resuming operation, however, the gas composition at the tip of the wire might change due to the crossover of produced oxygen and the potential of the Pt-WRE would be determined by a mixed potential. The SEM cross-section in Figure 4.1b shows that the Pt-WRE is located centrally between the two half-cell membranes. A misalignment of the Pt-WRE (e.g., bending of the tip of the wire) towards one of the electrodes can lead to erroneous impedance measurements due to inhomogeneous current distribution or, in the worst case, an electrical shortening of the cell.

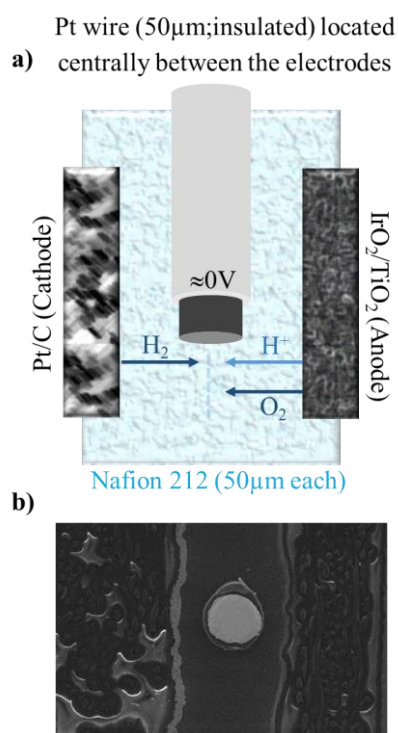


**Figure 4.1** a) Scheme of an MEA illustrating the placement of the Pt-WRE and the prevailing operation conditions. b) Cross-sectional SEM image of an MEA including a 50  $\mu\text{m}$  Pt-WRE laminated between two 50  $\mu\text{m}$  Nafion<sup>®</sup> membranes.

## 4.2 Reference Electrode MEA Fabrication

Since the Pt-wire (Goodfellow, Great Britain) is covered with a thin (9  $\mu\text{m}$ ) PTFE insulation, a scalpel is used to carefully scratch off roughly 0.5 cm at the tip of the wire (MEA-side; see ① in Figure 4.2). The tip is centrally placed within the membrane and roughly 1 cm insulation at the end of the wire exiting the cell is also scratched off, which is used to electrically contact the wire (contact-side; see ② in Figure 4.2). The MEA-side of the wire is then dipped into a 20 wt.-% Nafion<sup>®</sup> solution (20 wt.-% ionomer, D2021 from IonPower, USA) and dried at ambient conditions. The MEA fabrication itself is similar to the standard MEA fabrication method. Therefore, the prepared wire was placed centrally between two Nafion<sup>®</sup> 212 membranes (50  $\mu\text{m}$  thick, from Quintech, Germany) and together with the already prepared cathode and anode decal, the setup was hotpressed at 155  $^{\circ}\text{C}$  for 3 minutes at a pressure of 2.5 MPa. An additional layer of PP foil (40  $\mu\text{m}$  from Profol, Germany) was added at the interface with the cell hardware to provide additional mechanical stability (see ③ in Figure 4.2). By weighing the decals before and after hot-pressing, the actual weight of the electrodes was determined. Except when labeled differently, the loading was kept constant at  $0.3 \pm 0.1 \text{ mg}_{\text{Pt}} \text{ cm}^{-2}_{\text{geo}}$  for the hydrogen cathode and  $2.0 \pm 0.1 \text{ mg}_{\text{Ir}} \text{ cm}^{-2}_{\text{geo}}$  for the oxygen anode.

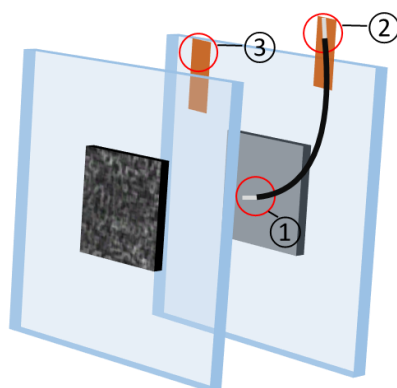


**Figure 4.2** Scheme of an MEA assembly with a Pt-WRE.

When assembling the Pt-WRE/MEA setup one has to make sure, that the Pt-wire is not placed in parallel with the heating rods of the cell (see Figure 4.3a). A parallel alignment of the Pt-wire with the heating rods led to an electrical interference (similar to an inductive coil) and thus an instable and continuously increasing potential of the Pt-wire. Therefore, the Pt-WRE was always assembled perpendicular to the heating rods (see Figure 4.3b).

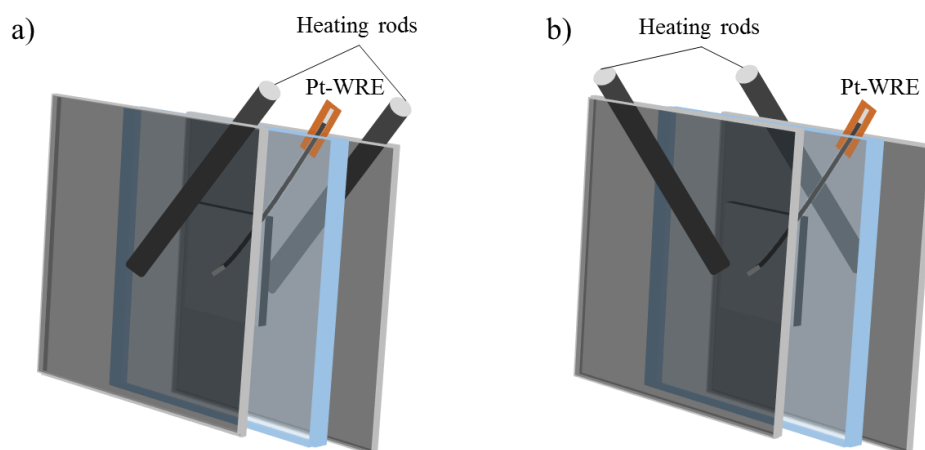


**Figure 4.3** Scheme of the alignment of the Pt-WRE towards the heating rods of the cell.

### 4.3 Electrochemical Characterization

For the reference electrode measurements, an automated test station from Greenlight Innovation using a potentiostat equipped with a current booster (BioLogic VSP 300) was used to perform all electrochemical measurements of the MEAs. Throughout the whole measurement, the anode was supplied with  $5 \text{ mL}_{\text{H}_2\text{O}} \text{ min}^{-1}$  deionized (DI) water and the temperature was maintained at  $80 \text{ }^\circ\text{C}$ . Compared to the standard protocol, after reaching the desired cell temperature of  $80 \text{ }^\circ\text{C}$ , the cathode was flushed with dry  $\text{H}_2$  at  $50 \text{ nccm}$  at ambient pressure to assess the functionality of the reference electrode. When the Pt-wire is centrally placed, and ionically as well as electrically contacted, the potential of the wire should be close to  $0 \text{ V}_{\text{RHE}}$  and also  $0 \text{ V}$  with respect to the  $\text{H}_2$  cathode potential. Afterwards the cell was conditioned at  $1 \text{ A cm}^{-2}_{\text{geo}}$  for  $30 \text{ min}$ . Polarization curves were taken at ambient pressure ( $1 \text{ bar}_a$ ), by either increasing the cell potential stepwise from  $1.3$  to  $1.9 \text{ V}$  or by increasing the current density stepwise from  $0.01$  to  $4 \text{ A cm}^{-2}$ . Each potential or current step, was held for at least  $5 \text{ min}$ , while only the last  $10 \text{ s}$  of either the cell voltage and current density were averaged for each point. At the end of each current or potential step an electrochemical impedance spectrum of the cell was recorded from usually  $100 \text{ kHz}$  to  $100 \text{ mHz}$ , recording  $10$  points per decade and at each point at least  $5$  repetitions were averaged. Both galvanostatic as well as potentiostatic measurements were performed. The amplitude was controlled between the WE&CE. In case it was measured in potentiostatic mode the amplitude was set to  $5$  or  $10 \text{ mV}$ , and in case it was measured in galvanostatic mode the amplitude was set to  $20 \text{ mA}$  for current densities between  $10 - 30 \text{ mAcm}^{-2}_{\text{geo}}$ ,  $40 \text{ mA}$  for a current density of  $50 \text{ mAcm}^{-2}_{\text{geo}}$  and  $60 \text{ mA}$  for current densities  $\geq 100 \text{ mAcm}^{-2}_{\text{geo}}$ .

## 4.4 Analysis of the Electrochemical Impedance Spectra

The aim of implementing a Pt-wire as a reference electrode was to obtain the spectra of anode and cathode, and thus the individual performance losses of the full-cell. Using a BioLogic potentiostat equipped with a current booster (BioLogic VSP 300), two impedance spectra can be recorded simultaneously, while the third one is calculated based on the two recorded ones. As a first indication that the Pt-WRE did not lead to any additional disturbances during the measurement, the full-cell spectra were considered first. In Figure 4.4, full-cell spectra of a Pt-WRE cell are shown. The spectrum consists of an inductive contribution at high frequencies (>12 kHz) and a large semi-circle at lower frequencies, which is decreasing in diameter with increasing current density. Since the charge-transfer kinetics of the OER are significantly slower compared to the kinetics of the HER (see chapter 2.1.2), the large semi-circle is commonly attributed to the charge-transfer resistance of the OER ( $R_{CT,OER}$ ),<sup>121-122</sup> and hence can be described by a simplified Butler-Volmer relation (high overpotentials; equation 4.1). Clearly, the decreasing diameter of the semi-circle observed with increasing current densities is in good agreement with the impedance response for Tafel kinetics (see equation 4.1). The HFR of the full-cell spectrum of  $\approx 93 \text{ m}\Omega\text{cm}^2_{\text{geo}}$  is in this case estimated from the intercept with the x-axis ( $\text{Re}(Z)$ ), which, as will be shown later (chapter 5.7), is only slightly higher than the HFR obtained by a proper fit of an appropriate equivalent circuit fit. With the used cell setup the total electrical resistance (i.e., the sum of contact resistances between the GDL||flow-field and PTL||flow-field as well as the bulk resistances of the GDL and the PTL) is  $\approx 12 \text{ m}\Omega\text{cm}^2_{\text{geo}}$ <sup>27</sup> as discussed earlier (chapter 2.1.3), while the ohmic resistance of one  $50 \mu\text{m}$  Nafion<sup>®</sup> membrane at  $80 \text{ }^\circ\text{C}$  when operated with liquid water ranges between  $\approx 41 - 54 \text{ m}\Omega\text{cm}^2_{\text{geo}}$ .<sup>27</sup> Since the HFR is the sum of both the electrical as well as the membrane resistance, using two  $50 \mu\text{m}$  Nafion<sup>®</sup> membrane should result in a total ohmic resistance of  $\approx 94 - 120 \text{ m}\Omega\text{cm}^2_{\text{geo}}$  and is in good agreement with the recorded  $\approx 93 \text{ m}\Omega\text{cm}^2_{\text{geo}}$ , thus suggesting that the implementation of the Pt-WRE does not lead to any artefacts in the full-cell impedance measurements.

$$R_{CT,OER} \approx \frac{\Delta\eta_{OER}}{\Delta i} = \frac{R \cdot T}{\alpha \cdot F} \cdot \frac{1}{i} \quad 4.1$$

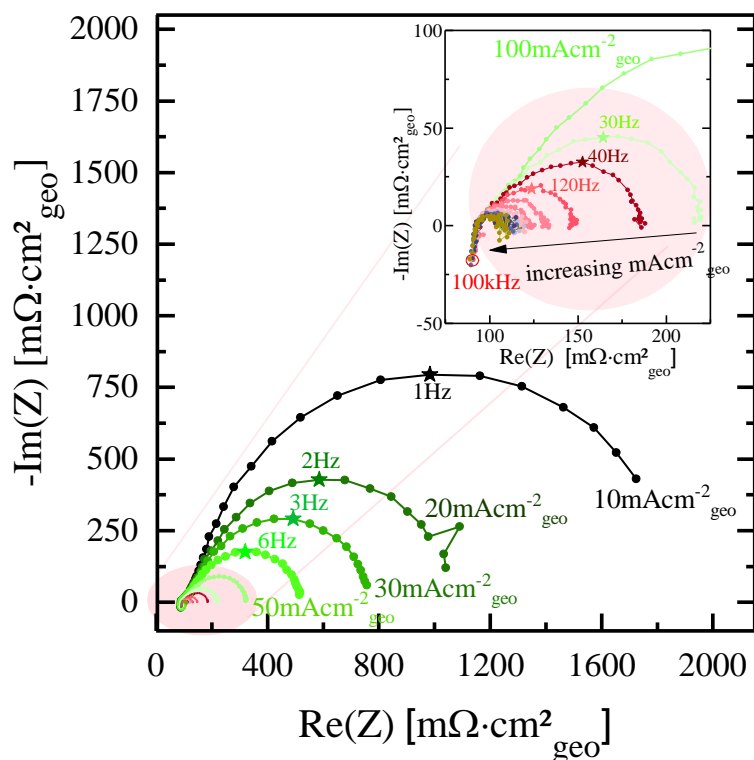


**Figure 4.4** Electrochemical impedance spectra (100 kHz – 300 mHz) of the full-cell at different current densities (0.01 – 4  $\text{Acm}^{-2}_{\text{geo}}$ ) of a  $5 \text{ cm}^2$  PEM water electrolysis cell recorded at  $80 \text{ }^\circ\text{C}$  and ambient pressure (1  $\text{bar}_{\text{a,cathode}}$ , 1  $\text{bar}_{\text{a,anode}}$ ), and  $5 \text{ mL}_{\text{H}_2\text{O}} \text{ min}^{-1}$  at the anode. MEA specifications:  $\approx 1.3 \text{ mg}_{\text{Ir}} \text{ cm}^{-2}_{\text{MEA}}$  anode and  $\approx 0.3 \text{ mg}_{\text{Pt}} \text{ cm}^{-2}_{\text{MEA}}$  cathode loading, using two Nafion<sup>®</sup> 212 ( $\approx 50 \text{ }\mu\text{m}$ ) membranes and a  $50 \text{ }\mu\text{m}$  Pt-wire with a  $9 \text{ }\mu\text{m}$  PTFE insulation as a reference electrode. The frequencies given in the figure indicate the peak frequency of the respective semi-circle.

More interesting, however, are the individual contributions of both half-cells as a function of current density. Figure 4.5a and Figure 4.5b depicts the impedance spectra of the anode, while in Figure 4.5c and Figure 4.5d the impedance spectra of the cathode are shown, both measured simultaneously via the Pt-WRE while recording the full-cell spectra depicted in Figure 4.4. The HFR of the individual half-cell can be taken as a first indication, whether the reference electrode is placed properly and whether the impedance spectra can be used for further evaluation. Both the anode as well as the cathode HFR ( $\approx 50 \text{ m}\Omega\text{cm}^2_{\text{geo}}$ ), extracted from the intercept with the x-axis, is close to but smaller than the HFR expected for a single  $50 \text{ }\mu\text{m}$  Nafion<sup>®</sup> membrane ( $\approx 53 - 66 \text{ m}\Omega\text{cm}^2_{\text{geo}}$ ) for the used setup.<sup>27</sup> The SEM already confirmed that the Pt-WRE is centrally placed between the two electrodes; however, the membrane seems to be thinned around the tip (see Figure 4.1), which would explain the somewhat lower HFR observed. Taking a closer look at the impedance spectra of the anode (Figure 4.5a), the spectra at low current densities are similar to the full-cell spectra, exhibiting an inductive branch at high frequencies ( $>12 \text{ kHz}$ ) followed by a semi-circle, with a diameter decreasing with increasing

current density. At current densities  $>100 \text{ mAcm}^{-2}_{\text{geo}}$ , however, the spectra start to develop an additional inductive feature (see Figure 4.5b). While the observed decreasing semi-circle with increasing current densities agrees well with the decreasing OER charge transfer resistances according to the Tafel-relation (equation 4.1), and thus obviously represents the OER kinetics, the observed inductive feature at low frequencies cannot be explained easily. Although the peak frequency of the respective semi-circle is rather low (within the Hz-range; e.g., 1 Hz at  $10 \text{ mAcm}^{-2}_{\text{geo}}$ ) for the R||C-element to represent the OER kinetics, the frequencies are similar to the peak frequency of the respective semi-circle within the full-cell spectra (see Figure 4.4). In case the observed semi-circles do not represent the OER kinetics but mass-transport losses, which is rather unlikely at these low current densities, no linear Tafel relationship should be obtained, since the OER kinetics would be influenced by mass-transport losses. Since, however, as will be shown later (see Figure 4.16), a linear Tafel relationship is observed, it is unlikely that the observed semi-circle represents mass-transport losses rather than the OER kinetics. Therefore, it is assumed that even though the frequencies are lower than would be expected for OER kinetics, the recorded semi-circle can be attributed to the OER kinetics.

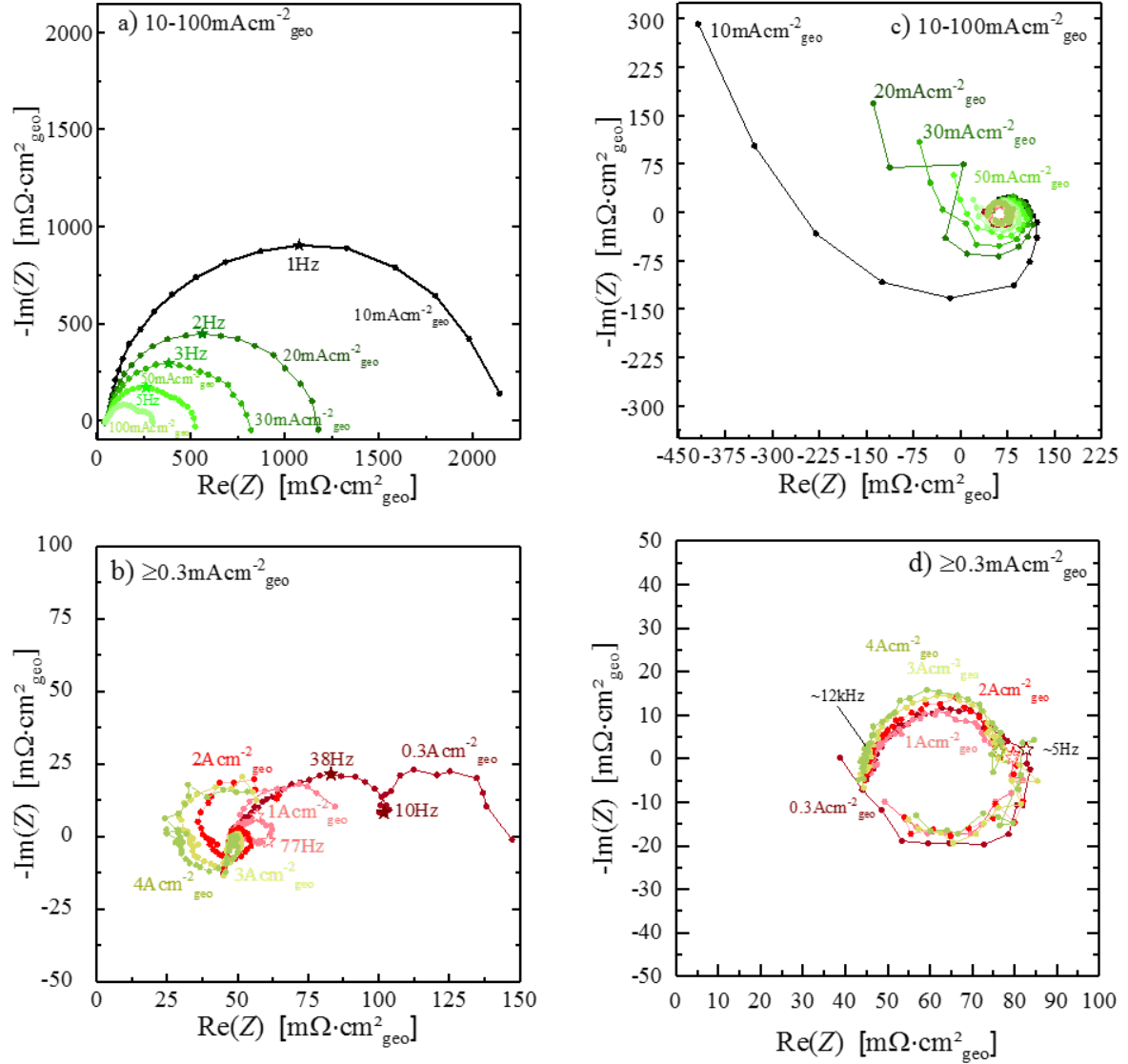


**Figure 4.5** Electrochemical impedance spectra of a) the anode at low and b) at high current densities, and c) the cathode at low and d) at high current densities of a 5 cm<sup>2</sup> PEM water electrolysis cell recorded at 80 °C and ambient pressure (1 bar<sub>a,cathode</sub>, 1 bar<sub>a,anode</sub>), and 5 mL<sub>H<sub>2</sub>O</sub> min<sup>-1</sup> at the anode.

The cathode impedance spectra depicted in Figure 4.5c and Figure 4.5d exhibit an inductive branch at high frequencies (>12 kHz), followed by a semi-circle, which gets inductive at frequencies <5 Hz. While at small current densities (Figure 4.5c) the semi-circle slightly decreases with increasing current density, it remains constant at current density >300 mAcm<sup>-2</sup><sub>geo</sub> (Figure 4.5d). As the semi-circle observed can most likely be attributed to the charge transfer kinetics of the HER,<sup>121</sup> and thus can be described by a linearized Butler-Volmer relation (equation 4.2), it is no surprise that no significant change with current density can be observed.



$$R_{CT,HER} \equiv \frac{\partial \eta_{HER}}{\partial i} = \frac{R \cdot T}{i_o \cdot 2 \cdot F \cdot rf} \quad 4.2$$

Assuming an electrochemical active surface area ECSA of  $A_{Pt,el}=60 \text{ m}^2\text{g}^{-144}$  and a loading of  $L_{Pt}=0.3 \text{ mg}_{Pt}\text{cm}^{-2}_{geo}$  the roughness factor ( $rf$ ) for a Pt/C cathode is  $rf=180 \text{ cm}^2_{Pt}\text{cm}^{-2}_{geo}$ . Using an exchange current density for the HER at  $80 \text{ }^\circ\text{C}$  of  $i_{o,HER}=250 \text{ mAcm}_{metal}^{-2}$ ,<sup>123</sup> the estimated charge-transfer resistance for the HER would be  $R_{CT,HER}\approx 0.34 \text{ m}\Omega\text{cm}^2_{geo}$ . Clearly, the calculated charge-transfer resistance is two orders of magnitude smaller than the one measured ( $R_{CT,HER}\approx 34 \text{ m}\Omega\text{cm}^2_{geo}$ ), but it is close to what was observed for a similar type of catalyst in the literature.<sup>55</sup> The calculated charge-transfer for the HER is based on the assumption that the Pt/C catalyst is solely exposed to a hydrogen-rich atmosphere. During operation, however, produced oxygen can diffuse through the membrane from the anode into the cathode compartment and recombine with hydrogen at the Pt/C catalyst to water, reducing the overall partial pressure of hydrogen in the cathode compartment. However, the partial pressure of hydrogen would need to be significantly smaller to explain such a high overall resistance for the cathode, wherefore it is rather unlikely that the observed feature within the cathode impedance spectra represents the HER/HOR kinetics. Up to now, there is no straightforward explanation for the cathode impedance spectrum, however, using a less active HER catalyst or a membrane exhibiting a lower oxygen crossover might help to understand the cathode impedance features.

## 4.5 Analysis of the Inductive Loop at Low Frequencies

### 4.5.1 Electrical Circuit Setup – Cable Configuration

Depending on the applied cable configuration (electrical circuit; Figure 4.6), two spectra are recorded during the measurement, whereas the third one is calculated based on the other two. Therefore, two different cable connections were used, where either the half-cell spectra of the cathode or the anode was calculated, in order to exclude any electrical interferences due to the used cable configuration.

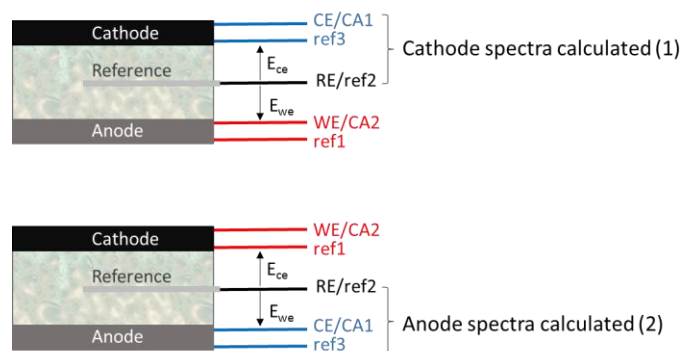


**Figure 4.6** Schematic of two different electrical circuits using the Pt-reference setup.

In Figure 4.7, the individual half-cell spectra along with the full-cell spectra at 1 A/cm<sup>2</sup> are depicted. While the full-cell spectrum (blue shaded spectra) was measured in both cases and hence, is expected to remain constant, the individual half-cell spectra remain constant as well. In both cases the cathode spectrum consists of a large semi-circle and an additional inductive part at low frequencies (green shaded spectra), whereas the anode spectrum (red shaded spectra) comprises a smaller semi-circle at high frequencies followed by an inductive loop at smaller frequencies (<60 Hz). Since the obtained half-cell spectra are identical, any electrical interferences by the potentiostat due to the used cable configuration can be ruled out.

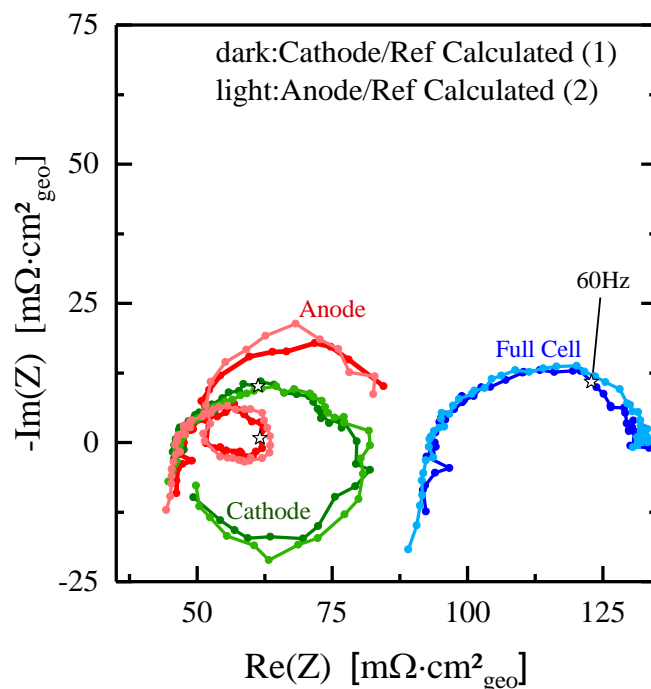


**Figure 4.7** Electrochemical impedance spectra of the anode (red spectra), the cathode (green spectra), and the full-cell (blue spectra) at 1 Acm<sup>-2</sup><sub>geo</sub> of a 5 cm<sup>2</sup> PEM water electrolysis cell recorded at 80 °C and ambient pressure (1 bar<sub>a,cathode</sub>, 1 bar<sub>a,anode</sub>), and 5 mL<sub>H<sub>2</sub>O</sub> min<sup>-1</sup> at the anode. Two different electrical setups were used (see Figure 4.6). The hollow black stars mark the characteristic frequency of 60 Hz in the individual spectra. Same MEA specifications as in Figure 4.4.

#### 4.5.2 Influence of Membrane Thickness

A change in oxygen crossover from anode to cathode according to the applied current,<sup>59</sup> while recording an impedance spectrum, the applied amplitude can cause a fluctuation of the oxygen permeation and thus a change in oxygen concentration at the tip of the Pt-wire. In chapter 5.7 it will be shown that the potential at the Pt-WRE is caused by the gas composition present at the tip of the wire: (i) if hydrogen is the prevalent gas, the potential will be close to the potential of a reversible hydrogen electrode ( $\approx 0$  V); (ii) in case there is an excess of oxygen, the potential will be biased towards the thermodynamic potential of water splitting ( $\approx 1.18$  V assuming standard activity of protons and oxygen at  $80^\circ\text{C}$ ). Therefore, a small change of the prevalent gas composition at the tip of the wire during an impedance measurement can lead to a changing potential of the reference electrode. Since a stable potential of the reference electrode is a prerequisite for an unambiguous impedance measurement, a fluctuating reference potential can lead to erroneous impedance measurements.<sup>51, 124</sup> Depending on the applied amplitude and the corresponding change in current and thus the amount of oxygen produced, the gas composition at the reference electrode can change during an impedance measurement if the local  $\text{H}_2$  and  $\text{O}_2$  partial pressures at the electrode/membrane interface vary with current density (Figure 4.8; see chapter 5.7).

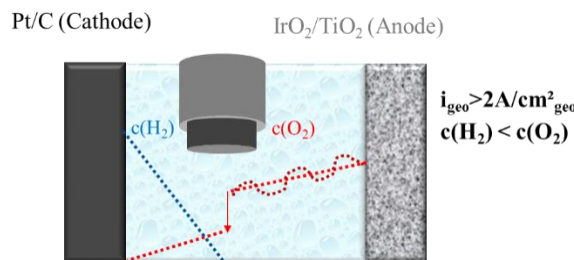


**Figure 4.8** Schematic of the change in gas composition at the Pt-WRE caused by the applied amplitude during an impedance measurement. The dotted lines represent the  $\text{H}_2$  and  $\text{O}_2$  concentration profiles within the membrane, showing a scenario where the local flux of  $\text{O}_2$  at the Pt-WRE position is  $>1/2$  of the local flux of  $\text{H}_2$ .

Based on equation 4.3 the diffusion coefficient for oxygen ( $D_{\text{O}_2}$ ) in Nafion<sup>®</sup> at  $80^\circ\text{C}$  can be calculated to be  $\approx 1.2 \cdot 10^{-6} \text{ cm}^2\text{s}^{-1}$ .<sup>125</sup> In case, however, the diffusion of oxygen in water is considered to be the dominant path the diffusion coefficient is  $\approx 4.1 \cdot 10^{-5} \text{ cm}^2\text{s}^{-1}$ .<sup>126-127</sup>

$$D_{\text{O}_2} = 3.1 \cdot 10^{-3} \cdot \exp\left(\frac{-2768}{T}\right) [\text{cm}^2\text{s}^{-1}] \quad 4.3$$

For a diffusion length of  $x = 50 \mu\text{m}$  (from the electrode/membrane interface to the center of the Pt-WRE), this would result in a corresponding time constant (see equation 4.4) for oxygen diffusion in Nafion<sup>®</sup> and water of  $\tau_{\text{Nafion}^\circledast} \approx 20 \text{ s}$  and  $\tau_{\text{H}_2\text{O}} \approx 0.6 \text{ s}$ .

$$\tau = \frac{x^2}{D}$$

4.4

Schalenbach et al.<sup>128</sup> showed that gas permeation can occur through both the solid phase (dry Nafion<sup>®</sup>) and water. Assuming that the time constant for oxygen permeation through a fully humidified 50  $\mu\text{m}$  Nafion<sup>®</sup>212 membrane is in the order of seconds (0.6 – 20 s), the corresponding characteristic frequency would be  $\approx 50 \text{ mHz} - 1.6 \text{ Hz}$ . As shown in Figure 4.7 the inductive loop starts to occur at frequencies  $< 60 \text{ Hz}$ . Additionally, the osmotic water drag can influence the water content within the membrane, thus shifting the characteristic time constant to lower frequencies. Considering the above estimates, a change in gas composition due to the applied current amplitude might be possible and might thus be responsible for the inductive loop at low frequencies. Using a thicker membrane at the anode side (see Figure 4.9), however, should shift the times constants to even lower frequencies (e.g., for a 100  $\mu\text{m}$  Nafion<sup>®</sup> membrane the characteristic frequencies would be  $\approx 10 \text{ mHz} - 40 \text{ mHz}$ ). Therefore, a 100  $\mu\text{m}$  Nafion<sup>®</sup> membrane was used at the anode, while a 15  $\mu\text{m}$  membrane was used at the cathode (see Figure 4.10).

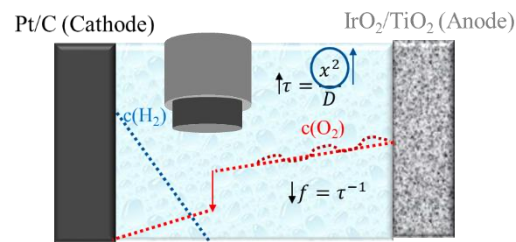


**Figure 4.9** Schematic of the influence of the membrane thickness on the characteristic time constant

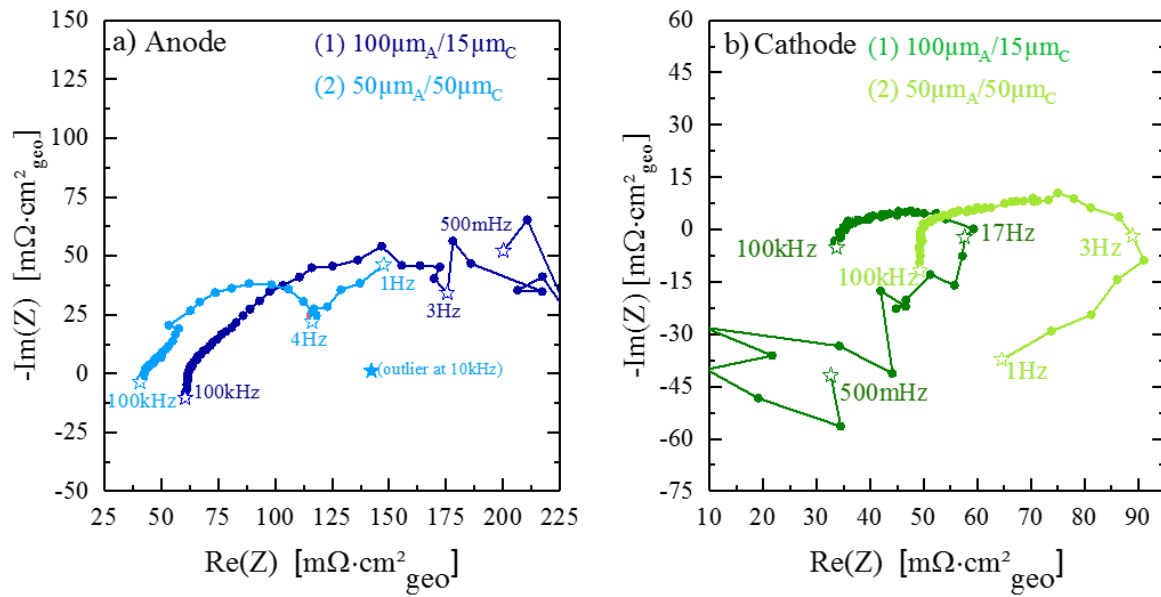


**Figure 4.10** Electrochemical impedance spectra of a) anode and b) cathode utilizing different membrane thicknesses at  $0.2 \text{ A cm}^{-2}_{\text{geo}}$  of a  $5 \text{ cm}^2$  PEM water electrolysis cell recorded at  $80 \text{ }^\circ\text{C}$  and ambient pressure ( $1 \text{ bar}_{\text{a,cathode}}$ ,  $1 \text{ bar}_{\text{a,anode}}$ ), and  $5 \text{ mL}_{\text{H}_2\text{O}} \text{ min}^{-1}$  at the anode. MEA specifications:  $\approx 1.8 \pm 0.2 \text{ mg}_{\text{Ir}} \text{ cm}^{-2}_{\text{MEA}}$  anode and  $\approx 0.2 \pm 1 \text{ mg}_{\text{Pt}} \text{ cm}^{-2}_{\text{MEA}}$  cathode loading, using either (2) two Nafion<sup>®</sup> 212 ( $\approx 50 \mu\text{m}$ ) membranes (light green and blue) or (1) a  $100 \mu\text{m}$  Nafion<sup>®</sup> 212 membrane at the anode and a  $15 \mu\text{m}$  Nafion<sup>®</sup> 212 membrane at the cathode (dark green and blue) and a  $50 \mu\text{m}$  Pt-wire with a  $9 \mu\text{m}$  PTFE insulation as a reference electrode. The blue star in Figure 4.10a marks an outlier recorded at  $10 \text{ kHz}$  during the impedance measurement of a  $50 \mu\text{m}_A/50 \mu\text{m}_C$  configuration.

The HFR recorded for both anode ( $\approx 50 \text{ m}\Omega\text{cm}^2_{\text{geo}}$ ) and cathode ( $\approx 43 \text{ m}\Omega\text{cm}^2_{\text{geo}}$ ) utilizing two  $50 \mu\text{m}$  membranes is in good agreement with what has been reported in literature.<sup>27</sup> Assuming that the swelling behavior is similar for all Nafion<sup>®</sup> membranes (see chapter 2.1.3), this would result in an ohmic resistance of  $\approx 19 \text{ m}\Omega\text{cm}^2_{\text{geo}}$  and  $\approx 86 \text{ m}\Omega\text{cm}^2_{\text{geo}}$  for the  $15 \mu\text{m}$  and  $100 \mu\text{m}$  membrane respectively (light blue and green in Figure 4.10a and b). The recorded HFR of the  $100 \mu\text{m}$  membrane is with  $\approx 60 \text{ m}\Omega\text{cm}^2_{\text{geo}}$  lower and the recorded HFR of the  $15 \mu\text{m}$  membrane is with  $\approx 35 \text{ m}\Omega\text{cm}^2_{\text{geo}}$  higher than expected (dark blue and green in Figure 4.10a and b). As was already discussed earlier, the membrane seems to be thinned around the Pt-wire tip and hence, it is possible that during the hot-pressing step the membrane creeps around the Pt-wire, resulting in a different HFR than expected. Clearly the impedance spectra look quite similar for both setups (a semi-circle representing the charge transfer kinetics), and the inductive loop still appears at similar frequencies for both cases and the utilization of a thicker membrane did not result in the disappearance of the inductive feature. However, since the HFR at the anode side is similar for both membranes ( $50 \text{ m}\Omega\text{cm}^2_{\text{geo}}$  vs  $60 \text{ m}\Omega\text{cm}^2_{\text{geo}}$ ) and assuming that the HFR has a linear relationship with the position of the Pt-wire, this would change the distance only by

$\approx 12 \mu\text{m}$  and the characteristic time frequency to only  $\approx 1 \text{ Hz}$ . Although the change in membrane thickness was not large enough to prove that it has no influence on the inductive feature, it is highly likely that the thickness of the membrane does not affect the impedance loop and that the cause is related to some other phenomenon.

### 4.5.3 Influence of the Applied Amplitude

The applied amplitude should be selected carefully in order to maintain linearity.<sup>51</sup> Therefore, different amplitudes were tested to exclude the influence of an incorrectly chosen amplitude. Figure 4.11 depicts the anode impedance spectra recorded at  $80 \text{ }^\circ\text{C}$  and  $1.6 \text{ V}$  corresponding to a current of  $0.66 \text{ A cm}^{-2}_{\text{geo}}$ , applying different voltage amplitudes ( $5 - 40 \text{ mV}$ ). As can be seen, independent of the chosen amplitude, the recorded impedance spectrum as well as the inductive feature remains constant and thus, the amplitude does not seem to be responsible for the inductive loop recorded at low frequencies. Moreover, by changing the magnitude of the amplitude, the local gas composition should change accordingly, being more pronounced at higher amplitudes. Since the extent of inductivity does not change with amplitude, this hints towards the gas composition not being responsible for the inductive loop.

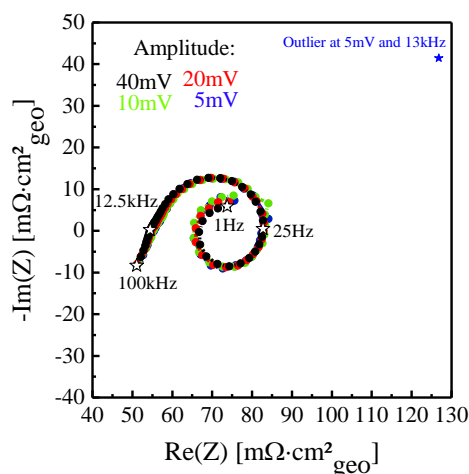


**Figure 4.11** Electrochemical impedance spectra (100 kHz – 1 Hz) of the anode at 1.6 V (cell voltage) and different amplitudes of a  $5 \text{ cm}^2$  PEM water electrolysis cell recorded at  $80 \text{ }^\circ\text{C}$  and ambient pressure ( $1 \text{ bar}_{\text{a,cathode}}$ ,  $1 \text{ bar}_{\text{a,anode}}$ ), and  $5 \text{ mL}_{\text{H}_2\text{O}} \text{ min}^{-1}$  at the anode. MEA specifications:  $\approx 0.8 \text{ mg}_{\text{Ir}} \text{ cm}^{-2}_{\text{MEA}}$  anode and  $\approx 0.1 \text{ mg}_{\text{Pt}} \text{ cm}^{-2}_{\text{MEA}}$  cathode loading, using two Nafion<sup>®</sup> 212 ( $\approx 50 \mu\text{m}$ ) membranes and a  $50 \mu\text{m}$  Pt-wire with a  $9 \mu\text{m}$  PTFE insulation as a reference electrode.

#### 4.5.4 Comparison with the Literature

In the literature, different explanations can be found describing the origin of an inductive feature at low frequencies. Sorsa et al.<sup>55</sup> used a Pt/C ring that was spray coated symmetrically on the membrane on the opposite site of the individual electrodes and electrically connected the Pt/C rings via a Pt wire sandwiched between the two half-cell MEAs. They simultaneously recorded the individual half-cell spectra while cycling the cell between 1 Acm<sup>-2</sup> for 60 s and OCV for 300 s. While in this case the reference electrode cannot be used to control the individual half-cell potentials, since it deviates by roughly -200 mV vs SHE, it was used to record individual impedance spectra. They showed that the anode impedance spectra comprise two main processes, namely mass transport and charge transfer resistances. The latter is assigned to the semi-circle observed at lower frequencies ( $\tau \approx 10 - 200$  ms corresponding to 100 Hz – 5 Hz) and is decreasing with current density, whereas the mass transport losses occur at higher frequencies ( $\tau \approx 0.8$  ms corresponding to 1250 Hz) and increase with current density. Although it is rather surprising that the charge transfer kinetics are attributed to the RC-circuit at lower frequencies, since mass transport phenomena usually appear at lower frequencies than those described to the OER kinetics, the anode impedance spectra recorded within this study do not show any inductive feature. No frequency information is provided within the impedance spectra, wherefore it is hard to judge whether an inductive feature might be overlapped by the semi-circles, since the cathode spectra show a distinct inductive loop at low frequencies, similar to the one recorded within our study (see Figure 4.5). Especially at higher current densities, the inductive loop observed in their cathode spectra becomes more pronounced in their study. Taking a closer look at the impedance spectra of the cathode, however, reveals an unlikely high HFR ( $\approx 250$  m $\Omega$ cm<sup>2</sup><sub>geo</sub>) for the used Nafion<sup>®</sup> 115 membrane, for which no explanation was provided. Ultimately, they concluded that the inductive loop is caused by carbon corrosion of the cathode catalyst layer due to the formation of H<sub>2</sub>O<sub>2</sub> and F<sup>-</sup> and that these processes would have to be considered when applying an equivalent circuit model (ECM) for fitting the impedance spectra.

Kuhn et al.<sup>129</sup> used an insulated carbon filament, where only the tip is in direct contact with the membrane. This type of reference electrode can only be used for impedance measurements, since the potential at the tip of the wire is undefined. In this case, the half-cell spectra during the operation of a PEM-FC were recorded. Within the cathode impedance spectrum they observed an additional inductive loop, which they attributed to oxygenated species adsorbing on the surface of the catalyst.<sup>129</sup> While they did not elaborate it in further detail in their study,

they examined it further in a second study, where the same type of reference electrode was applied.<sup>130</sup> Herein, the inductive loop present at low frequencies and within the cathode spectra exhibited a similar characteristic frequency at its maximum, pointing towards a potential independent process. They attributed it to the formation of  $\text{OH}_{\text{ad}}$ , indicating a chemical step within the reaction mechanism of the ORR.

Schneider et al.<sup>131</sup> operated a nine-fold segmented cell at sub-saturated conditions and simultaneously recorded the impedance spectra of the single cells. In the sub-saturated part of the cell they observed an additional inductive loop at low frequencies. They attributed it to the development of gas oscillation along the flow channels, since the applied sinusoidal signal can lead to a change in water concentration in the gas channels and thus, a change in membrane conductivity.<sup>131</sup>

Lastly, Pivac et al.<sup>132</sup> summarized and discussed several possible explanations describing an inductive feature at low frequencies in the impedance spectra of PEM-FC. It can either be ascribed to side reaction with intermediate species – such as adsorption processes on the catalyst surface or  $\text{H}_2\text{O}_2$  or  $\text{PtO}_x$  formation – or to water transport characteristics, e.g., a change in water generation or in proton conductivity. Ultimately, they concluded that the interpretation at low frequencies is still not straightforward.

In summary, the only viable explanation for the observed inductive loop in our study might be an oscillation of the water content and flux within the membrane. Since the Pt-wire reference electrode applied in this study is centrally placed within the MEA and the water flux within the membrane can also change according to the applied amplitude and current, this might lead to the observed inductive feature due to a change in hydration state of the membrane. However, up to this point no clear evidence was found for the inductive loop recorded within this study.

## 4.6 Analysis of the Anode Impedance Spectra

Even though the inductive loop at low frequencies remains an open question, the inductive artifacts are only observed at high current densities within the anode impedance spectra (Figure 4.5b). To extract any kinetic information, however, the small current densities are sufficient (e.g.,  $10 - 100 \text{ mAcm}^{-2}_{\text{geo}}$  for the determination of the Tafel slope; see Figure 2.2). Hence, a simplified transmission line model was used to fit the anode impedance spectra at low current densities to extract the Tafel slope (i.e., the charge transfer resistance), the capacitance as well as the proton sheet resistance. Figure 4.12 illustrates the transmission line model used to fit the anode spectra.



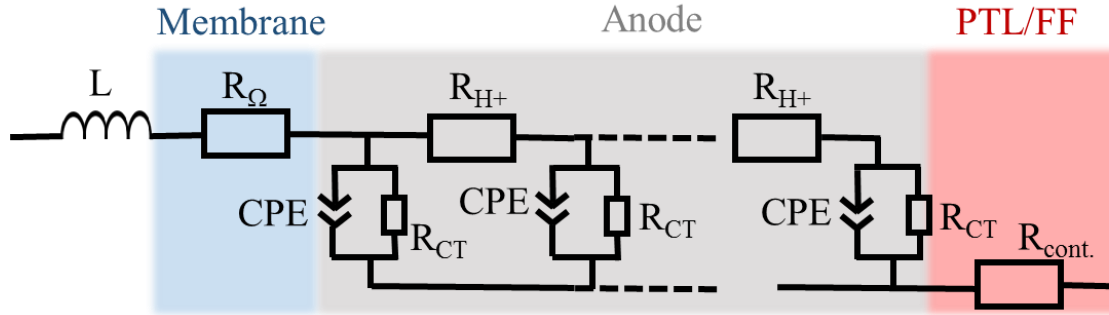


**Figure 4.12** One-dimensional transmission line model showing the inductance of the system ( $L$ ) in series with the through-plane proton transport resistance of the membrane ( $R_{\Omega}$ ), the incremental proton sheet resistance ( $R_{H+}$ ), and the electrical resistance ( $R_{cont.}$ ) mainly originating from the contact resistance at the electrode||PTL interface. These resistances are coupled with an incremental RC-element, describing the charge transfer kinetics ( $R_{CT}$ ) and the electrode capacitance ( $C_i$ ) which is potential dependent.

When fitting the anode spectrum at  $50 \text{ mAcm}^{-2}_{geo}$ , none of these parameters was fixed and the recorded data as well as the obtained fit are depicted in Figure 4.13a. At high frequencies, the intercept with the x-axis depicts the HFR, followed by a  $45^\circ$  degree line representing the proton sheet resistance and a subsequent semi-circle associated with the charge transfer kinetics of the OER. The charge transfer resistance of the OER is non-linear, and the overpotential increases proportional to the logarithm of the current (Tafel kinetics; equation 4.5). Hence, due to the small current density applied, the charge transfer resistance is dominant and the obtained fit seems to match rather nicely. Since the residuals are randomly but equally distributed around the zero line and less than 5% (see Figure 4.13b), we assume that the underlying model represents the occurring processes quite well.

$$\eta \propto TS \cdot \log\left(\frac{i}{i_0}\right) \quad 4.5$$

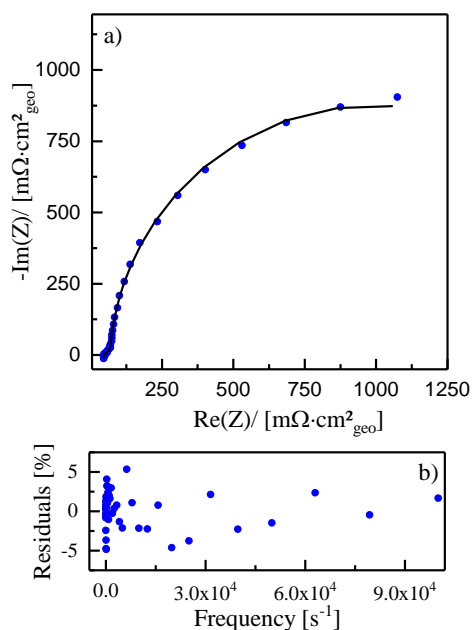


**Figure 4.13** a) Electrochemical impedance spectra (100 kHz – 1 Hz) of the anode at 50 mAcm<sup>-2</sup><sub>geo</sub> (black line) and the corresponding fit (blue circles) derived from the TLM model depicted in Figure 4.12 of a 5 cm<sup>2</sup> PEM water electrolysis cell recorded at 80 °C and ambient pressure (1 bar<sub>a,cathode</sub>, 1 bar<sub>a,anode</sub>), and 5 mL<sub>H2O</sub> min<sup>-1</sup> at the anode. b) Corresponding residuals. MEA specifications: ≈1.3 mg<sub>Ir</sub> cm<sup>-2</sup><sub>MEA</sub> anode and ≈0.3 mg<sub>Pt</sub> cm<sup>-2</sup><sub>MEA</sub> cathode loading, using two Nafion® 212 (≈50 μm) membranes and a 50 μm Pt-wire with a 9 μm PTFE insulation as a reference electrode.

In table 4.1 the obtained parameters are listed. The HFR calculated based on the fit (45.7 mΩcm<sup>2</sup><sub>geo</sub>) matches quite well with the HFR for a 50 μm Nafion® membrane obtained in the literature, illustrating that the Pt-WRE is centrally placed within the MEA.<sup>27</sup> Bernt et al.<sup>27</sup> estimated the proton sheet resistance for an electrode containing 11.6 wt.-% to be between 14 – 30 mΩcm<sup>2</sup><sub>geo</sub>. Hence, the proton sheet resistance derived from the impedance fit (65.9 mΩcm<sup>2</sup><sub>geo</sub>) is roughly twice as large as would be expected for a 12 wt.-% ionomer electrode. Usually, the proton sheet resistance is determined in so called “blocking conditions”, when the charge-transfer resistance is infinitely large.<sup>40, 47</sup> In this case, however, the lowest current density (50 mAcm<sup>-2</sup><sub>geo</sub>) was used to determine the proton sheet resistance and thus, the charge transfer resistance might already have an impact on the fit of R<sub>H+</sub>. To ensure a proper determination of the proton sheet resistance, an additional impedance spectrum should be recorded, where the charge transfer kinetics are infinitely large (e.g., H<sub>2</sub>/N<sub>2</sub> regime or at potentials below the OER regime) so that the ECM can be simplified. The charge transfer resistance can also be extracted from the polarization curve based on the Tafel relation (equation 4.6), once the proton sheet resistance as well as the ohmic resistance are accounted for. Based on equations 2.24 – 2.26, the effective proton sheet resistance can be calculated.

$$R_{CT} = \frac{TS}{2.303} \cdot \frac{1}{i} \quad 4.6$$

In Figure 4.14 the polarization curve as well as the  $iR$ - and  $R_{H^+}$ -free polarization curves along with the HFR are shown.

**Table 4.1** Physical parameters obtained by fitting the impedance spectrum recorded at  $50 \text{ mAcm}^{-2}_{\text{geo}}$  (Figure 4.13a) with the TLM depicted in Figure 4.12.

Parameter		
HFR	$0.009 \Omega$	$45.7 \text{ m}\Omega\text{cm}^2_{\text{geo}}$
$R_{H^+}$	$0.013 \Omega$	$65.9 \text{ m}\Omega\text{cm}^2_{\text{geo}}$
$R_{CT}$	$0.370 \Omega$	$1.85 \Omega\text{cm}^2_{\text{geo}}$
Capacity	$0.446 \text{ F}$	$89 \text{ mFcm}^{-2}_{\text{geo}}$
Alpha	$0.965$	

The charge transfer resistance at  $50 \text{ mAcm}^{-2}$  estimated based on the Tafel relation (equation 4.6 with a Tafel slope of  $52 \text{ mVdec}^{-1}$  taken from Figure 4.14) results in  $2.26 \Omega\text{cm}^2_{\text{geo}}$ . In comparison to the one calculated based on the here used TLM model ( $1.85 \Omega\text{cm}^2_{\text{geo}}$ ; table 4.1), the difference is only  $\approx 20\%$ , which is quite reasonable. However, both the fitting of the impedance spectra as well as the determination of the Tafel slope are quite parameter sensitive, and a small deviation in one of the parameters would lead to a different result. For example, when the Tafel slope is determined between  $0.01 - 0.05 \text{ Acm}^{-2}_{\text{geo}}$  yielding  $48 \text{ mVdec}^{-1}$ , the charge transfer resistance calculated from equation 4.6 is  $1.95 \Omega\text{cm}^2_{\text{geo}}$ , and hence differs by only 6% from the TLM fit in table 4.1. Therefore, the charge transfer resistance obtained from the impedance measurement matches quite well with the one estimated by the Tafel relationship. Since the double-layer capacity cannot be measured directly at higher potentials we assume that the capacity extracted from the CV at  $\approx 1.25 \text{ V}$  (see Figure 4.15) remains roughly constant. The capacity derived from the impedance measurement ( $\approx 89 \text{ mFcm}^{-2}_{\text{geo}}$ ) is roughly half of the one deduced from the CV ( $\approx 157 \text{ mFcm}^{-2}_{\text{geo}}$ ). Bernt et al.<sup>27</sup> did not observe any difference in capacity within this range of ionomer content, wherefore this cannot explain this 2-times higher capacity. Nonetheless, they also observed a higher capacity extracted from the CV compared to the one they estimated based on the impedance measurement, which they attributed to the fast electrosorption processes during cycling and the associated pseudocapacitance.<sup>47</sup> Up to now, we cannot explain this difference, but since there is no information on whether there is an

underlying redox-couple masked by the OER, we believe that the obtained capacities are sufficiently close to demonstrate the application of the Pt-WRE at this point.

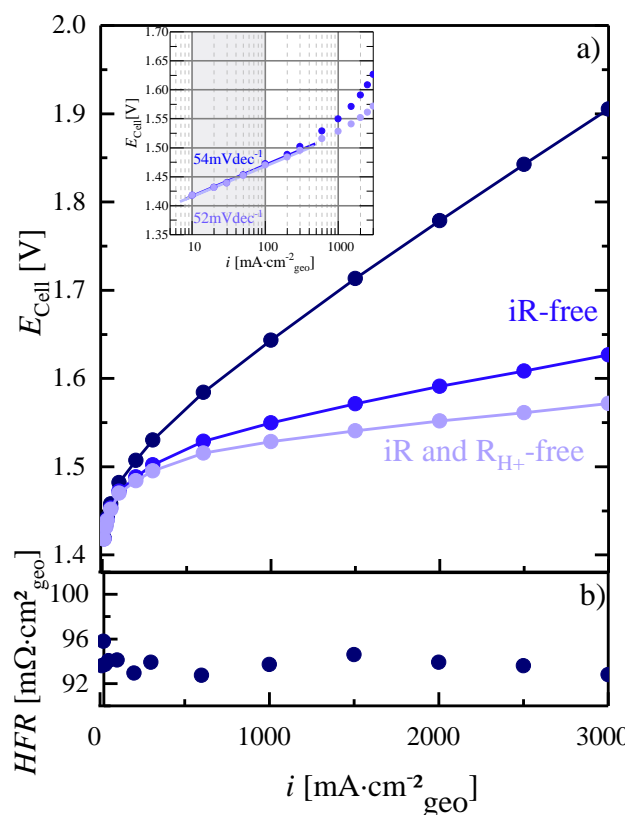


**Figure 4.14** PEM-WE performance data recorded at 80 °C and ambient pressure. a)  $E_{\text{cell}}$  vs  $i$  performance (dark blue symbols), HFR-free performance data (light blue symbols), and the  $iR$ - and  $R_{H^+}$ -free performance data (purple symbols) with an anode water-feed of  $5 \text{ mL}_{\text{H}_2\text{O}} \text{ min}^{-1}$  of an MEA including a Pt-WRE (100  $\mu\text{m}$  membrane); inset: Tafel plots of  $E_{\text{HFR-free}}$  and  $E_{\text{HFR+RH+-free}}$  vs  $i$  (data from Figure 4.14a and table 4.1); Tafel slopes were determined between  $0.01 \text{ A cm}^{-2}_{\text{geo}}$  and  $0.1 \text{ A cm}^{-2}_{\text{geo}}$  (gray shaded region); b) corresponding HFR values (extracted from the intercept in the Nyquist plot). Same MEA specifications as in Figure 4.13.

The second parameter of the CPE next to the capacitance is alpha, which accounts for any structural inhomogeneity of the electrode surface.<sup>133</sup> As can be seen in table 4.1, the alpha value obtained from the impedance fit is sufficiently close to  $\alpha = 1$ , which is expected for PEM-WE and PEM-FC electrodes.

In summary, using a TLM for fitting the anode impedance spectrum recorded with the Pt-WRE at low current densities delivers physical parameters, providing a more precise depiction of the individual processes occurring during operation.

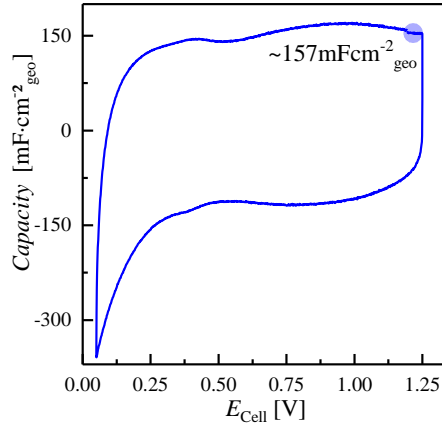


**Figure 4.15** Cyclic voltammogram (CV) recorded at 50 mV/s, 80 °C, ambient pressure, and 5 mL<sub>H<sub>2</sub>O</sub> min<sup>-1</sup> (anode)/ 50 nccm H<sub>2</sub> (cathode). Same MEA specifications as in Figure 4.13.

As already mentioned, the determination of the Tafel-slope from the polarization curve is prone to errors, since all other occurring losses need to be accounted for. Hence, if one were able to derive the charge transfer resistances at each current density individually, a more precise determination would be possible. Therefore, the impedance spectra recorded during the polarization curve up to a current density of 1 Acm<sup>-2</sup><sub>geo</sub> was fitted using the TLM in Figure 4.12. At some point, the semi-circle of the charge transfer resistance merges with the 45° line of the proton sheet resistance and an unambiguous determination of R<sub>H+</sub> is not possible, wherefore we kept R<sub>H+</sub> = 65.9 mΩcm<sup>2</sup><sub>geo</sub> constant during the fit (i.e., the value obtained for the fit at 50 mAcm<sup>-2</sup>). Moreover, as already shown in chapter 4.4, the anode impedance spectra feature an inductive loop at low frequencies. To avoid any adulteration of the derived parameters due to the influence of the inductive loop, the fit was applied to a specific current and frequency range (see table 4.2).

**Table 4.2** Current and frequency range for the application of the TLM to analyze the anode impedance spectra

Current density [mAcm <sup>-2</sup> <sub>geo</sub> ]	Frequency-Range
0.01-0.05	100 kHz-1 Hz
0.10-0.20	100 kHz-2 Hz
0.30-0.60	100 kHz-6 Hz
1.00	100 kHz-122 Hz

Based on the charge transfer resistance obtained from the TLM as a function of the inverse current using equation 4.6, the Tafel slope can be determined (Figure 4.16). Independent of the current range the Tafel slope derived from the charge transfer equates to  $\approx 43 \text{ mVdec}^{-1}$  and thus, is roughly  $10 \text{ mVdec}^{-1}$  lower compared to the one obtained by a linearization of the polarization curve (see Figure 4.14a). Since the small current densities in this analysis have a greater impact on the Tafel slope, a small deviation at high current densities (e.g., due to a less accurate fit) would make less of a difference. In summary, if the charge transfer resistance is calculated based on equation 4.6, the charge transfer resistance for the used catalyst ( $\text{IrO}_2/\text{TiO}_2$ ; Umicore) will be smaller than what has been derived from the polarization curve.

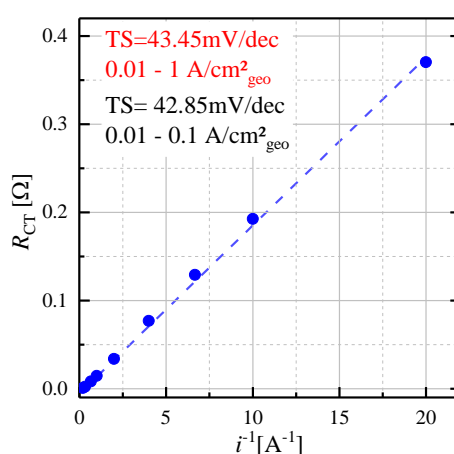


**Figure 4.16** Charge transfer resistance of the anode as function of the inverse current using equation 4.6; The charge transfer is estimated by applying the TLM to the anode the impedance data shown in Figure 4.5a and b. Same MEA specifications as in Figure 4.13.

Besides the charge transfer resistance, the capacitance as well as alpha can be derived from the TLM and are depicted in Figure 4.17. While alpha remains rather constant and close to one, the anode capacitance determined from the anode impedance data increases with current. Although the capacitance is roughly half ( $\approx 90 \text{ mFcm}^{-2}_{\text{geo}}$ ) of what is estimated based on the CV (Figure 4.15) at lower current densities ( $< 250 \text{ mAcm}^{-2}_{\text{geo}}$ ), at  $1 \text{ Acm}^{-2}_{\text{geo}}$  the capacitance obtained from the anode impedance data ( $\approx 150 \text{ mFcm}^{-2}_{\text{geo}}$ ) is close to the one obtained from the CV ( $157 \text{ mFcm}^{-2}_{\text{geo}}$  at 1.2 V).

Even though only part of the anode impedance spectra was used to determine these single parameters, the values obtained are in good agreement of what would be expected. Up to this point, no explanation has been found for the inductive loop observed at lower frequencies and an unbiased impedance measurement and hence, fitting is not possible. Nevertheless, it was shown that by using the right TLM and only part of the recorded impedance spectra one can

still obtain physically meaningful parameters, which allow a more precise deconvolution of the individual processes occurring during operation.

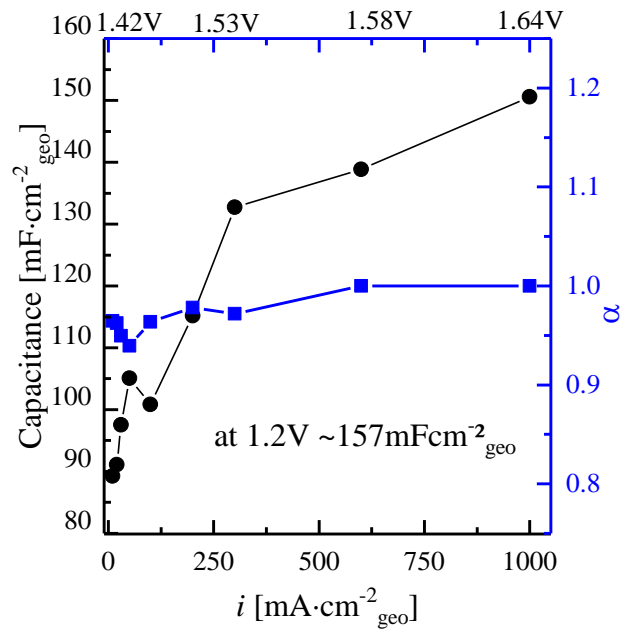


**Figure 4.17** Capacitance (black circles) and alpha (blue squares) derived from the anode impedance as function of the current density; Both are estimated based on the TLM in Figure 4.12 from the impedance measurements recorded during the polarization curve (Figure 4.14). The same MEA was used as in Figure 4.13





## 5 Scientific Contributions

The following sections show the scientific contributions made by this PhD research as published work in peer-reviewed journals. In section 5.1, the current challenges in catalyst development for PEM-WE are revealed, starting from the right choice of catalyst material, describing the reliability of catalyst screening tools, and exploring accelerated stress tests. The next section (5.2) deals with the development and characterization of a highly active OER catalyst, where iridium is deposited on conductive ATO, thereby enabling an OER catalyst with a lower iridium packing density, which is one prerequisite to enable large scale PEM water electrolysis.

In order to accelerate catalyst development screening tools are necessary to access the activity and stability of newly developed catalysts. RDE or other half-cell based methods are commonly used. Therefore, in section 5.3, the frequently used method (application of constant current) to access the stability of OER catalysts using the RDE technique will be carefully evaluated. It will be shown, that the obtained stability is greatly influenced by the accumulation of oxygen bubbles within the catalyst layer. The shielding of active sites by oxygen bubbles leads to the loss in performance as well as to a loss of active material. In section 5.4, it will be demonstrated that the accumulation of oxygen bubbles during an RDE measurement can be prevented when additional ultrasonication is applied. Subsequently (section 5.5), it will be shown that neither the application of constant current or potential nor potential cycling can be used to estimate the lifetime of an OER catalyst using the RDE technique. The results obtained from RDE are directly compared to the stability measured in an MEA in a PEM-WE: while the catalyst operates stable in an MEA, a severe decrease in performance can be observed in RDE.

Since it was shown that the RDE method cannot be used to determine the stability of an OER catalyst, accelerated stress tests are necessary to access the lifetime of an OER catalyst on a reasonable time scale. Therefore, in section 5.6, an AST mimicking the fluctuating power supply by renewable energies is proposed, where times of operation and idle periods alternate. During idle periods, an additional interfacial resistance was shown to develop leading to a decrease in performance and to the passivation of the Ti-PTL in combination with the formation of a hydrous iridium-oxide. By introducing a Pt-wire reference electrode it will be shown in-situ in section 5.7, that an additional contact resistance at the anode is indeed responsible for the decrease in performance.

## 5.1 Current Challenges in Catalyst Development for PEM Water Electrolysis

The following review article “Current Challenges in Catalyst Development for PEM Water Electrolyzer” was submitted to *Chemie Ingenieur Technik* in July 2019 and accepted for publication in October 2019 as an open access article under the terms of Creative Commons Attributions License (CC BY 4.0).<sup>134</sup> One can find the article under the permanent web-link: <https://onlinelibrary.wiley.com/doi/full/10.1002/cite.201900101>

This review highlights the current challenges in catalyst development for PEM-WE. Although hydrogen production via electrochemical water splitting in a PEM-WE is a promising method with respect to the aimed decarbonization of the energy sector, one major obstacle is the harsh environment (high potentials and high acidity) during operation, which limits the choice of electrocatalysts to the platinum group metals. While the Pt loading on the cathode side can easily be reduced due to the fast kinetics toward the HER, the sluggish kinetics of the OER on the currently used iridium-based catalysts form an obstacle. Therefore, considering the abundance along with the costs for iridium a significant reduction in iridium loading (40-folds) is required to enable a GW-range application. It is shown that, in theory, a reduction of the iridium loading down to  $0.05 \text{ mg}_{\text{Ir}}\text{cm}^{-2}_{\text{geo}}$  along with a significant decrease of the Ir-specific power density ( $\text{g}_{\text{Ir}}\text{kW}^{-1}$ ) is possible with today’s commercial catalyst materials.<sup>134</sup> In a study by Bernt et al.<sup>65</sup> it was shown, that low loadings of one commonly used catalyst namely an  $\text{IrO}_2$  coated  $\text{TiO}_2$  support ( $\text{IrO}_2/\text{TiO}_2$ ; Elyst Ir75 0480 from Umicore, Germany) result in inhomogeneous catalyst layers and thus in additional performance losses. Although, the activity of today’s iridium based OER catalysts might be sufficient, obtaining a homogenous catalyst layer at low iridium loadings requires the development of electrocatalysts with a lower iridium packing density ( $\text{g}_{\text{Ir}}\text{cm}^{-3}$ ) is needed. One approach would be to disperse nanoparticles of Ir or  $\text{IrO}_2$  on conductive high-surface area support materials (e.g., ATO), similar to the concept used for Pt/C electrocatalysts.

To access the activity as well as stability of newly developed catalysts reliable screening tests are needed. Most commonly methods based on RDE or flow-channel configurations have to be used. While the activity measured in RDE vs MEA is within the same order of magnitude, the OER catalyst stability obtained from RDE (couple of hours) differs significantly from the one measured in an MEA (ten thousands of hours). It was shown that the fast increase in potential is associated with the accumulation of oxygen bubbles within the catalyst layer during an RDE

measurement.<sup>115</sup> Since neither RDE nor flow-channel measurements provide reliable stability results, accelerated stress tests are required to assess the long-term stability of electrocatalysts. An accelerated stress test, where times of operation alternate with idle periods to mimic the fluctuating power supply of renewable energies, showed that idle periods (no current is supplied) should be avoided in order to maintain a constant performance.


### **Author contributions**

Fabrication of membrane electrode assemblies and electrochemical testing in a PEM-WE cell was performed by M.B., A.H.-W., C.S., and J.S. Fabrication of catalyst inks and electrochemical testing in RDE was performed by M.F.T. Analysis of the experimental test results was done by M.B., A.H.-W., M.T.F., C.S., and J.S. M.B. and A.H.-W. wrote the manuscript that was edited by H.A.G. All authors discussed the experimental results and revised the manuscript.

# Current Challenges in Catalyst Development for PEM Water Electrolyzers

Maximilian Bernt<sup>1,\*,†</sup>, Alexandra Hartig-Weiß<sup>2,‡</sup>, Mohammad Fathi Tovini<sup>2</sup>, Hany A. El-Sayed<sup>2</sup>, Carina Schramm<sup>2</sup>, Jonas Schröter<sup>1,2</sup>, Christian Gebauer<sup>3</sup>, and Hubert A. Gasteiger<sup>2,\*</sup>

DOI: 10.1002/cite.201900101

 This is an open access article under the terms of the Creative Commons Attribution License, which permits use, distribution and reproduction in any medium, provided the original work is properly cited.

This work addresses current challenges in catalyst development for proton exchange membrane water electrolyzers (PEM-WEs). To reduce the amount of iridium at the oxygen anode to levels commensurate with large-scale application of PEM-WEs, high-structured catalysts with a low packing density are required. To allow an efficient development of such catalysts, activity and durability screening tests are essential. Rotating disk electrode measurements are suitable to determine catalyst activity, while accelerated stress tests on the MEA level are required to evaluate catalyst stability.

**Keywords:** Accelerated stress test, Catalyst, Iridium, Oxygen evolution reaction, PEM electrolysis

*Received:* July 15, 2019; *revised:* August 22, 2019; *accepted:* October 15, 2019

## 1 Introduction

With its high power density and excellent load-following capability, proton exchange membrane water electrolysis (PEM-WE) presents a promising technology for sustainable hydrogen production in the context of large-scale energy storage [1–3]. However, due to the harsh environment (low pH, potential > 1.5 V and high oxygen concentration on the anode) in a PEM-WE, the choice of electrocatalysts is limited to platinum group metals (PGMs). Typically, carbon supported platinum (Pt/C) is used for the hydrogen evolution reaction (HER) on the cathode, while iridium (Ir) based catalysts are used for the oxygen evolution reaction (OER) on the anode. Even though high catalyst loadings are commonly applied ( $\approx 0.5$ – $1.0 \text{ mg}_{\text{Pt}} \text{ cm}^{-2}$  on the cathode and  $\approx 2 \text{ mg}_{\text{Ir}} \text{ cm}^{-2}$  on the anode [4]), catalyst materials account for only  $\approx 5\%$  of the total cost in today's relatively small (kW range) systems [5]. However, for larger systems (MW range), the contribution of balance-of-plant costs and other stack components will be much lower, so that catalyst costs are expected to become a major cost contributor [6]. Additionally, the limited availability of Ir will become a concern when PEM-WE installation capacities reach the GW-scale. For this scenario, a recent study by our group shows that a significant reduction of the Ir loading from currently  $\approx 2 \text{ mg}_{\text{Ir}} \text{ cm}^{-2}$  to only  $\approx 0.05 \text{ mg}_{\text{Ir}} \text{ cm}^{-2}$  would be required to enable a large-scale application of PEM-WEs [3, 7].

A reduction of the Pt loading on the cathode was shown to be possible without any impact on performance due to the extremely fast HER kinetics of Pt in acidic electrolytes [2, 7–9]. For the Ir catalyst, on the other hand, the OER kinetic penalty of a reduction in Ir loading for an IrO<sub>2</sub> based OER catalyst is illustrated in Fig. 1. The solid red line presents the measured data for an MEA (membrane elec-

trode assembly) with a Nafion<sup>®</sup> 212 membrane ( $\approx 50 \mu\text{m}$ ), a Pt loading of  $\approx 0.35 \text{ mg}_{\text{Pt}} \text{ cm}^{-2}$  on the cathode, and an Ir loading of  $\approx 2 \text{ mg}_{\text{Ir}} \text{ cm}^{-2}$  on the anode at a temperature of 80 °C and ambient pressure (taken from Fig. 4a in reference [10]). Due to the thin membrane and the optimized electrode structure, a cell voltage efficiency with respect to the lower heating value of hydrogen (LHV) of 70 %<sub>LHV</sub> (corresponding to a cell voltage of 1.79 V) can be reached at a current density of  $4 \text{ A cm}^{-2}$  [10], equating to a cell energy consumption of  $\approx 48 \text{ kWh kg}_{\text{H}_2}^{-1}$ . Based on the typically observed Tafel kinetics for IrO<sub>2</sub> based OER catalysts with a Tafel slope of  $\text{TS} \approx 50 \text{ mV decade}^{-1}$  [10], the kinetic OER overpotential increase ( $\Delta\eta_{\text{OER}}$ ) when the catalyst loading is reduced from 2 to  $0.05 \text{ mg}_{\text{Ir}} \text{ cm}^{-2}$  would equate to a cell voltage increase of  $\approx 80 \text{ mV}$  (from  $\Delta\eta_{\text{OER}} = \text{TS} \log[2/0.05]$ ). Assuming that all other voltage losses are not affected by the reduction of OER catalyst loading, the voltage vs. current density curve would simply be shifted upwards by 80 mV, as is shown by the red dashed line in Fig. 1.

<sup>†</sup>Dr. Maximilian Bernt, Jonas Schröter  
maximilian.bernt@tum.de

Bayerisches Zentrum für angewandte Energieforschung, Walther-Meissner-Straße 6, 85748 Garching, Germany.

<sup>‡</sup>Alexandra Hartig-Weiß, Mohammad Fathi Tovini, Dr. Hany A. El-Sayed, Carina Schramm, Jonas Schröter, Prof. Dr. Hubert A. Gasteiger  
hubert.gasteiger@tum.de

Technische Universität München, Chair of Technical Electrochemistry, Department of Chemistry and Catalysis Research Center, Lichtenbergstraße 4, 85748 Garching, Germany.

<sup>3</sup>Dr. Christian Gebauer

Heraeus Deutschland GmbH & Co. KG, Heraeus Precious Metals, Heraeusstraße 12–14, 63450 Hanau, Germany.

<sup>\*</sup> These authors contributed equally to this work.



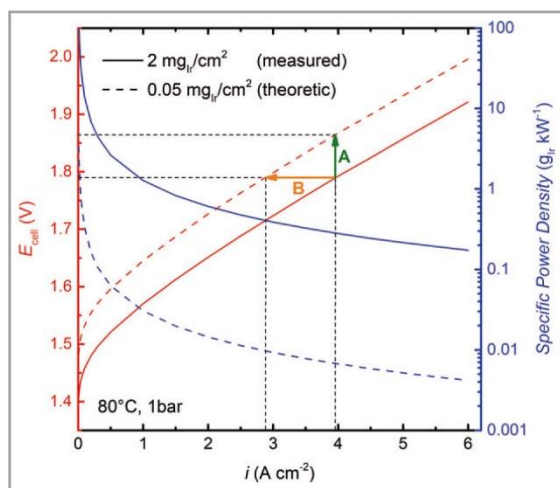


**Figure 1.** Ambient pressure PEM-WE performance curves measured for an MEA with a  $50\text{ }\mu\text{m}$  thick Nafion<sup>®</sup> 212 membrane and catalyst loadings of  $\approx 2\text{ mg}_{\text{Ir}}\text{ cm}^{-2}$  and  $\approx 0.35\text{ mg}_{\text{Pt}}\text{ cm}^{-2}$  at a temperature of  $80\text{ }^{\circ}\text{C}$  (solid red line;  $5\text{ cm}^2$  single-cell data taken from reference [10]). The dashed red line gives the projected performance curve for an Ir loading of  $0.05\text{ mg}_{\text{Ir}}\text{ cm}^{-2}$ , calculated based on the OER kinetics of the  $\text{IrO}_2$  catalyst and the assumption that all other voltage losses are not affected by the reduction of OER catalyst loading. The blue lines represent the Ir-specific power density as a function of current density for Ir loadings of  $2\text{ mg}_{\text{Ir}}\text{ cm}^{-2}$  (solid line) and  $0.05\text{ mg}_{\text{Ir}}\text{ cm}^{-2}$  (dashed line). The arrows illustrate the consequence of lowering the Ir loading while keeping either the current density constant (path A) or while keeping the cell voltage (i.e., the efficiency) constant (path B).

With regards to the Ir-specific cell power density (i.e., the Ir loading divided by the cell power density, in units of  $\text{g}_{\text{Ir}}\text{ kW}^{-1}$ ), the projected performance loss when reducing the Ir loading by a factor of 40 (i.e., from 2 to  $0.05\text{ mg}_{\text{Ir}}\text{ cm}^{-2}$ ) would still result in a  $\approx 30$ -fold reduction of the Ir-specific power density (see solid vs. dashed blue line in Fig. 1). In other words, the performance metrics projection for this 40-fold lowering of the Ir loading can be viewed in either one of two ways: i) if keeping the current density constant, the cell voltage at  $4\text{ A cm}^{-2}$  would increase by  $\approx 80\text{ mV}$  to  $1.87\text{ V}$ , which corresponds to an increase of the cell energy consumption by  $\approx 4\%$  to  $\approx 50\text{ kWh kg}_{\text{H}_2}^{-1}$  ( $\approx 67\%$   $\text{LHV}$  efficiency), but the Ir-specific power density would be reduced from  $\approx 0.3\text{ g}_{\text{Ir}}\text{ kW}^{-1}$  to  $\approx 0.007\text{ g}_{\text{Ir}}\text{ kW}^{-1}$  (see path A marked in Fig. 1); or, ii) when keeping the efficiency constant at  $70\%$   $\text{LHV}$ , the current density would have to be decreased by  $\approx 27\%$  to  $\approx 2.9\text{ A cm}^{-2}$ , but the Ir-specific power density would still be substantially reduced to  $\approx 0.01\text{ g}_{\text{Ir}}\text{ kW}^{-1}$  (see path B in Fig. 1). Both strategies would lead to a reduction of the Ir-specific power density to the  $\leq 0.01\text{ g}_{\text{Ir}}\text{ kW}^{-1}$ , which would be required for GW-scale applications of PEM-WEs [7]. It also should be noted, however, that the voltage efficiencies of  $\geq 70\%$   $\text{LHV}$  at current densities  $> 2\text{ A cm}^{-2}$  shown in Fig. 1 can only be achieved with thin membranes [11, 12] ( $\approx 50\text{ }\mu\text{m}$  here vs.  $\approx 200\text{ }\mu\text{m}$  in today's

commercial electrolyzers), which in turn requires special mitigation strategies to prevent the formation of explosive  $\text{H}_2/\text{O}_2$  mixtures in the anode compartment [13].

The analysis presented above suggests that the requirements for a large-scale application of PEM-WEs could be met by reducing the Ir loading to  $0.05\text{ mg}_{\text{Ir}}\text{ cm}^{-2}$ . However, such a drastic reduction of Ir loading is not possible with today's commercial catalyst materials. In case of the titanium oxide supported  $\text{IrO}_2$  ( $\text{IrO}_2/\text{TiO}_2$ ) catalyst (Elyst Ir75 0480 from Umicore, Germany) that was used at an Ir loading of  $2\text{ mg}_{\text{Ir}}\text{ cm}^{-2}$  for the performance curve shown in Fig. 1 (solid red line), the catalyst layer becomes very thin and inhomogeneous when its loading is reduced to  $< 0.5\text{ mg}_{\text{Ir}}\text{ cm}^{-2}$ , resulting in a much higher performance loss than expected based simply on the OER kinetics losses [7]. That analysis shows that while the OER activity of today's commercial Ir based catalysts would be sufficient to allow a drastic reduction in iridium loading at only minor performance losses, high-structured catalysts, i.e., catalysts with a much reduced iridium packing density in the electrode, will be required to enable the fabrication of a homogeneous catalyst layer at such low Ir loadings. For example, the iridium packing density of the here used  $\text{IrO}_2/\text{TiO}_2$  catalyst in the anode electrode is  $\approx 2.3\text{ g}_{\text{Ir}}\text{ cm}^{-3}$  (corresponding to a layer thickness of  $\approx 4.3\text{ }\mu\text{m (mg}_{\text{Ir}}\text{ cm}^{-2})^{-1}$  [7]), which is  $\approx 30$ -fold larger than that of a typical carbon supported platinum catalyst used in fuel cells or in the electrolyzer cathode ( $\approx 0.08\text{ g}_{\text{Pt}}\text{ cm}^{-3}$  or  $\approx 125\text{ }\mu\text{m (mg}_{\text{Pt}}\text{ cm}^{-2})^{-1}$  for a 15 wt % Pt/C catalyst [7]). In the following section, different concepts to develop such a high-structured catalyst will be discussed.

## 2 Concepts for Ir-Based OER Catalyst Development

In state-of-the-art PEM-WEs, unsupported Ir or  $\text{IrO}_2$  based catalysts are used for the OER on the anode [4]. There are different possible approaches to create a high-structured catalyst which would enable the fabrication of electrodes with ultra-low Ir loadings and with sufficient thickness ( $\approx 4\text{--}8\text{ }\mu\text{m}$  [7]). One strategy is to maximize the noble metal dispersion by supporting thin films or nanoparticles of Ir or  $\text{IrO}_2$  on high-surface area support materials, a concept similar to the Pt/C catalyst used for the electrolyzer cathode or for PEM fuel cell electrodes. The high electrochemical potential on the anode side of  $> 1.4\text{ V}$ , however, precludes the use of carbon supports which would get oxidized to  $\text{CO}_2$  under these conditions [14, 15]. On the other hand, titanium dioxide ( $\text{TiO}_2$ ) is a stable, commercially available, and inexpensive material [16], and is frequently used as a catalyst support for Ir [17, 18]. However, a relatively high amount of Ir or  $\text{IrO}_2$  ( $> 40\text{ wt }%$ ) is required to generate sufficient electric conductivity by forming a contiguous network/film of Ir or  $\text{IrO}_2$  nanoparticles [19, 20], since  $\text{TiO}_2$  itself is not conductive. A conductive and stable support material would eliminate the need for a percolating

network of Ir or IrO<sub>2</sub> to provide sufficient conductivity across the catalyst layer and, hence, enable lower Ir loadings. Antimony doped tin oxide (ATO) [21–24] and niobium doped titanium oxide (NTO) [25] have been proposed as potential support materials, but their long-term stability for PEM electrolysis still needs to be verified. Another promising support option are titanium suboxides that have a higher intrinsic conductivity compared to ATO [26,27], but further research is required to show if this high conductivity can be maintained during prolonged electrolyzer operation. Tungsten doped titanium oxide (W<sub>x</sub>Ti<sub>1-x</sub>O<sub>2</sub>) has been presented as another potential support material and high performance and sufficient stability over 1000 h at an Ir loading of 0.2 mg<sub>Ir</sub> cm<sup>-2</sup> has been demonstrated [28]. In the absence of a suitable support material, alternative catalyst structures, such as Ir based nanowires [29], nanostructured thin films (NSTFs) [30], or core-shell structures [6,22] along with improved catalyst layer manufacturing techniques, like reactive spray deposition [6], present another pathway to achieve lower Ir loadings.

Within the Kopernikus P2X project [31], different approaches to reduce the iridium loading were investigated by the project partners Greenerity GmbH, Heraeus Deutschland GmbH & Co.KG, the Ludwig-Maximilians-University Munich (LMU), and the Technical University of Munich (TUM), which yielded a new high-structured catalyst with reduced iridium packing density ( $\approx 0.46 \text{ g}_{\text{Ir}} \text{ cm}^{-3}$ ), which at a loading of  $\approx 0.3 \text{ mg}_{\text{Ir}} \text{ cm}^{-2}$  still enables a sufficiently thick electrode of  $\approx 6.5 \mu\text{m}$ . Its performance at this loading and thickness is compared in Fig. 2 (green line) to that of the commercial IrO<sub>2</sub>/TiO<sub>2</sub> catalyst at the higher loading of  $2.5 \text{ mg}_{\text{Ir}} \text{ cm}^{-2}$  with an electrode thickness of  $\approx 11 \mu\text{m}$  (red line). Even though the catalyst loading was reduced by a factor of  $\approx 8$ , a slightly higher performance was obtained for the new catalyst. This presents an important first step to a significant reduction of the Ir loading required for a large-

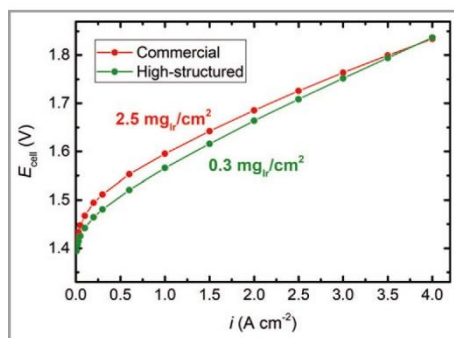


**Figure 2.** Ambient pressure electrolyzer performance (5 cm<sup>2</sup> single cell) at 80 °C for an MEA with a commercial catalyst (IrO<sub>2</sub>/TiO<sub>2</sub>, Umicore) with an anode Ir loading of 2.5 mg<sub>Ir</sub> cm<sup>-2</sup> (red) compared to a new high-structured catalyst material with an Ir loading of  $\approx 0.3 \text{ mg}_{\text{Ir}} \text{ cm}^{-2}$  (green). MEAs were prepared with  $\approx 50 \mu\text{m}$  Nafion<sup>®</sup> 212 membranes and a cathode Pt loading of 0.3 mg<sub>Pt</sub> cm<sup>-2</sup>; the cell hardware and the other cell components are as described in reference [10].

scale application of PEM-WE. At a cell voltage of 1.79 V corresponding to a cell voltage efficiency of 70 %<sub>LHV</sub>, the current density for both catalysts is  $\approx 3.4 \text{ A cm}^{-2}$ , which would correspond to Ir-specific power densities of  $\approx 0.41 \text{ g}_{\text{Ir}} \text{ kW}^{-1}$  and  $\approx 0.05 \text{ g}_{\text{Ir}} \text{ kW}^{-1}$  for the  $2.5 \text{ mg}_{\text{Ir}} \text{ cm}^{-2}$  and the  $0.3 \text{ mg}_{\text{Ir}} \text{ cm}^{-2}$  anode, respectively. For this new Ir-based OER catalyst, the projected Ir-specific power density would already be within a factor of 5–10 of the above stated target of  $0.01 \text{ g}_{\text{Ir}} \text{ kW}^{-1}$ . However, the development of such new OER catalysts requires fast and reliable screening methods to identify promising materials within a reasonable time scale. Possible methods and the associated challenges will be discussed in the following section.

### 3 Screening of OER Catalyst Activity and Stability

In order to evaluate the activity/stability of novel OER catalysts, screening tests based on rotating disk electrode (RDE) or flow-channel configurations [18,32,33] are commonly used. Typically, RDE measurements are performed in a three-electrode cell using a reversible hydrogen electrode (RHE) as a reference electrode, a high surface area gold (Au) mesh as a counter electrode, and a disk working electrode with a polycrystalline gold disk embedded in a PTFE body (Pine Research Instrumentation, USA). Often, diluted sulfuric acid is used as a liquid electrolyte and, in contrast to MEA measurements, only a few milligrams of catalyst are needed to assess the OER activity as well as the catalyst stability. The small amount of catalyst needed is one main advantage of using the RDE technique. New synthesis routes often yield only a few milligrams of catalyst material, and prescreening the OER activity along with the catalyst stability is beneficial for pre-selecting promising materials before a lot of effort is taken to produce several grams of catalyst which are required for MEA preparation and testing in an electrolyzer.

Fig. 3a shows the high-frequency resistance (HFR) corrected cell voltage vs. the logarithm of the mass-normalized current density (a so-called Tafel plot), often used to assess OER activity and kinetics, for the IrO<sub>2</sub>/TiO<sub>2</sub> catalyst (Umicore) measured at 40 °C, both with the RDE technique in argon-purged 0.1 M H<sub>2</sub>SO<sub>4</sub> and in a PEM electrolyzer at  $\approx 1 \text{ bar}_{\text{abs}} \text{ O}_2$ . The observed Tafel slope is quite similar for these two different measurement configurations ( $\approx 50 \text{ mV dec}^{-1}$ ), indicating that the prevailing OER reaction mechanism is similar in both environments. When referencing the OER activity at an HFR-corrected voltage of 1.5 V vs. the reversible hydrogen reference electrode potential, the activity of the Umicore (IrO<sub>2</sub>/TiO<sub>2</sub>) catalyst measured by the RDE technique ( $21 \text{ A g}_{\text{Ir}}^{-1}$ ) is roughly twice as high as when measuring the same catalyst in an MEA ( $10 \text{ A g}_{\text{Ir}}^{-1}$ ). While this difference of a factor of two is unclear at the moment, the obtained OER mass activities are still close enough to provide a reasonable prediction of



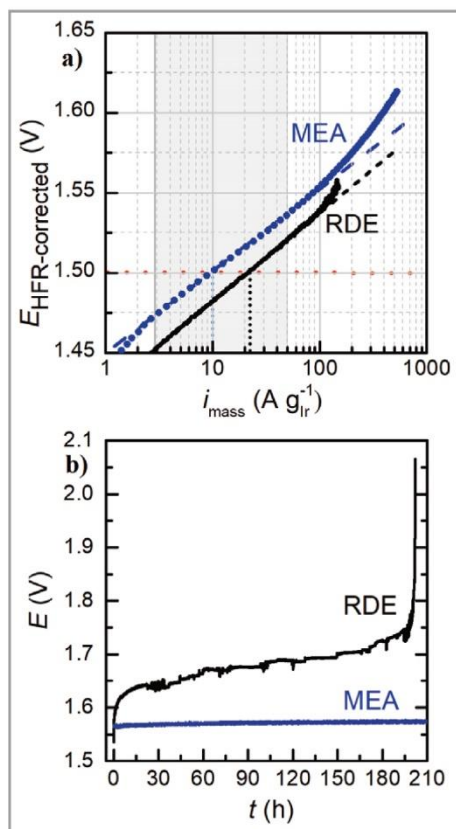


**Figure 3.** Evaluation of the OER activity and the stability of the Umicore catalyst ( $\text{IrO}_2/\text{TiO}_2$ ) by the RDE technique (in 0.1 M  $\text{H}_2\text{SO}_4$  at  $10 \text{ mV s}^{-1}$ , purged with pure argon) and in a  $5 \text{ cm}^2$  single-cell PEM-WE (also at  $10 \text{ mV s}^{-1}$  and at  $\approx 1 \text{ bar}_{\text{abs}}$   $\text{O}_2$  pressure) at  $40^\circ\text{C}$ : a) Tafel-plots of HFR-corrected cell voltage vs. the logarithm of the mass-normalized current density obtained by the RDE technique (black line) or by measuring an MEA in a single-cell PEM-WE (blue circles); b) chronopotentiometry at the same mass-specific current density of  $70 \text{ A g}_{\text{Ir}}^{-1}$  for an RDE (black) at a loading of  $0.4 \text{ mg}_{\text{Ir}} \text{ cm}^{-2}$  and a geometric current density of  $28 \text{ mA cm}^{-2}$  and for an MEA measurement (blue) at a loading of  $2.0 \text{ mg}_{\text{Ir}} \text{ cm}^{-2}$  and a geometric current density of  $139 \text{ mA cm}^{-2}$ .

the performance of a new OER catalyst in an electrolyzer on the basis of RDE data.

Other than estimating the OER activity of novel catalysts, obtaining an estimate for their long-term stability is of crucial importance for a successful implementation in a real system. Research groups synthesizing new OER catalysts often use a chronopotentiometric (CP) RDE experiment, as it can be conducted with only mg-quantities of catalyst. There, a constant current is applied and the corresponding increase in potential is correlated with catalyst stability. Fig. 3b shows the resulting potential transient for a constant mass specific current density of  $70 \text{ A g}_{\text{Ir}}^{-1}$  applied to the commercial  $\text{IrO}_2/\text{TiO}_2$  catalyst whose performance was shown in Fig. 2 (red line), both using the RDE technique (at a loading of  $0.4 \text{ mg}_{\text{Ir}} \text{ cm}^{-2}$  and a geometric current density

of  $28 \text{ mA cm}^{-2}$ ) and MEA measurements in a  $5 \text{ cm}^2$  single-cell (at a loading of  $2.0 \text{ mg}_{\text{Ir}} \text{ cm}^{-2}$  and a geometric current density of  $139 \text{ mA cm}^{-2}$ ). In case of the RDE measurements, the potential increases significantly within the first  $\approx 200 \text{ h}$ , until it finally jumps to  $> 2 \text{ V}$ . On the contrary, measuring the catalyst stability in the MEA shows a constant performance over the same time period, which is consistent with previous studies, where it was shown that a PEM-WE can operate for thousands of hours at constant current without any significant loss in performance [34]. In the literature, the increasing potential observed in RDE measurements is ascribed to the dissolution of active material until its complete loss, at which point the potential jump occurs [35]. However, it was recently shown by our group that the increase in potential is caused by the shielding of active sites due to the accumulation of oxygen bubbles trapped within the catalyst layer and that it cannot be correlated to catalyst degradation [36]. The accumulation of oxygen in the catalyst layer and partial shielding of the active sites results in a lower effective catalyst surface area. To provide the same total current the effective current density at the remaining active sites will increase leading to the observed increase in potential. Thus, the rising potential and the accompanied degradation of the catalyst is a result of the partial shielding of active sites by oxygen bubbles and cannot be related to the intrinsic stability of the catalyst. In general, filling the catalyst layer with oxygen bubbles would be a relatively fast process. However, we believe that some of the formed oxygen bubbles recombine and get removed by rotation leading to a slower accumulation of oxygen in the catalyst layer. Other occurring mechanisms, like changes of the wettability or the hydrophobicity of the catalyst might play an important role and have to be studied in more detail. In summary, we have to conclude that RDE measurements as well as iridium dissolution experiments in liquid electrolyte based electrochemical cells [32] are not a reliable predictor for the lifetime of newly developed OER catalysts, since trapped oxygen bubbles within the catalyst layer decrease the apparent stability of the catalyst by orders of magnitude compared to MEA measurements.

Nevertheless, degradation protocols are necessary to assess the long-term stability of newly developed OER catalysts in real PEM-WE systems. As already mentioned, under constant current operation the detected performance losses in PEM-WEs are rather small ( $< 4 \mu\text{V h}^{-1}$ ) [34], so that at least 1000 h of testing would be required to obtain a voltage loss of only  $\approx 4 \text{ mV}$ . Since other non-catalyst related variables such as temperature variations or membrane thinning can mask such small changes even longer test durations on the order of several thousands of hours would be required which is not feasible and would slow down the development and implementation of new OER catalysts dramatically. Therefore, accelerated stress tests (ASTs) are required to mimic operation and trigger certain degradation mechanisms on a shorter time-scale. One such example would derive from the need to couple water electrolysis with

fluctuating renewable energy sources, in which case the intermittent power supply would result in PEM-WE operation alternating between hydrogen generation when power is available and idle periods, where no current is supplied. In a recent study by our group, a test protocol was developed, where the cell was operated at 80 °C and an H<sub>2</sub>/O<sub>2</sub> pressure of 10/1 bar<sub>abs</sub>, at which condition it was cycled between high (3 A cm<sup>-2</sup>) and low current densities (0.1 A cm<sup>-2</sup>), followed by idle periods where no or almost no current was supplied [37]. During the idle period, the cell was either left at open circuit voltage (referred to as OCV-AST) or was polarized at 1.3 V<sub>RHE</sub> (referred to as reference test).

Fig. 4a depicts the voltage profile during one cycle for both the reference test (blue circles) and the OCV-AST (black line). During the reference test, a cell potential of 1.3 V was maintained during the idle period, requiring an applied current of  $\approx 1 \text{ mA cm}^{-2}$  [37], while during the OCV-AST no current/voltage was applied to the electrolyzer cell during the idle period, resulting in a drop of the cell voltage to  $\approx 0 \text{ V}$  within a couple of minutes. This observed decrease in cell voltage is caused by an accumulation of hydrogen in the anode compartment due to hydrogen crossover through the membrane from the cathode side, where a hydrogen pressure of 10 bar<sub>abs</sub> was maintained [11]. This H<sub>2</sub>-rich gas-phase at 80 °C leads to the reduction of the surface of the crystalline IrO<sub>2</sub> of the catalyst (IrO<sub>2</sub>/TiO<sub>2</sub>, Umicore) to metallic iridium, accompanied by a concomitant drop of the anode potential to  $\approx 0 \text{ V}_{\text{RHE}}$  [37, 38]. Upon resuming operation, the anode potential will again increase to  $\approx 1.4\text{--}1.8 \text{ V}_{\text{RHE}}$  (depending on the current density, Fig. 4), where metallic iridium will be oxidized to an amorphous hydrous Ir(OH)<sub>x</sub> that is more active towards the OER [38, 39]. Thus, during the OCV-AST the cell voltage is continuously cycled between  $\approx 0 \text{ V}_{\text{RHE}}$  and  $\approx 1.4\text{--}1.8 \text{ V}_{\text{RHE}}$ , resulting in a repetitive transition of the surface of the iridium catalyst between high and low iridium oxidation states, which we ascribe to be the cause of the iridium dissolution into the membrane observed by post-mortem transmission electron microscopy (TEM) [37], analogous to what occurs during the voltage-cycling induced platinum dissolution in a PEM fuel cell [40]. Note that the here advanced hypothesis is different from that proposed by Cherevko et al. [41], who on the basis of half-cell experiments in an aqueous sulfuric acid electrolyte proposed that the intrinsic dissolution rate of hydrous iridium oxide is higher than that of crystalline IrO<sub>2</sub>. Owing to the high iridium loading in the here shown OCV-AST, the effect of iridium dissolution on the OER activity is very small ( $< 20 \text{ mV}$  [37]) and the vast majority of the observed performance losses after 718 OCV-AST cycles (red diamonds Fig. 4b) are due to an increase of the HFR (red diamonds Fig. 4c). On the other hand, no loss of performance and no increase of the HFR is observed for the reference test after 500 cycles (blue circles in Fig. 4b), where the anode potential was always kept positive of 1.3 V<sub>RHE</sub>. Both the increase

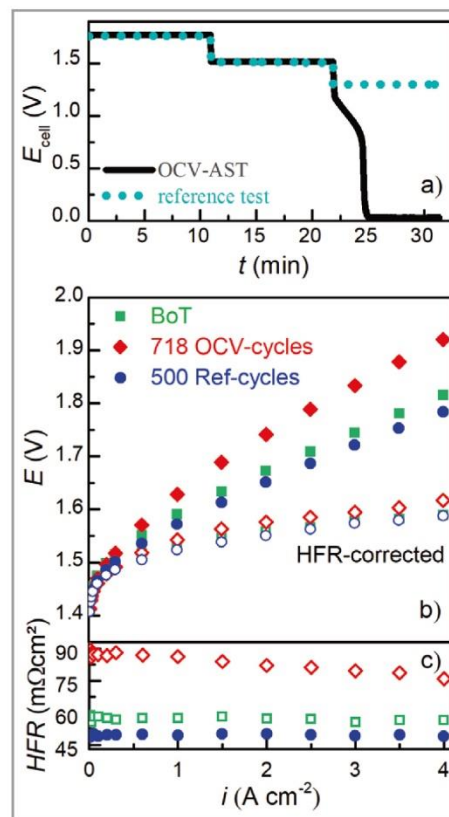


**Figure 4.** a) Cell potential during the accelerated stress test (AST) at 80 °C and 10:1 bar<sub>abs</sub> H<sub>2</sub>/O<sub>2</sub> to mimic an intermittent power supply of a PEM-WE, with periods of low and high current density followed by OCV ("OCV-AST", black solid line), and of a reference test in which the potential is held at 1.3 V during idle periods ("reference test", blue dotted line). b) Ambient pressure PEM-WE  $E_{\text{cell}}$  vs.  $i$  performance (filled symbols) and HFR-free performance data (hollow symbols) conducted at 80 °C at beginning-of-test (BoT, green symbols), and after either 718 OCV-cycles (red symbols) or after 500 cycles of the reference test (blue symbols) recorded during the AST shown in Fig. 4a. c) Corresponding HFR values. MEA specifications: anode loading of 1.75 mg<sub>Ir</sub> cm<sup>-2</sup> (IrO<sub>2</sub>/TiO<sub>2</sub>; Umicore); 50 μm thick Nafion<sup>®</sup> 212; cathode loading of 0.2 mg<sub>Pt</sub> cm<sup>-2</sup> (45.8 wt % Pt/C, Tanaka); for details see reference [37].

in HFR as well as the formation of a hydrous Ir(OH)<sub>x</sub> phase clearly shown by cyclic voltammetry [37] are both related to cycling the anode potential between  $\approx 0 \text{ V}_{\text{RHE}}$  during the OCV-periods and high potentials when current is applied to the electrolyzer. The main cause for an increasing HFR along with the observed performance decrease over the course of the OCV-AST can be related to the formation of an additional interfacial resistance on the anode side of the MEA. This additional resistance is the result of a higher contact resistance due to the passivation of the Ti-PTL (porous transport layer) in combination with the less electrically conductive Ir(OH)<sub>x</sub> [37]. In summary, significant degradation of an electrolyzer MEA can occur during



extended OCV periods during which the anode potential is allowed to decay to  $\approx 0 V_{\text{RHE}}$ , a situation which should be avoided in a PEM-WE, at least when using non-coated Ti-PTLs.

#### 4 Conclusions

In this work, an overview of the current challenges in catalyst development for PEM-WEs is given. Due to the limited availability of iridium which is currently the only viable option as an oxygen evolution reaction (OER) catalyst, a reduction of the iridium loading from currently  $\approx 2 \text{ mg}_{\text{Ir}} \text{ cm}^{-2}$  to only  $\approx 0.05 \text{ mg}_{\text{Ir}} \text{ cm}^{-2}$ , i.e., by a factor of 40 is required in order to enable a large-scale application of PEM-WEs. While the activity of current Ir-based catalysts would generally be sufficient to achieve the proposed target values for Ir loading at only minor performance losses (only 4% increase of the cell energy consumption to produce 1 kg of  $\text{H}_2$ ), the development of catalyst structures with a much lower iridium packing density compared to current catalyst materials is absolutely required to realize homogeneous catalyst layers at very low Ir loadings. Several pathways to develop such high-structured catalysts (i.e., catalysts with a low iridium packing density) have been proposed in the literature. Here we show first results that demonstrate that for a high-structured catalyst a reduction of the Ir loading by a factor  $\approx 8$  is possible, even with a slightly improved efficiency compared to a commercial Benchmark catalyst. With this new OER catalyst developed by Heraeus, the Ir-specific power density at an efficiency of 70%<sub>LHV</sub> ( $\equiv 1.79 \text{ V}$ ) of  $\approx 0.05 \text{ g}_{\text{Ir}} \text{ kW}^{-1}$  can be achieved at  $> 3 \text{ A cm}^{-2}$  with a 50  $\mu\text{m}$  thick Nafion<sup>®</sup> membrane.

To make the development of new catalyst materials more efficient, activity and durability screening methods are required to allow a fast identification of promising materials. The rotating disk electrode (RDE) method which is commonly used to evaluate catalyst performance is shown to be suitable for a characterization of catalyst activity, while OER catalyst stability tests are affected by measurement artefacts and, hence, do not give meaningful information about catalyst lifetime. Consequently, accelerated stress tests (AST) on the membrane electrode assembly (MEA) level are required to evaluate catalyst stability at realistic operating conditions. A test protocol simulating an intermittent power supply by cycling between open circuit voltage (OCV) and operating potentials is presented as an example for such an AST. Here, the recurring transition between reducing and oxidizing conditions leads to the dissolution of Ir and the formation of a contact resistance between electrode and PTL resulting in a much higher degradation rate compared to a reference experiment without OCV periods. The information gained from this experiment helps to identify harmful operating conditions that need to be avoided in real PEM-WE systems.

This work was funded by the Bavarian Ministry of Economic Affairs and Media, Energy and Technology through the project ZAE-ST (storage technologies) and by the German Federal Ministry of Education and Research (BMBF) in the framework of the Kopernikus P2X project (funding number 03SFK2V0). We would like to thank Martina Kemmer (Heraeus Deutschland GmbH & Co. KG) for the synthesis of catalyst materials. Additionally, we would like to acknowledge Jan Byrknæs and Christian Eickes (Greenerity GmbH) as well as Thomas Bein, Michael Beetz, Daniel Böhm, Sebastian Häring, Alexander Hufnagel (Ludwig-Maximilians-University Munich) and Dina Fattakhova (Forschungszentrum Jülich) for the valuable discussions regarding catalyst development and MEA testing.



**Maximilian Bernt** is a postdoctoral researcher at ZAE Bayern. After studying physics at the Technical University of Munich he joined the group of Prof. Hubert Gasteiger to work in the field of PEM water electrolysis in collaboration with the ZAE Bayern. He received his PhD from the Technical University of Munich in 2019.

His research focusses on the development and electrochemical investigation of new materials for PEM water electrolysis.



**Alexandra Hartig-Weiß** is a PhD student at the Chair of Technical Electrochemistry at Technical University of Munich. She studied applied chemistry at the Georg-Simon-Ohm Hochschule in Nuremberg in cooperation with AREVA NP GmbH in Erlangen (dual studies) and obtained her Bachelor of Science in 2013. Afterwards she studied

chemical engineering at the TU Munich and concluded her Master of Science in 2015. Her work focuses on the development and optimization of membrane electrode assemblies for PEM water electrolyzer regarding their performance and long-term stability.



**Mohammad Fathi Tovini** is a Ph.D. student at the Chair of Technical Electrochemistry at Technical University of Munich. He received his M.Sc. in materials science and nanotechnology at Bilkent University in Ankara in 2015 and obtained his B.Sc. in 2013. His research focuses on the development of model catalysts for oxygen evolu-

tion reaction in PEM fuel cells and PEM water electrolyzers.



**Hany A. El-Sayed** is a post-doctoral fellow at the Chair of Technical Electrochemistry at Technical University of Munich. Leading a small group of PhD students in the research group of Prof. Hubert Gasteiger, El-Sayed's research efforts focus on the development of novel catalysts for proton exchange membrane fuel cells and electrolyzers.

El-Sayed received his PhD in physical chemistry in 2011 from the University of Calgary, where he performed research under the supervision of Prof. Viola Birss in the area of electrochemical materials science. His PhD research work included the development of nano-templates using electrochemical approaches and using them for nano-electrode array formation.



**Carina Schramm** is currently a chemistry student in her bachelor studies at the Technical University of Munich. She wrote her bachelor thesis in the field of PEM water electrolysis at the Chair of Technical Electrochemistry where she optimized catalyst layers based on novel high-structured catalyst materials.



**Jonas Schröter** is a Ph.D. student at the Institute for Energy Conversion and Storage at Ulm University. He obtained his Bachelor degree in physics at the University of Augsburg in 2016 and his Master degree in applied and engineering physics at the Technical University of Munich in 2018. During his master thesis he worked on the

experimental analysis of PEM water electrolysis at the Chair of Technical Electrochemistry and the ZAE Bayern. Currently, he develops an electrical propulsion for airplanes powered by a fuel cell and battery hybrid system.



**Christian Gebauer** is working for the Heraeus Deutschland GmbH & Co. KG in the business unit of Heraeus Precious Metal. Here, his current work is in the Innovation department, where he's heading a group for electrochemical applications of precious metals with a strong focus on fuel cell and electrolyzer cata-

lysts. He obtained his doctoral degree in Chemistry in 2016 at the institute of Physical Chemistry – Institute of Surface Chemistry and Catalysis – at Ulm University. His research was focused on surface sensitive analytics and applied electrochemistry.



**Hubert Gasteiger** received his PhD in chemical engineering from UC Berkeley in 1993, followed by post-doctoral fellowships at the Lawrence Berkeley Laboratory and Ulm University. He moved on to join the Fuel Cell Activities program of GM/Opel (USA), leading catalyst and membrane electrode assembly (MEA) research. In 2007, he joined Acta S.p.A. (Italy), working on alkaline membrane-based technologies. After a one-year visiting professorship at MIT (2009) he was appointed Chair of Technical Electrochemistry at the Technical University of Munich, where he is now focusing on materials, electrodes, and diagnostics development for fuel cells, electrolyzers, and lithium-ion batteries.

## Abbreviations

AST	accelerated stress test
ATO	antimony doped tin oxide
CP	chronopotentiometry
HER	hydrogen evolution reaction
LHV	lower heating value
NSTF	nanostructured thin film
NTO	niobium doped titanium oxide
OCV	open circuit voltage
OER	oxygen evolution reaction
PEM-WE	proton exchange membrane water electrolysis
PGM	platinum group metal
Pt/C	carbon supported platinum
RDE	rotating disc electrode
RHE	reversible hydrogen electrode

## References

- [1] A. Buttler, H. Spliethoff, *Renewable Sustainable Energy Rev.* **2018**, *82*, 2440–2454. DOI: <https://doi.org/10.1016/j.rser.2017.09.003>
- [2] K. E. Ayers, N. Danilovic, R. Ouimet, M. Carmo, B. Pivovar, M. Bornstein, *Annu. Rev. Chem. Biomol. Eng.* **2019**, *10* (1), 219–239. DOI: <https://doi.org/10.1146/annurev-chembioeng-060718-030241>
- [3] U. Babic, M. Suermann, F. N. Büchi, L. Gubler, T. J. Schmidt, *J. Electrochem. Soc.* **2017**, *164* (4), F387–F399. DOI: <https://doi.org/10.1149/2.1441704jes>
- [4] M. Carmo, D. L. Fritz, J. Mergel, D. Stolten, *Int. J. Hydrogen Energy* **2013**, *38* (12), 4901–4934. DOI: <https://doi.org/10.1016/j.ijhydene.2013.01.151>
- [5] L. Bertuccioli, A. Chan, D. Hart, F. Lehner, B. Madden, E. Standen, *Study on development of water electrolysis in the EU*, Final Report, element energy, Cambridge, UK **2014**. ([www.fch.europa.eu/sites/default/files/FCHJUElectrolysisStudy\\_FullReport%20\(ID%20199214\).pdf](http://www.fch.europa.eu/sites/default/files/FCHJUElectrolysisStudy_FullReport%20(ID%20199214).pdf))
- [6] K. E. Ayers, J. N. Renner, N. Danilovic, J. X. Wang, Y. Zhang, R. Maric, H. Yu, *Catal. Today* **2016**, *262*, 121–132. DOI: <https://doi.org/10.1016/j.cattod.2015.10.019>
- [7] M. Bernt, A. Siebel, H. A. Gasteiger, *J. Electrochem. Soc.* **2018**, *165* (5), F305–F314. DOI: <https://doi.org/10.1149/2.0641805jes>
- [8] J. Durst, A. Siebel, C. Simon, F. Hasché, J. Herranz, H. A. Gasteiger, *Energy Environ. Sci.* **2014**, *7* (7), 2255–2260. DOI: <https://doi.org/10.1039/C4EE00440J>
- [9] J. Durst, C. Simon, F. Hasché, H. A. Gasteiger, *J. Electrochem. Soc.* **2015**, *162* (1), F190–F203. DOI: <https://doi.org/10.1149/2.0981501jes>
- [10] M. Bernt, H. A. Gasteiger, *J. Electrochem. Soc.* **2016**, *163* (11), F3179–F3189. DOI: <https://doi.org/10.1149/2.0231611jes>
- [11] M. Bernt, *Analysis of Gas Permeation Phenomena in a PEM Water Electrolyzer Operated at High Pressure and Current Density*, AiMES, Cancun, Mexico, September **2018**.
- [12] G. Bender, M. Carmo, T. Smolinka, A. Gago, N. Danilovic, M. Mueller, F. Ganci, A. Fallisch, P. Lettenmeier, K. A. Friedrich, K. Ayers, B. Pivovar, J. Mergel, D. Stolten, *Int. J. Hydrogen Energy* **2019**, *44* (18), 9174–9187. DOI: <https://doi.org/10.1016/j.ijhydene.2019.02.074>
- [13] C. Klose, P. Trinke, T. Böhm, B. Bensmann, S. Vierrath, R. Hanke-Rauschenbach, S. Thiele, *J. Electrochem. Soc.* **2018**, *165* (16), F1271–F1277. DOI: <https://doi.org/10.1149/2.1241814jes>
- [14] T. Y. Paul, W. Gu, J. Zhang, R. Makharia, F. T. Wagner, H. A. Gasteiger, in *Polymer Electrolyte Fuel Cell Durability* (Eds: F. N. Büchi, M. Inaba, and T. J. Schmidt), Springer, New York **2009**.
- [15] F. Wagner, S. Yan, P. Yu, in *Handbook of Fuel Cells* (Eds: W. Vielstich, H. A. Gasteiger, and H. Yokokama), Wiley, New York **2009**.
- [16] G. Auer, P. Woditsch, A. Westerhaus, J. Kischkewitz, W. Griebler, M. Rohe, M. Liedekerke, in *Ullmann's Encyclopedia of Industrial Chemistry*, Wiley-VCH, Weinheim **2000**.
- [17] P. Mazúr, J. Polonský, M. Paidar, K. Bouzek, *Int. J. Hydrogen Energy* **2012**, *37* (17), 12081–12088. DOI: <https://doi.org/10.1016/j.ijhydene.2012.05.129>
- [18] E. Oakton, D. Lebedev, M. Povia, D. F. Abbott, E. Fabbri, A. Fedorov, M. Nachtgael, C. Copéret, T. J. Schmidt, *ACS Catal.* **2017**, *7* (4), 2346–2352. DOI: <https://doi.org/10.1021/acscatal.6b03246>
- [19] R. E. Fuentes, J. Farrell, J. W. Weidner, *Electrochem. Solid-State Lett.* **2011**, *14* (3), 5–7. DOI: <https://doi.org/10.1149/1.3528163>
- [20] E. Oakton, D. Lebedev, A. Fedorov, F. Krumeich, J. Tillier, O. Sereida, T. J. Schmidt, C. Copéret, *New J. Chem.* **2016**, *40* (2), 1834–1838. DOI: <https://doi.org/10.1039/C5NJ02400E>
- [21] H. S. Oh, H. N. Nong, P. Strasser, *Adv. Funct. Mater.* **2015**, *25* (7), 1074–1081. DOI: <https://doi.org/10.1002/adfm.201401919>
- [22] H. N. Nong, H. S. Oh, T. Reier, E. Willinger, M. G. Willinger, V. Petkov, D. Teschner, P. Strasser, *Angew. Chem. Int. Ed.* **2015**, *54* (10), 2975–2979. DOI: <https://doi.org/10.1002/anie.201411072>
- [23] V. Müller, M. Rasp, J. Rathouský, B. Schütz, M. Niederberger, D. Fattakhova-Rohlfing, *Small* **2010**, *6* (5), 633–637. DOI: <https://doi.org/10.1002/smll.200901887>
- [24] V. Skoromets, H. Nèmec, J. Kopeček, P. Kužel, K. Peters, D. Fattakhova-Rohlfing, A. Vetushka, M. Müller, K. Ganzerová, A. Fejfar, *J. Phys. Chem. C* **2015**, *119* (33), 19485–19495. DOI: <https://doi.org/10.1021/acs.jpcc.5b05091>
- [25] Y. Liu, J. M. Szeifert, J. M. Feckl, B. Mandlmeier, J. Rathouský, O. Hayden, D. Fattakhova-Rohlfing, T. Bein, *ACS Nano* **2010**, *4* (9), 5373–5381. DOI: <https://doi.org/10.1021/nn100785j>
- [26] S. Siracusano, V. Baglio, C. D'Urso, V. Antonucci, A. S. Aricó, *Electrochim. Acta* **2009**, *54* (26), 6292–6299. DOI: <https://doi.org/10.1016/j.electacta.2009.05.094>

- [27] L. Wang, P. Lettenmeier, U. Golla-Schindler, P. Gazdzicki, N. A. Cañas, T. Morawietz, R. Hiesgen, S. S. Hosseiny, A. S. Gago, K. A. Friedrich, *Phys. Chem. Chem. Phys.* **2016**, *18* (6), 4487–4495. DOI: <https://doi.org/10.1039/C5CP05296C>
- [28] H. Xu, B. Rasimick, R. Stone, S. Zhao, L. Yan, *High-Performance, Long-Lifetime Catalysts for Proton Exchange Membrane Electrolysis*, Annual Progress Report, Giner Inc., Newton MA **2017**. ([https://www.hydrogen.energy.gov/pdfs/progress17/ii\\_b\\_2\\_xu\\_2017.pdf](https://www.hydrogen.energy.gov/pdfs/progress17/ii_b_2_xu_2017.pdf))
- [29] S. M. Alia, S. Shulda, C. Ngo, S. Pylypenko, B. S. Pivovar, *ACS Catal.* **2018**, *8* (3), 2111–2120. DOI: <https://doi.org/10.1021/acscatal.7b03787>
- [30] K. A. Lewinski, D. van der Vliet, S. M. Luopa, *ECS Trans.* **2015**, *69* (17), 893–917. DOI: <https://doi.org/10.1149/06917.0893ecst>
- [31] Kopernikus P2X project funded by the German Ministry of Education and Research (BMBF), <https://www.kopernikus-projekte.de/en/projects/power2x> (Accessed on June 29, 2019)
- [32] S. Geiger, O. Kasian, B. R. Shrestha, A. M. Mingers, K. J. Mayrhofer, S. Cherevko, *J. Electrochem. Soc.* **2016**, *163* (11), 3132–3138. DOI: <https://doi.org/10.1149/2.0181611jes>
- [33] T. Reier, M. Oezaslan, P. Strasser, *ACS Catal.* **2012**, *2* (8), 1765–1772. DOI: <https://doi.org/10.1021/cs3003098>
- [34] K. E. Ayers, E. B. Anderson, K. Dreier, K. W. Harrison, *ECS Trans.* **2013**, *50* (49), 35–46. DOI: <https://doi.org/10.1149/05049.0035ecst>
- [35] H. S. Oh, H. N. Nong, T. Reier, M. Gliech, P. Strasser, *Chem. Sci.* **2015**, *6* (6), 3321–3328. DOI: <https://doi.org/10.1039/C5SC00518C>
- [36] H. A. El-Sayed, A. Weiß, L. F. Olbrich, G. P. Putro, H. A. Gasteiger, *J. Electrochem. Soc.* **2019**, *166* (8), 458–464. DOI: <https://doi.org/10.1149/2.0301908jes>
- [37] A. Weiß, A. Siebel, M. Bernt, T. H. Shen, V. Tileli, H. A. Gasteiger, *J. Electrochem. Soc.* **2019**, *166* (8), 487–497. DOI: <https://doi.org/10.1149/2.0421908jes>
- [38] P. J. Rheinländer, *Stability and OER Activity of IrO<sub>x</sub> in PEM Water Electrolysis*, 231<sup>st</sup> ECS Meeting, New Orleans, LA, May **2017**.
- [39] T. Reier, D. Teschner, T. Lunkenbein, A. Bergmann, S. Selve, R. Kraehnert, R. Schlögl, P. Strasser, *J. Electrochem. Soc.* **2014**, *161* (9), 876–882. DOI: <https://doi.org/10.1149/2.0411409jes>
- [40] P. J. Ferreira, Y. Shao-Horn, D. Morgan, R. Makharia, S. Kocha, H. A. Gasteiger, *J. Electrochem. Soc.* **2005**, *152* (11), 2256–2271. DOI: <https://doi.org/10.1149/1.2050347>
- [41] S. Cherevko, T. Reier, A. R. Zeradjanin, Z. Pawolek, P. Strasser, K. J. Mayrhofer, *Electrochem. Commun.* **2014**, *48*, 81–85. DOI: <https://doi.org/10.1016/j.elecom.2014.08.027>



## 5.2 Iridium Oxide Catalyst Supported on Antimony - Doped Tin Oxide for High Oxygen Evolution Reaction Activity in Acidic Media

In this section the article “Iridium Oxide Catalyst Supported on Antimony Doped Tin Oxide for High Oxygen Evolution Reaction Activity in Acidic Media”<sup>135</sup> is presented, which has been submitted to *ACS Applied Nano Materials* in November 2019 and accepted for publication in February 2020. Reprinted (adapted) with permission from (Iridium Oxide Catalyst Supported on Antimony-Doped Tin Oxide for High Oxygen Evolution Reaction Activity in Acidic Media; Alexandra Hartig-Weiss, Melanie Miller, Hans Beyer, Alexander Schmitt, Armin Siebel, Anna T. S. Freiberg, Hubert A. Gasteiger, and Hany A. El-Sayed; *ACS Applied Nano Materials* 2020 3 (3), 2185-2196; DOI: 10.1021/acsnm.9b02230). Copyright (2021) American Chemical Society.

The permanent web-link for the article is:

<https://pubs.acs.org/doi/pdf/10.1021/acsnm.9b02230>

In this study, one approach to design a catalyst with a lower packing density by using a high surface area ( $50 \text{ m}^2\text{g}^{-1}$ ) and highly conductive ( $2 \text{ Scm}^{-1}$ ) ATO (antimony doped tin oxide) support material for iridium nanoparticles is demonstrated. The hydrothermal method was used to synthesize the ATO, which was calcined afterwards in an  $\text{O}_2/\text{Ar}$  mixture at  $600 \text{ }^\circ\text{C}$ . Iridium particles, aiming for a particle size of  $\approx 3 \text{ nm}$  to obtain the highest activity possible were synthesized using the polyol method. In a subsequent step, using an ethylene glycol solution, the iridium particles were deposited on the ATO. Aiming for different iridium loadings (wt.-% Ir) on ATO, the respective amounts of iridium and ATO were mixed. TEM images showed that the particle size of iridium (namely,  $1.6 \pm 0.4 \text{ nm}$  for 11.0 wt.-% Ir) was almost identical for the prepared catalysts containing different iridium loadings (wt.-% Ir), which was expected since the iridium nanoparticles were synthesized in a separate step. Additionally, the TEM images revealed the degree of dispersion changes with iridium loading, resulting in the highest dispersion at the lowest loading (11.0 wt.-% Ir).

An RDE setup was used to analyze the electrochemical activity toward the OER of the different synthesized catalysts and of two commercially available catalysts (Ir-black und  $\text{IrO}_2/\text{TiO}_2$ ) for comparison. The as-prepared iridium particles are of metallic nature and to prevent any additional oxidation current during the OER activity determination, the iridium was

electrochemically converted to hydrous iridium oxide by potential cycling prior to OER measurements. Although a steady state CV was reached during cycling, XPS measurements showed that the outer surface layer consists of hydrous iridium oxide, while there is still some electrochemical inaccessible metallic iridium buried in the core.

A comparison of the OER activity determined at room temperature and at a potential of 1.5 V<sub>RHE</sub> showed an increasing mass specific activity with decreasing iridium loading for the Ir/ATO catalysts. The highest OER activity was determined to be  $\approx 185 \text{ Ag}_{\text{Ir}}^{-1}$  for the 11 wt.-% Ir/ATO, which is  $\approx 35$  times higher compared to IrO<sub>2</sub>/TiO<sub>2</sub> ( $\approx 5 \text{ Ag}_{\text{Ir}}^{-1}$ ) and is still  $\approx 4$  times higher compared to Ir-black ( $\approx 48 \text{ Ag}_{\text{Ir}}^{-1}$ ). Even at temperatures more relevant to applications (80 °C) and at a potential of 1.45 V<sub>RHE</sub>, the 11.0 wt.-% Ir/ATO ( $\approx 1100 \text{ Ag}_{\text{Ir}}^{-1}$ ) significantly outperforms the two commercial available catalysts ( $\approx 190 \text{ Ag}_{\text{Ir}}^{-1}$  for Ir-black and  $\approx 45 \text{ Ag}_{\text{Ir}}^{-1}$  for IrO<sub>2</sub>/TiO<sub>2</sub>). Usually potentials within the Tafel region, where kinetic losses are dominant, are used for activity determination. Due to an earlier onset of mass-transport related losses, a lower potential for the OER activity determination needed to be chosen at higher temperatures. The high OER activity in combination with the lower packing density ( $\approx 0.27 \text{ g}_{\text{Ir}}\text{cm}^{-3}$ ) seems to be promising for enabling low iridium loadings in a PEM-WE, while still maintaining a homogenous catalyst layer and sufficiently good performance.

### **Author contributions**

Catalyst synthesis was performed by M.M., A. Schmitt and H.A.E.-S. Physicochemical characterization was done by M.M., A. Schmitt, A. Siebel, A.T.S.F., and H.A.E.-S. Fabrication of catalyst inks and electrochemical testing in RDE was performed by A.H.-W. and H.A.E.-S. Analysis of the experimental test results was done by A.H.-W., M.M., A. Schmitt, A. Siebel, A.T.S.F., and H.A.E.-S. H.A.E.-S. wrote the manuscript that was edited by H.A.G. All authors discussed the experimental results and revised the manuscript.



# Iridium Oxide Catalyst Supported on Antimony-Doped Tin Oxide for High Oxygen Evolution Reaction Activity in Acidic Media

Alexandra Hartig-Weiss,\* Melanie Miller, Hans Beyer, Alexander Schmitt, Armin Siebel, Anna T. S. Freiberg, Hubert A. Gasteiger, and Hany A. El-Sayed\*

Cite This: *ACS Appl. Nano Mater.* 2020, 3, 2185–2196

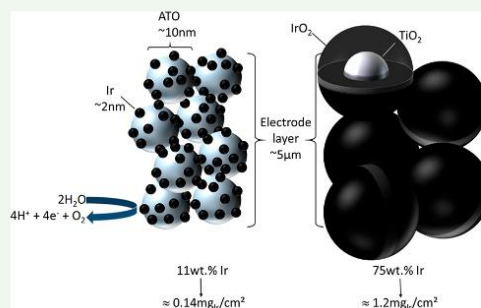
Read Online

ACCESS |

Metrics & More

Article Recommendations

**ABSTRACT:** Lowering of the oxygen evolution reaction (OER) noble metal catalyst loading on the anode of a polymer electrolyte membrane water electrolysis (PEMWE) is a necessity for enabling the large-scale hydrogen production based on this technology. This study introduces a remarkably active OER catalyst that is based on the dispersion of Ir nanoparticles on a highly conductive oxide support. The catalyst was designed in a way to combine all characteristics that have been reported to enhance the OER activity on an Ir oxide-based catalyst, including high catalyst dispersion and controlling the Ir catalyst particle size, so that this design approach provides both high surface area to Ir mass ratio and at the same time ensures maximum synergistic interaction with the oxide support, termed strong metal–support interaction (SMSI). This was achieved through using a high surface area (50 m<sup>2</sup>/g) and highly conductive antimony-doped tin oxide support (2 S/cm), where combining a high catalyst dispersion and maximum SMSI resulted in a very high OER activity of the Ir/ATO catalyst ( $\approx 1100$  A/g<sub>Ir</sub>, at 80 °C and 1.45 V<sub>RHE</sub>). This enhanced activity will allow a significant reduction (ca. 75-fold) in the precious metal catalyst loading when this catalyst is implemented in the anode of a PEMWE.



**KEYWORDS:** oxygen evolution reaction, SMSI, electrocatalysis, PEM electrolyzer, iridium, catalytic activity, ATO

## 1. INTRODUCTION

Hydrogen is considered a clean and efficient energy carrier that is likely to be used as an alternative to fossil fuels in many of the applications used today. In particular, for transportation applications, where hydrogen serves as an energy carrier, the use of hydrogen in replacement of fossil fuels would provide immediate benefits in terms of reducing emissions and therefore will have a positive long-term environmental impact as long as the hydrogen is produced from nonfossil renewable resources.<sup>1</sup> So far, water electrolysis is considered one of the most promising and practical ways of producing clean hydrogen from renewable electric power.<sup>2,1</sup> At low temperatures, water electrolysis is performed in alkaline or polymer electrolyte membrane (PEM, acidic) electrolyzers.<sup>3</sup> The main advantages of the polymer electrolyte membrane water electrolysis (PEMWE) are the high efficiency at high current densities, system compactness, ease of maintenance, and rapid response to startups and shutdowns; therefore, PEMWE has achieved great attention over the past years.<sup>2,3</sup> Moreover, PEM electrolyzers have the advantage of producing hydrogen at elevated pressures, allowing for a direct storage in pressurized tanks and thus saving additional energy for mechanical compression.<sup>1,4</sup> However, a key limitation of PEMWE is the

high cost due to the use of high loadings of noble metals at the electrodes, which are necessary due to the highly acidic media originating from the ionomer used as a binder in the catalyst layer as well as the perfluorosulfonic membrane used in a PEMWE.<sup>2</sup> While the platinum loading on the cathode side can be reduced significantly without any loss in performance,<sup>5</sup> high loadings are required at the anode due to the sluggish kinetics of the oxygen evolution reaction (OER). Iridium is typically used as the most stable catalyst for the OER reaction in PEMWE, but its high cost (\$1480 per troy ounce)<sup>6</sup> and scarcity require the development of strategies to reduce the precious metal content of Ir-based OER catalysts, increase the Ir utilization, and achieve higher activity toward the OER. Even though Bernt et al. recently showed that a reduction of Ir loading down to 0.5 mg<sub>Ir</sub>/cm<sup>2</sup> is possible with commercially available catalysts, a lower packing density, which can be

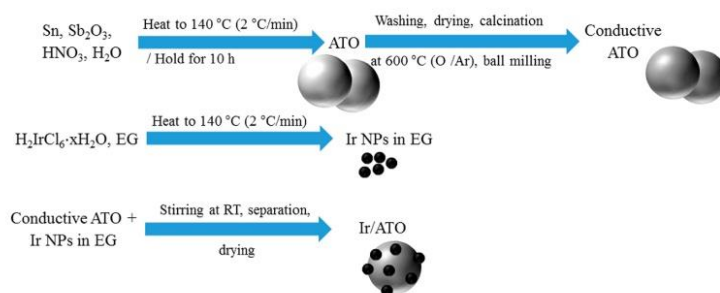
Received: November 13, 2019

Accepted: February 26, 2020

Published: February 26, 2020



Scheme 1



realized by supporting the active material on a suitable support and thus lowering the Ir content per unit volume ( $\text{g}_{\text{Ir}}/\text{cm}^3$ ), is necessary to reach a target of  $\approx 0.01 \text{ g}_{\text{Ir}}/\text{kW}$  at 70%<sub>LHV</sub> ( $\equiv 1.79 \text{ V}$ ).<sup>5,7</sup> One approach that has been proven to be successful is the dispersion of Ir particles on a high surface area support,<sup>8</sup> enabling an increase of accessible surface area ( $\text{m}^2/\text{g}$ ) by decreasing the Ir particle size and increasing the surface to mass ratio of the catalyst.<sup>9</sup> This increase of surface to mass ratio will also result in a lower packing density, thereby fostering the fabrication of sufficiently thick catalyst layers although low loadings are used. Carbon support materials, which are used in polymer electrolyte fuel cells, cannot be used due to their corrosion at high anodic potential during the OER reaction.<sup>10</sup> Therefore, several support materials have been investigated as alternative to carbon, which include  $\text{TiO}_2$ ,<sup>11</sup>  $\text{Nb}_2\text{O}_5$ ,<sup>12</sup>  $\text{SnO}_2$ ,<sup>13</sup>  $\text{TaC}$ ,<sup>14</sup>  $\text{TiC}$ ,<sup>15</sup>  $\text{NbC}$ ,<sup>15</sup>  $\text{WC}$ ,<sup>15</sup>  $\text{FTO}$ ,<sup>16</sup>  $\text{ITO}$ ,<sup>16</sup> and antimony-doped tin oxide (ATO).<sup>8,17,18</sup> While some of these support materials (e.g., ATO and TaC) exhibit a sufficiently high electronic conductivity, others (e.g.,  $\text{Nb}_2\text{O}_5$  and  $\text{SnO}_2$ ) needed to be mixed with relatively large quantities of Ir oxide to realize reasonable electronic conductivities. Among these, ATO is found to be the most suitable catalyst support due to its relatively high electronic conductivity, its stability under OER conditions in a PEMWE (high anodic potentials in an acidic environment), and its thermal stability.<sup>8</sup> Controversially, some recent studies showed that ATO might not be stable at high anodic potentials, which is attributed to the leaching of Sb.<sup>19</sup> However, these studies were performed in liquid electrolyte, and up to now these measurements cannot be used to reliably predict the stability in a PEMWE.<sup>20</sup> Puthiyapura et al. reported the improved OER activity of  $\text{IrO}_2$  supported on ATO compared to pure  $\text{IrO}_2$ , and the improved activity was attributed to the better dispersion of the  $\text{IrO}_2$  catalyst on the ATO support.<sup>8</sup> However, the loading of Ir on ATO was still quite high (>60 wt %) in their approach, which was required to provide a sufficiently high conductivity similar to that of  $\text{IrO}_2$ . ATO does not only increase the apparent OER activity of the Ir-based catalyst through the enhanced dispersion, but it has also been recently reported that the interaction of the Ir-based catalyst with the oxide support, known as strong metal–support interaction (SMSI), resulted in enhancing the intrinsic activity of the Ir catalyst through the electronic effect.<sup>21,22</sup> The high electronic conductivity of the ATO has also been recently reported to affect the overall performance of the Ir–ATO catalyst.<sup>23</sup> In a very recent study by Ohno et al., where the dispersion of  $\text{IrO}_x$ -nanoparticles on doped Me– $\text{SnO}_2$  supports (Me = Sb, Ta, and Nb) was investigated, they showed that a high electronic conductivity of the catalyst is crucial for

reaching high performance.<sup>24</sup> While in RDE all Me– $\text{SnO}_2$  supported catalysts have similar performance, a significant difference was observed within the MEA measurements. The decreased performance in MEA was attributed to the inadequate conductivity of the catalyst and thus a higher ohmic resistance. Because in RDE only a thin catalyst layer ( $\approx 60 \text{ nm}$ ) is applied, a low conductivity will not lead to a significant resistance. However, within single cell (MEA) measurements, where the catalyst layers are roughly  $10 \mu\text{m}$ , a low conductivity will lead to a lower utilization of the catalyst layers and thus to a lower performance. Hence, a high electronic conductivity of the catalyst as well as the support is necessary to achieve low iridium content as well as high performance. In this study, we demonstrate how combining all of the aforementioned features, including the use of highly dispersed Ir nanoparticles, of a highly electrically conductive ATO support ( $2 \text{ S/cm}$ ) that allows for low Ir loadings due to a reduced packing density, and the utilization of the SMSI effect can result in a very active OER catalyst that outperforms all commercially available catalysts currently in use.

## II. EXPERIMENTAL SECTION

**ATO Synthesis.** Antimony-doped tin oxide with a molar ratio (Sb:Sn) of 5:95 was synthesized by using a hydrothermal method.<sup>25</sup> The synthesis was performed in a fume hood to avoid inhalation of any released toxic gases. In an open 100 mL PTFE autoclave liner, 30.0 mL of concentrated  $\text{HNO}_3$  (69 wt %, puriss. p.a., Sigma-Aldrich) was added to 50.0 mL of deionized water. To this acidic solution, 2.0 g of granulated tin (16.9 mmol, Sn, granulates, 0.425–2.0 mm,  $\geq 99.5\%$ , ACS reagent, Sigma-Aldrich) and 130 mg of antimony(III) oxide powder (0.440 mmol,  $\text{Sb}_2\text{O}_3$ , nanopowder, <250 nm,  $\geq 99.9\%$ , Sigma-Aldrich) were added at once under vigorous stirring. A significant  $\text{NO}_2$  release occurred upon the formation of a yellowish colloid. After 10 min, the autoclave (HighPreactor BR-100, Berghof) was sealed and heated to 140 °C at a heating rate of 2 °C/min. This temperature was held for 10 h, and then the reaction mixture was passively cooled to room temperature (RT) overnight. A bluish powder was obtained and separated from the liquid phase by centrifugation. The powder was washed thoroughly with deionized water until the filtrated wash solution reached a pH of 6. After the final washing step with ethanol, the powder was dried overnight in static air at 70 °C. The resulting dry powder was calcined in a tube furnace (Carbolite) in a gas flow mixture of 20% oxygen ( $\text{O}_2$ ) in argon (Ar) (both 5.0 grade, Westfalen) with a flow rate of 400 mL/min. The samples were heated to 600 °C at 5 °C/min and held at 600 °C for 3 h. After passive cooldown to RT in the furnace, the calcined samples were ground in a planetary ball mill (Pulverisette 7 Premium Line, Fritsch) to break up the formed agglomerates during calcination. In this process, ca. 2 g of ATO was suspended in 6 mL of 2-propanol and filled into a 45 mL  $\text{ZrO}_2$  milling jar containing 20  $\text{ZrO}_2$  balls ( $\phi$  10 mm). Six milling cycles of 10 min each and 1 min pause between



the cycles were conducted at 200 rpm. Again, the product was separated by centrifugation and dried at 70 °C in static air overnight.

**Synthesis of Ir Catalyst.** The polyol synthesis setup consisted of a 100 mL three-neck flask placed in a heating mantle (WHG 2, Winkler) on a magnetic stirrer and was equipped with a reflux condenser, a thermometer and a temperature controller (Model 310, J-KEM Scientific), a magnetic stirring bar inside the flask, and a glass capillary for the Ar purging. In a typical polyol synthesis, 183 mg of dihydrogen hexachloroiridate(IV) hydrate (0.450 mmol,  $\text{H}_2\text{IrCl}_6 \cdot x\text{H}_2\text{O}$ , 99.98%, trace metal basis, Sigma-Aldrich) was dissolved in 10 mL of ethylene glycol (EG, 99.8%, anhydrous, Sigma-Aldrich) in a small vial at RT under vigorous stirring. After complete dissolution, the solution was transferred into the aforementioned three-neck flask that contained 80 mL of ethylene glycol. The total concentration of iridium was  $5 \times 10^{-3}$  mol/L in a total volume of 90 mL. The solution was purged with Ar for 60 min to minimize the  $\text{O}_2$  content before heating. During heating, the solution was stirred moderately (~500 rpm) and the Ar atmosphere was maintained. The solution was heated to 140 °C with a heating rate of ~2 °C/min to allow the formation of Ir nanoparticles, and then the reaction mixture was allowed to cool to RT.

**Preparation of ATO-Supported Iridium Catalysts.** The prepared Ir nanoparticles were slowly added to the corresponding amount of ATO, which has been dispersed in 35 mL of ethylene glycol and sonicated for at least 30 min. The reaction mixture was stirred at 500 rpm at RT in air for 3 days to allow the nanoparticles to deposit on the ATO. Afterward, the prepared catalyst was separated via centrifugation (Eppendorf centrifuge 5810, refrigerated) at 11500 rpm and 5 °C and washed twice with isopropanol with 5 min sonication in between the centrifugation steps. The obtained black powder was dried at 70 °C in static air overnight. Ir loadings of 20, 30, and 40 wt % were targeted, while experimentally, 11.0, 15.3, and 23.4 wt % loadings were obtained due to incomplete Ir deposition on the ATO support.

**Physicochemical Characterization.** Energy dispersive X-ray analysis (EDX) was employed to study the elemental composition of the prepared catalysts using a JCM-6000Plus from JEOL. The total Ir content of the sample (the Ir loading of the catalyst in wt %) was calculated via the obtained actual atomic ratio Ir/(Sn + Sb) from the measurement. The accuracy of the determination method was tested with a mixture of Ir (Ir-black, >93%, Johnson Matthey) and ATO ( $\text{SnO}_2/\text{Sb}_2\text{O}_3$ , nanopowder, <50 nm particle size, ≥99.5% trace metals basis, Sigma-Aldrich) of known composition, and the error was found to be ±1.5%. Considering this slight deviation and the proven excellent reproducibility of the measurements, the obtained EDX results for the iridium content in Ir/ATO materials were considered reliable within this error margin.

Morphology and particle size of the materials were investigated by using TEM analysis. A very small amount of sample was dispersed in isopropanol and then deposited onto a carbon-coated copper grid (Cu, 400 mesh, Formvar carbon film, Science Services). The obtained samples were analyzed under a Philips CM100EM with an acceleration voltage of 100 kV and a resolution of 0.5 nm.

The oxidation states of the synthesized Ir/ATO nanoparticles and electrochemically oxidized Ir/ATO particles were analyzed by X-ray photoelectron spectroscopy (XPS). Analyses of the samples were performed on a Kratos Axis Supra spectrometer using monochromatic Al K $\alpha$  radiation at an energy of 1486.6 eV. All spectra were recorded at a total power of 225 W, 15 kV, and 15 mA anode current. The samples were drop-casted in floating mode onto a stainless steel sample bar, which was then outgassed (overnight) in an ultrahigh-vacuum chamber to remove moisture and contaminants, so that the pressure in the chamber during the analysis was  $<1.0 \times 10^{-8}$  Torr. The narrow Ir 4f spectra were collected between 58.5 and 72 eV binding energy (BE) by using a step size of 0.05 eV and a pass energy of 20 eV, whereas for the represented data five spectra were averaged (3 min each). All the binding energy values were calibrated by using the adventitious carbon signal ( $C 1s = 284.8$  eV) as reference. The XPS data analysis was performed with the Casa XPS software. A Shirley function was used as background. As reported in the literature,

the Ir 4f core spectra exhibit a distinct asymmetric line shape.<sup>26–28</sup> A functional Lorentzian line shape was used for both iridium metal and hydrous iridium oxide, whereas the parameters were set to LF(0.6, 1, 150, 300) and LF(0.3, 1.5, 25, 150), respectively.<sup>26</sup> The fits of the doublets of the Ir 4f<sub>7/2</sub> and Ir 4f<sub>5/2</sub> were fixed with respect to the fwhm and an area ratio of 4:3.

Electrical conductivity of powder samples was determined by measuring the corresponding current while applying a constant voltage at a constant pressure. An ~300 mg sample was placed in a homemade sample holder with a PTFE tube that was filled with the sample, which was then compressed by a mechanical press PE-011 from MAUTHE. The press capacity was adjusted to 400 kg (~140 MPa), and the thickness of the compressed pellet (the sample mass was adjusted as to get a final thickness of ca. 3 mm) was read from the scale on the die. The measurements were performed at RT at ambient air. The conductivity was measured by using a chronoamperometry technique performed on a potentiostat (SP-200 from BIOLOGIC). The voltages used for the measurements were 1, 2, 4, and 8 mV applied over 2 min each, and the corresponding average conductivity was calculated from the obtained currents.

The surface area of the ATO powder was determined by nitrogen adsorption and desorption measurements. The surface area of ~200 mg of sample powder was determined after outgassing for 15 h at 90 °C. The measurements were performed on an autosorb-iQ instrument (Quantachrome Instruments), and the surface area was calculated by the Brunauer–Emmett–Teller (Multi-Point-BET) method.

**Electrochemical Setup and Measurement Procedure.** The electrochemical measurements (cyclic voltammetry (CV), linear polarization (LSV), and electrochemical impedance spectroscopy (EIS)) were performed in a glass three-electrode electrochemical cell. A reversible hydrogen electrode (RHE) and a high surface area gold (Au) mesh were used as reference and counter electrodes, respectively. The RHE reference electrode was either directly connected to the cell or via a Luggin capillary. Rotating ring–disk electrodes (RRDEs) with a 5 mm diameter polycrystalline Au electrode and a platinum (Pt) ring (Pine Research Instrumentation, USA) supported by a PTFE or PEEK body (Pine Research Instrumentation, USA) were used as working electrodes. The reference potential was calibrated in hydrogen saturated electrolyte prior to every experiment using the Pt ring of the electrode. All potentials in this article are given with respect to RHE.

Electrolyte solutions were prepared from high-purity  $\text{H}_2\text{SO}_4$  (Ultrapur, 96%, Merck Millipore KGaA) and ultrapure water (18.2 M $\Omega$  cm at 20 °C Merck Millipore KGaA). Ar,  $\text{O}_2$ , and  $\text{H}_2$  used for purging of the electrolyte were of high purity (6.0 grade, Westfalen AG).

Electrochemical measurements were performed using an Autolab potentiostat (PGSTAT302N, Metrohm AG, Switzerland) and a rotator (Pine Research Instrumentation, USA) with a poly(ether ether ketone) shaft. Prior to any electrochemical measurements, a cyclic voltammogram of the gold working electrode was recorded in the supporting electrolyte to verify the cleanliness of Au disk and the cell. Afterward, the electrode was removed, dried, and coated with the catalyst ink by drop-casting and finally dried under a low nitrogen flow. The catalyst-coated electrode was then dipped in the Ar-saturated electrolyte, and the noncompensated electrolyte resistance was determined by EIS from 100 kHz to 100 Hz at open circuit potential (OCP) with an amplitude of 10 mV. The potential was then cycled between 0.05 and 1.45  $V_{\text{RHE}}$  at 100 mV/s to convert all metallic Ir(0) into hydrous Ir oxide. Afterward, the electrolyte solution was purged for 10 min with  $\text{O}_2$ , and a few polarization curves were recorded from 1.2 to 1.7  $V_{\text{RHE}}$  at 5 mV/s and 2500 rpm. The second anodic scan was used for OER activity evaluation throughout the study. The polarization curves were only corrected for the reference potential as well as for the ohmic resistance.

**Electrode and Ink Preparation.** Prior to every measurement, the Au working electrode was polished with 0.3  $\mu\text{m}$   $\text{Al}_2\text{O}_3$  polishing suspension (Buhler AG) and sonicated 3 × 3 min in ultrapure water. Inks were prepared by adding ultrapure water to the dry catalyst (Ir/ATO) to obtain the desired suspension concentration. The catalyst



suspension was sonicated for 30 min in a sonication bath (Elmasonic S 30 H, Elma Schmidbauer GmbH) to achieve a homogeneous dispersion. The temperature of the bath was maintained at lower than 35 °C to avoid evaporation of the solvent. No binding agent was added to the catalyst suspension.

### III. RESULTS AND DISCUSSION

The aim of this study is to prepare an OER catalyst with a low Ir loading on a conductive oxide, where the electrical conductivity is carried mainly by the oxide support, and therefore it is crucial that the oxide support exhibits high electrical conductivity. According to a previous study in our group, antimony-doped tin oxide (ATO) fulfills all the requirements to serve as a conductive catalyst support.<sup>25</sup> Therefore, the ATO used in this study was synthesized accordingly through a hydrothermal method from chlorine-free precursors,<sup>25</sup> followed by calcination and milling steps. Further details about the ATO synthesis and characterization (XRD, electrical conductivity, and BET analysis) can be found in the former study by our group.<sup>25</sup>

The homemade ATO (5 mol % Sb–SnO<sub>2</sub>) is characterized by its high electrical conductivity ( $\approx 2$  S/cm) and high surface area ( $\approx 50$  m<sup>2</sup>/g) compared to those of commercially available ATO (Sn<sub>2</sub>O/Sb<sub>2</sub>O<sub>3</sub>, nanopowder, <50 nm particle size,  $\geq 99.5\%$  trace metals basis, Sigma-Aldrich), which exhibits a 2 orders of magnitude lower conductivity ( $5 \times 10^{-2}$  S/cm). The conductivity achieved for the homemade ATO, even though lower compared to the often used IrO<sub>2</sub>/TiO<sub>2</sub> catalyst ( $\approx 50$  S/cm) (IrO<sub>2</sub>/TiO<sub>2</sub> with 75 wt % iridium; Elyst Ir75 0480 from Umicore), should be sufficiently high to allow a reduction of Ir loading. Based on the results of a recent study by Ohno et al., the conductivity of the homemade ATO ( $\approx 2$  S/cm) used in this study should be sufficiently high to avoid any additional ohmic losses, mainly observed in thick catalyst layers ( $\approx 10$   $\mu$ m).<sup>24</sup>

It is well-established for many electrochemical reactions, such as oxygen reduction reaction (ORR), methanol oxidation reaction, and carbon monoxide oxidation reaction, that there is a correlation between catalyst particle size and electrochemical activity.<sup>9</sup> It was found that there is a critical particle size that shows the highest activity. This is a result of two competing effects: the catalyst dispersion which increases with decreasing particle size (resulting in increasing mass activity of the catalyst) and the specific activity which decreases with decreasing particle size. In all investigated cases, the critical size, at which the maximum activity is obtained, is in the 2–4 nm range.<sup>9</sup> In addition to the particle size effect, the choice of the support material was also found to greatly influence the catalyst activity through the SMSI. For instance, Au nanoparticles supported on titanium oxide were reported to be significantly more active than when supported on carbon for gas phase and electrochemical oxidation of carbon monoxide.<sup>9</sup> The ORR activity of Pt supported on Ta<sub>0.3</sub>Ti<sub>0.7</sub>O<sub>2</sub> was found to be higher than that of Pt supported on carbon due to the electronic effect of the support on the Pt, as was confirmed by X-ray absorption near-edge structure analysis.<sup>29</sup> Therefore, even though the loading is reduced, the right choice of support material might lead to an enhanced activity due to SMSI.

In the current work, the target hydrous Ir oxide nanoparticle size is ca. 3 nm, so it is in the size range at which the highest reaction activity was reported for many other catalytic reactions as mentioned above. As the as-synthesized Ir nanoparticles are mostly metallic and the electrochemical

oxidation results in hydrous Ir oxide, the metallic Ir nanoparticles should be synthesized in a specific size, which upon oxidation results in ca. 3 nm hydrous Ir oxide nanoparticles. Considering the bulk density of metallic Ir and hydrous Ir oxide, 22.6 and 2.0 g/cm<sup>3</sup>,<sup>30</sup> respectively, a metallic Ir nanoparticle of 1.5 nm should theoretically convert into a 3.2 nm particle upon electrochemical oxidation, assuming all Ir converts to hydrous Ir oxide. Based on what is known from the literature, this particle size is promising with respect to catalyst dispersion and SMSI.<sup>21</sup>

The polyol method was used to produce Ir nanoparticles of ca. 1.5 nm diameter, whereby the particle size control was achieved through the heating profile. Heating for longer periods of time during synthesis results in nanoparticle size increase (data are not shown).

Figure 1a shows a TEM image of ATO used for the synthesis of all Ir/ATO catalysts reported in this study, where

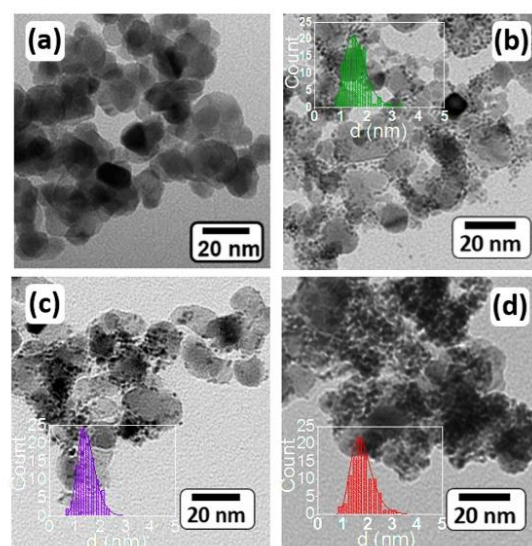


**Figure 1.** TEM of (a) ATO support material, TEM, and particle size distribution histograms of (b) 11.0, (c) 15.3, and (d) 23.4 wt % Ir/ATO catalysts. The average diameters and size distributions of the Ir nanoparticles were estimated from at least 150 particles in various TEM images.

spherical particles with a particle size in the range of 10–20 nm were obtained, agglomerated to secondary structures on the order of 100 nm. Three Ir/ATO catalysts were synthesized with Ir loadings of  $11.0 \pm 1.5$ ,  $15.3 \pm 1.5$ , and  $23.4 \pm 1.5$  wt %, as estimated by energy dispersive X-ray (EDX) analysis performed on the catalyst powder. The Ir particle size distribution of the respective catalysts is shown as inset in each TEM image. The number-averaged diameters and the standard deviations of the nanoparticles were  $1.6 \pm 0.4$ ,  $1.5 \pm 0.3$ , and  $1.8 \pm 0.4$  nm for 11.0, 15.3, and 23.4 wt % Ir/ATO catalysts, respectively. No difference in Ir particle size was observed among the various catalysts since Ir nanoparticles were separately made and then mixed with corresponding amounts of ATO to yield a specific catalyst loading. The only difference that can be seen from the TEM images (Figure 1b,c) is the degree of dispersion of Ir particles, where the lowest

dispersion of Ir on ATO was obtained for the highest loading of 23.4 wt % (Figure 1d), while the 11.0 wt % Ir/ATO catalyst exhibited the highest Ir dispersion. In other words, better dispersion of the Ir nanoparticles is obtained by decreasing the Ir loading, and therefore fewer Ir agglomerates are observed (Figure 1b).

As the Ir/ATO catalysts consist of metallic Ir, with Ir oxide only at the surface (as evidenced by XPS analysis) of the Ir nanoparticles due to oxidation of the surface when exposed to air, the catalysts were subjected to potential cycling to convert metallic Ir into hydrous Ir oxide and thus avoid Ir oxidation current during OER activity determination. Figure 2 shows the

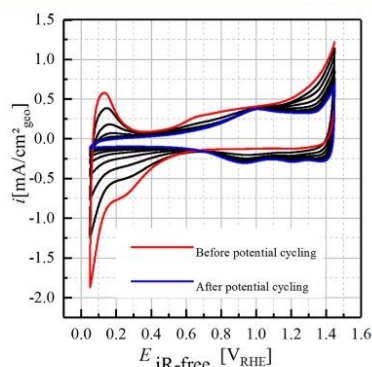


**Figure 2.** Initial CV (red) and after 10 cycles (blue) of Ir/ATO (11.0 wt %) in Ar-saturated 0.1 M H<sub>2</sub>SO<sub>4</sub> at 50 mV/s and 25 °C. The catalyst loading is 17 μg<sub>Ir</sub>/cm<sup>2</sup><sub>disk</sub>.

cyclic voltammetry of 11.0 wt % Ir/ATO catalyst in Ar-saturated 0.1 M H<sub>2</sub>SO<sub>4</sub> solution at a scan rate of 50 mV/s. It can be seen that the first cycle (red CV) shows a characteristic set of H-UPD (hydrogen underpotential deposition) peaks at 0.05–0.6 V<sub>RHE</sub>, indicating the metallic state, at least partially, of the as-synthesized Ir nanoparticles on ATO. Upon potential cycling (50 mV/s) between 0.05 and 1.45 V<sub>RHE</sub>, the H-UPD peaks rapidly decreased in size, indicating the conversion of the catalyst from metallic Ir to a hydrous Ir oxide, and a steady-state CV (blue CV) is ultimately obtained for the formed hydrous Ir oxide. The main set of redox peaks, centered at around 1.0 V<sub>RHE</sub>, is due to the Ir<sup>3+</sup>/Ir<sup>4+</sup> redox reaction, and upon potential cycling, it is anticipated that this set of peaks increases in size due to a complete conversion to hydrous Ir oxide formation, but this was not seen here.<sup>31</sup>

In contrast to the almost constant features observed at ~1.0 V<sub>RHE</sub>, the H-UPD features at low cathodic potentials (0.05–0.3 V<sub>RHE</sub>) continue to decrease with potential cycling, meaning Ir(0) is still oxidized; however, the increase in amount of hydrous Ir oxide cannot be observed in the CV. This may be attributed to the strong metal–support interaction (SMSI) that may alter the electrochemical behavior of the forming oxide; however, the investigation of such SMSI is not the focus of this study. The other two catalysts, 15.3 and 23.4 wt % Ir/ATO, showed exactly the same electrochemical behavior upon potential cycling as the 11.0 wt % Ir/ATO.

The fitted data of the Ir 4f XPS spectra of the three Ir/ATO catalysts (Figure 3a,b,d) confirm that the as-synthesized Ir nanoparticles on ATO are composed of metallic Ir(0) and Ir(IV); the latter may correspond to the molecular formula of Ir(OH)<sub>4</sub>. Table 1 shows the detailed information obtained from peak fitting, indicating that the three catalysts have similar

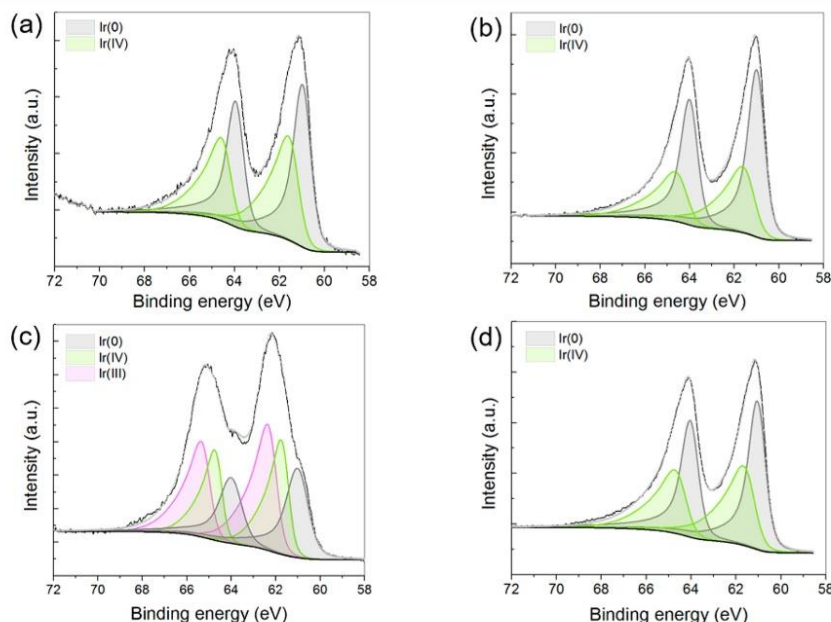


**Figure 3.** Detailed Ir 4f XPS spectra of as-synthesized Ir/ATO catalysts: (a) 11.0, (b) 15.3, and (d) 23.4 wt %. (c) XPS spectra of the electrochemically oxidized 11.0 wt % Ir/ATO catalyst. The parameters for the deconvolution of the Ir(0) (gray), the Ir(IV) (green), and the Ir(III) (red) species are listed in Table 1.



**Table 1. Parameters of the Ir 4F XPS Fits: Binding Energy (BE), Full Width at Half-Maximum (FWHM), Raw Peak Area (RPA), and Component Atomic Concentration (at. % conc)**

OER catalyst	name	BE (eV)	FWHM (eV)	RPA	at. % conc
23.4 wt % Ir/ATO	Ir(0) 4f	60.99	1.30	41725	100
	Ir(0) 4f 7/2	60.94	0.86	14857	35
	Ir(0) 4f 5/2	63.95	0.86	11142	27
	Ir(IV) 4f 7/2	61.43	1.20	9049	22
15.3 wt % Ir/ATO	Ir(IV) 4f 5/2	64.45	1.20	6786	16
	Ir(0) 4f	61.11	1.42	62213	100
	Ir(0) 4f 7/2	61.00	0.87	19346	31
	Ir(0) 4f 5/2	64.00	0.87	15167	24
11 wt % Ir/ATO	Ir(IV) 4f 7/2	61.49	1.16	15225	25
	Ir(IV) 4f 5/2	64.56	1.16	12192	20
	Ir(0) 4f	61.14	1.50	12429	100
	Ir(0) 4f 7/2	60.92	0.88	3857	31
11 wt % Ir/ATO (after oxidation)	Ir(0) 4f 5/2	63.91	0.86	2893	23
	Ir(IV) 4f 7/2	61.44	1.06	3281	26
	Ir(IV) 4f 5/2	64.44	0.99	2461	20
	Ir(0) 4f	62.16	2.06	26482	100
	Ir(0) 4f 7/2	60.94	1.13	4585	17
	Ir(0) 4f 5/2	63.94	1.15	3438	13
	Ir(IV) 4f 7/2	61.63	0.80	4612	17
	Ir(IV) 4f 5/2	64.63	0.76	3459	13
	Ir(III) 4f 7/2	62.21	0.94	5936	22
	Ir(III) 4f 5/2	65.21	0.93	4452	18

Ir(0) to Ir(IV) ratios. Specifically, the atomic weight percentage of Ir/(Ir oxide) in the Ir nanoparticles was found to be 54/(46), 56/(44), and 62/(38)% for 11.0, 15.3, and 23.4 wt % Ir/ATO, respectively (as calculated from Table 1). Based on the average Ir particle diameter of 1.5–1.8 nm (see Figure 1), the Ir oxide content is consistent with a surface monolayer of Ir(OH)<sub>4</sub> on a metallic iridium core (calculated assuming spherical particles and using the covalent radius of Ir of 141 pm).

Although the potential cycling of the Ir/ATO catalysts between 0.05 and 1.45 V<sub>RHE</sub> ultimately results in a steady-state CV with no H-UPD features, indicating full oxidation of Ir(0),<sup>32</sup> the XPS results (Figure 3c) reveal that the Ir nanoparticles are composed of Ir(0), Ir(III), and Ir(IV) after potential cycling. The overall amount of Ir(0) detected is greatly reduced by potential cycling from 54% to 30%. These results suggest that there is still metallic Ir(0) in the core of the nanoparticles, which is not electrochemically accessible under the aforementioned cyclic voltammetry conditions. This can be attributed to the formation of a compact anhydrous oxide layer (inner oxide layer) between the hydrous Ir oxide (outer oxide layer) and the metallic Ir(0) core.<sup>31</sup> During potential cycling, the oxidation state of the outer surface layer changes from a metallic iridium (Ir(0)) to a hydrous Ir oxide (III/IV), while the forming compact layer shields the metallic core from the solution, resulting in a gradual decrease in the H-UPD features, but at the same time protecting the rest of the metal core from oxidation.<sup>31</sup> Thus, extensive potential cycling may result in complete oxidation of the Ir(0) core due to exposing the metallic core to solution and to further oxidation.

The catalytic activity for the oxygen evolution reaction (OER) of the Ir/ATO catalysts was examined in O<sub>2</sub>-saturated 0.1 M H<sub>2</sub>SO<sub>4</sub> at room temperature (25 °C) by using rotating

disk cyclic voltammetry at a constant areal loading of 3.7 μg<sub>Ir</sub>/cm<sup>2</sup>. Figure 4a shows OER polarization curves (not *iR*-corrected and normalized to the geometric disk area) of the Ir/ATO catalysts compared to commercial Ir-black (99.8%, metals basis, Alfa Aesar) and IrO<sub>2</sub>/TiO<sub>2</sub> (IrO<sub>2</sub>/TiO<sub>2</sub> with 75 wt % iridium, Elyst Ir75 0480 from Umicore) reference catalysts, both commercially available, while Figure 4b shows the corresponding iridium mass-normalized OER activities. It is evident that the Ir/ATO catalysts significantly outperform the Ir-black and IrO<sub>2</sub>/TiO<sub>2</sub> reference catalysts over the whole potential range. The OER catalytic activity rises in the order: IrO<sub>2</sub>/TiO<sub>2</sub> < Ir-black < 23.4 wt % Ir/ATO < 15.3 wt % Ir/ATO < 11.0 wt % Ir/ATO. Concomitant with an increasing OER activity, the onset potential for the OER is shifted to lower overpotentials for the Ir/ATO catalysts, resulting in higher efficiencies when applied in a PEMWE. The enhanced OER mass activities of Ir/ATO catalysts over Ir-black and IrO<sub>2</sub>/TiO<sub>2</sub> are attributed to the significant increase in the hydrous Ir oxide active surface area because of the use of small Ir nanoparticles (1.5–1.8 nm). On top of the active surface area increase, the high dispersion of the Ir catalyst on the conductive ATO support, ensuring high utilization of the OER active sites, might further enhance the OER activity. Lowering the packing density (g<sub>Ir</sub>/cm<sup>3</sup>), realized by increasing the surface area (m<sup>2</sup>/g) and the dispersion of iridium, is decisive for the production of a cost-efficient OER catalyst, which is not exhibited by the two commercial OER catalysts investigated here.

The bar diagram in Figure 4c shows the mass activities of the three Ir/ATO catalysts and two reference catalysts determined at 1.5 V<sub>RHE</sub>. The most active Ir/ATO (11 wt %; ~185 A/g<sub>Ir</sub>) is at least 35 times more active than the IrO<sub>2</sub>/TiO<sub>2</sub> (~5 A/g<sub>Ir</sub>) catalyst and about 4 times more active than the Ir-black (48 A/g<sub>Ir</sub>) catalyst at 25 °C. The OER activities were extracted from Figure 4b at 1.5 V<sub>RHE</sub> and after subtracting the baseline current at 1.45 V<sub>RHE</sub> that corresponds to the Au oxide formation peak current and any capacitive contribution.

The *iR*-free Tafel plots obtained from the fits of the polarization curves of all the catalysts are shown in Figure 4d. The Tafel slopes (TS) obtained for the Ir/ATO catalysts are in the range 45–52 mV/dec, similar to the one measured for the Ir-black (55 mV/dec) catalyst, whereas the IrO<sub>2</sub>/TiO<sub>2</sub> exhibits the largest TS (66 mV/dec). The obtained TS for the IrO<sub>2</sub>/TiO<sub>2</sub> is in good agreement with the 60 mV/dec slope typically reported for IrO<sub>2</sub>-based catalysts in H<sub>2</sub>SO<sub>4</sub> solutions.<sup>33–35</sup> The 60 mV/dec slope is believed to be associated with an electrochemical reaction whose rate-determining step involves a chemical step subsequent to the first electron transfer step.<sup>36–39</sup> Because there is a strong correlation between the hydration state of the iridium and the OER activity,<sup>40,41</sup> the lower TS measured for the Ir/ATO as well as the Ir-black compared to the IrO<sub>2</sub>/TiO<sub>2</sub> can be explained by the formation of a hydrous Ir oxide, which exhibits higher OER activity compared to a thermally treated IrO<sub>2</sub>.<sup>40</sup> The fact that the Ir/ATO catalysts exhibit an even smaller TS than Ir-black suggests that there is an enhancement in the OER reaction kinetics due to SMSI between the hydrous Ir oxide and the Sb–SnO<sub>2</sub> support.<sup>23,35,13</sup> It has been reported that the OER reaction rate can be enhanced by the rapid removal/oxidation of hydroxyl OH<sub>ad</sub> species that might adsorb as intermediates on the OER active site of the hydrous Ir oxide surface.<sup>42,43</sup> SnO<sub>2</sub> could catalyze such oxidation of OH<sub>ad</sub> to O<sub>ad</sub> on the

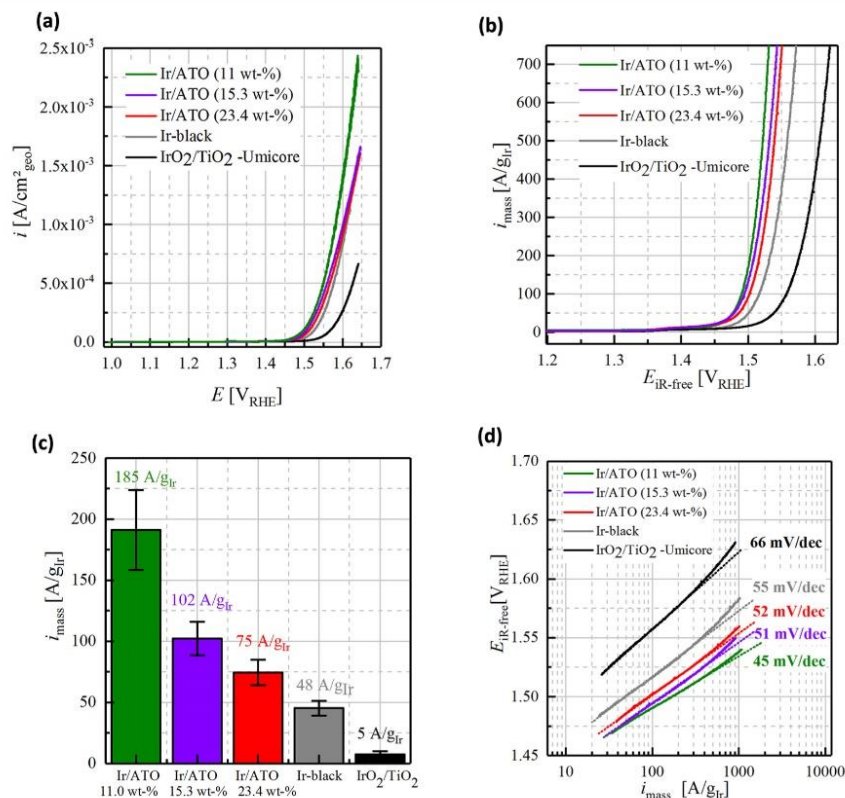


**Figure 4.** Electrochemical OER polarization curves (a) geometric and (b) Ir mass-normalized current densities, (d) corresponding Tafel slopes, and (c) mass activities determined at 1.5 V<sub>RHE</sub> of the Ir/ATO catalysts (11.0, 15.3, and 23.4 wt %) as well as of Ir-black and of IrO<sub>2</sub>/TiO<sub>2</sub> reference catalysts. All measurements were performed in O<sub>2</sub>-saturated 0.1 M H<sub>2</sub>SO<sub>4</sub> at 25 °C. Catalysts loading: 3.7 μg<sub>Ir</sub>/cm<sup>2</sup><sub>disk</sub>. Scan rate: 5 mV/s (2500 rpm).

hydrous Ir oxide surface, thus promoting the reaction kinetics and altering the TS.<sup>23</sup>

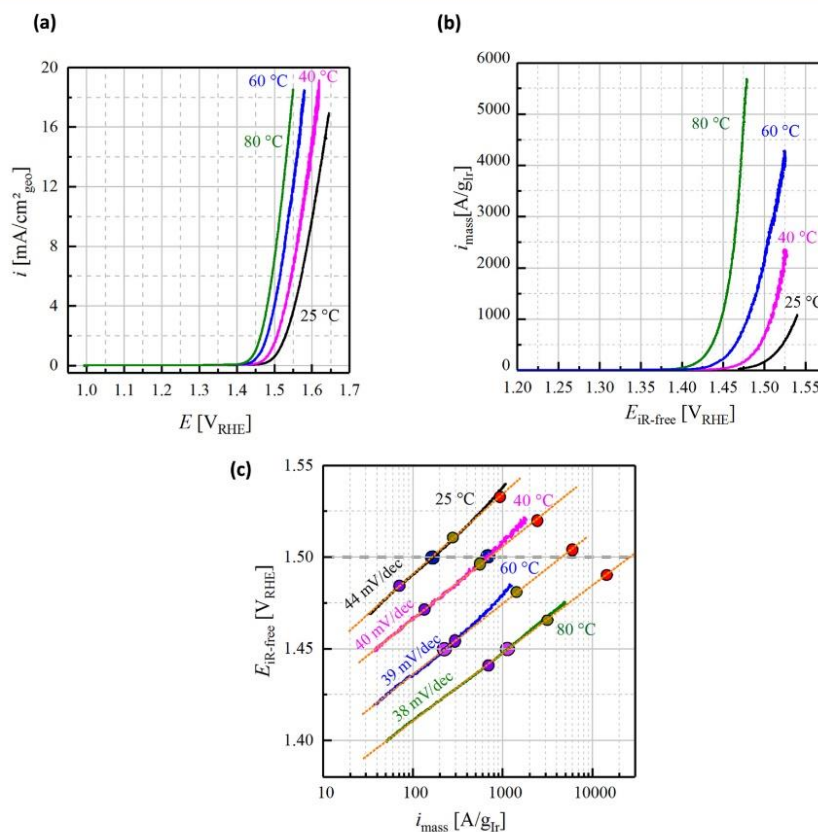
As most low-temperature PEM electrolyzers typically operate at temperatures up to 60 °C,<sup>44,5</sup> the OER activity of the most active catalyst, 11 wt % Ir/ATO, was investigated at temperatures higher than 25 °C to give an indication of the realistic activity this catalyst may provide when implemented in a real application.

Figure 5a depicts the OER polarization curves (not *i*<sub>R</sub>-corrected and normalized to the geometric disk area) of the 11.0 wt % Ir/ATO catalyst measured at four different temperatures in the range 25–80 °C, while Figure 5b shows the corresponding iridium mass normalized activities of the catalyst at the same temperatures. Increasing the temperature from 25 to 80 °C leads to a less positive shift of the apparent onset potential from 1.47 to 1.39 V<sub>RHE</sub>, indicating enhanced kinetics at higher temperatures. The determination of the OER mass activities is commonly done at an *i*<sub>R</sub>-free potential of 1.5 V<sub>RHE</sub> where kinetic losses are dominant (Tafel region) and mass-transport related losses, which can occur at high geometric current densities due to partial shielding of the catalyst layer by oxygen bubbles, can be excluded. Clearly, a proper determination of the activity at 1.5 V<sub>RHE</sub> is not possible at higher temperatures (60 and 80 °C) due to the occurrence of mass-transport losses. Therefore, the activity at lower

temperatures (25 and 40 °C) was determined at the commonly used *i*<sub>R</sub>-free potential of 1.5 V<sub>RHE</sub>, while at high temperatures, a lower potential (1.45 V<sub>RHE</sub>) was used. Quite clearly, the Tafel lines at 25 and 40 °C very well represent the measured OER data up to ≈1.53 V<sub>iR-free</sub> and to ≈1.51 V<sub>iR-free</sub>, respectively, so that the mass specific OER activity of the Ir/ATO catalyst at 1.5 V<sub>iR-free</sub> can be determined with high fidelity to be ≈166 A/g<sub>Ir</sub> at 25 °C and ≈686 A/g<sub>Ir</sub> at 40 °C (coinciding with the geometric current density of ≈0.6 and of ≈2.5 mA/cm<sup>2</sup> at 1.5 V<sub>iR-free</sub>, respectively). On the other hand, at 60 °C the deviation between the Tafel line and the actual data occurs already at ≈1.47 V<sub>iR-free</sub> and thus the activity was determined at 1.45 V<sub>RHE</sub>, yielding ≈230 A/g<sub>Ir</sub>. Finally, at 80 °C excessively large geometric current densities would be required to reach 1.5 V<sub>iR-free</sub> so that also here the best approach is to use 1.45 V<sub>iR-free</sub> for determining the mass activity, yielding ≈1100 A/g<sub>Ir</sub>.

From Tafel plots, the OER mass activity (80 °C) at 1.45 V<sub>RHE</sub> of the 11.0 wt % Ir/ATO catalyst is determined to be 1100 A/g<sub>Ir</sub>. In comparison with other studies, the activity of the 11.0 wt % Ir/ATO catalyst at room temperature (25 °C; ≈166 A/g<sub>Ir</sub>) is among the highest OER activity reported in the literature,<sup>45</sup> whereas at higher temperatures, a similar type of catalyst (11 wt % IrO<sub>x</sub> on Sb-SnO<sub>2</sub>) synthesized by Ohno et al. exhibits a 3 times higher activity (≈3000 A/mg<sub>Ir</sub>) in a liquid cell at 1.45 V<sub>RHE</sub> and 80 °C.<sup>24</sup> However, the catalyst





**Figure 5.** Electrochemical OER polarization curves (a) geometric and (b) Ir mass-normalized current densities and (c) corresponding  $iR$ -corrected Tafel plots of Ir/ATO (11.0 wt %) at 25, 40, 60, and 80 °C. All measurements were performed in  $O_2$ -saturated 0.1 M  $H_2SO_4$  rotating at 2500 rpm. Catalysts loading:  $3.7 \mu g_{Ir}/cm^2_{disk}$ . Scan rate: 5 mV/s. Using the reference potential at each temperature ( $E^0$ ), we can determine the activities at given OER overpotentials ( $\eta = 0.20$  V, purple circles;  $\eta = 0.225$  V, green circles;  $\eta = 0.25$  V, red circles) as well as at  $1.5 V_{iR-free}$  (blue circles) and at  $1.45 V_{iR-free}$  (light purple circles).

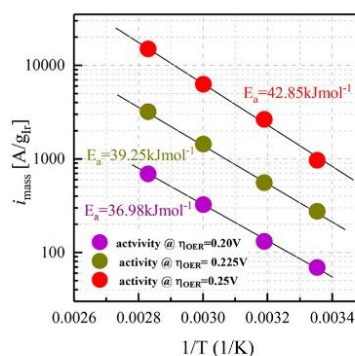
synthesized by Ohno et al. showed a significantly lower performance in a MEA ( $450 A/g_{Ir}$  at  $1.45 V_{RHE}$ ) due to the low electronic conductivity of the catalyst layer. Hence, even though the performance of the herein studied catalyst measured in a liquid electrolyte is lower, the high conductivity of the applied ATO should be beneficial to enable high performance in single cell measurements (MEA) without an additional loss in performance. In general, the high activity, which can most likely be attributed to the high catalyst surface area and good dispersion, and hence results in a reduced packing density ( $\approx 0.27 g_{Ir}/cm^3$ ) compared to a commercial catalyst (Umicore  $IrO_2/TiO_2$ :  $\approx 2.3 g_{Ir}/cm^3$ ), can be achieved with this catalyst design, therefore allowing a reduction of the Ir loading at the anode side of an electrolyzer as explained later.<sup>5</sup>

For the following analysis of activation energy, an estimate of the OER kinetics was obtained by extrapolating the Tafel kinetics observed at lower current densities to  $1.5 V_{iR-free}$  as is shown in Figure 5c. The iridium mass-normalized OER activities estimated at temperatures between 25 and 80 °C in 0.1 M  $H_2SO_4$  were used to draw the corresponding Arrhenius plots at various overpotentials, 0.20 V (purple solid circles, Figures 5c and 6a), 0.225 V (green solid circles), and 0.25 V

(red solid circles), as displayed in Figure 6a. The overpotentials were referenced to the standard reference potential at each temperature ( $E^0$ ; see Figure 6b) as well as to a partial pressure of  $O_2$ , calculated individually for each temperature considering an ambient pressure of 1 bar and the corresponding water vapor pressure (see eqs 1 and 2) and a constant partial pressure of  $H_2$  ( $p_{H_2} = 0.969 \text{ bar}_a$ ). Moreover, since the reversible potential of the reference ( $E_{rev}^{ref}$ ) changes along with temperature (eq 4), the temperature of the reference compartment was measured separately, and the reversible cell potential was corrected for the potential of the reference electrode accordingly. Herein, it was assumed that the first deprotonation step is complete ( $Ka_1 \approx 10^3$ ), while the second deprotonation step ( $Ka_2 \approx 10^{-2}$ ) is incomplete, yielding a concentration of  $c(H^+) \approx 0.11 \text{ mol L}^{-1}$ . Overpotentials lower than 0.20 V or higher than 0.25 V were avoided to make sure all activity values used to determine the activation energy at a constant overpotential (eq 3) were within the experimental or near-experimental Tafel lines.<sup>44</sup>

$$E_{rev} = E_{rev}^0 + \frac{RT}{2F} \ln \left[ \frac{a(H_2) \sqrt{a(O_2)}}{a(H_2O)} \right] \quad (1)$$

(a)



(b)

Temperature (°C)	E° (V)	+0.200 V	Activity (A/g <sub>Ir</sub> )	+0.225 V	Activity (A/g <sub>Ir</sub> )	+0.250 V	Activity (A/g <sub>Ir</sub> )
25	1.284	1.484	69	1.509	275	1.534	967
40	1.272	1.472	131	1.497	556	1.522	2635
60	1.256	1.456	325	1.481	1438	1.506	6267
80	1.241	1.441	693	1.466	3196	1.491	14984

**Figure 6.** (a) Arrhenius plot of the OER activity data presented in Figure 5c at given constant OER overpotential  $\eta_{\text{OER}}$ . All measurements were performed in O<sub>2</sub>-saturated 0.1 M H<sub>2</sub>SO<sub>4</sub>, 2500 rpm. Catalysts loading: 3.7  $\mu\text{g}_{\text{Ir}}/\text{cm}^2_{\text{disk}}$  (11.0 wt % Ir/ATO). Scan rate: 5 mV/s. (b) Standard OER potential at various temperatures ( $E^\circ$ ) and  $iR$ -free potentials for a given OER overpotential (0.20, 0.225, and 0.25 V) and the corresponding OER activities.

$$E_{\text{rev}}^0 = 1.2291\text{V} - 0.0008456\text{V}(T - 298.15\text{K}) \quad (2)$$

$$-R \left( \frac{\partial \ln(i)}{\partial 1/T} \right) \Bigg|_{\eta=\text{const}} = E_{\text{act}}(\eta=\text{const}) \quad (3)$$

$$E_{\text{rev}}^{\text{ref}} = E_{\text{rev}}^0 - \frac{RT}{2F} \ln \left[ \frac{p_{\text{H}_2} (c^\theta)^2}{p^\theta c(\text{H}^+)^2} \right] \quad (4)$$

The OER activation energy on the Ir/ATO catalyst was determined to be approximately 37, 39, and 43 kJ/mol at overpotentials of 0.20, 0.225, and 0.25 V, respectively. The activation energy values reported here are similar to those reported in a very recent study by Suermann et al. for the OER reaction (50–45 kJ/mol for overpotentials between 0.20 and 0.25 V) based on Ir-black or IrO<sub>2</sub>/TiO<sub>2</sub> catalyst.<sup>46</sup> In our study, a hydrous iridium oxide, which is known to exhibit a higher activity than crystalline IrO<sub>2</sub>, was studied, while Suermann et al. applied an IrO<sub>2</sub>-based catalyst.<sup>41,47</sup> The higher activity exhibited by an amorphous iridium oxide might explain the slightly lower activation energy obtained in this study. Because of the narrow potential range used in this study to determine the activation energy, no clear correlation between a change in overpotential and activation energy can be drawn. However, in general, a decreasing activation energy with increasing overpotential would be expected based on the Tafel kinetics. Nevertheless, the observed range of activation energies matches quite well with the activation energies obtained by Suermann et al. and lies within the error range observed in their study ( $\eta = 0.2\text{--}0.3\text{ V}$ ;  $E_a \approx 39\text{--}52\text{ kJ mol}^{-1}$ ).<sup>46</sup>

The performance of the Ir/ATO (11.0 wt %) catalyst at 80 °C was compared with the reference catalysts, Ir-black and IrO<sub>2</sub>/TiO<sub>2</sub>. Figure 7a shows the  $iR$ -free anodic polarization curves for Ir/ATO (11.0 wt %) and the two reference catalysts in O<sub>2</sub>-saturated 0.1 M H<sub>2</sub>SO<sub>4</sub> solution at 80 °C, in which the current was normalized by the iridium mass, while Figure 7b shows the corresponding Tafel plots of the three catalysts. The OER onset potential of the Ir/ATO is at  $\sim 1.39\text{ V}_{\text{RHE}}$ , i.e., 40 and 70 mV less positive than that of Ir-black and IrO<sub>2</sub>/TiO<sub>2</sub> catalysts, respectively. The difference in Tafel slopes at high temperature is consistent with that obtained at lower temperature (Figure 4d) and is most likely due to the interaction of the hydrous Ir oxide with the ATO support, which results in a lower TS for the Ir/ATO catalysts as explained earlier. The OER polarization curves clearly show the significant difference in OER activity at 80 °C between the Ir/ATO (11.0 wt %) catalyst and the reference catalysts (Figure 7c). The OER activity values reported in Figure 7c are determined from the Tafel plots (Figure 7b) at 1.45  $\text{V}_{\text{RHE}}$  from the experimental Tafel lines (solid lines in Figure 7c). This clearly shows that the synthesized Ir/ATO catalyst ( $\approx 1100\text{ A/g}_{\text{Ir}}$ ) outperforms both the Ir-black ( $\approx 190\text{ A/g}_{\text{Ir}}$ ) and the IrO<sub>2</sub>/TiO<sub>2</sub> ( $\approx 45\text{ A/g}_{\text{Ir}}$ ) drastically, thereby proving that by dispersing a high surface area Ir catalyst on a conductive oxide support, superior OER activities can be achieved. Therefore, measurements employing the 11.0 wt % Ir/ATO as an anode catalyst layer in a PEMWE are in progress, where the actual activity due to the absence of mass transport should be exploited.

It has been recently shown that the Pt loading on the cathode side of an electrolyzer can be reduced to very low



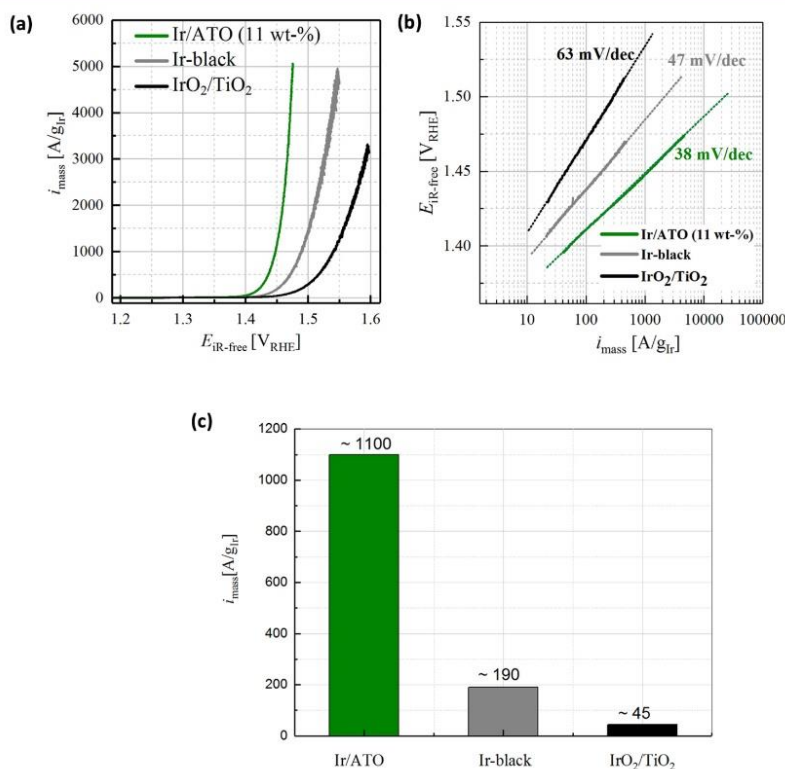


**Figure 7.** Electrochemical OER polarization curves (a) Ir-mass-normalized current densities and (b) corresponding  $iR$ -corrected Tafel plots of Ir/ATO (11.0 wt %), Ir-black and  $\text{IrO}_2/\text{TiO}_2$  (Umicore) catalysts, and (c) OER activities (determined from Tafel plots) at  $80^\circ\text{C}$  at  $1.45 V_{\text{RHE}}$ . All measurements were performed in  $\text{O}_2$ -saturated  $0.1 \text{ M H}_2\text{SO}_4$ . Catalysts loading:  $3.7 \mu\text{g}_{\text{Ir}}/\text{cm}^2_{\text{disk}}$ . Scan rate:  $5 \text{ mV/s}$ .

values, such as  $0.025 \text{ mg}_{\text{Pt}}/\text{cm}^2$ , without any negative effect on the performance of the electrolyzer.<sup>5</sup> This was only possible because of the fast kinetics of the hydrogen evolution reaction (HER). On the other hand, the kinetics of OER on the anode is slower than that of the HER, and therefore high loadings of the OER catalyst ( $\approx 2 \text{ mg}_{\text{Ir}}/\text{cm}^2$ ) are typically used at the anode to compensate for such slow kinetics of the OER. It has been recently demonstrated that by using a thermally treated  $\text{IrO}_2/\text{TiO}_2$  as an OER catalyst the loading can be reduced to  $\approx 1 \text{ mg}_{\text{Ir}}/\text{cm}^2$  without sacrificing the anode performance at operational current densities ( $\geq 1 \text{ A}/\text{cm}^2$ ).<sup>5</sup> It was even suggested in that study that very low Ir loadings might be achieved without significantly affecting the performance. However, because of the extremely high Ir content (75 wt % Ir) of the OER catalyst used in that study,<sup>5</sup> as well as all commercially available OER catalysts, achieving such low loadings was not possible due to the inhomogeneity of the very thin catalyst layer, resulting in a significant decrease in performance. The use of an OER active catalyst that is characterized by a low iridium packing density ( $\text{g}_{\text{Ir}}/\text{cm}^3$ ) will help achieve low Ir loadings on the anode with reasonably thick electrocatalyst layers that are homogeneous enough to not influence the anode performance. Generally, the OER activity of the  $\text{IrO}_2/\text{TiO}_2$  (Umicore) catalyst would be sufficient to realize low loadings; however, because of the large packing density ( $\text{g}_{\text{Ir}}/\text{cm}^3$ ), inhomogeneous catalyst layers would be conceived, resulting in an additional loss in

performance. In comparison to that, the low packing density of the Ir/ATO (11.0 wt %) catalyst would allow for a significant decrease in loading down to  $0.015\text{--}0.025 \text{ mg}_{\text{Ir}}/\text{cm}^2$ , i.e., similar to that of the Pt catalyst at the cathode side. The performance of such low loadings and the durability of the Ir/ATO catalyst in a PEM electrolyzer are currently under investigation.

#### IV. CONCLUSION

In this study, we have successfully designed and synthesized an OER catalyst that combines all parameters that have been reported to enhance OER activity of oxide-supported Ir catalyst. The catalyst consists of Ir nanoparticles supported on antimony-doped tin oxide (ATO), and it exhibits the highest OER activity reported in the literature based on initial activity measurements. The very high OER activity is a result of the careful catalyst design in which the size of the Ir oxide nanoparticles is controlled in the 2–4 nm range, and therefore it provides both high surface to mass ratio and at the same time might enhance the synergetic interaction with the oxide support, called strong metal–support interaction (SMSI). The very high electrical conductivity of the ATO ( $2 \text{ S}/\text{cm}$ ) used in this study and its high surface area ( $50 \text{ m}^2/\text{g}$ ) along with a high catalyst dispersion results in a very high OER activity of the Ir/ATO catalyst ( $1100 \text{ A}/\text{g}_{\text{Ir}}$  at  $80^\circ\text{C}$ , at  $1.45 V_{\text{RHE}}$ ). In contrast to the state-of-the-art OER catalysts that require high Ir loadings, the low loading Ir catalyst (Ir/ATO) presented here

can help to reduce the precious metal loading on the anode of a PEMWE by several orders of magnitude, which is an important step for facilitating the scaled-up manufacturing of PEM water electrolyzers.

## AUTHOR INFORMATION

### Corresponding Authors

**Hany A. El-Sayed** – Chair of Technical Electrochemistry, Technical University of Munich D-85748 Garching, Germany; [orcid.org/0000-0002-8769-8258](https://orcid.org/0000-0002-8769-8258); Email: hany.el-sayed@tum.de

**Alexandra Hartig-Weiss** – Chair of Technical Electrochemistry, Technical University of Munich D-85748 Garching, Germany; [orcid.org/0000-0001-7094-5016](https://orcid.org/0000-0001-7094-5016); Email: alexandra.weiss@tum.de

### Authors

**Melanie Miller** – Chair of Technical Electrochemistry, Technical University of Munich D-85748 Garching, Germany

**Hans Beyer** – Chair of Technical Electrochemistry, Technical University of Munich D-85748 Garching, Germany

**Alexander Schmitt** – Chair of Technical Electrochemistry, Technical University of Munich D-85748 Garching, Germany

**Armin Siebel** – Chair of Technical Electrochemistry, Technical University of Munich D-85748 Garching, Germany;

[orcid.org/0000-0001-5773-3342](https://orcid.org/0000-0001-5773-3342)

**Anna T. S. Freiberg** – Chair of Technical Electrochemistry, Technical University of Munich D-85748 Garching, Germany;

[orcid.org/0000-0002-7885-7632](https://orcid.org/0000-0002-7885-7632)

**Hubert A. Gasteiger** – Chair of Technical Electrochemistry, Technical University of Munich D-85748 Garching, Germany;

[orcid.org/0000-0001-8199-8703](https://orcid.org/0000-0001-8199-8703)

Complete contact information is available at: <https://pubs.acs.org/10.1021/acsnm.9b02230>

### Notes

The authors declare no competing financial interest.

## ACKNOWLEDGMENTS

The authors gratefully acknowledge the German Ministry of Education and Research for financial support of this work within the Kopernikus project P2X (03SFK2 V0). The authors thank Philipp Rheinländer, Dr. Maximilian Bernt, Jan Schwämmlein, Dr. Gregor Harzer, and Dr. Pankaj Madkikar (Chair of Technical Electrochemistry, Technical University of Munich, Germany) for fruitful scientific discussions. Thanks are also extended to Prof. Hendrick Dietz and Christian Sigl (Walter Schottky Institute, Technical University of Munich) for helping with TEM analysis.

## REFERENCES

- (1) Barbir, F. PEM electrolysis for production of hydrogen from renewable energy sources. *Sol. Energy* **2005**, *78*, 661–669.
- (2) Carmo, M.; Fritz, D. L.; Mergel, J.; Stolten, D. A comprehensive review on PEM water electrolysis. *Int. J. Hydrogen Energy* **2013**, *38*, 4901–4934.
- (3) Buttler, A.; Spliethoff, H. Current status of water electrolysis for energy storage, grid balancing and sector coupling via power-to-gas and power-to-liquids. *Renewable Sustainable Energy Rev.* **2018**, *82*, 2440–2454.
- (4) Suermann, M.; Schmidt, T. J.; Büchi, F. N. Cell Performance Determining Parameters in High Pressure Water Electrolysis. *Electrochim. Acta* **2016**, *211*, 989–997.

- (5) Bernt, M.; Siebel, A.; Gasteiger, H. A. Analysis of Voltage Losses in PEM Water Electrolyzers with Low Platinum Group Metal Loadings. *J. Electrochem. Soc.* **2018**, *165*, F305–F314.

(6) InfoMine. Iridium Prices and Iridium Price Charts. <http://www.infomine.com/investment/metal-prices/iridium/> (accessed January 29, 2020).

- (7) Bernt, M.; Weiß, A.; Tovini, M. F.; El-Sayed, H. A.; Schramm, C.; Schröter, J.; Kemmer, M.; Gebauer, C.; Gasteiger, H. A. Current Challenges in Catalyst Development for PEM Water Electrolyzers. *Chemie Ingenieur Technik* [Online].

(8) Puthiyapura, V. K.; Mamlouk, M.; Pasupathi, S.; Pollet, B. G.; Scott, K. Physical and electrochemical evaluation of ATO supported IrO<sub>2</sub> catalyst for proton exchange membrane water electrolyser. *J. Power Sources* **2014**, *269*, 451–460.

(9) Hayden, B. E. Particle size and support effects in electrocatalysis. *Acc. Chem. Res.* **2013**, *46*, 1858–1866.

(10) Maass, S.; Finsterwalder, F.; Frank, G.; Hartmann, R.; Merten, C. Carbon support oxidation in PEM fuel cell cathodes. *J. Power Sources* **2008**, *176*, 444–451.

(11) Siracusano, S.; Baglio, V.; D'Urso, C.; Antonucci, V.; Aricò, A. S. Preparation and characterization of titanium suboxides as conductive supports of IrO<sub>2</sub> electrocatalysts for application in SPE electrolyzers. *Electrochim. Acta* **2009**, *54*, 6292–6299.

(12) Puthiyapura, V. K.; Pasupathi, S.; Basu, S.; Wu, X.; Su, H.; Varaganandiyar, N.; Pollet, B.; Scott, K. RuxNb<sub>1-x</sub>O<sub>2</sub> catalyst for the oxygen evolution reaction in proton exchange membrane water electrolyzers. *Int. J. Hydrogen Energy* **2013**, *38*, 8605–8616.

(13) Ferro, S.; Rosestolato, D.; Martínez-Huitle, C. A.; De Battisti, A. On the oxygen evolution reaction at IrO<sub>2</sub>-SnO<sub>2</sub> mixed-oxide electrodes. *Electrochim. Acta* **2014**, *146*, 257–261.

(14) Polonský, J.; Petrushina, I. M.; Christensen, E.; Bouzek, K.; Prag, C. B.; Andersen, J.; Bjerrum, N. J. Tantalum carbide as a novel support material for anode electrocatalysts in polymer electrolyte membrane water electrolyzers. *Int. J. Hydrogen Energy* **2012**, *37*, 2173–2181.

(15) Karimi, F.; Peppley, B. A. Metal Carbide and Oxide Supports for Iridium-Based Oxygen Evolution Reaction Electrocatalysts for Polymer-Electrolyte-Membrane Water Electrolysis. *Electrochim. Acta* **2017**, *246*, 654–670.

(16) Oh, H.-S.; Nong, H. N.; Strasser, P. Preparation of Mesoporous Sb-, F-, and In-Doped SnO<sub>2</sub> Bulk Powder with High Surface Area for Use as Catalyst Supports in Electrolytic Cells. *Adv. Funct. Mater.* **2015**, *25*, 1074–1081.

(17) Mohanta, P. K.; Glökler, C.; Arenas, A. O.; Jörissen, L. Sb doped SnO<sub>2</sub> as a stable cathode catalyst support for low temperature polymer electrolyte membrane fuel cell. *Int. J. Hydrogen Energy* **2017**, *42*, 27950–27961.

(18) Han, B.; Risch, M.; Belden, S.; Lee, S.; Bayer, D.; Mutoro, E.; Shao-Horn, Y. Screening Oxide Support Materials for OER Catalysts in Acid. *J. Electrochem. Soc.* **2018**, *165*, F813–F820.

(19) Geiger, S.; Kasian, O.; Mingers, A. M.; Mayrhofer, K. J. J.; Cherevko, S. Stability limits of tin-based electrocatalyst supports. *Sci. Rep.* **2017**, *7*, 1074.

(20) El-Sayed, H. A.; Weiß, A.; Olbrich, L. F.; Putro, G. P.; Gasteiger, H. A. OER Catalyst Stability Investigation using RDE Technique – A stability measure or an Artifact? *J. Electrochem. Soc.* **2019**, *166*, F1–F7.

(21) Oh, H.-S.; Nong, H. N.; Reier, T.; Bergmann, A.; Gliech, M.; Ferreira de Araújo, J.; Willinger, E.; Schlögl, R.; Teschner, D.; Strasser, P. Electrochemical Catalyst–Support Effects and Their Stabilizing Role for IrO<sub>x</sub> Nanoparticle Catalysts during the Oxygen Evolution Reaction. *J. Am. Chem. Soc.* **2016**, *138*, 12552–12563.

(22) Nong, H. N.; Oh, H.-S.; Reier, T.; Willinger, E.; Willinger, M.-G.; Petkov, V.; Teschner, D.; Strasser, P. Oxide-supported IrNiO(x) core-shell particles as efficient, cost-effective, and stable catalysts for electrochemical water splitting. *Angew. Chem., Int. Ed.* **2015**, *54*, 2975–2979.

(23) Ohno, H.; Nohara, S.; Kakinuma, K.; Uchida, M.; Miyake, A.; Deki, S.; Uchida, H. Remarkable Mass Activities for the Oxygen



Evolution Reaction at Iridium Oxide Nanocatalysts Dispersed on Tin Oxides for Polymer Electrolyte Membrane Water Electrolysis. *J. Electrochem. Soc.* **2017**, *164*, F944–F947.

(24) Ohno, H.; Nohara, S.; Kakinuma, K.; Uchida, M.; Uchida, H. Effect of Electronic Conductivities of Iridium Oxide/Doped SnO<sub>2</sub> Oxygen-Evolving Catalysts on the Polarization Properties in Proton Exchange Membrane Water Electrolysis. *Catalysts* **2019**, *9*, 74.

(25) Beyer, H.; Metzger, M.; Sicklinger, J.; Wu, X.; Schwenke, K. U.; Gasteiger, H. A. Antimony Doped Tin Oxide—Synthesis, Characterization and Application as Cathode Material in Li-O<sub>2</sub> Cells. *J. Electrochem. Soc.* **2017**, *164*, A1026–A1036.

(26) Freakley, S. J.; Ruiz-Esquius, J.; Morgan, D. J. The X-ray photoelectron spectra of Ir, IrO<sub>2</sub> and IrCl<sub>3</sub> revisited. *Surf. Interface Anal.* **2017**, *49*, 794–799.

(27) Hettterscheid, D. G. H.; van der Ham, C. J. M.; Diaz-Morales, O.; Verhoeven, M. W. G. M. T.; Longo, A.; Banerjee, D.; Niemantsverdriet, J. W. H.; Reek, J. N. H.; Feiters, M. C. Early stages of catalyst aging in the iridium mediated water oxidation reaction. *Phys. Chem. Chem. Phys.* **2016**, *18*, 10931–10940.

(28) Pfeifer, V.; Jones, T. E.; Velasco Vélez, J. J.; Massué, C.; Arrigo, R.; Teschner, D.; Girgsdies, F.; Scherzer, M.; Greiner, M. T.; Allan, J.; Hashagen, M.; Weinberg, G.; Piccinin, S.; Hävecker, M.; Knop-Gericke, A.; Schlögl, R. The electronic structure of iridium and its oxides. *Surf. Interface Anal.* **2016**, *48*, 261–273.

(29) Kumar, A.; Ramani, V. Strong Metal–Support Interactions Enhance the Activity and Durability of Platinum Supported on Tantalum-Modified Titanium Dioxide Electrocatalysts. *ACS Catal.* **2014**, *4*, 1516–1525.

(30) White, R. E.; Bockris, J. O.; Conway, B. E. *Modern Aspects of Electrochemistry* **1986**, *18*.

(31) Pickup, P. G.; Birss, V. I. A model for anodic hydrous oxide growth at iridium. *J. Electroanal. Chem. Interfacial Electrochem.* **1987**, *220*, 83–100.

(32) El Sawy, E. N.; Birss, V. I. Nano-porous iridium and iridium oxide thin films formed by high efficiency electrodeposition. *J. Mater. Chem.* **2009**, *19*, 8244–8252.

(33) Marshall, A. T.; Haverkamp, R. G. Electrocatalytic activity of IrO<sub>2</sub>–RuO<sub>2</sub> supported on Sb-doped SnO<sub>2</sub> nanoparticles. *Electrochim. Acta* **2010**, *55*, 1978–1984.

(34) Oh, H.-S.; Nong, H. N.; Reier, T.; Glich, M.; Strasser, P. Oxide-supported Ir nanodendrites with high activity and durability for the oxygen evolution reaction in acid PEM water electrolyzers. *Chem. Sci.* **2015**, *6*, 3321–3328.

(35) Liu, G.; Xu, J.; Wang, Y.; Wang, X. An oxygen evolution catalyst on an antimony doped tin oxide nanowire structured support for proton exchange membrane liquid water electrolysis. *J. Mater. Chem. A* **2015**, *3*, 20791–20800.

(36) Reier, T.; Oezaslan, M.; Strasser, P. Electrocatalytic Oxygen Evolution Reaction (OER) on Ru, Ir, and Pt Catalysts. *ACS Catal.* **2012**, *2*, 1765–1772.

(37) Hu, J. Oxygen evolution reaction on IrO<sub>2</sub>-based DSA® type electrodes. *Int. J. Hydrogen Energy* **2004**, *29*, 791–797.

(38) Trasatti, S. Electrocatalysis in the anodic evolution of oxygen and chlorine. *Electrochim. Acta* **1984**, *29*, 1503–1512.

(39) Bockris, J. O. Kinetics of Activation Controlled Consecutive Electrochemical Reactions. *J. Chem. Phys.* **1956**, *24*, 817–827.

(40) Cherevko, S.; Reier, T.; Zeradjanin, A. R.; Pawolek, Z.; Strasser, P.; Mayrhofer, K. J. Stability of nanostructured iridium oxide electrocatalysts during oxygen evolution reaction in acidic environment. *Electrochem. Commun.* **2014**, *48*, 81–85.

(41) Reier, T.; Teschner, D.; Lunkenbein, T.; Bergmann, A.; Selve, S.; Kraehnert, R.; Schlögl, R.; Strasser, P. Electrocatalytic Oxygen Evolution on Iridium Oxide. *J. Electrochem. Soc.* **2014**, *161*, F876–F882.

(42) Xu, J.; Liu, G.; Li, J.; Wang, X. The electrocatalytic properties of an IrO<sub>2</sub>/SnO<sub>2</sub> catalyst using SnO<sub>2</sub> as a support and an assisting reagent for the oxygen evolution reaction. *Electrochim. Acta* **2012**, *59*, 105–112.

(43) Rossmeisl, J.; Qu, Z.-W.; Zhu, H.; Kroes, G.-J.; Nørskov, J. K. Electrolysis of water on oxide surfaces. *J. Electroanal. Chem.* **2007**, *607*, 83–89.

(44) Bernt, M.; Gasteiger, H. A. Influence of Ionomer Content in IrO<sub>2</sub>/TiO<sub>2</sub> Electrodes on PEM Water Electrolyzer Performance. *J. Electrochem. Soc.* **2016**, *163*, F3179–F3189.

(45) Spöri, C.; Briois, P.; Nong, H. N.; Reier, T.; Billard, A.; Kühl, S.; Teschner, D.; Strasser, P. Experimental Activity Descriptors for Iridium-Based Catalysts for the Electrochemical Oxygen Evolution Reaction (OER). *ACS Catal.* **2019**, *9*, 6653–6663.

(46) Suermann, M.; Schmidt, T. J.; Büchi, F. N. Comparing the kinetic activation energy of the oxygen evolution and reduction reactions. *Electrochim. Acta* **2018**, *281*, 466–471.

(47) Rasten, E.; Hagen, G.; Tunold, R. Electrocatalysis in water electrolysis with solid polymer electrolyte. *Electrochim. Acta* **2003**, *48*, 3945–3952.

## 5.3 OER Catalyst Stability Investigation Using RDE Technique: A Stability Measure or an Artifact?

The following section deals with the article “OER Catalyst Stability Investigation Using RDE Technique: A Stability Measure or an Artifact?”,<sup>115</sup> which was submitted to the *Journal of Electrochemical Society* in February 2019 and accepted for publication in April 2019 as an open access article distributed under the terms of the Creative Commons Attribution 4.0 License (CC BY). The study was presented by H.A.E.-S. at the 2018 MRS Fall Meeting in Boston, Massachusetts. The permanent web-link for the article is: <https://iopscience.iop.org/article/10.1149/2.0301908jes/pdf>

A commonly used method to assess the long-term stability of an OER catalyst from RDE measurements is the application of a constant current (e.g., 10 mAcm<sup>-2</sup><sub>disk</sub>). The observed gradual increase in potential, terminating in a sudden jump in potential (>2 V) is attributed to the degradation of the catalyst and thus to its stability. While in a PEM-WE catalysts operate stable with only a marginal loss in performance over ten thousands of hours, the stability obtained in an RDE setup is orders of magnitude lower. Within this study, an Ir/ATO catalyst was used to reveal the discrepancy of lifetimes measured by the RDE technique vs in an MEA.

Therefore, the stability of an 11.0 wt.-% Ir/ATO catalyst was analyzed using an RDE setup. By applying three different geometric current densities (mAcm<sup>-2</sup><sub>disk</sub>), the stability of the catalyst was assessed. At a higher current density, a more severe increase in potential was observed, and the final jump in potential occurred earlier (e.g., after ≈20 h for 5.50 mAcm<sup>-2</sup><sub>disk</sub> compared to ≈30 min for 27.5 mAcm<sup>-2</sup><sub>disk</sub>). The potential measured at the end of test (after the jump in potential) was similar to the one measured on a bare Au disk, meaning that no catalyst is left at the electrode surface or it is electrochemically not accessible. If the increase in potential were indeed related to the degradation of the catalyst, the severity should depend on the mass-specific current density (Ag<sup>-1</sup><sub>Ir</sub>). Therefore, the loading was changed while the mass-specific current density was kept constant. The results, however, showed that although the same mass-specific current was used, a lower loading and thus a lower geometric current density resulted in a higher apparent stability.

Considering these observations, the overall oxygen production rate (dependent on the geometric current density) and thus the formation of oxygen bubbles within the catalyst layer seems to influence the stability of the catalyst. An additional hint that the formation of oxygen bubbles is partially responsible for the rapid increase in potential is the fast decrease in performance

when cycling the electrode within the OER regime. However, after purging the electrolyte with Ar for 30 min, roughly 40% of the activity was regained. This suggests that during operation oxygen bubbles get trapped within the catalyst layer and lead to the shielding of active sites. To prove that the stability measurements using an RDE setup are falsified by the accumulation of oxygen bubbles, constant current measurements were performed, where a CV was recorded after a pre-defined increase in potential (e.g., 45 mV, which equals one Tafel slope value). In case the potential increase is related to catalyst degradation, after a potential increase by one Tafel slope suggests that only  $\approx 10\%$  of the catalyst should have remained on the surface of the electrode substrate (according to the Tafel equation). The CVs measured after a 30 min Ar purge, however, indicate that even after a potential increase corresponding to three TS values as well as after the potential jump occurred ( $>2$  V), there is still  $\approx 50\%$  of catalyst surface present on the electrode substrate. This confirms, that the accumulation of oxygen bubbles within the catalyst layer leads to the shielding of active sites, and thus to an increase in potential at the still accessible sites to provide the applied current. Ultimately, the local increase in potential results in the dissolution and degradation of the catalyst. If the accumulation of oxygen bubbles could be prevented, the thus induced degradation would be avoided.

In summary, this study showed that the commonly used technique to access the stability of an OER catalyst by RDE is not reliable, since it is influenced by trapped oxygen bubbles within the catalyst layer and the thus induced shielding of active catalyst surface area.

### **Author contributions**

Fabrication of catalyst inks and electrochemical testing in RDE was performed by L.F.O., G.P.P. and H.A.E.-S.. Analysis of the experimental test results was done by L.F.O. and H.A.E.-S. A.W. and H.A.E.-S. supervised the students L.F.O. and G.P.P. H.A.E.-S. wrote the manuscript that was edited by H.A.G. All authors discussed the experimental results and revised the manuscript.





## OER Catalyst Stability Investigation Using RDE Technique: A Stability Measure or an Artifact?

Hany A. El-Sayed,<sup>\*,z</sup> Alexandra Weiß,<sup>\*</sup> Lorenz F. Olbrich, Garin P. Putro, and Hubert A. Gasteiger<sup>\*\*</sup>

Chair of Technical Electrochemistry, Technical University of Munich, D-85748, Garching, Germany

The rotating disk electrode (RDE) technique was frequently used for investigating the stability of oxygen evolution reaction (OER) catalysts under galvanostatic conditions, where the increase in potential is reported to be due to catalyst degradation. The galvanostatic RDE stability test typically results in catalyst life-time of several hours, although the same catalyst can last for thousands of hours in a PEM electrolyzer under similar conditions, a discrepancy that is still unresolved. In this work, we present a careful examination of the use of the RDE technique as a tool for the investigation of the OER catalyst stability. Our findings provide a clear evidence that the change in potential during the stability test is not related at all to catalyst degradation, but is rather due to an experimental artifact caused by nano- and micro-bubbles formed within the pores of the catalyst layer during the OER, which cannot be removed by electrode rotation. Instead, they accumulate and shield the OER active sites from the electrolyte, resulting in an increase of the potential, which is mistakenly interpreted as catalyst degradation in previous literature. Thus, reliable OER catalyst stability tests other than testing in a real electrolyzer cell still needs to be designed.

© The Author(s) 2019. Published by ECS. This is an open access article distributed under the terms of the Creative Commons Attribution 4.0 License (CC BY, <http://creativecommons.org/licenses/by/4.0/>), which permits unrestricted reuse of the work in any medium, provided the original work is properly cited. [DOI: 10.1149/2.0301908jes]



Manuscript submitted February 14, 2019; revised manuscript received April 1, 2019. Published April 23, 2019.

The development of oxygen evolution reaction (OER) catalysts for polymer electrolyte membrane water electrolysis (PEMWE) requires the use of reliable methods for both activity and stability testing. To date, IrO<sub>x</sub>-based materials, state-of-the-art catalysts for OER in acidic media, have been optimized for the highest OER activity through controlling catalyst morphology and the type of the oxide support.<sup>1-5</sup>

It is very well-established that the OER catalyst activity can be reliably estimated by using rotating disk electrode (RDE) or flow-channel methods in half-cells or by full-cell testing in an electrolyzer.<sup>6-12</sup> On the other hand, the evaluation of OER catalyst stability over the whole lifetime under realistic conditions is not practical, as the current industrial life-time targets are five to ten years.<sup>13</sup> Therefore, accelerated degradation tests using cells with liquid electrolyte or actual proton exchange membrane (PEM) electrolyzer are performed in order to carry out comparative stability studies of various catalysts.<sup>14-19</sup> A protocol for the OER catalyst stability using RDE was proposed by the Joint Center for Artificial Photosynthesis (JCAP) group and is now frequently used by other research groups.<sup>20</sup> In this protocol, OER catalyst stability is determined using galvanostatic electrolysis, where a constant current (e.g., 10 mA/cm<sup>2</sup><sub>disk</sub>) is applied in a RDE configuration at a constant rotation rate of 1600 RPM and the change in potential as a function of time is monitored for a few hours.<sup>20</sup> The increase of the potential during the test is considered as an evidence of catalyst “deactivation”, while a steady potential indicates a stable catalyst. The authors indicated that this stability protocol does not distinguish between the various mechanisms of catalyst deactivation; like corrosion, material degradation, or surface passivation.

This protocol was then used by other researchers to compare the stability of their developed OER catalysts against reference materials. For example, Oh et al. reported the enhanced stability of antimony-doped tin oxide (ATO)-supported Ir nanodendrites (ND) over all of their investigated reference catalysts, including carbon-supported Ir nanoparticles, Ir-black, Ir-ND, and Ir-ND/C.<sup>21</sup> The authors reported that when a constant current density of 10 mA/cm<sup>2</sup><sub>disk</sub> is applied on all of the catalysts, all reference materials showed a gradual increase of the potential as a function of time, followed by a sudden potential jump, which the authors considered an indication of complete catalyst degradation.<sup>21</sup> Only Ir-ND/ATO showed a very small increase in potential for 15 hours without any potential jump, suggesting the superior stability of this catalyst compared to the refer-

ence materials.<sup>21</sup> Using the same protocol, Oh et al. reported another study on the existence of the strong metal-support interaction (SMSI) in IrO<sub>x</sub>/ATO (compared to IrO<sub>x</sub>/C).<sup>18</sup> In that study, the absence of a potential jump over 15 hours of testing in case of IrO<sub>x</sub>/ATO and the observation of a potential jump after 10 hours for IrO<sub>x</sub>/C was interpreted by the authors to indicate a superior stability of IrO<sub>x</sub>/ATO vs. IrO<sub>x</sub>/C, which may attribute to the SMSI effects. Wang et al. also used the same approach and concluded on the superior stability of their developed aerogel catalyst (Ir/SnO<sub>2</sub>:Sb-mod-V) over conventional catalysts, again using the potential jump as an indication of full catalyst degradation.<sup>22</sup> Zhang et al. reported the stability test of Ir catalyst anchored on 3D graphite foam using the same RDE stability protocol, where no potential jump was observed up to 10 hours for the developed catalyst, with no comparison to any reference material.<sup>23</sup>

Geiger et al. noticed that the galvanostatic RDE stability test overlooks many aspects and that the catalyst life-time defined by the potential jump is inconsistent with stability results from a PEM electrolyzer, in which a catalyst can be stable under similar operating conditions (current density, pH, temperature, etc.) for ten thousands of hours. The discrepancy indicates that this RDE stability test may have some limitations.<sup>13</sup> Furthermore, they showed that the catalyst life-time, measured by RDE, depends on the nature of the electrode substrate on which the catalyst powder is being supported. Specifically, it was suggested that the potential jump, used as an indicator of full catalyst degradation, is actually due to glassy carbon passivation, making the catalyst no longer electrochemically accessible due to the high contact resistance, ultimately leading to the sudden potential jump. Consequently, other electrode substrates were tested to avoid materials that passivate at high potential, and it was recommended that gold and boron-doped diamond should be used as they show better stability of the catalyst under investigation, while glassy carbon and fluorine-doped tin oxide electrodes were deemed unsuitable for such stability tests.<sup>13</sup> Although Geiger et al. found that the potential jump depends on the electrode substrate, the results still do not explain the inconsistency between stability results from an electrolyzer and those from an RDE test.

In general, the potential increase during a galvanostatic RDE stability test can result from passivation of the RDE electrode substrate, from catalyst degradation (dissolution), from physical detachment of catalyst material or from the accumulation of oxygen bubbles. In this study, a homemade iridium catalyst supported on antimony-doped tin oxide (ATO), recently reported to provide extremely high OER activity,<sup>8</sup> is used to identify the main cause for the potential increase in a galvanostatic stability test and to conclude whether the galvanostatic RDE

\*Electrochemical Society Student Member.

\*\*Electrochemical Society Fellow.

<sup>z</sup>E-mail: hany.el-sayed@tum.de



stability test is a reliable technique to determine the stability of OER catalysis.

### Experimental

**ATO support synthesis.**—Following the procedure developed by Beyer et al., antimony-doped tin oxide (ATO) with a molar Sb:Sn ratio of 5:95 is prepared in an open 100 ml autoclave with a PTFE liner (HighPreactor BR-100, Berghof), where 30.0 ml concentrated HNO<sub>3</sub> (69 wt%, puriss. p.a., Sigma Aldrich) are added to 50.0 ml deionized water. 2.0 g tin (16.9 mmol, Sn, granulates, 0.425–2.0 mm, ≥ 99.5%, ACS reagent, Sigma Aldrich) and 130 mg antimony(III) oxide powder (0.440 mmol, Sb<sub>2</sub>O<sub>3</sub>, nanopowder, < 250 nm, ≥ 99.9%, Sigma Aldrich) are added at once to the acidic solution under vigorous stirring.<sup>30</sup> After 10 minutes, the autoclave is sealed and heated to 140°C at a heating rate of 2°C/min. This temperature is held for 10 h, followed by cooling the reaction mixture passively to room temperature. A bluish powder is obtained and separated from the liquid phase by centrifugation. The powder is washed thoroughly with deionized water until the washing water reaches pH 6. After the final washing step with ethanol, the powder is dried overnight in static air at 70°C. The resulting dry powder is calcined in a tube furnace (Carbolite) in a gas flow of 20% O<sub>2</sub> in Ar (both 5.0-grade, Westfalen) with a flow rate of 400 ml/min. The samples are heated to 600°C at 5°C/min and held at 600°C for 3 h. After passive cool down to room temperature in the furnace, the calcined samples are ground in a planetary ball mill (Pulverisette 7 Premium Line, Fritsch) in order to break up the formed agglomerates during calcination. In this process, ca. 2 g of ATO are suspended in 6 ml isopropanol and filled into a 45 ml ZrO<sub>2</sub> milling jar containing 20 ZrO<sub>2</sub> balls (Ø 10 mm). Six milling cycles of 10 min each and 1 min pause between the cycles are conducted at 200 rpm. Again, the product is separated by centrifugation and dried overnight at 70°C in static air.

**Synthesis of Ir nanoparticles.**—The polyol synthesis setup consists of a 100 ml three-neck flask with magnetic stirrer placed in a heating mantle (WHG 2, Winkler), equipped with a reflux condenser, a thermometer, and a temperature controller (Model 310, J-KEM Scientific). Additionally, there is a glass capillary, which is connected to a high purity argon supply (5.0-grade, Westfalen). The whole system is sealed off with septa. In a typical polyol synthesis, 183 mg dihydrogen hexachloroiridate(IV) hydrate (0.450 mmol, H<sub>2</sub>IrCl<sub>6</sub> × H<sub>2</sub>O, 99.98%, trace metal basis, Sigma Aldrich) are dissolved in 10 ml ethylene glycol (EG, 99.8%, anhydrous, Sigma Aldrich) in a small vial at room temperature under vigorous stirring. After complete dissolution, the solution is transferred into a three-neck flask with another 80 ml of ethylene glycol. The total iridium concentration is 5 · 10<sup>-3</sup> mol/l in a total volume of 90 ml. The solution is purged with argon for 60 min in order to minimize the O<sub>2</sub> content before heating. During heating, the solution is stirred moderately (at approx. 500 RPM) under argon. The solution is heated up to 140°C at a heating rate of approx. 2°C/min, where it is held for one hour, after which time the reaction mixture is allowed to cool down to room temperature.

**Preparation of ATO-supported iridium catalysts.**—The prepared iridium nanoparticles are slowly added to the ATO suspended in 35 ml ethylene glycol by sonication for at least 30 min. The reaction mixture is stirred at 500 RPM at room temperature under air for three days until all the nanoparticles are deposited on the ATO. Afterwards, the prepared catalyst is separated via centrifugation at 11500 RPM and 5°C, and washed twice with isopropanol with 5 min sonication in between the centrifugation steps. The obtained black powder is dried at 70°C in static air overnight. The morphology and composition of the final catalyst was confirmed using transmission electron microscopy (Philips CM100 EM) and energy dispersive X-ray analysis (JCM-6000Plus from JEOL).

**Electrochemical setup and measurement procedure.**—The electrochemical measurements (cyclic voltammetry, galvanostatic polar-

ization, and electrochemical impedance spectroscopy (EIS)) were performed in a glass three-electrode electrochemical cell. A reversible hydrogen electrode (RHE) and a high surface area Au wire were used as reference and counter electrodes, respectively. The RHE reference electrode was either directly connected to the cell or via a Luggin capillary. Rotating ring-disk electrodes (RRDEs) with a 5 mm diameter polycrystalline gold (Au) electrode and a Pt ring supported by a PTFE-body (Pine Research Instrumentation, USA) were used as working electrodes. The reference potential was calibrated in H<sub>2</sub>-saturated electrolyte prior to every experiment using the platinum ring of the RRDE and all potentials in this publication are given with respect to RHE.

Electrolyte solutions were prepared from high purity H<sub>2</sub>SO<sub>4</sub> (Ultrapur, 96%, Merck Millipore KGaA, Germany) by addition of ultrapure water (18.2 MΩ·cm at 20°C, Merck Millipore KGaA, Germany). Ar, O<sub>2</sub>, and H<sub>2</sub> used for purging of the electrolyte were of high purity (6.0-grade, Westfalen AG).

Electrochemical measurements were performed using an Autolab potentiostat (PGSTAT302N, Metrohm AG) and a rotator (Pine Research Instrumentation) with a polyether ether ketone shaft. Prior to any electrochemical measurements, a cyclic voltammogram of the gold working electrode was recorded in the supporting electrolyte to verify the cleanliness of the Au disk and the cell. Afterwards, the electrode was removed, dried, and coated with the catalyst ink that was allowed to dry under a low flow of nitrogen.

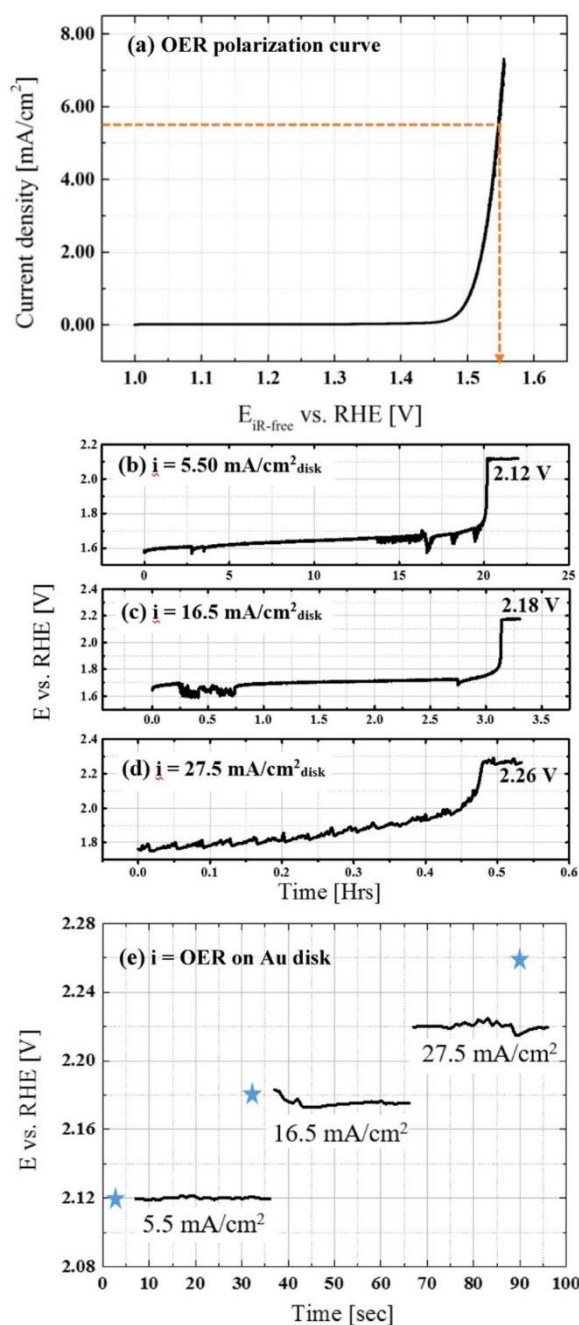
The coated electrode was then dipped into the Ar-purged electrolyte and the electrolyte resistance between reference and working electrode was determined by EIS from 100 kHz to 100 Hz at open circuit potential (OCP) with an amplitude of 10 mV. The potential was then cycled at least 20 times between 0.05 and 1.45 V RHE at 100 mV/s to convert all metallic iridium into (hydrated) iridium oxide. Afterwards, the electrolyte solution was replaced by fresh 0.1 M H<sub>2</sub>SO<sub>4</sub> and saturated with O<sub>2</sub>. After fully saturating the electrolyte with O<sub>2</sub>, polarization curves were recorded from 1.2 V<sub>RHE</sub> to 1.7 V<sub>RHE</sub> at 10 mV/s at a rotation rate of 2500 RPM. Galvanostatic experiments were carried out directly after the linear polarization curves, whereby a constant current density was applied and the resulting potential was recorded over time.

**Electrode and ink preparation.**—Prior to every measurement, the Au working electrode was polished with 0.3 μm Al<sub>2</sub>O<sub>3</sub> polishing suspension (Buhler AG) and sonicated various times in ultrapure water. Inks were prepared by adding ultrapure water to the dry catalyst (11 wt% Ir/ATO) to obtain a catalyst ink concentration of 1 mg<sub>Cat</sub>/1 ml. The catalyst suspension was sonicated for 30 min in a sonication bath (Elmasonic S 30 H, Elma Schmidbauer GmbH) to achieve a homogeneous dispersion. The temperature of the bath was maintained at less than 35°C to avoid evaporation of the solvent. No polymeric binder was added to the catalyst suspension.

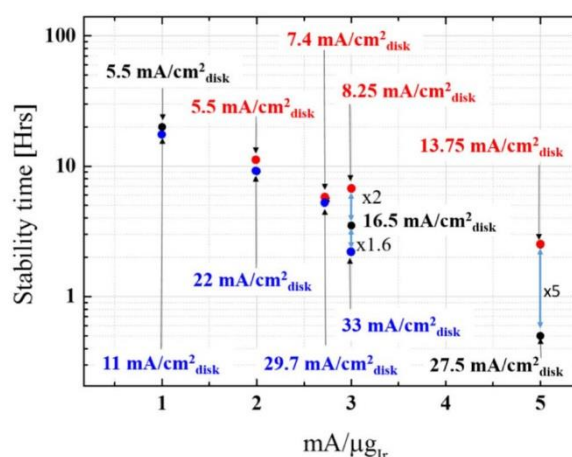
### Results and Discussion

Fig. 1a shows a typical OER polarization curve (iR-corrected) of 11 wt% Ir/ATO catalyst (deposited on a gold disk) in O<sub>2</sub>-saturated 0.1M H<sub>2</sub>SO<sub>4</sub> solution at 20 mV/s and 2500 RPM, while Fig. 1b shows a galvanostatic stability test obtained by applying a mass-specific current density of 1 mA/μg<sub>Ir</sub> for a catalyst loading of 5.50 μg<sub>Ir</sub>/cm<sup>2</sup><sub>disk</sub> (equivalent to 5.50 mA/cm<sup>2</sup><sub>disk</sub>) for several hours. It can be seen that the starting potential (1.57 V) of the potential-time transient at 5.50 μg<sub>Ir</sub>/cm<sup>2</sup><sub>disk</sub> (see Fig. 1b) fits reasonably well with the potential obtained at the same current density (1.55 V) for a conventional RDE experiment (see orange line in Fig. 1a). The potential gradually increases with time, which according to the literature indicates a degradation of the catalyst layer until its complete degradation once the potential jump is observed. At that point, a constant potential of ca. 1.12 V is observed, most likely due to the OER taking place solely on the Au substrate after catalyst degradation. The catalyst was found to be stable for 20 hours under these conditions, but when the applied current density was increased from 5.50 to 16.5 mA/cm<sup>2</sup><sub>disk</sub>





**Figure 1.** OER polarization curve (20 mV/s) (a) and galvanostatic stability transients at (b)  $5.50 \text{ mA/cm}^2_{\text{disk}}$ , (c)  $16.5 \text{ mA/cm}^2_{\text{disk}}$ , and (d)  $27.5 \text{ mA/cm}^2_{\text{disk}}$  for an 11 wt% Ir/ATO catalyst in O<sub>2</sub>-saturated 0.1 M H<sub>2</sub>SO<sub>4</sub> at 2500 RPM and 25°C. Catalyst loading is  $5.50 \mu\text{g}_{\text{Ir}}/\text{cm}^2_{\text{disk}}$  on a polycrystalline Au electrode. (e) Potential at different current densities obtained under the same conditions for a polycrystalline Au disk without catalyst, with the blue asterisks indicating the potential obtained after the potential jump in (b-d).



**Figure 2.** Effect of catalyst loading ( $2.75 \mu\text{g}_{\text{Ir}}/\text{cm}^2_{\text{disk}}$  (red dots),  $5.50 \mu\text{g}_{\text{Ir}}/\text{cm}^2_{\text{disk}}$  (black dots), and  $11.0 \mu\text{g}_{\text{Ir}}/\text{cm}^2_{\text{disk}}$  (blue dots)), and mass-specific current density on catalyst stability.

(i.e., from 1 to 3 mA/ $\mu\text{g}_{\text{Ir}}$ ), the catalyst was stable for only 3.5 hours as shown in Fig. 1c. Increasing the applied current even further to  $27.5 \text{ mA/cm}^2_{\text{disk}}$  (i.e., to 5 mA/ $\mu\text{g}_{\text{Ir}}$ ), the catalyst was stable for only 30 min (see Fig. 1d). In all cases, the overall behavior is the same: first, a gradual increase in potential, followed by a potential jump and a final potential plateau. To confirm that the final potential plateaus are indeed due to the OER on the Au substrate, the same current densities ( $5.50$ ,  $16.5$ , and  $27.5 \text{ mA/cm}^2_{\text{disk}}$ ) were applied to the Au electrode in the absence of any catalyst, and the corresponding potentials (black lines in Fig. 1e) were compared to the final potential plateaus (indicated by blue stars in Figs. 1e). The reasonably close agreement between these potential values confirms that after the potential jump there either is no catalyst remaining on the electrode substrate or that the catalyst becomes electrically completely disconnected from the Au surface and therefore electrochemically inaccessible.

These results so far suggest that when the catalyst loading on the disk is kept constant ( $5.50 \mu\text{g}_{\text{Ir}}/\text{cm}^2_{\text{disk}}$  in this case), the larger the applied current, the higher is the catalyst degradation rate, which supports the results reported in the literature where the OER stability test is mostly considered a suitable tool to quantify OER catalyst stability. If this were to be correct and if the potential increase is indeed due to catalyst degradation, then the degradation rate for a specific catalyst should be dependent only on the applied mass-specific current density (current per OER active site) and not on the geometric current density. This, however, cannot be confirmed by the results shown in Figs. 1a–1d, as both mass-specific current density and geometric current density vary simultaneously.

To deconvolute the effects of geometric ( $\text{mA/cm}^2_{\text{disk}}$ ) and mass-specific ( $\text{mA}/\mu\text{g}_{\text{Ir}}$ ) current densities, the catalyst loading on the disk was changed ( $2.75$ ,  $5.50$ , and  $11.0 \mu\text{g}_{\text{Ir}}/\text{cm}^2_{\text{disk}}$ ) while fixing the mass-specific current density by varying the geometric current density. This should result in the same stability time, if the degradation rate is dependent only on the mass-specific current density. Surprisingly, Fig. 2 shows that when the catalyst loading on the disk was changed from  $5.50 \mu\text{g}_{\text{Ir}}/\text{cm}^2_{\text{disk}}$  (black dots) to  $2.75 \mu\text{g}_{\text{Ir}}/\text{cm}^2_{\text{disk}}$  (red dots), a 5-fold increase in the stability was obtained when a constant current of 5 mA/ $\mu\text{g}_{\text{Ir}}$  was applied. Decreasing the catalyst loading while maintaining the applied mass-specific current density results in a lower geometric current density, therefore decreasing the overall rate of O<sub>2</sub> production. This may indicate that the created oxygen bubbles are somehow influencing the stability time by shielding the OER active sites from the electrolyte, where a lower O<sub>2</sub> evolution rate seems to result in a longer stability time (see Fig. 2). The same behavior was observed for 3 mA/ $\mu\text{g}_{\text{Ir}}$ , where the catalyst loading on the disk



was decreased from  $5.50 \mu\text{g}_{\text{Ir}}/\text{cm}^2_{\text{disk}}$  (black dots) to  $2.75 \mu\text{g}_{\text{Ir}}/\text{cm}^2_{\text{disk}}$  (red dots), leading to a two-fold increase in the stability time for the lower catalyst loading. Increasing the catalyst loading on the disk from  $5.50 \mu\text{g}_{\text{Ir}}/\text{cm}^2_{\text{disk}}$  (black dots) to  $11.0 \mu\text{g}_{\text{Ir}}/\text{cm}^2_{\text{disk}}$  (blue dots), while applying the same mass-specific current density of  $3 \text{ mA}/\mu\text{g}_{\text{Ir}}$  resulted in a 1.6-fold decrease of the stability time, again showing higher stability for a lower catalyst loading. The influence of the catalyst loading at constant mass-specific current density on the stability time decreased from  $5 \text{ mA}/\mu\text{g}_{\text{Ir}}$  to  $3 \text{ mA}/\mu\text{g}_{\text{Ir}}$ , which is most likely due to the decrease in the  $\text{O}_2$  evolution rate. When the  $\text{O}_2$  evolution rate (i.e., the geometric current density) was further decreased by applying  $2.75 \text{ mA}/\mu\text{g}_{\text{Ir}}$  using loadings of either  $2.75 \mu\text{g}_{\text{Ir}}/\text{cm}^2_{\text{disk}}$  (red dots) or  $11.0 \mu\text{g}_{\text{Ir}}/\text{cm}^2_{\text{disk}}$  (blue dots), no significant change in stability time was observed. This was also observed for mass-specific current densities of  $1 \text{ mA}/\mu\text{g}_{\text{Ir}}$  and  $2 \text{ mA}/\mu\text{g}_{\text{Ir}}$ , suggesting that the influence of the evolved  $\text{O}_2$  bubbles on the stability time is much smaller at low mass-specific current densities, which generally means at low catalyst loadings or of low geometric current densities. If the  $\text{O}_2$  bubbles formed during the galvanostatic RDE-based OER stability test are at least partially responsible for the potential increase, they should have a similar effect on the linear scan polarization curves of the catalyst during OER activity determination, i.e., the activity should decrease as a function of the cycle number due to the gradual accumulation of oxygen bubbles.

Figure 3a shows mass-specific OER polarization curves (iR-corrected) of 11 wt% Ir/ATO catalyst (deposited on a Au electrode) in  $\text{O}_2$ -saturated  $0.1 \text{ M H}_2\text{SO}_4$  at  $10 \text{ mV/s}$ ,  $25^\circ\text{C}$ , and  $2500 \text{ RPM}$ , where it can be seen that the OER currents decrease upon potential cycling ( $1.4 - 1.55 \text{ V}_{\text{RHE}}$ ). This decrease cannot be attributed to the passivation of the Au disk substrate, as Au passivation at the upper scan potential of  $1.7 \text{ V}$  is limited to a monolayer of Au oxide,<sup>24</sup> which does not impose a significant resistance. The physical detachment of the catalyst material is also excluded, as it usually would result in a sudden and arbitrary decrease in the current upon cycling, which was not observed here. Thus, the gradual decrease of the OER current upon potential cycling is either due to catalyst degradation or due to the gradual accumulation of oxygen gas bubbles within the pores of the catalyst layer, thereby blocking electrolyte access to a fraction of the OER active sites.

To distinguish between these two possibilities, the RDE setup was purged with Ar for 30 min directly after the OER testing (Fig. 3a) while switching the electrode to OCP (open circuit potential), then this was followed by taking another polarization curve under  $\text{O}_2$  atmosphere. This experiment is designed based on the assumption that during the OER, oxygen bubbles are formed on the catalyst layer surface as well as within the pores of the layer. While the nano- and micro-bubbles that form inside the catalyst layer can obviously not be removed by convection (i.e., rotation), contrary to the macro-bubbles that are formed on top of the catalyst layer and can be removed by convection, they could be removed by oxygen diffusion into the bulk of the electrolyte. However, even if the OER experiment were carried out under Ar atmosphere, the electrolyte in the vicinity of the catalyst layer would be saturated with  $\text{O}_2$  produced by the OER, so that removal of  $\text{O}_2$  bubbles via dissolution and diffusion cannot occur. On the other hand, once the electrode is put into OCP and once the RDE setup is purged with Ar,  $\text{O}_2$  bubbles can be removed via dissolution and diffusion. This effect is explored in the experiments shown in Fig. 3. In Fig. 3a, the potential control was stopped and the electrode was kept under OCP, while the solution was purged with Ar at  $2500 \text{ RPM}$ . If the accumulation of bubbles were the main cause for the “apparent degradation”, some or all (depending on time) of the oxygen should be removed from the catalyst layer by diffusion. Fig. 3b shows three polarization curves, initial (2<sup>nd</sup> cycle), after 30 cycles, and after Ar purging, all recorded under  $\text{O}_2$  atmosphere. It can be clearly seen that Ar purging recovers part of the activity lost after 30 cycles. For example, at  $1.5 \text{ V}_{\text{RHE}}$ , the initial OER activity was found to be  $172 \text{ A/g}_{\text{Ir}}$  (black line in Fig. 3b), and decreased to  $88 \text{ A/g}_{\text{Ir}}$  after 30 cycles (blue line in Fig. 3b), i.e., ca 50% of the OER activity was lost. After Ar purging for 30 min, the OER activity recovered to  $122 \text{ A/g}_{\text{Ir}}$  (red line in Fig. 3b), i.e., 40% of the lost activity was regained. These results suggest that the nano- and

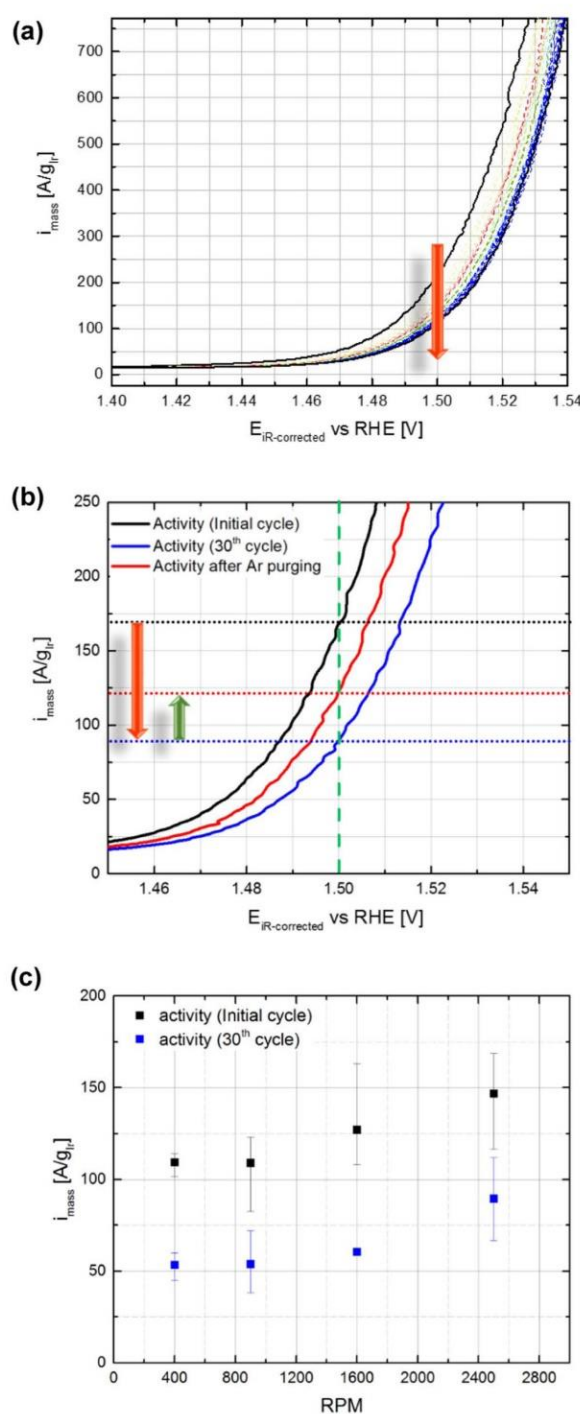


**Figure 3.** Mass-specific OER polarization curves (iR-corrected) of the 11 wt% Ir/ATO catalyst (deposited on a Au electrode) in  $\text{O}_2$ -saturated  $0.1 \text{ M H}_2\text{SO}_4$  at  $10 \text{ mV/s}$ ,  $25^\circ\text{C}$ , and  $2500 \text{ RPM}$ . The catalyst loading was  $22.4 \mu\text{g}_{\text{Ir}}/\text{cm}^2_{\text{disk}}$ , and the potential was cycled between  $1.2$  and  $1.7 \text{ V}$  vs. RHE (a) for 30 cycles, and (b) before (initial and 30<sup>th</sup> cycle) and after Ar purging for 30 min at OCP. (c) Effect of RPM on the OER mass-specific activities measured at  $1.5 \text{ V}_{\text{RHE}}$  from initial and 30<sup>th</sup> cycles.



micro-bubbles within the pores of the catalyst layer are responsible for the current decrease during potential cycling.

To examine the hypothesis of the blockage by O<sub>2</sub> bubbles, the OER polarization curves were measured at 400–2500 RPM and the current decay (at 1.5 V<sub>RHE</sub>) as a function of potential cycle number was observed. Each rotation speed was studied using a freshly catalyst-coated Au electrode, where a catalyst loading of 22.4 μg<sub>Ir</sub>/cm<sup>2</sup><sub>disk</sub> was used. Fig. 3c shows that the OER activity determined at 1.5 V<sub>RHE</sub> from the initial cycle depends on the rotation rate where it decreases by decreasing the rotation rate. This clearly indicates that the accumulation of bubbles within the porosity of the catalyst layer occurs from the very beginning of the experiment and that its effect on OER activity can be even observed at the initial cycle. The same behavior was also observed for OER activities determined from the 30<sup>th</sup> cycle, where the highest OER activity was reported at 2500 RPM (ca. 83 A/g<sub>Ir</sub>), which is about 50% of that reported at the same RPM from the initial cycle (ca. 150 A/g<sub>Ir</sub>).

To verify whether the accumulation of O<sub>2</sub> bubbles within the pores of the catalyst layer is responsible for the typical potential increase during a galvanostatic stability test, the Ir/ATO catalyst was subjected to a constant OER current and the experiment was stopped once a pre-defined potential increase was reached. This experiment is based on the assumption that if the potential increase over galvanostatic aging were mainly due to catalyst degradation, as suggested by many researchers in the literature, the correlation between the measured potential increase and the available OER active sites would have to be consistent with the Tafel equation. And hence, the available active surface area of the catalyst over the course of the experiment, i.e., the roughness factor (*rf*) of the catalyst layer supported on the RDE substrate (in units of cm<sup>2</sup><sub>cat</sub>/cm<sup>2</sup><sub>disk</sub>), would have to be directly correlated to the kinetic OER overpotential ( $\eta$ , given in mV):

$$\eta = TS \cdot \log\left(\frac{i}{i_0}\right) - TS \cdot \log(rf) \quad [1]$$

where, *TS* is the Tafel slope in mV/dec, *i* is the geometric OER current density in mA/cm<sup>2</sup><sub>disk</sub>, and *i*<sub>0</sub> is the exchange current density of the catalyst for the OER in mA/cm<sup>2</sup><sub>cat</sub>. Since in the galvanostatic aging test the current density *i* is constant, as is the catalyst exchange current density *i*<sub>0</sub>,  $\eta$  would only depend on the effective roughness factor *rf* as described by the second term on the right-hand-side of equation 1. The roughness factor, in turn, could decrease by catalyst dissolution or by the ionic disconnection of the catalyst by trapped O<sub>2</sub> bubbles.

For example, for a potential increase that is equivalent to one Tafel slope (TS), there should be a corresponding 10-fold decrease in the number of OER active sites (i.e., a 10-fold decrease of the *rf*). As the TS of Ir/ATO catalysts has been reported to be around 45 mV/dec,<sup>8</sup> the galvanostatic stability test was designed in a way to allow the potential to increase by one TS (45 mV) from the starting potential. The system was then purged with Ar under OCP for 30 min to allow O<sub>2</sub> bubbles to diffuse away from the pores of the catalyst layer, while maintaining the 2500 RPM rotation, and then a CV was measured under Ar and compared to the pristine CV. This approach was applied after different potential increases of 1x TS (45 mV), 2x TS (90 mV), 3x TS (135 mV), and after the potential jump was observed. Each potential increase experiment was conducted using a freshly prepared electrode with an identical loading of 11.2 μg<sub>Ir</sub>/cm<sup>2</sup><sub>disk</sub>. In all cases, the CV obtained under Ar after the stability test was compared to that before the stability test. Fig. 4a shows that, when a constant current density of 11.2 mA/cm<sup>2</sup><sub>disk</sub> is applied (corresponding to 1 mA/μg<sub>Ir</sub>), an initial potential of 1.6 V<sub>RHE</sub> was reproducibly obtained for all measurements and that the same gradual increase in potential with time was observed for all samples. Fig. 4b shows all CVs collected after a 30 min of Ar purging at OCP carried out directly after a given potential increase was reached; a CV of the pristine catalyst is given for reference. If the gradual change in potential were mainly due to catalyst degradation, an increase in potential of one TS should result in a 10-fold loss of catalyst surface area, i.e., in a 10-times smaller CV compared to the pristine CV. Analogously, for potential increases correspond-

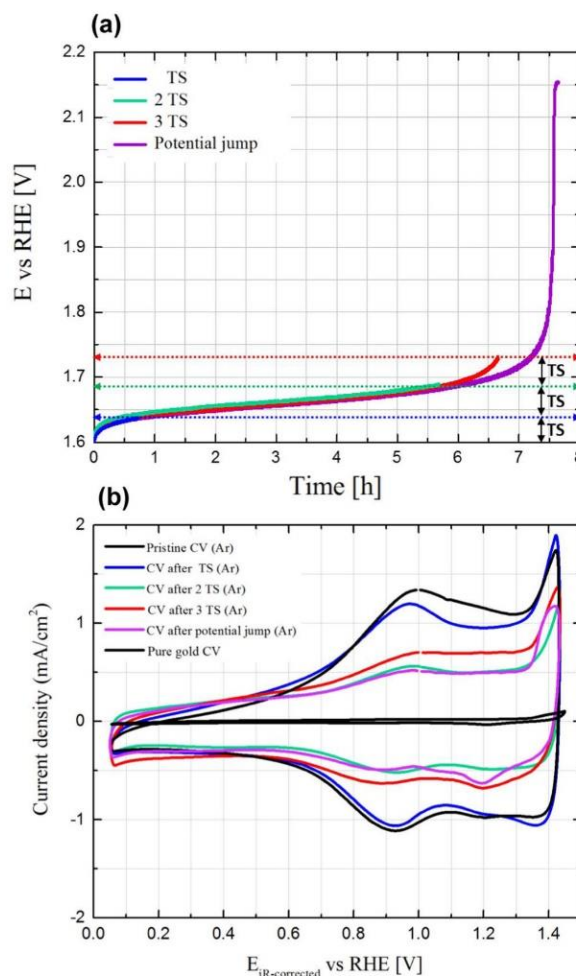


**Figure 4.** (a) Potential evolution vs. time in galvanostatic stability tests at 11.2 mA/cm<sup>2</sup><sub>disk</sub> and 2500 RPM for 11 wt% Ir/ATO catalyst in O<sub>2</sub>-saturated 0.1 M H<sub>2</sub>SO<sub>4</sub> with catalyst loading of 11.2 μg<sub>Ir</sub>/cm<sup>2</sup><sub>disk</sub> (≡ 1 mA/μg<sub>Ir</sub>) until the potential has increased to 45 mV (≡ TS; blue line), 90 mV (≡ 2 TS; green line), 135 mV (≡ 3TS; red line), and to its final value after the potential jump (by roughly 550 mV). A fresh catalyst sample was used for each experiment. (b) Corresponding CVs after the stability tests and after 30 min hold at OCP under Ar at 2500 RPM, taken in Ar-saturated 0.1 M H<sub>2</sub>SO<sub>4</sub> at 100 mV/s at 0 RPM.

ing to 2x TS or 3x TS, only 1% or 0.1% of the catalyst surface area should be remaining after the stability test, and therefore their corresponding CVs should be 100- or 1000-times smaller than the pristine CV. After the potential jump, no active catalyst surface area should be left, and only the characteristic CV of the gold substrate should be obtained. However, Fig. 4b clearly shows that all CVs exhibit the main set of redox peaks centered at around 0.95 V, which is due to the Ir<sup>3+</sup>/Ir<sup>4+</sup> redox reaction. Surprisingly, none of the CVs shows the surface area loss which would be expected if the potential gain during the galvanostatic aging test were due to catalyst degradation/dissolution. Specifically, the CV obtained after a potential increase of one TS (blue line in Fig. 4b) would be expected to be an order of magnitude smaller than that of the pristine CV (black line in Fig. 4b). In fact, the results clearly show that there is almost no loss of catalyst surface area observed in this case, as the CVs are almost identical. By the same argument, the CVs obtained after potential increases corresponding to 2 TS and 3TS values could be expected to be two and three orders of



magnitude smaller than that of the pristine CV, respectively. However, they are only ca. 50% smaller than the initial CV. In addition, even the CV obtained after the potential jump shows that ca. 50% of the catalyst surface area of the pristine catalyst is still remaining. These results clearly show that the potential increase during the galvanostatic stability test has nothing to do with catalyst surface area loss due to degradation/dissolution, and that the apparent OER activity loss is mainly due to an artifact of O<sub>2</sub> bubbles accumulating in the pores of the catalyst layer. The displacement of electrolyte within/near the catalyst layer by evolved oxygen apparently leads to a loss of ionic contact and thus to a substantial reduction of the effective active surface area, concomitant with an increase in OER overpotential. Nano- and micro-bubbles formed within/near the catalyst layer cannot be removed by rotation, unless they coalesce at the catalyst layer surface from where they can be removed into the bulk of the electrolyte by forced convection. In summary, our data suggest that the increase of the potential in galvanostatic RDE-based stability test is primarily due to a shielding of the majority of the catalyst surface area by evolved O<sub>2</sub> gas rather than due to catalyst degradation/dissolution. Once essentially all of the OER active sites are ionically disconnected by trapped oxygen, the observed potential jump will occur.

A remaining question is why different OER catalysts exhibit different “apparent” stability times in the RDE-based galvanostatic stability test, even in cases where the same catalyst loading and the same geometric current density were used.<sup>13,21,25</sup> While under these nominally identical testing conditions the rate of O<sub>2</sub> evolution is the same, the fraction of the nano- and micro-bubbles accumulating in the porous layer still depends on additional material-specific parameters. These include: i) catalyst layer thickness that depends on the active material (e.g., iridium) packing density; ii) porosity of the catalyst layer (pore size, volume, and connectivity) that depends on catalyst morphology; iii) hydrophobic/hydrophilic properties of the catalyst (i.e., the active material and the support); and, iv) adhesion of the catalyst to the RDE substrate (e.g., gold). Therefore, different catalysts may exhibit different stability times in the RDE-based galvanostatic stability test as long as they are different in at least one of the above listed properties.

Our data undoubtedly explain the inconsistency between stability results from catalysts tested in MEAs (membrane electrode assemblies) in PEM electrolyzers and results from testing the same catalysts in the galvanostatic RDE-based stability test, whereby the apparent catalyst durability in the latter is orders of magnitude shorter than in actual electrolyzers.<sup>26</sup> Furthermore, the results presented in our study also show that the commonly used galvanostatic RDE-based stability test does not provide a measure of catalyst degradation/dissolution, which also puts in question the viability of the reported OER catalyst dissolution rates with respect to electrode potential carried out using half-cells with aqueous electrolytes.<sup>13,21,27–29</sup> Again, this is reflected by the orders of magnitude higher dissolution rates obtained by measurements in liquid electrolyte vs. those in actual PEM electrolyzers.<sup>26</sup>

### Conclusions

In this work, we carefully examined the viability of the galvanostatic RDE-based stability test as a tool for benchmarking or even quantifying OER catalyst durability. Although this test has been utilized for several years to compare the stability of various OER catalysts, its results are inconsistent with those obtained from PEM electrolyzers. Our results demonstrate that the galvanostatic RDE-based stability test does not provide a measure of OER catalyst degradation/dissolution. We provide evidence that this is mainly because of the accumulation of oxygen bubbles within the catalyst layer and/or near its interface with the electrolyte, preventing electrolyte contact to the majority of the catalyst surface which reduces the active catalyst surface area and thus gradually increases the OER potential, ultimately leading to a sudden potential jump to very high potentials, which is commonly interpreted as a complete degradation of the catalyst. However, since holding the catalyst for extended time at OCP under argon was shown here to substantially recover cata-

lyst activity and catalyst surface area (measured by cyclic voltammetry), the time until the occurrence of a large potential jump in the galvanostatic RDE-based stability test is not a measure of catalyst degradation, as assumed erroneously in the literature. Therefore, we believe that this test cannot be used to benchmark OER catalyst stability, underlined by the observation that the stability of iridium-based OER catalysts in PEM electrolyzers is tens of thousands of hours in contrast to only hours in the galvanostatic RDE-based stability test.

### Acknowledgment

Financial support in the frame of the innoKA project (BMW, 03ET6096A) is acknowledged. Thanks are extended to Melanie Miller (Department of Chemistry - University of Cambridge, England) for carrying out the very first set of exploratory experiments and for providing the Ir/ATO catalyst for this study. The authors thank Dr. Gregor Harzer, Dr. Armin Siebel, Maximilian Bernt, and Jan Schwämmlein (Chair of Technical Electrochemistry, Technical University of Munich, Germany) for fruitful scientific discussion.

### ORCID

Hany A. El-Sayed  <https://orcid.org/0000-0002-8769-8258>

### References

1. S. Siracusano, V. Baglio, C. D'Urso, V. Antonucci, and A. S. Arico, *Electrochimica Acta*, **54**(26), 6292 (2009).
2. V. K. Puthiyapura, S. Pasupathi, S. Basu, X. Wu, H. Su, N. Varaganapandiyam, B. Pollet, and K. Scott, *International Journal of Hydrogen Energy*, **38**(21), 8605 (2013).
3. S. Ferro, D. Rosestolato, C. A. Martínez-Huitle, and A. de Battisti, *Electrochimica Acta*, **146**, 257 (2014).
4. J. Polonský, I. M. Petrushina, E. Christensen, K. Bouzek, C. B. Prag, J. Andersen, and N. J. Bjerrum, *International Journal of Hydrogen Energy*, **37**(3), 2173 (2012).
5. F. Karimi and B. A. Peppley, *Electrochimica Acta*, **246**, 654 (2017).
6. P. Lettenmeier, L. Wang, U. Golla-Schindler, P. Gazdzicki, N. A. Canas, M. Handl, R. Hiesgen, S. S. Hosseiny, A. S. Gago, and K. A. Friedrich, *Angewandte Chemie (International ed. in English)*, **55**(2), 742 (2016).
7. E. Oaktou, D. Lebedev, M. Povia, D. F. Abbott, E. Fabbri, A. Fedorov, M. Nachtgeal, C. Copéret, and T. J. Schmidt, *ACS Catal.*, **7**(4), 2346 (2017).
8. H. Ohno, S. Nohara, K. Kakinuma, M. Uchida, A. Miyake, S. Deki, and H. Uchida, *J. Electrochem. Soc.*, **164**(9), F944 (2017).
9. T. Reier, M. Oezaslan, and P. Strasser, *ACS Catal.*, **2**(8), 1765 (2012).
10. S. Zhao, A. Stocks, B. Rasimick, K. More, and H. Xu, *J. Electrochem. Soc.*, **165**(2), F82 (2018).
11. N. H. Kwon, M. Kim, X. Jin, J. Lim, I. Y. Kim, N.-S. Lee, H. Kim, and S.-J. Hwang, *NPG Asia Mater.*, **10**(7), 659 (2018).
12. Y.-T. Kim, P. P. Lopes, S.-A. Park, A.-Y. Lee, J. Lim, H. Lee, S. Back, Y. Jung, N. Danilovic, V. Stamenkovic, J. Erlebacher, J. Snyder, and N. M. Markovic, *Nature Communications*, **8**(1), 1449 (2017).
13. S. Geiger, O. Kasian, A. M. Mingers, S. S. Nicley, K. Haenen, K. J. J. Mayrhofer, and S. Cherevko, *ChemSusChem*, **4**(1), 15 (2017).
14. A. S. Arico, S. Siracusano, N. Briguglio, V. Baglio, A. Di Blasi, and V. Antonucci, *J Appl Electrochem.*, **43**(2), 107 (2013).
15. C. Rakousky, U. Reimer, K. Wippermann, M. Carmo, W. Lueke, and D. Stolten, *Journal of Power Sources*, **326**, 120 (2016).
16. K. E. Ayers, E. B. Anderson, K. Dreier, and K. W. Harrison, *ECS Transactions*, **50**(49), 35 (2013).
17. S. M. Alia, B. Rasimick, C. Ngo, K. C. Neyerlin, S. S. Kocha, S. Pylypenko, H. Xu, and B. S. Pivovar, *J. Electrochem. Soc.*, **163**(11), F3105 (2016).
18. H.-S. Oh, H. N. Nong, T. Reier, A. Bergmann, M. Gliech, J. Ferreira de Araújo, E. Willinger, R. Schlögl, D. Teschner, and P. Strasser, *J. Am. Chem. Soc.*, **138**(38), 12552 (2016).
19. S. Geiger, O. Kasian, M. Ledendecker, E. Pizzutilo, A. M. Mingers, W. T. Fu, O. Diaz-Morales, Z. Li, T. Oellers, L. Fruchter, A. Ludwig, K. J. J. Mayrhofer, M. T. M. Koper, and S. Cherevko, *Nat Catal.*, **1**(7), 508 (2018).
20. C. C. L. McCrory, S. Jung, J. C. Peters, and T. F. Jaramillo, *Journal of the American Chemical Society*, **135**(45), 16977 (2013).
21. H.-S. Oh, H. N. Nong, T. Reier, M. Gliech, and P. Strasser, *Chem. Sci.*, **6**(6), 3321 (2015).
22. L. Wang, F. Song, G. Ozouf, D. Geiger, T. Morawietz, M. Handl, P. Gazdzicki, C. Beauger, U. Kaiser, R. Hiesgen, A. S. Gago, and K. A. Friedrich, *J. Mater. Chem. A*, **5**(7), 3172 (2017).
23. J. Zhang, G. Wang, Z. Liao, P. Zhang, F. Wang, X. Zhuang, E. Zschech, and X. Feng, *Nano Energy*, **40**, 27 (2017).

24. S. Cherevko, A. A. Topalov, A. R. Zeradjanin, I. Katsounaros, and K. J. J. Mayrhofer, *RSC Adv.*, **3**(37), 16516 (2013).
25. H. N. Nong, H.-S. Oh, T. Reier, E. Willinger, M.-G. Willinger, V. Petkov, D. Teschner, and P. Strasser, *Angewandte Chemie (International ed. in English)*, **54**(10), 2975 (2015).
26. S. Cherevko, *Current Opinion in Electrochemistry*, **8**, 118 (2018).
27. S. Cherevko, S. Geiger, O. Kasian, A. Mingers, and K. J. Mayrhofer, *J. Electroanal. Chem.*, **773**, 69 (2016).
28. S. Cherevko, S. Geiger, O. Kasian, A. Mingers, and K. J. Mayrhofer, *J. Electroanal. Chem.*, **774**, 102 (2016).
29. S. Cherevko, T. Reier, A. R. Zeradjanin, Z. Pawolek, P. Strasser, and K. J. Mayrhofer, *Electrochem. Commun.*, **48**, 81 (2014).



## 5.4 OER Catalyst Durability Tests Using the Rotating Disk Electrode Technique - the Reason Why This Leads to Erroneous Results

The next chapter deals with the article “OER Catalyst Durability Tests Using the Rotating Disk Electrode Techniqiue- the Reason Why This Leads to Erroneous Results”,<sup>136</sup> which was submitted to *ACS Applied Energy Materials* in August 2020 and accepted for publication in October 2020. Reprinted (adapted) with permission from (OER Catalyst Durability Tests Using the Rotating Disk Electrode Technique: The Reason Why This Leads to Erroneous Conclusions; Alexandra Hartig-Weiss, Mohammad Fathi Tovini, Hubert A. Gasteiger, and Hany A. El-Sayed; *ACS Applied Energy Materials* 2020 3 (11), 10323-10327; DOI: 10.1021/acsaem.0c01944). Copyright (2021) American Chemical Society.

The article can be found under its permanent web-link:

<https://pubs.acs.org/doi/pdf/10.1021/acsaem.0c01944>

The stability of oxygen evolution reaction catalysts measured in RDE or half-cell configurations is orders of magnitude lower compared that obtained by MEA measurements. It was shown in a previous study (see chapter 5.3) that the accumulation of oxygen bubbles within the catalyst layer is at least partially responsible for the fast increase in potential due to the shielding of active sides. In the literature, however, different hypotheses exists to explain this difference (e.g. passivation of the backing electrode<sup>114</sup> or depletion of OER active sites<sup>137</sup>). To unravel the origin of the fast decay in performance observed of OER catalysts when measured in RDE or other half-cell configurations was the main focus of this study.

Using an RDE setup and cycling the potential of an iridium disk between 1.2 and 1.65 V<sub>RHE</sub> at a rotation rate of 2500 rpm, a rapid decay in performance ( $\approx 70\%$  after 20 cycles) can be observed. Since the decay in performance is similar to what was observed also for catalysts in nano-particulate form, the passivation of the backing electrode<sup>114</sup> cannot be the main reason to explain the rapid loss in performance. By applying additional sonication, the observed decay in performance is significantly lower ( $\approx 30\%$  after 20 cycles). While the other processes (depletion of OER active sites<sup>137</sup> and loss of active sites capable of forming Ir(V)=O species<sup>138</sup>) are time and potential dependent, sonication of the cell by means of an ultra-sonication bath should result in a more efficient removal of oxygen bubbles and thus might prevent their accumulation within the catalyst layer. Although the loss in performance observed with this setup is less severe, it is

still continuously declining. Most likely, the power of the ultrasonication bath is not sufficiently high to prevent the accumulation of bubbles completely. Therefore, an ultrasonication horn, where the power can be adjusted, was placed inside the solution in the vicinity of the electrode. Applying a constant current ( $10 \text{ mAcm}^{-2}_{\text{disk}}$ ) while the electrode is rotated at 400 rpm and no sonication is applied, a significant increase in potential ( $\approx 100 \text{ mV}$ ) can be observed already within 450 s. Employing additional ultrasonication not only leads to a  $\approx 50 \text{ mV}$  lower starting potential, proving that already within the first couple of seconds oxygen bubbles can accumulate within the catalyst layer, but also results in a stable potential over time. It has to be noted that a sufficiently high enough power of the ultrasonication is required to ensure an efficient removal of oxygen bubbles. While this setup could be used to prove that the accumulation of oxygen bubbles leads to a rapid decay in performance due to shielding of active sites, it is not applicable for testing the stability of OER catalysts since most of them consist of nano-particles and ultrasonication would lead to the physical detachment of the catalyst.

#### **Author contributions**

Fabrication of catalyst inks and electrochemical testing in RDE was performed by H.A.E.-S. Analysis of the experimental test results was done by H.A.E.-S. A.H.-W. and M.F.T. wrote the manuscript that was edited by H.A.G. All authors discussed the experimental results and revised the manuscript.



## OER Catalyst Durability Tests Using the Rotating Disk Electrode Technique: The Reason Why This Leads to Erroneous Conclusions

Alexandra Hartig-Weiss,<sup>†</sup> Mohammad Fathi Tovini,<sup>†</sup> Hubert A. Gasteiger, and Hany A. El-Sayed\*

Cite This: ACS Appl. Energy Mater. 2020, 3, 10323–10327

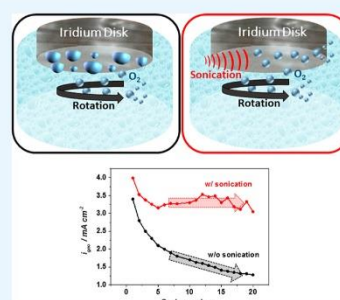
Read Online

ACCESS |

Metrics &amp; More

Article Recommendations

**ABSTRACT:** This study reveals the physical origin of the rapid performance decay when measuring the activity and durability of oxygen evolution reaction (OER) catalysts using the rotating disk electrode (RDE) technique or other half-cell test configurations with liquid electrolyte. By subjecting the electrochemical cell or the electrolyte to ultrasonication while conducting a typical RDE-based measurement of the OER performance of a polycrystalline iridium-disk electrode, we demonstrate that it is the accumulation of microscopic oxygen bubbles that is responsible for the rapid OER catalyst performance decay observed during RDE experiments.



**KEYWORDS:** oxygen evolution reaction, iridium, rotating disk electrode, PEM water electrolysis, accelerated stress tests

Polymer electrolyte membrane water electrolysis (PEM-WE) is considered to be one of the most promising technologies for the production of pure hydrogen.<sup>1,2</sup> One of its major drawbacks is the sluggish kinetics of the oxygen evolution reaction (OER) of the currently used iridium-based catalysts, and research in this field is thus focused on finding catalysts exhibiting high OER activities as well as long-term stability.<sup>3–5</sup> It is well-established now that OER activities can be reliably measured in liquid electrolytes using cyclic voltammetry (CV) in stagnant electrolyte, the rotating disk electrode (RDE) technique, and flow-channel approaches,<sup>5–10</sup> i.e., in half-cell configurations with liquid electrolytes or, alternatively, by testing membrane electrode assemblies (MEAs) in PEM-WEs.<sup>9,11–13</sup> However, the OER catalyst lifetime determined in half-cell measurements with liquid electrolyte is orders of magnitude less than that measured in a PEM-WE.<sup>9,10</sup> In order to accelerate catalyst development without the necessity of producing a few grams of newly synthesized catalysts that are needed for PEM-WE measurements, accelerated stress tests (ASTs) using methods that require only several milligrams of catalysts (namely, half-cell tests with liquid electrolyte) are needed. Unfortunately, all OER performance measurements in half-cell configurations with liquid electrolyte exhibit a rapid activity decay that has puzzled researchers for decades;<sup>14–16</sup> this rapid activity decay also seems to be responsible for the many orders of magnitude shorter catalyst lifetime observed in RDE measurements if compared to measurements with the same catalyst in PEM-WEs.<sup>9,10</sup> Therefore, identifying the origin of the catalyst

performance decay (with respect to activity and stability) obtained in half-cell experiments with liquid electrolyte is crucial in order to develop meaningful ASTs that can be conducted with small amounts of catalysts and that would thus allow one to accelerate the development of OER catalysts.

Four different hypotheses can be found in the literature explaining the rapid performance decay of OER catalysts measured in half-cells with liquid electrolyte: *Hypothesis I*, formation of an additional contact resistance between the catalyst layer and the electrode substrate due to the passivation of the electrode substrate during the measurement;<sup>17</sup> *Hypothesis II*, the depletion of the OER-active species due to the formation of an anhydrous Ir oxide at the catalyst surface upon continuous polarization of the OER catalyst in the OER potential range;<sup>18</sup> *Hypothesis III*, loss of active sites capable of forming the Ir(V)=O species via progressive cross-linking of iridium atoms<sup>15</sup> (these species, Ir(V)=O, were proposed to be sufficiently electron deficient to undergo nucleophilic attack by substrate water and form the O–O bond); and *Hypothesis IV*, shielding of the catalyst active sites by the trapped oxygen microbubbles at the surface of the electrode and/or within the

Received: August 12, 2020

Accepted: October 13, 2020

Published: October 19, 2020





catalyst layer.<sup>10</sup> With the help of ultrasonication, this study provides solid evidence that the microscopic oxygen bubbles shielding the OER-active sites (Hypothesis IV) are the main origin of the rapid OER performance decay in half-cell configurations with liquid electrolyte, as demonstrated by RDE measurements.

A three-electrode cell with a reversible hydrogen electrode (RHE) as a reference electrode and a high surface area Au wire as a counter electrode was used for all electrochemical measurements. As working electrode, a rotating ring-disk electrode (RRDE) consisting of a 5 mm diameter polycrystalline iridium disk (Pine Research Instrumentation, USA) and a platinum ring embedded in a PTFE body (Pine Research) were used. For measurements where the cell or the electrolyte was subjected to ultrasonication, the electrochemical cell was either partially immersed in an ultrasonic bath (S 30 H, Elmasonic, Germany) or the tip of a horn sonicator (Branson 450 Digital Sonifier, Branson Ultrasonics Corp., USA) was directly immersed in the electrolyte in the vicinity of the electrode surface. Prior to each measurement, the reference electrode potential was calibrated in a H<sub>2</sub>-saturated electrolyte using the platinum ring of the RRDE assembly, and all potentials are referenced versus RHE. A 0.1 M H<sub>2</sub>SO<sub>4</sub> electrolyte was prepared by mixing high purity H<sub>2</sub>SO<sub>4</sub> (Ultrapur, 96%, Merck Millipore KGaA, Germany) and ultrapure water (18.2 MΩ cm at 20 °C, Merck Millipore). An Autolab potentiostat (PGSTAT302N, Metrohm AG) and a rotator (Pine Research) with a polyether ketone shaft were used to perform the electrochemical measurements. Electrochemical impedance spectroscopy (EIS) in the frequency range of 100 kHz to 100 Hz at open circuit potential (OCP) was used to determine the noncompensated solution resistance between the reference and working electrodes.

In order to investigate the OER performance decay, the potential of the Ir disk was cycled between 1.2 and 1.65 V<sub>RHE</sub> at 20 mV s<sup>-1</sup>. Figure 1A shows the successive anodic sweeps of the iridium disk at a rotation rate of 2500 rpm. A continuous decay in performance of the electrode over the course of potential cycling is observed in the absence of ultrasonication (black curves in Figure 1A). The geometric current densities extracted from the curves in Figure 1A at a potential of 1.55 V<sub>RHE</sub> are shown in Figure 1B versus the number of potential cycles, illustrating the severe performance loss of the iridium disk, with the current density continuously decreasing from an initial value of ~3.4 to ~1.3 mA cm<sup>-2</sup> after 20 cycles (black circles). Since this performance decay of the iridium disk is analogous to the performance decay that is observed with a catalyst layer deposited on a disk electrode substrate (i.e., in a so-called thin-film RDE experiment),<sup>10,12,19</sup> the formation of an additional contact resistance between the catalyst layer and the disk electrode substrate due to the passivation of the latter (Hypothesis I, proposed by Geiger et al.<sup>17</sup>) can be excluded as the main reason for the rapid OER activity performance decay.

Next we will examine Hypothesis IV, namely, whether microscopic oxygen bubbles that form on the surface of the iridium disk are the cause of the observed rapid performance decay. In order to investigate this hypothesis, the RDE cell was placed in an ultrasonic bath in order to facilitate the removal of possibly formed microscopic oxygen bubbles on the surface of the iridium disk. Surprisingly, using an identical potential cycling procedure in the presence of cell ultrasonication, the OER performance remained relatively constant over the course of successive voltage cycles (red curve in Figure 1A). While the

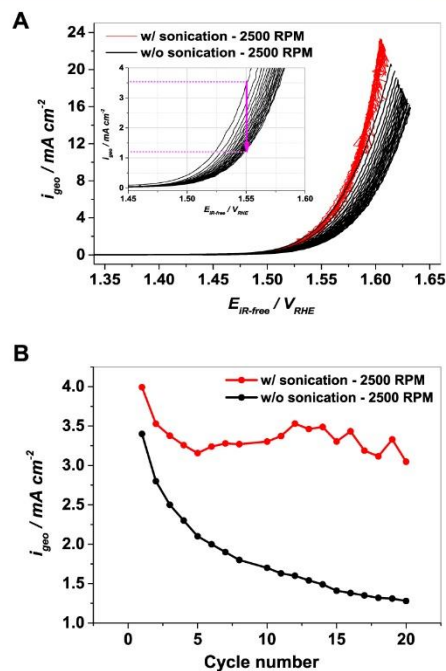


**Figure 1.** (A) OER cyclic voltammetry (anodic sweeps) of a polycrystalline Ir disk in non-deaerated 0.1 M H<sub>2</sub>SO<sub>4</sub> at a scan rate of 20 mV s<sup>-1</sup> and a rotation rate of 2500 rpm without ultrasonication (black line) and with ultrasonication (red line) of the cell in an ultrasonic bath. The inset is a close-up of successive anodic sweeps in the absence of ultrasonication. (B) Decay in the OER current density extracted from the OER polarization curves (A) at 1.55 V<sub>RHE</sub> versus the number of successive sweeps.

application of sonication does not affect the formation of an anhydrous Ir oxide (Hypothesis II) nor the progressive cross-linking of iridium atoms (Hypothesis III), as these are both potential and time dependent processes, ultrasonication is expected to improve the removal of microscopic oxygen bubbles that are forming on the Ir-disk surface or, by extension, on the catalyst layer surface in a thin-film RDE experiment. Hence, the depletion of OER-active sites on the catalyst surface according to Hypotheses II<sup>18</sup> and III<sup>15</sup> does not seem to be responsible for the observed performance decay. At the same time it is noted that the current density measured at 1.55 V<sub>RHE</sub> decreases within the first 5 cycles from an initial value of ~4.0 to ~3.2 mA cm<sup>-2</sup>, even though it remains rather constant (~3.3 mA cm<sup>-2</sup>) after 5 cycles (red circles in Figure 1B). This suggests that already within the first cycle, oxygen bubbles are continuously accumulating on the Ir-disk surface, shielding more and more OER-active sites. Therefore, the applied ultrasonication is not strong enough to fully remove the produced microscopic oxygen bubbles, while it is strong enough to demonstrate that the accumulation of microscopic oxygen bubbles is responsible for the observed rapid performance decay.

Applying a constant current (typically 10 mA cm<sup>-2</sup>) and monitoring the potential versus time in a half-cell configuration with liquid electrolyte is the prevalent OER catalyst stability test in the literature.<sup>4,20,21</sup> During this type of experiment, the increase in OER overpotential at constant current is



interpreted as catalyst degradation, ultimately resulting in a rapid jump of the potential to  $>2.1 V_{\text{RHE}}$ .<sup>4,10,17</sup> Figure 2A

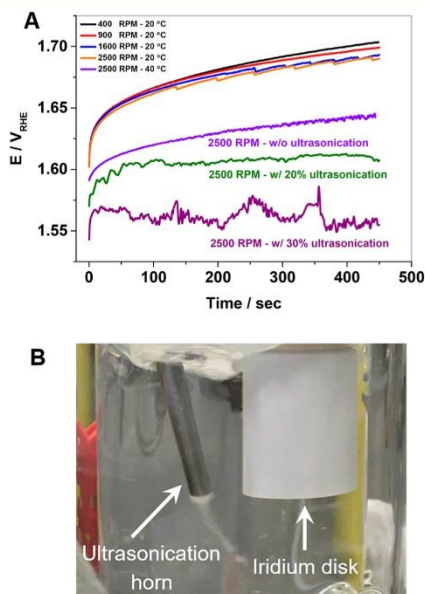


**Figure 2.** (A) Constant current experiment at  $10 \text{ mA cm}^{-2}_{\text{geo}}$  of a polycrystalline Ir disk in non-deaerated  $0.1 \text{ M H}_2\text{SO}_4$  without sonication at 400, 900, 1600, and 2500 rpm as well as at 2500 rpm when the electrolyte is subjected to ultrasonication by means of an ultrasonic horn at different ultrasonication power settings of 20% and 30%. (B) Picture of the RDE setup with the ultrasonic horn immersed in the electrolyte and placed in close proximity to the Ir-disk electrode.

shows the initial phase of such a constant current experiment for the iridium disk at  $10 \text{ mA cm}^{-2}_{\text{geo}}$ , where the first 300 ms after application of the current are not shown due to the strong capacitive contributions to the OER current at  $<300 \text{ ms}$ . As expected for the case where no ultrasonication is applied and the electrode is only rotated, the voltage rapidly increases within 450 s from  $\sim 1.6 V_{\text{RHE}}$  after 300 ms up to  $\sim 1.7 V_{\text{RHE}}$  at the lowest rotation rate of 400 rpm (black curve). The effect of the rotation rate is rather weak, showing an only  $\sim 10 \text{ mV}$  lower potential after 450 s at the highest rotation rate of 2500 rpm (orange curve).

Next we will examine the effect of ultrasonication on this rapid potential increase within the initial 450 s. However, as ultrasonication of the cell using the ultrasonic bath was shown to be unable to completely suppress the performance decay over the course of the initial sweeps (see red symbols in Figure 1B), it is unlikely that a constant current experiment with this type of ultrasonication would result in a stable OER performance over time. Therefore, a modular cup horn ultrasonicator with adjustable power was placed directly into the electrolyte, in close proximity to the iridium electrode (Figure 2B). Conducting the constant current experiment at the same current density of  $10 \text{ mA cm}^{-2}_{\text{geo}}$  at 2500 rpm and at an ultrasonicator power setting of 20% (green curve in Figure 2A), the voltage after the initial 300 ms is now  $\sim 30 \text{ mV}$  lower than without ultrasonication ( $\sim 1.57 V_{\text{RHE}}$ ) and the loss of OER performance after 450 s is  $80 \text{ mV}$  lower (orange curve).

The lower starting potential again implies that the accumulation of oxygen bubbles occurs immediately upon applying a constant current and that strong ultrasonication in conjunction with the rotation of the electrode seems to facilitate the removal of microscopic bubbles that are formed on the Ir-disk surface. However, even in this case, the potential increases within the first 100 s of the experiment before reaching a constant value, which suggests that the applied sonication is still not sufficient to completely prevent the accumulation of oxygen bubbles. Therefore, the sonication power was further increased to 30% (purple curve in Figure 2A), and as a result, the initial potential ( $\sim 1.55 V_{\text{RHE}}$ ) is lower by another  $\sim 20 \text{ mV}$ . Interestingly, unlike the other potential versus time transients, after  $\sim 5 \text{ s}$  the potential now remains constant at a very low value of  $\sim 1.56 V_{\text{RHE}}$  until the end of the experiment at 450 s, which implies that the rate of formation and removal of oxygen bubbles on the Ir-disk surface reaches a steady state without any further accumulation of oxygen bubbles. The observed behavior cannot be attributed to thermal effects during ultrasonication as the temperature never exceeded  $40 \text{ }^\circ\text{C}$  by the end of the experiment and that performing the constant current experiment without ultrasonication at  $40 \text{ }^\circ\text{C}$  (violet curve in Figure 2A) resulted in a continuously increasing potential and a plateau was never observed. This experiment thus firmly proves that the accumulation of microscopic oxygen bubbles is responsible for the performance decay (both with respect to activity and stability) observed in half-cell measurements with liquid electrolyte and that this must be the main origin of the large discrepancy (by many orders of magnitude) in OER catalyst stability when measured in half-cells with liquid electrolyte (e.g., by in RDE measurements) compared to measurements of the same catalyst in an MEA tested in a PEM-WE.<sup>9</sup>

It has to be noted that all experiments in this study were performed using an Ir-disk electrode, where ultrasonication does not affect the physical stability of the catalyst. However, catalysts for application in actual PEM-WEs are generally in particulate form, with primary catalyst particle agglomerate dimensions on the order of several hundred nanometers,<sup>22</sup> so that for the evaluation of their OER activity and stability in half-cells with liquid electrolyte the catalysts are drop-cast on an electrochemically inert electrode substrate (e.g., a glassy carbon or gold disk electrode substrate for RDE measurement). In this case, subjecting the cell or the electrolyte to ultrasonication would lead to a physical detachment of the catalyst particles from the electrode substrate, so that ultrasonication is not feasible. Nevertheless, the aim of this study was to prove that the accumulation of microscopic oxygen bubbles forming on the catalyst surface is the main origin of the observed rapid performance decay of OER catalysts in RDE experiments, independent of whether solid disk electrodes (such as the Ir disk in this study) or thin-film catalyst layers deposited on a disk electrode substrate are used.

Assuming that this hypothesis is true, one would perhaps expect that the performance decay should be fully reversible after removal of the oxygen bubbles by, e.g., equilibrating the electrode after the stability test in inter gas purged electrolyte for a long time. This is indeed true in cases where the electrode potential has not increased beyond  $\sim 1.65 V_{\text{RHE}}$  over the course of the experiment, but once the OER potential has significantly exceeded this value, a loss of catalyst surface and catalyst dissolution are observed.<sup>6,10</sup> If iridium or iridium oxide indeed undergo dissolution beyond  $\sim 1.65 V_{\text{RHE}}$ , it raises the question



as to why this phenomenon would not occur equally in the OER catalyst layer in the MEAs used in PEM-WEs. The answer is surprisingly straightforward: the OER catalyst layer potential ( $iR$ -corrected) in PEM-WEs never exceeds  $1.6 V_{\text{RHE}}$ , even at current densities as high as  $3\text{--}4 \text{ A cm}^{-2}$ ,<sup>9,22,23</sup> which thus explains the 4–5 orders of magnitude longer OER catalyst lifetimes observed in PEM-WEs compared to stability tests in half-cell configuration with liquid electrolyte, where the OER catalyst potential rapidly increases beyond  $1.65 V_{\text{RHE}}$ . The large difference in OER overpotential between these two measurement setups is, we believe, due to a different extent of shielding of the active catalyst by microscopic oxygen bubbles.

In summary, by comparing the OER performance decay of an Ir-disk electrode in an RDE configuration, either in the absence or in the presence of ultrasonication of the cell/electrolyte, we have shown not only that ultrasonication decreases the initial OER overpotential in constant current experiments but that it also can lead to a stable and  $\sim 150 \text{ mV}$  lower OER overpotential after 450 s of constant current polarization. Our analysis provides clear evidence that it is the shielding of the OER catalyst by microscopic oxygen bubbles (increasing over time) that is responsible for the observed OER performance decay in half-cell experiments with liquid electrolyte. The accompanied lowering of the OER catalyst utilization at a fixed constant current then increases the OER overpotentials to values high enough to induce iridium dissolution. The fact that the OER overpotentials for the same catalyst and for the same mass specific current density (in  $\text{A g}_{\text{Ir}}^{-1}$ ) are much lower in PEM-WEs suggests a different extent of OER catalyst shielding by microscopic oxygen bubble<sup>9</sup> and is a straightforward explanation for the 4–5 orders of magnitude higher catalyst lifetime in PEM-WEs compared to that determined in half-cells with liquid electrolyte.

## AUTHOR INFORMATION

### Corresponding Author

Hany A. El-Sayed – Chair of Technical Electrochemistry,  
Department of Chemistry and Catalysis Research Center,  
Technical University of Munich, D-85748 Garching, Germany;  
orcid.org/0000-0002-8769-8258; Email: hany.el-sayed@tum.de

### Authors

Alexandra Hartig-Weiss – Chair of Technical Electrochemistry,  
Department of Chemistry and Catalysis Research Center,  
Technical University of Munich, D-85748 Garching, Germany;  
orcid.org/0000-0001-7094-5016

Mohammad Fathi Tovini – Chair of Technical  
Electrochemistry, Department of Chemistry and Catalysis  
Research Center, Technical University of Munich, D-85748  
Garching, Germany

Hubert A. Gasteiger – Chair of Technical Electrochemistry,  
Department of Chemistry and Catalysis Research Center,  
Technical University of Munich, D-85748 Garching, Germany;  
orcid.org/0000-0001-8199-8703

Complete contact information is available at:  
<https://pubs.acs.org/10.1021/acsaem.0c01944>

### Author Contributions

<sup>†</sup>A.H.-W. and M.F.T. contributed equally to this work.

### Notes

The authors declare no competing financial interest.

## ACKNOWLEDGMENTS

We gratefully acknowledge the German Ministry of Education and Research for financial support of this work within the Kopernikus Project P2X (03SFK2 V0-2) and the innoKA Project (BMW, 03ET6096A).

## REFERENCES

- (1) Carmo, M.; Fritz, D. L.; Mergel, J.; Stolten, D. A comprehensive review on PEM water electrolysis. *Int. J. Hydrogen Energy* **2013**, *38*, 4901–4934.
- (2) Buttlar, A.; Spliethoff, H. Current status of water electrolysis for energy storage, grid balancing and sector coupling via power-to-gas and power-to-liquids: A review. *Renewable Sustainable Energy Rev.* **2018**, *82*, 2440–2454.
- (3) Böhm, D.; Beetz, M.; Schuster, M.; Peters, K.; Hufnagel, A. H.; Döblinger, M.; Böller, B.; Bein, T.; Fattakhova-Rohlfing, D. Efficient OER Catalyst with Low Ir Volume Density Obtained by Homogeneous Deposition of Iridium Oxide Nanoparticles on Macroporous Antimony-Doped Tin Oxide Support. *Adv. Funct. Mater.* **2020**, *30* (1), 1906670.
- (4) Oh, H.-S.; Nong, H. N.; Reier, T.; Glich, M.; Strasser, P. Oxide-supported Ir nanodendrites with high activity and durability for the oxygen evolution reaction in acid PEM water electrolyzers. *Chem. Sci.* **2015**, *6*, 3321–3328.
- (5) Hartig-Weiss, A.; Miller, M.; Beyer, H.; Schmitt, A.; Siebel, A.; Freiberg, A. T. S.; Gasteiger, H. A.; El-Sayed, H. A. Iridium Oxide Catalyst Supported on Antimony-Doped Tin Oxide for High Oxygen Evolution Reaction Activity in Acidic Media. *ACS Appl. Nano Mater.* **2020**, *3*, 2185–2196.
- (6) Cherevko, S.; Geiger, S.; Kasian, O.; Kulyk, N.; Grote, J.-P.; Savan, A.; Shrestha, B. R.; Merzlikin, S.; Breitbach, B.; Ludwig, A.; Mayrhofer, K. J. J. Oxygen and hydrogen evolution reactions on Ru, RuO<sub>2</sub>, Ir, and IrO<sub>2</sub> thin film electrodes in acidic and alkaline electrolytes: A comparative study on activity and stability. *Catal. Today* **2016**, *262*, 170–180.
- (7) Ohno, H.; Nohara, S.; Kakinuma, K.; Uchida, M.; Miyake, A.; Deki, S.; Uchida, H. Remarkable Mass Activities for the Oxygen Evolution Reaction at Iridium Oxide Nanocatalysts Dispersed on Tin Oxides for Polymer Electrolyte Membrane Water Electrolysis. *J. Electrochem. Soc.* **2017**, *164*, F944–F947.
- (8) Wakabayashi, N.; Takeichi, M.; Uchida, H.; Watanabe, M. Temperature dependence of oxygen reduction activity at Pt–Fe, Pt–Co, and Pt–Ni alloy electrodes. *J. Phys. Chem. B* **2005**, *109*, 5836–5841.
- (9) Bernt, M.; Hartig-Weiß, A.; Tovini, M. F.; El-Sayed, H. A.; Schramm, C.; Schröter, J.; Gebauer, C.; Gasteiger, H. A. Current Challenges in Catalyst Development for PEM Water Electrolyzers. *Chem. Ing. Tech.* **2020**, *92* (1–2), 31–39.
- (10) El-Sayed, H. A.; Weiß, A.; Olbrich, L. F.; Putro, G. P.; Gasteiger, H. A. OER Catalyst Stability Investigation using RDE Technique – A stability measure or an Artifact? *J. Electrochem. Soc.* **2019**, *166*, F458–F464.
- (11) Lettenmeier, P.; Wang, L.; Golla-Schindler, U.; Gazdzicki, P.; Canas, N. A.; Handl, M.; Hiesgen, R.; Hosseiny, S. S.; Gago, A. S.; Friedrich, K. A. Nanosized IrO(x)-Ir Catalyst with Relevant Activity for Anodes of Proton Exchange Membrane Electrolysis Produced by a Cost-Effective Procedure. *Angew. Chem., Int. Ed.* **2016**, *55*, 742–746.
- (12) Oakton, E.; Lebedev, D.; Povia, M.; Abbott, D. F.; Fabbri, E.; Fedorov, A.; Nachtegaal, M.; Copéret, C.; Schmidt, T. J. IrO<sub>2</sub>-TiO<sub>2</sub>: A High-Surface-Area, Active, and Stable Electrocatalyst for the Oxygen Evolution Reaction. *ACS Catal.* **2017**, *7*, 2346–2352.
- (13) Yu, H.; Danilovic, N.; Wang, Y.; Willis, W.; Poozhikunnath, A.; Bonville, L.; Capuano, C.; Ayers, K.; Maric, R. Nano-size IrOx catalyst of high activity and stability in PEM water electrolyzer with ultra-low iridium loading. *Appl. Catal., B* **2018**, *239*, 133–146.
- (14) Gottesfeld, S.; Srinivasan, S. Electrochemical and optical studies of thick oxide layers on iridium and their electrocatalytic activities

the oxygen evolution reaction. *J. Electroanal. Chem. Interfacial Electrochem.* **1978**, *86*, 89–104.

(15) Tang-Kong, R.; Chidsey, C. E. D.; McIntyre, P. C. Reversible Decay of Oxygen Evolution Activity of Iridium Catalysts. *J. Electrochem. Soc.* **2019**, *166*, H712–H717.

(16) Frazer, E. J.; Woods, R. The oxygen evolution reaction on cycled iridium electrodes. *J. Electroanal. Chem. Interfacial Electrochem.* **1979**, *102*, 127–130.

(17) Geiger, S.; Kasian, O.; Mingers, A. M.; Nicley, S. S.; Haenen, K.; Mayrhofer, K. J. J.; Cherevko, S. Catalyst Stability Benchmarking for the Oxygen Evolution Reaction: The Importance of Backing Electrode Material and Dissolution in Accelerated Aging Studies. *ChemSusChem* **2017**, *10*, 4140–4143.

(18) Tan, X.; Shen, J.; Semagina, N.; Secanell, M. Decoupling structure-sensitive deactivation mechanisms of Ir/IrO<sub>x</sub> electrocatalysts toward oxygen evolution reaction. *J. Catal.* **2019**, *371*, 57–70.

(19) Gutsche, C.; Moeller, C. J.; Knipper, M.; Borchert, H.; Parisi, J.; Plaggenborg, T. Synthesis, Structure, and Electrochemical Stability of Ir-Decorated RuO<sub>2</sub> Nanoparticles and Pt Nanorods as Oxygen Catalysts. *J. Phys. Chem. C* **2016**, *120*, 1137–1146.

(20) Santos, G. O. S.; Silva, L. R. A.; Alves, Y. G. S.; Silva, R. S.; Eguiluz, K. I. B.; Salazar-Banda, G. R. Enhanced stability and electrocatalytic properties of Ti/Ru Ir<sub>1</sub>-O<sub>2</sub> anodes produced by a new laser process. *Chem. Eng. J.* **2019**, *355*, 439–447.

(21) Huynh, M.; Ozel, T.; Liu, C.; Lau, E. C.; Nocera, D. G. Design of template-stabilized active and earth-abundant oxygen evolution catalysts in acid. *Chem. Sci.* **2017**, *8*, 4779–4794.

(22) Bernt, M.; Gasteiger, H. A. Influence of Ionomer Content in IrO<sub>2</sub>/TiO<sub>2</sub> Electrodes on PEM Water Electrolyzer Performance. *J. Electrochem. Soc.* **2016**, *163*, F3179–F3189.

(23) Weiß, A.; Siebel, A.; Bernt, M.; Shen, T.-H.; Tileli, V.; Gasteiger, H. A. Impact of Intermittent Operation on Lifetime and Performance of a PEM Water Electrolyzer. *J. Electrochem. Soc.* **2019**, *166*, F487–F497.



## 5.5 The Discrepancy in Oxygen Evolution Reaction Catalyst Lifetime Explained: RDE vs MEA – Dynamicity within the Catalyst Layer Matters

In this section the article “The Discrepancy in Oxygen Evolution Reaction Catalyst Lifetime Explained: RDE vs MEA – Dynamicity within the Catalyst Layer Matters”, which has been submitted to the *Journal of Electrochemical Society* in October 2020 and accepted for publication in January 2021.<sup>139</sup> The study was presented by H.A.E.-S. at the 236<sup>th</sup> Meeting of the Electrochemical Society in Atlanta (October 2019) and can be found under its abstract number: #I01F-1750. The study can be found under its permanent web-link: <https://iopscience.iop.org/article/10.1149/1945-7111/abdcc9/pdf>

Half-cell configurations such as RDE or flow-channel techniques are often used to access the activity as well as stability of OER catalysts. The lifetime obtained from these techniques, however, is orders of magnitudes lower compared to that measured in a membrane electrode assembly in a PEM-WE. Within this study, the techniques commonly used to assess the stability of a catalyst, such as constant current or constant potential holds as well as potential cycling, are tested for both configurations (RDE and MEA) and compared directly with each other. In order to justify a comparison of the stability obtained for the different configurations, the activity of an IrO<sub>2</sub>/TiO<sub>2</sub> catalyst was determined in an RDE and in an MEA configuration, and a comparison showed that the activity measured with an RDE (21 Ag<sup>-1</sup><sub>Ir</sub>) is twice as high as that recorded in an MEA (10 Ag<sup>-1</sup><sub>Ir</sub>) at 40 °C and 1.50 V<sub>RHE</sub>. A different utilization of the catalyst layer can be excluded, since the mass-specific capacitive currents of the MEA measurement is higher compared to the one measured in RDE. Since, however, different ionomer contents were used (11 wt.-% in MEA vs 1 wt.-% in RDE), this might explain the difference observed in activity. This was not studied any further, as the activities were sufficiently close.

Applying a constant current is a commonly used technique in the literature to estimate the lifetime of OER catalysts. In this case, a current density of 70 Ag<sup>-1</sup><sub>Ir</sub> was used for both configurations, and while the potential gradually increases during the RDE measurement, terminating in a potential jump (≈2 V), the potential remains stable for the MEA measurements over the recorded period of time (≈230 h). After purging, the electrolyte solution of the RDE setup with Ar for 30 min, the initial activity can be retrieved partially. The observed recovery in activity can be attributed to the efficient removal of trapped oxygen bubbles within the catalyst layer during purging. Due to the partial shielding of active sites, the still accessible sites

have to provide the same overall applied current, resulting in locally high potentials where iridium dissolution could occur. Hence, the observed decrease in performance during an RDE measurement is the result of a bubble-induced degradation, which is not happening to the same extent during an MEA measurement.

Another technique frequently used to estimate the stability of OER catalysts is the application of a constant potential and investigating the decrease in current. For both techniques, a decrease in current can be observed, however, on different time scales. While the current decreased by  $\approx 90\%$  after applying  $1.53 \text{ V}_{\text{RHE}}$  for 6 h for the RDE measurement, the observed decrease in activity for an MEA measurement was only  $\approx 50\%$  after  $\approx 24$  h. After recording a polarization curve as well as a CV, the activity was fully retrieved for the MEA measurement, whereas a 30 min Ar-purge could only recover  $\approx 60\%$  of the initial activity in the RDE configuration. Clearly, part of the catalyst degrades during the first chronoamperometric step due to the shielding of active sites by oxygen bubbles within the RDE setup.

So far, neither the application of a constant current nor constant potential hold can be used to reliably predict the stability of an OER catalyst by RDE. Since the stability during transient operation is of vital interest, a third option to assess the lifetime of OER catalysts is by potential cycling. Again, the performance decreases significantly within the first couple of cycles ( $\approx 60\%$  after 20 cycles) using an RDE setup and again could partially be retrieved ( $\approx 70\%$  of the initial activity) once the electrolyte was purged with Ar. In contrast to that, the performance was fairly stable when the same cycling protocol was applied in an MEA configuration. This study showed, that neither of these commonly applied stability tests can be used to reliably predict the lifetime of an OER catalyst when using an RDE setup. Due to a different extent of accumulation of oxygen bubbles within the catalyst layer, the degradation observed in the RDE configurations is more severe, and thus the predicted lifetime is significantly lower. The most viable explanation to why the extent of bubble accumulation is different between an RDE and an MEA setup is most likely related to the electro-osmotic drag of water across the catalyst layer and the fact that the reaction is biased towards the electrode||membrane interface within the catalyst layer of an MEA.

### **Authors contributions**

Fabrication of catalyst inks and electrochemical testing in RDE was performed by M.F.T. Fabrication of membrane electrode assemblies and electrochemical testing in a PEM-WE cell was performed by A.H.-W. Analysis of the experimental test results was done by M.F.T and

A.H.-W. A.H.-W. and M.F.T. wrote the manuscript that was edited by H.A.G. and H.A.E.-S.  
All authors discussed the experimental results and revised the manuscript.



**OPEN ACCESS**

## The Discrepancy in Oxygen Evolution Reaction Catalyst Lifetime Explained: RDE vs MEA - Dynamicity within the Catalyst Layer Matters


To cite this article: Mohammad Fathi Tovini *et al* 2021 *J. Electrochem. Soc.* **168** 014512

View the [article online](#) for updates and enhancements.

### Discover the EL-CELL potentiostats

- Fully independent test channels with Pstat / GStat / EIS
- Optionally with integrated temperature controlled cell chamber
- Unique Connection Matrix: Switch between full-cell and half-cell control at runtime

[www.el-cell.com](http://www.el-cell.com) +49 (0) 40 79012 734 [sales@el-cell.com](mailto:sales@el-cell.com)



**EL-CELL**<sup>®</sup>  
electrochemical test equipment

This content was downloaded from IP address 129.187.254.46 on 07/02/2021 at 12:09



## The Discrepancy in Oxygen Evolution Reaction Catalyst Lifetime Explained: RDE vs MEA - Dynamicity within the Catalyst Layer Matters

Mohammad Fathi Tovini,<sup>†</sup> Alexandra Hartig-Weiß,<sup>\*,\*</sup> Hubert A. Gasteiger,<sup>\*\*</sup> and Hany A. El-Sayed<sup>‡</sup>

Chair of Technical Electrochemistry, Department of Chemistry and Catalysis Research Center, Technical University of Munich, 85748 Garching, Germany

This study reveals the source of discrepancy between the lifetime of oxygen evolution reaction (OER) catalysts determined by rotating disk electrode (RDE) measurements vs that obtained in a membrane electrode assembly (MEA) in an electrolyzer. We show that the accumulation of microscopic oxygen bubbles in the pores of the electro-catalyst layer during the OER takes place in both RDE and MEA measurements. However, this accumulation was found to be much more significant in RDE measurements, where the shielding of almost all of the catalyst active sites by gas bubbles leads to rapid performance deterioration. This decrease in performance, albeit largely reversible, was found to also induce irreversible catalyst degradation, which could be avoided if the accumulation of microscopic bubbles is prevented. This type of artefact results in vastly under-estimated catalyst lifetimes obtained by RDE experiments, resulting in values that are orders of magnitude shorter than those obtained using MEA measurements, and a hypothesis for this discrepancy will be proposed. Therefore, electrochemical cells with liquid electrolytes are not reliable for OER catalyst lifetime determination.

This was paper 236 presented at the Atlanta, Georgia, Meeting of the Society, October 13–17, 2019.

© 2021 The Author(s). Published on behalf of The Electrochemical Society by IOP Publishing Limited. This is an open access article distributed under the terms of the Creative Commons Attribution 4.0 License (CC BY, <http://creativecommons.org/licenses/by/4.0/>), which permits unrestricted reuse of the work in any medium, provided the original work is properly cited. [DOI: 10.1149/1945-7111/abdcc9]



Manuscript submitted October 22, 2020; revised manuscript received December 21, 2020. Published January 29, 2021. *This paper is part of the JES Focus Issue on Proton Exchange Membrane Fuel Cell and Proton Exchange Membrane Water Electrolyzer Durability.*

Supplementary material for this article is available [online](#)

The slow kinetics of the oxygen evolution reaction (OER) is a major challenge in the electrochemical production of hydrogen from water by proton exchange membrane water electrolysis (PEM-WE). To date, IrO<sub>2</sub> and RuO<sub>2</sub> are the most investigated catalysts in the literature for OER catalysis.<sup>1–3</sup> In order to identify a suitable OER catalyst, its activity and long-term stability are of an equally critical importance. Reliable methods for screening the activity have been established using rotating disk electrode (RDE) and flow-channel techniques or testing membrane electrode assemblies (MEAs) in PEM-WEs.<sup>4–10</sup> However, the evaluation of the long-term stability of OER catalysts under realistic conditions is not feasible due to the rather low degradation rate in PEM-WEs, which would require 1000's of hours of testing to obtain significant degradation.<sup>11,12</sup> Therefore, accelerated degradation tests are required, which are typically performed in cells with liquid electrolyte or in PEM-WEs.<sup>12–17</sup> Generally, accelerated degradation tests are performed using one or more of three different methods: i) constant current holds (chronopotentiometry), ii) constant potential holds (chronoamperometry), and iii) potential cycling.<sup>18</sup>

Applying a constant current is the prevalent testing method in the literature.<sup>19</sup> In this method, which is carried out in an RDE setup, the increase in OER overpotential at constant current operation is taken as a measure for catalyst stability, where a drastic potential jump is interpreted as the end of life (EOL) of the catalyst.<sup>15,20–22</sup> Alternatively, constant potential and potential cycling methods are also utilized to perform accelerated degradation tests in which the deterioration of current as a function of time or cycle number is taken as representative of catalyst stability.<sup>8,23–29</sup>

It is well established now that there is a discrepancy between a catalyst lifetime obtained from RDE and PEM-WE under similar operating conditions.<sup>14,30,31</sup> The extremely short lifetime of a

catalyst obtained from RDE testing using the constant current method and indicated by the sudden potential jump was attributed to the disk electrode substrate passivation, making the catalyst no longer electrochemically accessible due to the high contact resistance.<sup>11</sup> On the other hand, Tan et al. evaluated a variety of Ir-based catalysts and showed that the phase transformation of the active sites from the highly OER-active hydrous Ir oxy-hydroxide to the less OER-active anhydrous-IrO<sub>x</sub> exerts a harsher oxidative condition (higher potentials) on the electrode.<sup>32</sup>

The OER catalyst performance loss during RDE based stability measurements can, at least in part, be ascribed to the passivation of the RDE disk material, to the dissolution and/ or the physical detachment of the OER catalyst (as evidenced by the quantification of dissolved Ir after RDE tests),<sup>32</sup> and to the accumulation of microscopic oxygen bubbles within the catalyst layer. In our recent studies, we discovered the effect of the latter on the stability results obtained from RDE experiments.<sup>31,33</sup> We have shown that the accumulation of microscopic oxygen bubbles in the pores of a catalyst layer during constant current electrolysis in RDE measurements is causing the apparent catalyst deactivation and failure.<sup>31</sup> The effect of such microscopic bubbles on the performance loss of a catalyst during a gas-evolving reaction was further proven by subjecting the electrochemical cell or the electrolyte to ultrasonication while conducting a typical RDE-based measurement.<sup>33,34</sup>

In this study, we demonstrate that the accumulation of microscopic oxygen bubbles in the catalyst layer strongly affects the outcome of RDE based durability tests, independent of whether they are based on constant current, constant potential, or potential cycling methods. In addition, we show that the same phenomenon leads to a decay of OER catalyst activity in PEM water electrolyzer based aging tests, in which case, however, the OER activity loss can be fully recovered, even after 100's of hours. We also provide an explanation as to why the accumulation of microscopic oxygen bubbles in the catalyst layer is detrimental in RDE testing, while in MEA based tests in an electrolyzer it only causes reversible degradation processes that are fully recoverable.

<sup>†</sup>These authors contributed equally to this work.

\*Electrochemical Society Student Member.

\*\*Electrochemical Society Fellow.

<sup>‡</sup>E-mail: hany.el-sayed@tum.de



## Experimental

**Rotating disk electrode (RDE).**—Electrochemical measurements were carried out in a water jacketed three-electrode cell using a reversible hydrogen electrode (RHE) as a reference electrode, a high surface area Au wire as a counter electrode and a rotating ring-disk electrode (RRDE) consisting of a 5 mm diameter polycrystalline Au disk and Pt ring supported by PTFE body (Pine Research Instrumentation, USA) as a working electrode. The reference electrode potential was calibrated in a H<sub>2</sub>-saturated electrolyte prior to each experiment using the Pt ring of the RRDE.

A 0.05 M H<sub>2</sub>SO<sub>4</sub> aqueous solution was used as electrolyte, which was prepared by mixing high purity H<sub>2</sub>SO<sub>4</sub> (Ultrapur, 96%, Merck Millipore KGaA, Germany) and ultra-pure water (18.2 MΩ cm at 20 °C, Merck Millipore KGaA, Germany). High purity Ar and H<sub>2</sub> (6.0-grade, Westfalen AG) were used to purge the electrolyte.

All RDE electrochemical measurements were performed using an Autolab potentiostat (PGSTAT302N, Metrohm AG) and a rotator (Pine Research Instrumentation) with a polyether ketone shaft. The electrode rotation rate was fixed at 2500 RPM and the electrolyte temperature was maintained at 40 °C using the water jacket. Freshly coated electrodes were dipped in Ar-saturated electrolyte and the non-compensated solution resistance between the reference and working electrode was determined by electrochemical impedance spectroscopy (EIS) from 100 kHz to 100 Hz at open circuit potential (OCP). Then, cyclic voltammetry (CV) was performed between 0.05–1.25 V vs RHE with 20 mVs<sup>-1</sup> scan rate for 10 cycles. Afterwards, the OER polarization curve was recorded between 1.2–1.55 V vs RHE at 10 mVs<sup>-1</sup>. The catalyst OER stability tests were performed by the constant current, constant potential and potential cycling methods in Ar-saturated electrolyte. The initial 100 ms of the constant current and constant potential measurements were excluded in the final graphs in order to eliminate the capacitive contributions to the OER current. This time approximately corresponds to five times the time constant (RC) of the RDE configuration, as calculated by EIS results (not shown here). Due to decay of the current during the constant potential stability measurements, an online iR compensation was utilized in order to apply a constant iR-free potential of 1.53 V<sub>RHE</sub> to the electrode according to the following equation:

$$E_{iR-free} = E_{measured} - i_{OER} \times R$$

where R is the high frequency resistance measured by EIS prior to each measurement.

Before each measurement, the Au working electrode was polished with 0.3 μm alumina polishing suspension (Buhler AG) and sonicated in ultrapure water for several times. The catalyst ink suspension was prepared using 10.46 mg of IrO<sub>2</sub> supported on TiO<sub>2</sub> (IrO<sub>2</sub>/TiO<sub>2</sub> with 75 wt.% iridium, Elyst Ir75 0480 from Umicore, Germany), 2 ml ultrapure water, and 2.4 μl Nafion<sup>®</sup> ionomer solution (5 wt.% ionomer, Sigma Aldrich) in order to achieve ≈1 wt.% ionomer content in the final coating. The suspension was sonicated for 30 min in a sonication bath (Elmasonic S 30 H, Elma Schmidbauer GmbH) in order to achieve a homogenous ink. The temperature of the bath was maintained below 35 °C in order to prevent solvent evaporation. Finally, 20 μl of the prepared ink was drop-casted on the cleaned Au working electrode in order to achieve an iridium loading of 0.4 mg<sub>Ir</sub> cm<sup>-2</sup><sub>disk</sub>. Since RDE is known to be a thin-film technique with controlled mass-transport, high loadings and thus, thick catalyst layers, should be avoided.<sup>35</sup> Due to the rather high packing density of the IrO<sub>2</sub>/TiO<sub>2</sub> catalyst (≈2.3 g<sub>Ir</sub>cm<sup>-3</sup>),<sup>36</sup> a loading of 0.4 mg<sub>Ir</sub> cm<sup>-2</sup><sub>disk</sub> already results in a ≈1.7 μm thick catalyst layer. Since this is already quite thick, a higher loading was not feasible within the RDE setup.

**Membrane electrode assembly (MEA) preparation and cell assembly.**—Using the decal transfer method, MEAs with an active area of 5 cm<sup>2</sup> were prepared. Platinum supported on Vulcan XC72

carbon (45.8 wt.% Pt/C, TEC10V50E from Tanaka, Japan) was used as a hydrogen evolution reaction (HER) catalyst on the cathode electrode and IrO<sub>2</sub> supported on TiO<sub>2</sub> (same as above) as an OER catalyst on the anode electrode. The inks were prepared by mixing de-ionized (DI) water (18 MΩ cm), 2-propanol (purity ≥ 99.9% from Sigma Aldrich) and Nafion<sup>®</sup> ionomer solution (20 wt.% ionomer, D2021 from IonPower, USA) together with the respective amount of catalyst. After mixing the suspension for 24 h using a roller mixer, where ZrO<sub>2</sub> grinding balls (5 mm diameter) were added to achieve a homogenous suspension, the ink was coated onto a thin plastic foil (PTFE, 50 μm thick, from Angst + Pfister, Germany) using the Mayer rod technique. After drying, 5 cm<sup>2</sup> decals were cut from the coating and hot-pressed onto a Nafion<sup>®</sup> 212 membrane (50 μm thick, from Quintech, Germany) at 155 °C for 3 min at a pressure of 2.5 MPa. The actual weight of the decals was determined by weighing the decals before and after the hot-pressing. Throughout the study, the loading was kept constant at 0.3 ± 0.1 mg<sub>Pt</sub> cm<sup>-2</sup><sub>MEA</sub> for the hydrogen cathode and 1.9 ± 0.2 mg<sub>Ir</sub> cm<sup>-2</sup><sub>MEA</sub> for the oxygen anode, respectively. Since low loadings (<0.6 mg<sub>Ir</sub>cm<sup>-2</sup><sub>geo</sub>) lead to additional performance losses due to an inhomogeneous catalyst<sup>37</sup> and in order to be more representative of state-of-the-art loadings (≈2.3 g<sub>Ir</sub>cm<sup>-3</sup>),<sup>38</sup> a rather high loading compared to the RDE setup was chosen for the MEA configuration. The ionomer content was ≈11 wt.%. Sintered titanium (from Mott Corporation, USA) with a porosity of ≈50% and a thickness of 280 ± 10 μm was used as a porous transport layer (PTL) on the anode, whereas on the cathode, a carbon fiber paper (TGP-H 120 T from Toray, no MPL, 20 wt.% PTFE) with a thickness of 370 ± 10 μm was used. The MEA and the PTLs were placed between the flow fields of the electrolyzer cell, and additional virgin PTFE sheets were used as gaskets. A compression of 25% for the carbon PTL was achieved by choosing the right thickness of the gaskets. Specific details about the cell hardware are reported elsewhere.<sup>39</sup>

**Electrochemical characterization of MEAs.**—An automated test station from Greenlight Innovation was used to perform all the electrochemical measurements of the MEAs. Throughout the whole test, the anode was supplied with 5 ml min<sup>-1</sup> deionized (DI) water, which was pre-heated to 80 °C for the MEA conditioning procedure and to 40 °C before the stability measurements. During the stability measurements, the cell temperature was kept constant at 40 °C and the produced gas on the anode side was diluted with nitrogen (100 nccm) to avoid the formation of an explosive gas mixture due to hydrogen permeation through the membrane into the anode compartment. Initially, the cell was conditioned at 1 A cm<sup>-2</sup> for 30 min at 80 °C under nitrogen atmosphere. Subsequently, three consecutive polarization curves were taken at ambient pressure (1 bar<sub>a</sub>) and 80 °C, by increasing the current density from 0.01 to 4 A cm<sup>-2</sup> stepwise and holding at each current for 5 min to ensure a stable cell voltage. The last 10 s of the cell voltage at each current density were averaged. Considering these polarization curves as part of the conditioning, they were not included in the analysis. Subsequently, another polarization curve was recorded at 40 °C, which was used as a reference (beginning of test, BOT). Additionally, AC impedance measurements were performed at each current density in a range from 100 kHz to 1 Hz. The amplitude of the current perturbation was adjusted for each step individually in order to fulfill the criteria of linearity, while still maintaining a sufficient signal to noise ratio. The high-frequency intercept with the real axis in a Nyquist plot was used to determine the high frequency resistance (HFR). At the beginning of test (BoT) as well as at the end of test (EoT), cyclic voltammograms (CVs) of the anode electrode were recorded by flushing the cathode counter electrode with dry H<sub>2</sub> (50 ml min<sup>-1</sup>) to ensure a stable reference potential and supplying the anode electrode with DI water (5 ml min<sup>-1</sup>). The CVs were recorded in a potential range of 0.05 V–1.25 V at 20 mV s<sup>-1</sup> and 40 °C. Moreover, a linear sweep voltammogram (LSV) was recorded at BoT in a potential range of 1.25–1.65 V at 10 mV s<sup>-1</sup> and 40 °C to determine the OER activity under CV conditions. During the chronoamperometric aging



test, the measured decay in current was found to lead to a small difference in Ohmic overpotential (BoT ( $61 \text{ A/g}_{\text{Ir}}$ )  $\approx 10 \text{ mV}$ ; EoT ( $33 \text{ A/g}_{\text{Ir}}$ )  $\approx 5 \text{ mV}$ ), therefore, no iR-compensation was required in this test.

### Results and Discussion

**Activity comparison of RDE and MEA measurements.**—To identify the main reason for the remarkably different catalyst lifetimes estimated using MEA and RDE, we have employed a variety of OER catalyst durability testing procedures using a commercially available OER catalyst ( $\text{IrO}_2/\text{TiO}_2$ ). As stability measurements require comparing applied potentials with corresponding currents or vice versa, it is important to confirm that both RDE and MEA measurements result in comparable OER activities. Therefore, the activities recorded from the two techniques were assessed.

Figure 1a shows the iridium mass-specific LSVs of the  $\text{IrO}_2/\text{TiO}_2$  catalyst in the OER potential region for three RDE measurements (green lines) and two MEA measurements (blue circles and squares); Fig. 1b shows the corresponding Tafel plots. The results clearly indicate that within each technique, the measurements are quite reproducible. However, comparing the two techniques, the mass-specific OER activities obtained in RDE measurements are higher than those obtained in MEAs. This difference in activity may be explained either by the poor utilization of the catalyst in the MEAs, by the different loadings used in the two techniques, or by the effect of the ionomer content (Further details can be found in supplementary note A-1 available online at [stacks.iop.org/JES/168/014512/mmedia](https://stacks.iop.org/JES/168/014512/mmedia)). A poor utilization of the catalyst in the MEAs is excluded as the mass-specific capacitive currents of the MEAs (blue lines in Fig. 1c) are almost twice as large as the ones recorded in RDE experiments (green lines in Fig. 1c). A closer look shows that the polarization curve measured in MEA seems to be off by a constant value of  $\approx 20 \text{ mV}$  over a wide range of current density. Bernt et al.<sup>40</sup> showed that a local increase in partial pressure of oxygen at the electrode can lead to an additional loss in performance. The same holds true for an increase in partial pressure of hydrogen. By using a similar approach as Bernt et al., the  $20 \text{ mV}$  higher potential measured in MEA would equate to a difference in oxygen partial pressure of  $\approx 10 \text{ bar}$  or in hydrogen partial pressure of  $\approx 2 \text{ bar}$  ( $\Delta p = p_{\text{gas,cat}} - p_{\text{gas,channel}}$ ). Although the values seem to be reasonable, Bernt et al. also showed a dependency on current density, which cannot be observed in this case. Hence, it is rather unlikely that an increase in partial pressure of oxygen and/or hydrogen within the catalyst layer is responsible for this discrepancy in activity.

It is, however, well known for platinum that high ionomer loadings can negatively impact the ORR activity<sup>35</sup> and thus the higher ionomer content used within the MEA configuration might explain the lower activity measured. As can be seen in figure A-1 within the supporting information the application of a higher ionomer content (20 wt.%) within the RDE configuration results in a significantly lower activity ( $\approx 3.5$ -times at  $1.5 \text{ V}_{\text{RHE}}$  (HFR-corrected)). Additionally, Bernt et al. showed that with increasing ionomer content, the activity is slightly decreasing.<sup>39</sup> Although no further studies were carried out to measure the change in activity as a function of ionomer content within the RDE configuration, we believe that the different ionomer contents used (1 wt.% ionomer in RDE measurements vs 11 wt.% in MEA measurements) are the origin of the discrepancy in OER activity measured by RDE and MEA. Nevertheless, the results obtained by both techniques are in reasonably good agreement; and therefore stability measurements were successfully assessed as shown in the next sections.

**Chronopotentiometric (CP) aging test.**—CP is the most frequently used method in the literature to estimate the stability of an OER catalyst by RDE measurements, where the observed increase in potential while applying a constant current is attributed to catalyst degradation, and ultimately to a complete loss of active

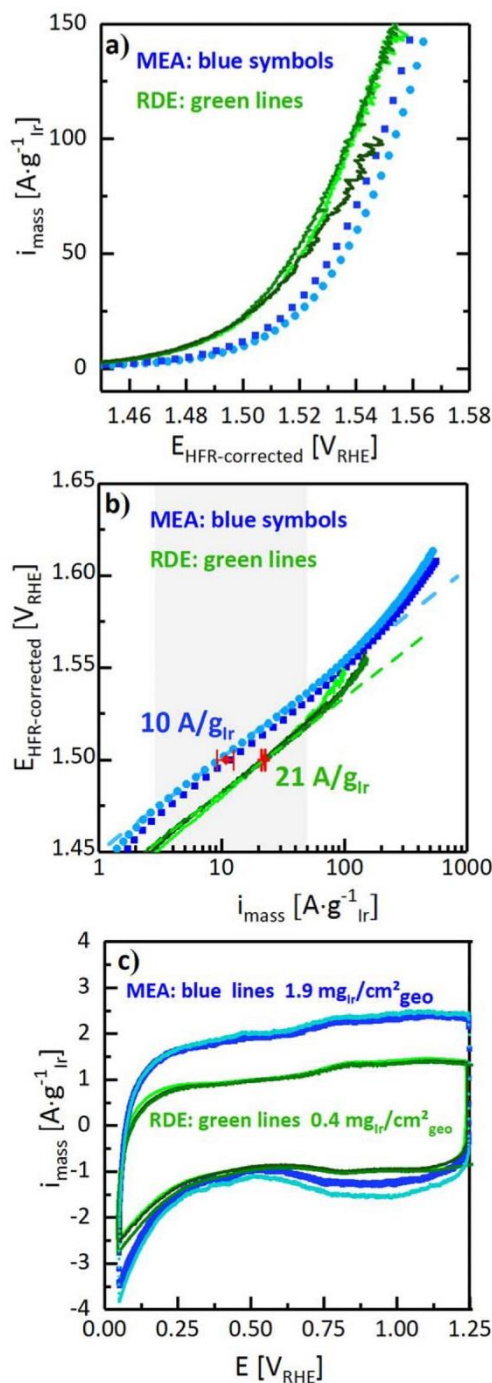


**Figure 1.** (a) Iridium mass-specific linear sweep voltammograms of the  $\text{IrO}_2/\text{TiO}_2$  catalyst at  $40^\circ\text{C}$  and  $10 \text{ mV s}^{-1}$  in MEAs (blue circles and squares) and in RDE experiments (green lines,  $0.05 \text{ M H}_2\text{SO}_4$ , Ar-saturated); (b) Tafel-plots (constructed from a) for three RDE measurements (green lines) and two MEA measurements (blue circles and squares), including the averaged activity determined at  $1.50 \text{ V}_{\text{RHE}}$  (HFR-corrected) indicated by the red symbols; (c) Cyclic voltammograms in the purely capacitive voltage region at  $20 \text{ mV s}^{-1}$  for three RDE measurements in Ar-saturated electrolyte (green lines) and for two MEA measurements with  $50 \text{ nccm H}_2$  at the cathode side (blue lines).

material.<sup>41–44</sup> Figure 2a shows the potential transient recorded in

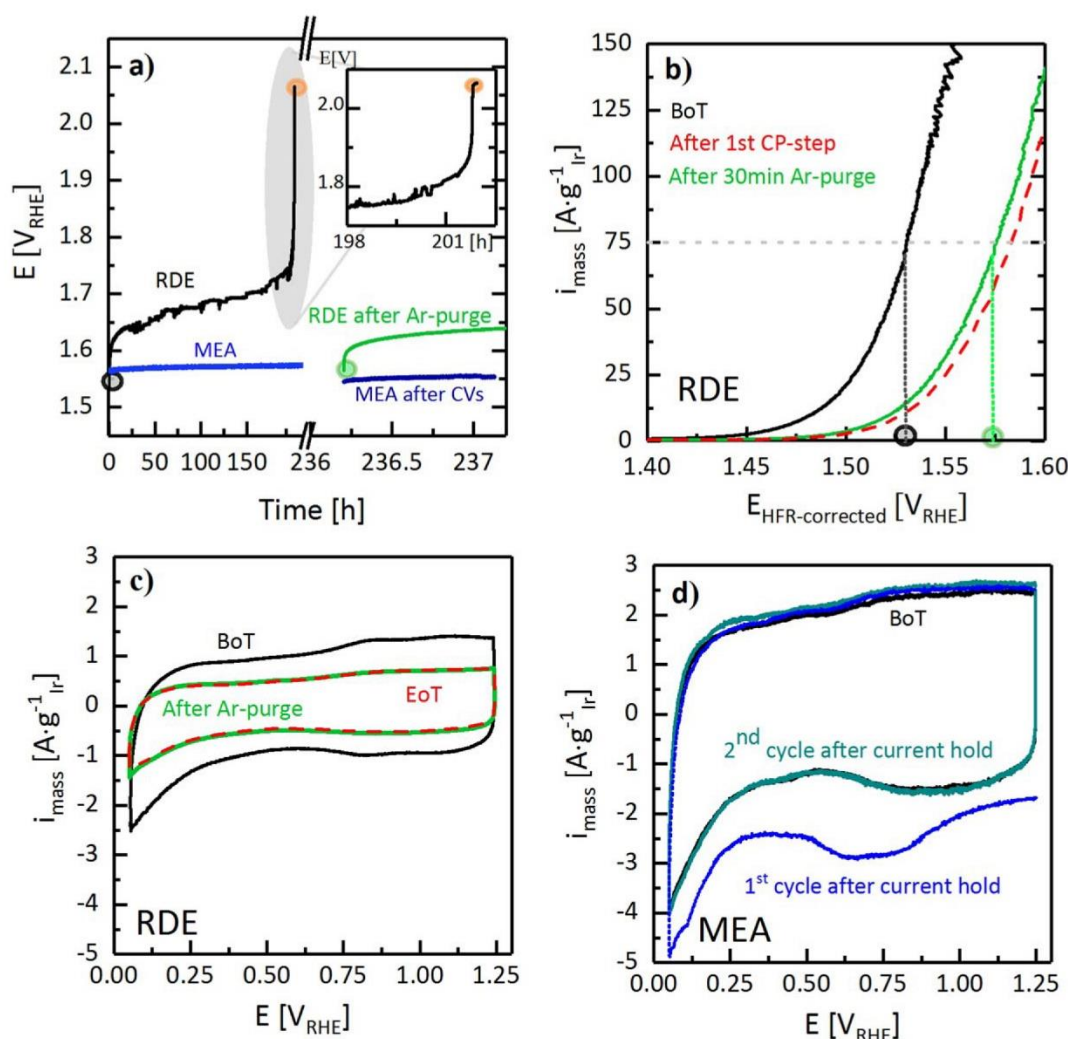


**Figure 2.** (a) Chronopotentiometry at  $70 \text{ A g}^{-1}_{\text{Ir}}$  of RDE measurements at BoT (black) and after purging with Ar for 30 min. (Ar-CV;  $20 \text{ mVs}^{-1}$ ) (green curve) and MEA measurements at BoT (light blue) and after CV ( $50 \text{ nccm H}_2$  at the cathode) (dark blue). Inset shows the last hours of the first CP-step of the RDE measurements. (b) Mass-specific polarization curves for RDE measurements at BoT (black), after first CP-step and Ar-CV (green) and after second CP-step (EoT) and Ar-CV (red) recorded at  $10 \text{ mV s}^{-1}$ . (c) Cyclic voltammograms for RDE measurements recorded at BoT (black), after first CP-step (green) and after second CP-step (dotted red) at  $20 \text{ mV s}^{-1}$  in an Ar-purged electrolyte. (d) Cyclic voltammograms recorded for MEA measurements at BoT (black) and after first CP-step at  $20 \text{ mV s}^{-1}$ , where the first (blue) and the second (cyan) cycles after first CP-step are shown.

MEA and RDE measurements at a current density of  $70 \text{ A g}^{-1}_{\text{Ir}}$ . In the RDE experiment, the potential increases continuously (black line in Fig. 2a) reaching  $\approx 1.75 \text{ V}$ , at which a sudden potential jump occurs. Subsequently, the potential levels out at  $\approx 2.1 \text{ V}$  (orange circle, Fig. 2a inset), a potential one would measure when the same geometric current is applied to a bare Au-disk.<sup>31</sup> This behavior is typically interpreted in the literature by the degradation of the catalyst.<sup>32,44</sup> According to Eq. 1, an increase in OER overpotential ( $\eta$ ) by one Tafel slope (TS; ca.  $50 \text{ mV}$  in this case) at a constant current ( $i$ ), should correspond to a 90% loss of electrochemically active surface area or electrode roughness factor Ref. 31. Therefore, and according to this degradation hypothesis, no catalyst should remain after a total potential increase of  $>400 \text{ mV}$  (black line in Fig. 2a).

$$\eta = TS \cdot \left[ \lg \left( \frac{i}{i_0} \cdot \frac{1}{rf} \right) \right] \quad [1]$$

However, after the applied current was stopped and the electrolyte was purged with Ar for 30 min at 2500 rpm, followed by applying the same current ( $70 \text{ A g}^{-1}_{\text{Ir}}$ ), the starting potential of this second CP-step was almost the same as that of the first CP-step, showing the same gradual increase of potential (green line in Fig. 2a). This result indicates that the catalyst did not collapse as suggested by the potential jump and that a correlation between this increase in potential and catalyst degradation seems highly unlikely. This increase in potential is related to an accumulation of microscopic oxygen bubbles and the concomitant shielding of active sites within the catalyst layer.<sup>31</sup> The formation and stability of such microscopic gas bubbles on the surface of gas evolving catalysts has been also shown by different imaging techniques such as total-internal reflection fluorescence (TIRF) microscopy, atomic force



microscopy (AFM) and X-ray radiography.<sup>45–47</sup> However, after the first CP-step was completed, the accumulated microscopic oxygen bubbles were removed by diffusion during the 30 min rotation in Ar-saturated electrolyte, which led to the re-exposure of active sites and performance recovery.

The potential increase was not detected in an MEA measurement in a PEM-WE, in fact, the performance was stable throughout the whole measurement period (~9 d) (light blue line in Fig. 2a). This drastic difference in the potential transient obtained in MEA vs RDE demonstrates that the RDE-based CP test cannot be reliably used to test the stability of OER catalysts.

After the initial CP-step with the MEA in the PEM-WE, OER polarization curves along with CVs are recorded and the same current is applied again (second CP-step, dark blue line Fig. 2a). Surprisingly, the initial potential of the second CP-step within the MEA configuration is even 10 mV smaller than that of the first CP-step and again showed a stable performance, a phenomenon observed elsewhere in literature, but never explained.<sup>48</sup> During operation, an increase in local partial pressure within the catalyst layer as well as the accumulation of oxygen bubbles is possible, however, distinguishing between the two is not trivial. The enhanced cell performance observed for the second CP-step within the MEA configuration might be related to either the microscopic oxygen bubbles formed and/or accumulated in the catalyst layer during the first CP-step or a developing local increase in oxygen and/or hydrogen partial pressure. Assuming that the increase in potential is only related to either an increase in partial pressure of oxygen or hydrogen, this would result in a pressure difference ( $\Delta p = p_{\text{gas,catalyst}} - p_{\text{gas,channel}}$ ) of  $\approx 2$  bar and  $\approx 0.5$  bar respectively, both of the values being reasonable. While an increase in oxygen or hydrogen partial pressure can subside during OCV or zero current, the trapped oxygen bubbles can either be physically detached/diffuse away during the recorded CV under the water flow, or reduced electrochemically by scanning to low cathodic potentials ( $< 1.0$  V) within the MEA configuration. The latter is indicated by the additional cathodic current observed in the first CV (blue line in Fig. 2d) obtained after the first CP-step that is not observed in the second subsequent CV (cyan line in Fig. 2d).

To prove that the active sites are indeed shielded by microscopic oxygen bubbles, CVs and polarization curves were recorded for the RDE measurements subsequent to each CP-step and a 30 min. Ar purge. Figure 2b shows the mass-specific polarization curves recorded at the BoT (black line), after the first CP-step, a 30 min. Ar purge, and a subsequent CV (green line), and after the second CP-step, a 30 min Ar purge, and a subsequent CV (red dotted line). Quite nicely, the potentials corresponding to the  $70 \text{ A g}^{-1}_{\text{Ir}}$  in the polarization curves are in good agreement with the initial values of both CP-steps (black and green circles in Figs. 2a and 2b), proving that the polarization curves and the initial potentials of the CP measurements can indeed be correlated. According to Eq. 1, no catalyst should remain after the potential jump. However, the polarization curves reveal that there is still a sufficiently high OER activity compared to a bare Au-disk,<sup>31</sup> although significantly smaller compared to the initial activity. Accordingly, comparing the OER activities at  $1.5 \text{ V}_{\text{RHE}}$  suggests that only  $\approx 20\%$  of the initial catalyst layer seems to remain, whereas  $\approx 80\%$  is lost due to “microscopic bubbles-induced degradation.” The accumulation of oxygen in the catalyst layer and partial shielding of the active sites result in an increasing potential at the remaining active sites to provide the same applied current. Consequently, the increased potential on the remaining active sites inevitably enhances iridium dissolution.<sup>49–52</sup> In fact, if the accumulation of microscopic bubbles could be avoided, no significant dissolution is expected to occur, since shielding a fraction of the catalyst layer is the main cause for the increasing potential and the accompanied iridium dissolution happening at the still accessible sites.

Figure 2c shows CVs measured at the BoT (black line), after the first CP-step (green line) and at EoT (red dotted line), each recorded after purging with Ar for 30 min to ensure a catalyst layer free of

microscopic bubbles. The CVs recorded after the both CP-steps show that at least half of the initial catalyst layer is still electrochemically accessible. Conclusively, this comparison demonstrates that using chronopotentiometry for estimating the stability of an OER catalyst in RDE measurements is not reliable, since the observed increase in potential seems to be exclusively caused by the accumulation of microscopic oxygen bubbles and the by subsequent shielding of active sites within the catalyst layer.

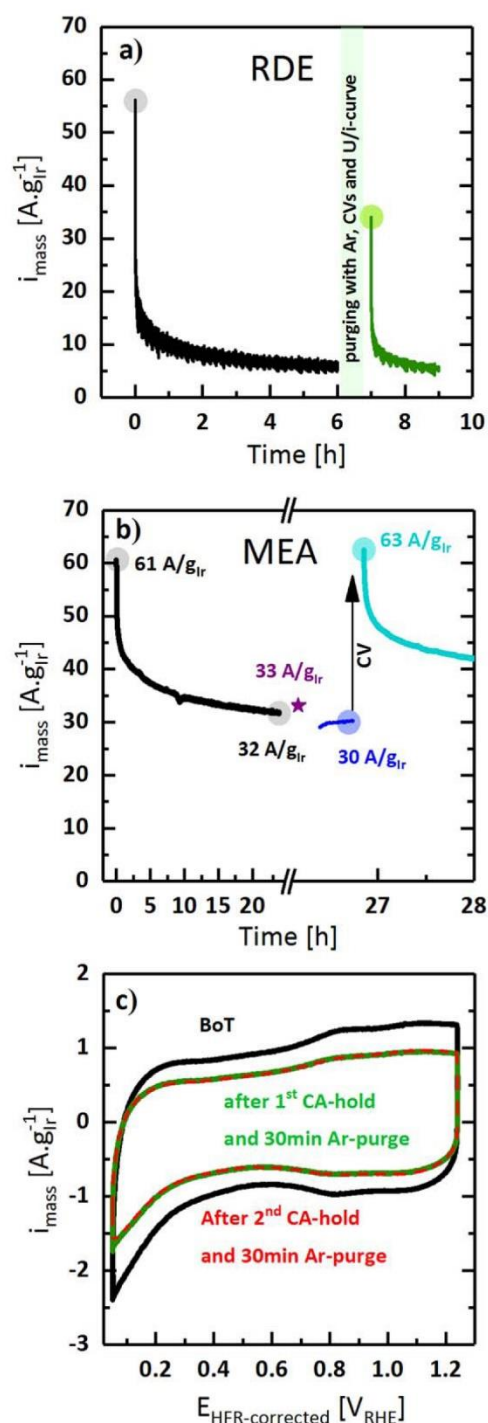
**Chronoamperometric (CA) aging test.**—The observed decrease in current during a constant potential measurement is attributed to catalyst degradation and is commonly correlated to the lifetime of an OER catalyst.<sup>14,29</sup> In this study, a constant potential of  $1.53 \text{ V}_{\text{RHE}}$  (iR-corrected) is applied and the corresponding current is recorded during the RDE and MEA measurements. Within the first few minutes of a CA measurement in an RDE, a rapid decrease in the mass-normalized current of almost 75% can be observed (Fig. 3a, black curve), followed by a more gradual decrease in current over the subsequent 6 h. The initial OER activity of  $56 \text{ A g}^{-1}_{\text{Ir}}$  is taken after 100 ms, so that capacitive contributions are negligible (see experimental section). If this drop in current over the first hour were related to catalyst degradation, then almost 85% of the catalyst would have to be lost, even though this catalyst was proven to be stable in a PEM-WE over hundreds of hours.<sup>17</sup> Therefore, this rapid drop in current must be related to the fast filling of the catalyst layer with microscopic oxygen bubbles, shielding a significant fraction of the active sites, so that the current decreases.<sup>31</sup> Applying the same potential after purging for 30 min with Ar resulted in an initial current that is only 60% ( $34 \text{ A g}^{-1}_{\text{Ir}}$ , green circle in Fig. 3a) of the initial current recorded for the first CA-step (gray circle in Fig. 3a), which again rapidly decays within the first hour of the second CA-step before it levels out ( $\sim 5 \text{ A g}^{-1}_{\text{Ir}}$ ). While the rapid decay in current during the CA-step can undoubtedly be related to the partial shielding of active sites by microscopic oxygen bubbles, the 40% lower initial current in the subsequent second CA-step suggests that the catalyst also partially degraded during first CA-step. Polarization curves recorded at BoT, after the first CA-step, and at EoT, are provided at the supplementary note A-2.

Figure 3c shows that the CVs recorded after the first and second CA-steps (each preceded by a 30 min Ar purge) are  $\sim 30\%$  smaller compared to the one measured at BoT (black curve in Fig. 3c), suggesting that roughly one third of the catalyst is degraded by the end of the experiment and that the decrease in current during a CA-step does not correlate to catalyst degradation. In summary, these results confirm that the stability of an OER catalyst cannot be examined by applying a constant potential in RDE measurements, since the current decrease is largely due to the shielding of active sites by microscopic oxygen bubbles, which are trapped in the catalyst layer.

Using the same catalyst in an MEA and testing it in a PEM-WE, it was found that the current decreased by  $\sim 50\%$  after  $\sim 24$  h (black curve in Fig. 3b), suggesting that half of the catalyst is either shielded or has degraded. The current at  $1.53 \text{ V}_{\text{RHE}}$  derived from a subsequently measured polarization curve after the first CA-step ( $33 \text{ A g}^{-1}_{\text{Ir}}$ , purple star in Fig. 3b) closely matches the steady-state current ( $32 \text{ A g}^{-1}_{\text{Ir}}$ ) at  $1.53 \text{ V}_{\text{RHE}}$  after the 24 h CA-step. The current at  $1.53 \text{ V}_{\text{RHE}}$  also remains essentially constant ( $30 \text{ A g}^{-1}_{\text{Ir}}$ ) over a subsequent potential hold (dark blue curve in Fig. 3b), which either means that the catalyst has indeed degraded or that the  $\text{O}_2$  bubbles are remaining in the catalyst layer.

Scanning the potential to below  $1 \text{ V}_{\text{RHE}}$  to remove the oxygen bubbles or to subside a local increase in oxygen and/or partial pressure in the catalyst layer, followed by a CA-step (turquoise curve in Fig. 3b), the same initial current at  $1.53 \text{ V}_{\text{RHE,HFR-corrected}}$  ( $63 \text{ A g}^{-1}_{\text{Ir}}$ ) as that obtained for the first CA-step ( $61 \text{ A g}^{-1}_{\text{Ir}}$ ) was obtained. This firmly proves that the performance decay during a CA step was solely due to shielding the active sites by oxygen bubbles or the increase in local partial pressure of oxygen and/or hydrogen. An increase in partial pressure, however, would occur instantly and not





**Figure 3.** (a) Chronoamperometry at 1.53 V<sub>RHE</sub> (internal iR-correction was applied) measured by RDE at BoT (black) and after first CA-hold (green). After each CA-hold, the electrolyte was purged with Ar for 30 min and a CV (see Fig. 3c) was recorded. (b) Chronoamperometry at 1.53 V<sub>RHE</sub> (HFR-corrected) measured in an MEA at BoT (black), the purple star represents the activity measured at 1.53 V<sub>RHE</sub> during a subsequent polarization curve, directly after the polarization curve (blue) and after a subsequent CV (turquoise). (c) Cyclic voltammograms recorded at BoT (black), after a 30 min. Ar-purge after the first CA-hold (green) and after a 30 min. Ar-purge after the second CA-hold at EoT (red dotted) at 20 mV s<sup>-1</sup>.

over hours (see gradual decay in current over hours in Fig. 3b), wherefore an increase in partial pressure seems rather unlikely. So far, it is not trivial to give a solid explanation for whether this reversible degradation in an MEA is due to the electrochemical reduction of O<sub>2</sub>, due to the removal of O<sub>2</sub> by diffusion, or an even more complex phenomenon.

Although the testing time in the MEA was much longer than that in the RDE configuration, no catalyst degradation was observed in the MEA, while for the RDE test, about 40% of the current could not be recovered. This confirms that using RDE measurements to predict the lifetime of a catalyst by applying a constant potential is not a valid approach, since the recorded drop in current is mostly due to the shielding of active sites by trapped microscopic oxygen bubbles and since the observed loss in OER activity is most likely a consequence of it. On the other hand, in MEA measurements, the current loss is reversible and it can be avoided by a proper design of the stability test.

**Potential cycling aging test.**—Undeniably, the OER catalyst stability during transient operation is of vital interest, since it will be an important consideration when coupling a PEM water electrolyzer with renewable energies that are inherently intermittent in power output.<sup>53–56</sup> By cycling the potential between idle periods (OCV) and times of operation (>1.4 V<sub>RHE</sub>), the fluctuating power supply is commonly mimicked in RDE durability tests, and the observed decrease in OER activity is attributed to catalyst degradation.<sup>5,7,14</sup> In this study, the potential was cycled between 1.3 V<sub>RHE</sub> and 1.6 V<sub>RHE</sub>, avoiding reducing conditions, which can affect the performance of a PEM water electrolyzer.<sup>17</sup> Figure 4a depicts the mass-normalized current [A g<sub>Ir</sub><sup>-1</sup>] extracted at 1.5 V<sub>RHE</sub> from the anodic scan of the respective cycle during RDE measurements as a function of cycle number. Evidently, the current significantly drops within the first two cycles by ~40% (cycles 1 and 2 in Fig. 4a), whereas the decrease slows down afterwards. After 20 cycles, only 40% of the initial activity is remaining (10 A g<sub>Ir</sub><sup>-1</sup>, Fig. 4a), which means that 20 cycles would be enough to degrade more than half of the catalyst, assuming that this deactivation is owing only to catalyst degradation. However, after purging with Ar for 30 min and recording a CV, three additional cycles were performed (green circles in Fig. 4a), showing that roughly 70% of the initial activity can be recovered (~15 A g<sub>Ir</sub><sup>-1</sup>, red dotted circle). While a significant fraction of the catalyst degradation can be recovered, some irreversible catalyst degradation must have occurred, although this irreversible degradation is not expected in the here used potential range.<sup>17,57</sup> Again, the microscopic oxygen bubbles must be directly responsible for the reversible degradation, and indirectly responsible for the irreversible degradation.

The anodic scans of the individual cycles in the above RDE experiment are shown in Fig. 4c, where it becomes quite clear that the second cycle (dark green curve) during the first cycling test and the first one (red dotted line) recorded after a 30 min. Ar purge and a CV are perfectly identical, clearly demonstrating the partial recovery of activity. It can therefore be concluded that part of the catalyst layer degraded during the cycling test since only 70% of the current can be recovered by Ar purge. The CVs recorded for the potential cycling stability test at the BoT and at EoT are shown in Fig. A3.

The same stability protocol was executed in an MEA and the results are shown in Fig. 4b. Obviously, the current (~12 A g<sub>Ir</sub><sup>-1</sup>) recorded at 1.50 V<sub>RHE</sub> during a polarization curve (purple diamond, measured galvanostatically beforehand) is similar to the current (~12.5 A g<sub>Ir</sub><sup>-1</sup>) obtained during the first anodic cycle at the same potential, whereas during the subsequent 200 cycles (light blue squares) the activity slightly decreases by ~10%. This decrease is often interpreted in the literature as degradation of the catalyst,<sup>5</sup> however, after recording a polarization curve and a subsequent CV between 0.05–1.25 V<sub>RHE</sub>, the activity increases to 16 A g<sub>Ir</sub><sup>-1</sup> at 1.50 V<sub>RHE</sub> (blue circles in Fig. 4b), i.e., to a value even higher than the one recorded during the very first cycle.

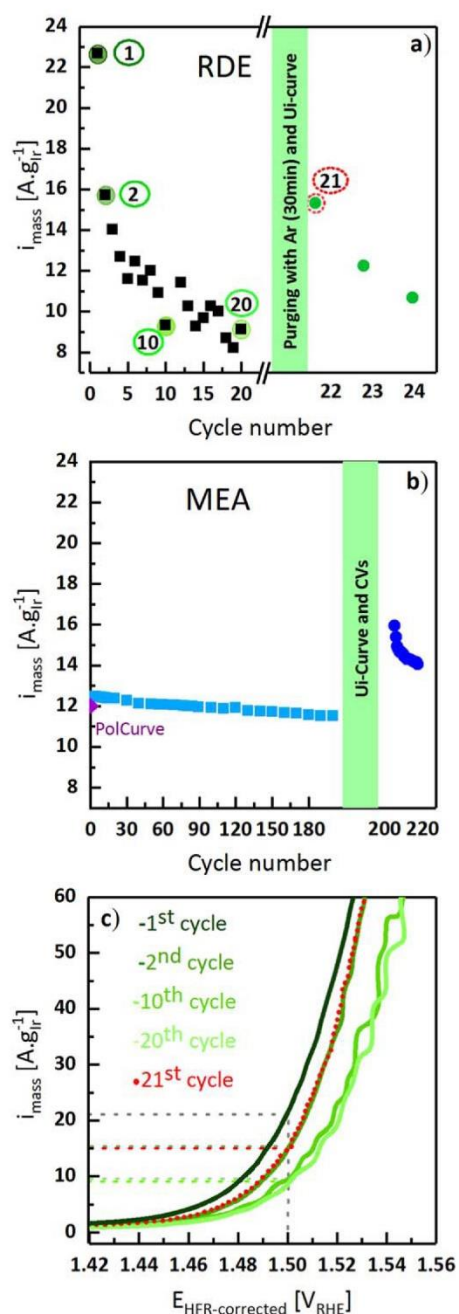


**Figure 4.** (a) Mass-specific currents, extracted at  $1.50 V_{\text{RHE}}$  of the anodic scan during cycling between  $1.3\text{--}1.60 V_{\text{RHE}}$  (iR-corrected) at  $10 \text{ mV s}^{-1}$  in RDE configuration, recorded for the initial 20 cycles (black squares) and for 3 cycles after a 30 min. Ar-purge, a CV and a polarization curve (green circles). (b) Mass-specific currents, extracted at  $1.50 V_{\text{RHE}}$  during cycling between  $1.3 V_{\text{RHE}}\text{--}1.60 V_{\text{RHE}}$  (HFR-corrected) with  $10 \text{ mV s}^{-1}$  in an MEA, for the initial 200 cycles (light blue squares) and for 20 cycles (dark blue circles) recorded after obtaining a polarization curve and a CV. The purple diamond represents the extracted current at  $1.50 V_{\text{RHE}}$  from the polarization curve recorded directly before the 200 cycles, and (c) Mass-specific anodic cycles (from RDE) recorded at  $10 \text{ mV s}^{-1}$  during cycling depicted for the first (dark green line), 2nd (green line), 10th (light green line), 20th (bright green line) and for the 22nd (red dotted line).

In contrast to the activity decrease over the course of the first 200 cycles, the decrease observed during the subsequent cycles is much more severe ( $\sim 13\%$  within 20 cycles). Both, the higher activity measured along with the observed fast decrease is related to the CV recorded directly before the second cycling, whereas the first cycling was recorded directly after measuring a polarization curve, during which large OER currents were drawn. By cycling the cell to lower cathodic potentials ( $<1.0 V_{\text{RHE}}$ ), as it was already shown in the previous section (Fig. 2d), the microscopic oxygen bubbles trapped within the catalyst layer can be removed and/or an increase in oxygen and/or hydrogen partial pressure can decay. Since the cell was polarized at high potentials prior to the first cycling, a certain fraction of the catalyst layer must have already been shielded or a partial pressure difference was already developed and hence, did already affect the performance. This would explain the apparently lower activity along with the smaller decrease in activity during the first 200 cycles (light blue squares). On the other hand, once the catalyst layer is free of any microscopic oxygen bubbles after a CV into the potential range where  $\text{O}_2$  can be reduced and any partial pressure buildup did subside, the catalyst can be fully utilized, which results in a high initial activity that, however, decays more rapidly due to the fast filling by microscopic oxygen bubbles and/or the increase in local partial pressure. In summary, this comparison shows that potential cycling cannot be used in RDE measurements to predict the lifetime of an OER catalyst, since the claimed degradation is caused by a shielding of active sites via trapped microscopic oxygen bubbles within the catalyst layer.

**MEA aging for the three different aging protocols.**—Each of the three investigated aging protocols showed that during MEA measurements in a PEM-WE, a fraction of the catalyst layer is shielded by microscopic oxygen bubbles and that by recording a CV to low potentials, the activity can be fully recovered. This suggests that there are no irreversible changes to the catalyst and the catalyst layer of the MEA during the test. Hence, the polarization curves recorded at BoT and at EoT should be identical, independent of which aging protocol is applied. The polarization curves representing the initial activity at BoT (black squares) and those recorded at the EoT for each aging protocol are depicted in Fig. 5a. In fact, the polarization curves at the end of the different stability tests match quite well with BoT performance, especially when the HFR-corrected curves are considered, thereby confirming that none of these aging tests caused any degradation of the catalyst and the catalyst layer. The corresponding HFRs as well as Tafel plots at BoT and at EoT are depicted in Fig. 5b. Further details regarding this figure can be found in supplementary note A-4.

We provide here a possible hypothesis (Fig. 6) as to why the effect of trapped oxygen bubbles is more pronounced in case of the RDE compared to MEA measurements. For this, we first focus on the processes occurring during MEA measurements in a PEM-WE. Since the through-plane electrical resistance within the catalyst layer is quite small ( $\approx 0.04 \text{ m}\Omega \text{ cm}^2_{\text{geo}}$ )<sup>17</sup> compared to the proton sheet resistance ( $14\text{--}30 \text{ m}\Omega \text{ cm}^2_{\text{geo}}$ ),<sup>57</sup> the OER reaction should mainly occur at the membrane/electrode interface (Fig. 6a).<sup>39</sup> Thus, although the reaction is occurring throughout the whole catalyst layer, the utilization of the catalyst layer should be highest at the membrane/electrode interface. The catalyst layer thickness at a loading of  $2 \text{ mg}_{\text{Ir}} \text{ cm}^{-2}_{\text{geo}}$  is  $\approx 8\text{--}10 \mu\text{m}$ ,<sup>37</sup> through which the produced oxygen has to escape. Within the OER catalyst layer, the local partial pressure of oxygen must thus increase, resulting in a pressure gradient from the membrane | electrode ( $P_{\text{O}_2, \text{M|E}}$ ) to the electrode | PTL interface ( $P_{\text{O}_2, \text{E|PTL}}$ ), illustrated by the blue curved line in Fig. 6a (marked as ①). This pressure difference might enhance the removal of oxygen within the catalyst layer towards the PTL, thereby minimizing the accumulation of oxygen within the catalyst layer.

The above consideration is only true, however, if a sufficiently large flux of water can be sustained from the electrode | PTL to the membrane | electrode interface. This, we believe, is provided by the



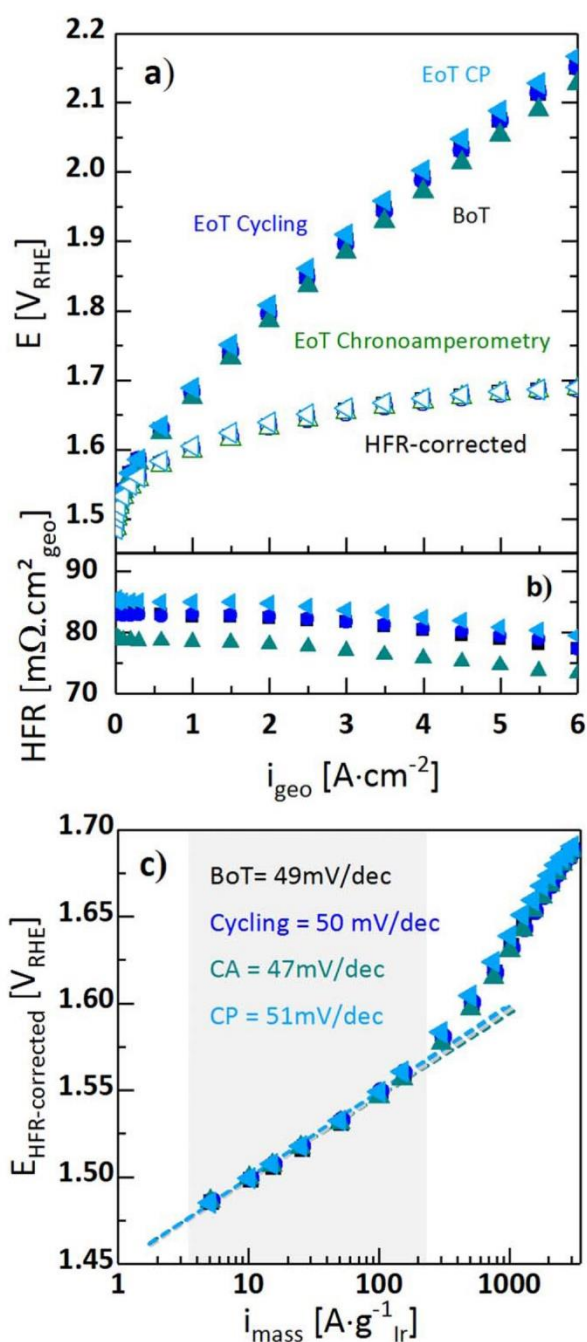


**Figure 5.** (a) Galvanostatically measured polarization curves at 40 °C recorded at BoT (black squares) and at EoT after 223 potential cycles between 1.3–1.60 V<sub>RHE</sub> (blue circles), after ~26 h of CA at 1.53 V<sub>RHE</sub> (green triangles), and after ~10 d of CP-hold at 70 A g<sup>-1</sup><sub>Ir</sub> (light blue triangles); The open symbols represent the HFR-corrected polarization curves. (b) The corresponding HFRs as a function of current density. (c) Mass-specific Tafel-plots (data replotted from (a) at BoT (red line) and at EoT after 223 cycles (blue circles), after ~26 h at 1.53 V<sub>RHE</sub> (green triangles) and after ~10 d at 70 A g<sup>-1</sup><sub>Ir</sub> (light blue triangles). Please note that in many instances the data points overlap so closely that not all of the four different symbols can be discerned in each instance.

electro-osmotic water drag from anode to cathode through the membrane (Fig. 6a, ②). The drag coefficient under electrolyzer

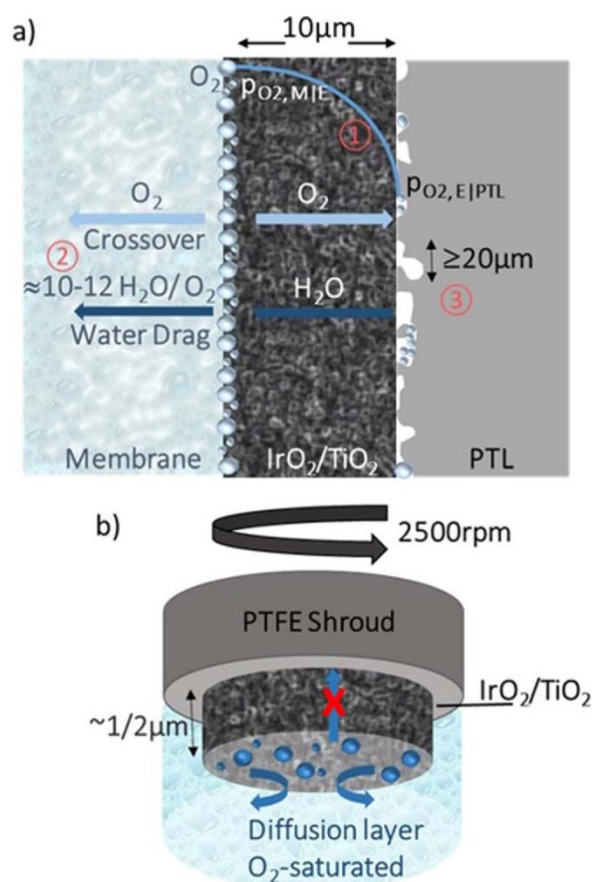


**Figure 6.** (a) Scheme of a single cell (MEA), illustrating possible reasons for a different degradation rate in MEA compared to an RDE: 1) pressure build-up within the catalyst layer; 2) electro-osmotic water drag and oxygen permeation; 3) restricting the size of a micro-bubble formed in an MEA | PTL interface to the pore diameter of the PTL. (b) Scheme of an RDE tip operation during OER operation.

operating conditions ranges between 2.5–3.2 H<sub>2</sub>O/H<sup>+</sup>, so that roughly 10–12 water molecules per produced oxygen molecule (4 H<sup>+</sup> per generated O<sub>2</sub>) are dragged through the membrane and, consequently, through the anode catalyst layer, i.e., ≈5–6 times the amount required to produce one O<sub>2</sub> molecules.<sup>58</sup> This electro-osmotic water drag will thus sustain a sufficiently large flux of water to the membrane | electrode interface, so that the current density distribution across the anode catalyst layer will be governed by the proton conduction resistance. In this case, oxygen will be produced at a higher rate near the membrane | electrode interface (see above), producing the  $p_{O_2}$  gradient sketched by ① in Fig. 6a, which in turn allows for an efficient removal of O<sub>2</sub> gas bubbles from the anode catalyst layer. Additionally, the pore size of the PTL (≥20 μm) may prevent the formation of macroscopic oxygen bubbles (0.1 – 1 mm) and thus the blockage of larger sections of the anode catalyst layer (Fig. 6, ③). Commonly, however, a pressurized operation is desirable, while the whole study was conducted at ambient pressure. Bernt et al. showed that an increase in pressure leads to a higher hydrogen crossover.<sup>59</sup> Assuming the same holds true for oxygen crossover, an even more efficient removal of oxygen bubbles is expected for operations at higher pressure. Since there was already no degradation observed in the case of ambient pressure operation, none is expected in the case of pressurized operation.



On the other hand, in the RDE configuration, the oxygen can only be removed by diffusion within the catalyst layer or by convection in the radial direction at the outer surface of the catalyst layer (blue arrows, Fig. 6b) into an O<sub>2</sub>-saturated electrolyte. Even in the absence of water transport resistances into the catalyst layer, the primary (i.e., conductivity-controlled) current distribution in this case favors the highest current density at the catalyst | electrolyte rather than at the disk | electrolyte interface, so no positive  $p_{O_2}$  gradient would be established from the disk | electrolyte to the catalyst | electrolyte interface to drive O<sub>2</sub> removal. In conclusion, the electro-osmotic drag of water across the catalyst layer of an MEA and the skewing of the OER current density distribution towards the membrane | electrode interface due to a minimized proton conduction resistance are the most likely reason for the apparently more effective O<sub>2</sub> bubble removal in an MEA configuration. If one would be able to design a measurement setup, where one can stimulate dynamicity within the catalyst layer during the measurement in liquid electrolyte, one might be able to predict the lifetime of a catalyst without the need of an MEA setup. One possibility to prevent the accumulation of bubbles would be the application of sonication during operation,<sup>33</sup> which, however, is not feasible with catalyst in nano-particulate form. To the best of our knowledge, up to now there is no other technique other than assessing the long-term stability within an MEA configuration, which can be used to reliably predict the lifetime of OER catalysts.

### Conclusions

In this study, the most commonly used methods to predict the lifetime of OER catalysts, namely chronoamperometry, chronopotentiometry and potential cycling, were conducted in both RDE and MEA cells and directly compared with each other. It was demonstrated that none of the three investigated aging tests in an RDE configuration provides a measure of OER catalyst degradation/dissolution. This is mainly attributed to the accumulation of oxygen bubbles within the catalyst layer, shielding most of the active sites in case of an RDE test, resulting in a rapid increase in potential, for a CP test, or a rapid decrease in current, for a CA or potential cycling test, which is commonly interpreted as degradation of the catalyst. The accumulation of bubbles was found to induce irreversible degradation of the catalyst, a phenomenon that we did not observe in an MEA test. In fact, we demonstrated that while a local increase in partial pressure of oxygen and/or hydrogen seems rather unlikely, the accumulation of microscopic oxygen bubbles takes place also in an MEA, but to a much less extent compared to RDE. Therefore, the degradations observed in MEA for all the methods were fully reversible and almost no irreversible catalyst degradation was observed.

In summary, none of the most commonly used methods in RDE measurements is applicable to predict the lifetime of OER catalysts, since the observed decrease in performance is solely caused by the shielding of active sites via trapped microscopic oxygen bubbles. If it would be possible to prevent the accumulation of the microscopic oxygen bubbles within the catalyst layer during the measurement, it might be possible to design a proper stability protocol for testing OER catalysts using RDE measurements.

### Acknowledgments

The authors gratefully acknowledge the German Ministry of Education and Research for financial support of this work within the Kopernikus project P2X (03SFK2V0) and the innoKA project (BMW, 03ET6096A). The authors would like to thank Dr. Maximilian Bernt and Paulette Loichet (Chair of Technical Electrochemistry, Technical University of Munich, Germany) for fruitful scientific discussion.

### Appendix

Supplementary information is available.

### ORCID

Mohammad Fathi Tovini  <https://orcid.org/0000-0003-4334-4471>  
Hubert A. Gasteiger  <https://orcid.org/0000-0001-8199-8703>

### References

1. S. Cherevko, T. Reier, A. R. Zeradjanin, Z. Pawolek, P. Strasser, and K. J. J. Mayrhofer, *Electrochem. Commun.*, **48**, 81 (2014).
2. O. Kasian, S. Geiger, P. Stock, G. Polymeros, B. Breitbach, A. Savan, A. Ludwig, S. Cherevko, and K. J. J. Mayrhofer, *J. Electrochem. Soc.*, **163**, F3099 (2016).
3. Y. Lee, J. Suntivich, K. J. May, E. E. Perry, and Y. Shao-Horn, *J. Phys. Chem. Lett.*, **3**, 399 (2012).
4. P. Lettenmeier, L. Wang, U. Golla-Schindler, P. Gazdzicki, N. A. Cañas, M. Handl, R. Hiesgen, S. S. Hosseiny, A. S. Gago, and K. A. Friedrich, *Angewandte Chemie (International ed. in English)*, **55**, 742 (2016).
5. E. Oaktou, D. Lebedev, M. Povia, D. F. Abbott, E. Fabbri, A. Fedorov, M. Nachtegaal, C. Copéret, and T. J. Schmidt, *ACS Catal.*, **7**, 2346 (2017).
6. H. Ohno, S. Nohara, K. Kakinuma, M. Uchida, A. Miyake, S. Deki, and H. Uchida, *J. Electrochem. Soc.*, **164**, F944 (2017).
7. T. Reier, M. Oezaslan, and P. Strasser, *ACS Catal.*, **2**, 1765 (2012).
8. S. Zhao, A. Stocks, B. Rasimick, K. More, and H. Xu, *J. Electrochem. Soc.*, **165**, F82 (2018).
9. N. H. Kwon, M. Kim, X. Jin, J. Lim, I. Y. Kim, N.-S. Lee, H. Kim, and S.-J. Hwang, *NPG Asia Mater.*, **10**, 659 (2018).
10. Y.-T. Kim et al., *Nat. Commun.*, **8**, 1449 (2017).
11. S. Geiger, O. Kasian, A. M. Mingers, S. S. Nicley, K. Haenen, K. J. J. Mayrhofer, and S. Cherevko, *ChemSusChem*, **10**, 4140 (2017).
12. K. E. Ayers, E. B. Anderson, K. Dreier, and K. W. Harrison, *ECSS Trans.*, **50**, 35 (2013).
13. C. Rakousky, U. Reimer, K. Wippermann, M. Carmo, W. Lueke, and D. Stolten, *J. Power Sources*, **326**, 120 (2016).
14. S. M. Alia, B. Rasimick, C. Ngo, K. C. Neyerlin, S. S. Kocha, S. Pylypenko, H. Xu, and B. S. Pivovar, *J. Electrochem. Soc.*, **163**, F3105 (2016).
15. H.-S. Oh, H. N. Nong, T. Reier, A. Bergmann, M. Gliech, J. Ferreira de Araújo, E. Willinger, R. Schlögl, D. Teschner, and P. Strasser, *JACS*, **138**, 12552 (2016).
16. S. Geiger et al., *Nat. Catal.*, **1**, 508 (2018).
17. A. Weiß, A. Siebel, M. Bernt, T.-H. Shen, V. Tileli, and H. A. Gasteiger, *J. Electrochem. Soc.*, **166**, F487 (2019).
18. C. Spöri, J. T. H. Kwan, A. Bonakdarpour, D. P. Wilkinson, and P. Strasser, *Angewandte Chemie (International ed. in English)*, **56**, 5994 (2017).
19. C. C. L. McCrory, S. Jung, J. C. Peters, and T. F. Jaramillo, *JACS*, **135**, 16977 (2013).
20. B. S. Yeo, *Nat. Catal.*, **2**, 284 (2019).
21. Y. Yao et al., *Nat. Catal.*, **2**, 304 (2019).
22. Y. Lin, Z. Tian, L. Zhang, J. Ma, Z. Jiang, B. J. Deibert, R. Ge, and L. Chen, *Nat. Commun.*, **10**, 162 (2019).
23. J. Guan, Z. Duan, F. Zhang, S. D. Kelly, R. Si, M. Dupuis, Q. Huang, J. Q. Chen, C. Tang, and C. Li, *Nat. Catal.*, **1**, 870 (2018).
24. J. Wang, L. Han, B. Huang, Q. Shao, H. L. Xin, and X. Huang, *Nat. Commun.*, **10**, 5692 (2019).
25. L. Cao et al., *Nat. Commun.*, **10**, 4849 (2019).
26. F. Shi, Z. Geng, K. Huang, Q. Liang, Y. Zhang, Y. Sun, J. Cao, and S. Feng, *Advanced science (Weinheim, Baden-Wuerttemberg, Germany)*, **5**, 1800575 (2018).
27. J. Kim, P.-C. Shih, K.-C. Tsao, Y.-T. Pan, X. Yin, C.-J. Sun, and H. Yang, *JACS*, **139**, 12076 (2017).
28. M. Tahir et al., *ACS Energy Lett.*, **2**, 2177 (2017).
29. Y. Wu, W. Sun, Z. Zhou, W. Q. Zaman, M. Tariq, L. Cao, and J. Yang, *ACS Omega*, **3**, 2902 (2018).
30. M. Bernt, A. Weiß, M. F. Tovini, H. A. El-Sayed, C. Schramm, J. Schröter, M. Kemmer, C. Gebauer, and H. A. Gasteiger, *Chem. Ing. Tech.*, **92**, 31 (2020).
31. A. W. H. A. El-Sayed, L. F. Olbrich, G. P. Putro, and H. A. Gasteiger, *J. Electrochem. Soc.*, **166**, F1 (2019).
32. X. Tan, J. Shen, N. Semagina, and M. Secanell, *J. Catal.*, **371**, 57 (2019).
33. A. Hartig-Weiss, M. F. Tovini, H. A. Gasteiger, and H. A. El-Sayed, *ACS Appl. Energy Mater.*, **3**, 10323 (2020).
34. B. G. Pollet, F. Foroughi, A. Y. Faid, D. R. Emberson, and M. H. Islam, *Ultrason. Sonochem.*, **69**, 105238 (2020).
35. K. Shinozaki, J. W. Zack, S. Pylypenko, B. S. Pivovar, and S. S. Kocha, *J. Electrochem. Soc.*, **162**, f1384 (2015).
36. M. Bernt, A. Hartig-Weiß, M. F. Tovini, H. A. El-Sayed, C. Schramm, J. Schröter, C. Gebauer, and H. A. Gasteiger, *Chem. Ing. Tech.*, **92**, 31 (2020).
37. M. Bernt, A. Siebel, and H. A. Gasteiger, *J. Electrochem. Soc.*, **165**, F305 (2018).
38. M. Carmo, D. L. Fritz, J. Mergel, and D. Stolten, *Int. J. Hydrogen Energy*, **38**, 4901 (2013).
39. M. Bernt and H. A. Gasteiger, *J. Electrochem. Soc.*, **163**, F3179 (2016).
40. M. Bernt and H. A. Gasteiger, *J. Electrochem. Soc.*, **163**, F3179 (2016).
41. O. Diaz-Morales, S. Raaijman, R. Kortlever, P. J. Kooyman, T. Wezendonk, J. Gascon, W. T. Fu, and M. T. M. Koper, *Nat. Commun.*, **7**, 12363 (2016).
42. L. Yang et al., *Nat. Commun.*, **9**, 5236 (2018).
43. C. Yang et al., *Nat. Commun.*, **11**, 1378 (2020).
44. H.-S. Oh, H. N. Nong, T. Reier, M. Gliech, and P. Strasser, *Chem. Sci.*, **6**, 3321 (2015).
45. E. Leonard, A. D. Shum, S. Normile, D. C. Sabarirajan, D. G. Yared, X. Xiao, and I. V. Zenyuk, *Electrochim. Acta*, **276**, 424 (2018).

46. L. Zhang, Y. Zhang, X. Zhang, Z. Li, G. Shen, M. Ye, C. Fan, H. Fang, and J. Hu, *Langmuir*, **22**, 8109 (2006).
47. R. Hao, Y. Fan, M. D. Howard, J. C. Vaughan, and B. Zhang, *Proc. Natl Acad. Sci.*, **115**, 5878 (2018).
48. A. S. Aricò, S. Siracusano, N. Briguglio, V. Baglio, A. Di Blasi, and V. Antonucci, *J. Appl. Electrochem.*, **43**, 107 (2013).
49. S. M. Alia and G. C. Anderson, *J. Electrochem. Soc.*, **166**, F282 (2019).
50. O. Kasian, J.-P. Grote, S. Geiger, S. Cherevko, and K. J. J. Mayrhofer, *Angewandte Chemie (International ed. in English)*, **57**, 2488 (2018).
51. D. N. Buckley and L. D. Burke, *J. Chem. Soc., Faraday Trans. 1 F*, **71**, 1447 (1975).
52. M. Pourbaix, *Atlas of Electrochemical Equilibria in Aqueous Solutions* (NACE International, Houston Texas, United States of America) 2nd edn. ed. (1974).
53. F. Barbir, *Sol. Energy*, **78**, 661 (2005).
54. R. E. Clarke, S. Giddey, F. T. Ciacchi, S. P. S. Badwal, B. Paul, and J. Andrews, *Int. J. Hydrogen Energy*, **34**, 2531 (2009).
55. C. Rakousky, U. Reimer, K. Wippermann, S. Kuhri, M. Carmo, W. Lueke, and D. Stolten, *J. Power Sources*, **342**, 38 (2017).
56. A. Buttler and H. Spliethoff, *Renew. Sustain. Energy Rev.*, **82**, 2440 (2018).
57. S. Cherevko, S. Geiger, O. Kasian, A. Mingers, and K. J. J. Mayrhofer, *J. Electroanal. Chem.*, **773**, 69 (2016).
58. W. Vielstich, A. Lamm, H. A. Gasteiger, and H. Yokokawa (ed.), *Handbook of Fuel Cells: Perfluorinated Membranes* (John Wiley & Sons, Ltd., Chichester, United Kingdom) (2010).
59. M. Bernt, J. Schröter, M. Möckl, and H. A. Gasteiger, *J. Electrochem. Soc.*, **167**, 124502 (2020).



## 5.6 Impact of Intermittent Operation on Lifetime and Performance of a PEM Water Electrolyzer

In the following section the article “Impact of Intermittent Operation on Lifetime and Performance of a PEM Water Electrolyzer” is presented, which was submitted to the *Journal of Electrochemical Society* in January 2019 and accepted for publication as an open access article under the terms of Creative Commons Attribution 4.0 License (CC BY) in April 2019. The study was shown at the 234<sup>th</sup> Meeting of the Electrochemical Society (October 2018) in Cancun by Alexandra Weiss and can be found under its abstract number: #I01F-1598). The article can be found under its permanent web-link: <https://iopscience.iop.org/article/10.1149/2.0421908jes>

PEM water electrolysis has the potential to be coupled with renewable energies, which, however, are inherently intermittent in their power output. Hence, the stability of a PEM water electrolyzer during a fluctuating power supply is of utter importance. Therefore, an accelerated stress test (AST) was developed within this study to mimic times of operation ( $3 \text{ Acm}^{-2}_{\text{geo}}$  and  $0.1 \text{ Acm}^{-2}_{\text{geo}}$ ) and idle periods (OCV). Since the cell was operated at differential pressure ( $10 \text{ bar}_{\text{cathode}}/1 \text{ bar}_{\text{anode}}$ ), the hydrogen can permeate from the cathode into the anode compartment during the OCV period and lead to the reduction of  $\text{IrO}_2$  and thus the formation of metallic iridium at the surface of the catalyst. The permeation of hydrogen and its accumulation within the anode compartment was confirmed by the cell voltage decay during the OCV period, where within a couple of minutes the voltage dropped close to the reversible potential of hydrogen ( $\approx 0 \text{ V}_{\text{RHE}}$ ).

The cell voltage development during the course of cycling was recorded at the two different current densities as a measure of stability. Although the performance improved initially after 10 OCV-cycles ( $\approx 50 \text{ mV}$ ) at both current densities ( $3 \text{ Acm}^{-2}_{\text{geo}}$  and  $0.1 \text{ Acm}^{-2}_{\text{geo}}$ ), over the course of cycling the performance gradually decreased. Polarizing the cell at  $1.3 \text{ V}$ , instead of leaving it at OCV, resulted in a stable performance. Polarization curves measured periodically throughout the measurement revealed that the improved performance observed during the OCV-test is correlated to improved OER kinetics, since the Tafel slope also decreased from initially  $60 \text{ mVdec}^{-1}$  to  $47 \text{ mVdec}^{-1}$  after 10 cycles. Additionally, the polarization curves showed that the decrease in performance over the course of OCV-cycling is related to an increasing HFR over time (BOT:  $\approx 56 \text{ m}\Omega\text{cm}^2_{\text{geo}}$ ; after 788 OCV-cycles:  $\approx 88 \text{ m}\Omega\text{cm}^2_{\text{geo}}$ ), since the  $iR$ -corrected performance remained nearly constant. During the reference test, when the cell is polarized at  $1.3 \text{ V}$  during the idle period, the Tafel slope as well as the HFR remained constant.

Hence, the improved performance along with the increase in HFR is related to the OCV-periods. Hydrated iridium-oxide is known to be more active towards the OER than crystalline IrO<sub>2</sub> and might explain the improved activity observed. This was confirmed by CVs recorded periodically during the OCV-test, where after 10 OCV-cycles H-UPD features, typical for metallic iridium, along with the Ir(III)/Ir(IV)-redox features are emerging. In comparison, the CVs recorded within the reference test remained constant over the course of cycling, showing only capacitive features, which is typical for a crystalline IrO<sub>2</sub>.

The main reason for the observed decrease in performance during the OCV-test was correlated to the increasing HFR. Any cationic contamination was excluded, since the HFR could not be recovered by boiling the cycled membrane in sulfuric acid. It is known, however, that the Ti-PTL (porous transport layer) used at the anode can passivate at high potentials, resulting in an additional contact resistance. This was confirmed by determining the contact resistance of the cycled Ti-PTL ex-situ. Both the passivation of the Ti-PTL and the formation of hydrated iridium-oxide, which is electrically less conductive compared to crystalline IrO<sub>2</sub>, led to an additional interfacial resistance.

In conclusion, when coupling a PEM-WE with renewable energies, it is important that idle periods where no current is supplied are avoided to ensure a stable performance.

### **Author contributions**

Fabrication of catalyst inks, membrane electrode assemblies, and electrochemical testing in a PEM-WE cell was performed by A.W., A.S., and M.B. Analysis of the experimental test results was done A.S. A.W. wrote the manuscript that was edited by H.A.G. All authors discussed the experimental results and revised the manuscript.



## Impact of Intermittent Operation on Lifetime and Performance of a PEM Water Electrolyzer

A. Weiß,<sup>1,\*</sup> A. Siebel,<sup>1,\*,z</sup> M. Bernt,<sup>1,2,\*</sup> T.-H. Shen,<sup>3</sup> V. Tileli,<sup>3</sup>  
and H. A. Gasteiger<sup>1,\*\*</sup>

<sup>1</sup>Chair of Technical Electrochemistry, Department of Chemistry and Catalysis Research Center, Technical University of Munich, 85747 Garching, Germany

<sup>2</sup>Bayerisches Zentrum für angewandte Energieforschung, 85748 Garching, Germany

<sup>3</sup>Institute of Materials, École Polytechnique Fédérale de Lausanne, CH-1015 Lausanne, Switzerland

The aim of this study is to provide a better understanding of performance degrading mechanisms occurring when a proton exchange membrane water electrolyzer (PEM-WE) is coupled with renewable energies, where times of operation and idle periods alternate. An accelerated stress test (AST) is proposed, mimicking a fluctuating power supply by operating the electrolyzer cell between high ( $3 \text{ A cm}^{-2}_{\text{geo}}$ ) and low current densities ( $0.1 \text{ A cm}^{-2}_{\text{geo}}$ ), alternating with idle periods during which no current is supplied and the cell rests at open circuit voltage (OCV). Polarization curves, periodically recorded during the OCV-AST, reveal an initial increase in activity ( $\approx 50 \text{ mV}$  after 10 cycles) followed by a significant decrease in performance during prolonged OCV cycling due to an increasing high frequency resistance (HFR) ( $\approx 1.6$ -fold after 718 cycles). These performance changes can clearly be related to the OCV periods, since they are not observed in a reference experiment where the OCV period is replaced by a potential hold at 1.3 V. The origin of the phenomena, which are responsible for the initial performance gain as well as the subsequent decay are analyzed via detailed electrochemical and physical characterization of the MEAs, and an operating strategy to prevent performance degradation is proposed.

© The Author(s) 2019. Published by ECS. This is an open access article distributed under the terms of the Creative Commons Attribution 4.0 License (CC BY, <http://creativecommons.org/licenses/by/4.0/>), which permits unrestricted reuse of the work in any medium, provided the original work is properly cited. [DOI: 10.1149/2.0421908jes]



Manuscript submitted January 3, 2019; revised manuscript received April 8, 2019. Published April 29, 2019. This was Paper 1606 presented at the Cancun, Mexico, Meeting of the Society, September 30-October 4, 2018.

In light of the fact that the energy demand is ever-increasing and that renewable energy sources, inherently intermittent in energy output, are becoming more and more important, an efficient way of storing energy is of crucial importance. One prominent example for an energy carrier meeting these requirements is gaseous hydrogen, produced in a polymer electrolyte membrane water electrolyzer (PEM-WE) via electrochemical water splitting.<sup>1,2</sup> The reliability of a PEM-WE has already been reported for  $\approx 60,000$  h of operation, showing only a marginal loss in performance.<sup>3-4</sup> In an ideal scenario, PEM-WE systems would be coupled with renewable energy sources in order to fully utilize their output by converting temporary excess energy into  $\text{H}_2$ .<sup>5</sup> This dynamic mode of operation involves frequent load changes and idle periods during which no current is supplied.<sup>2,6-8</sup> While it is well known that alkaline water electrolyzers must be operated with a so-called protective current in stand-by/idle conditions (i.e., when no power is provided by renewable energy sources) in order to avoid a substantial performance degradation,<sup>4,7,9-10</sup> very little is known about the gravity of this effect in PEM-WEs, even though it will be an important consideration for coupling PEM-WEs with renewable energy sources.<sup>6,11</sup> In this paper, we will try to further investigate this phenomenon, but first will briefly review the most common failure mechanisms of PEM-WEs.

A commonly observed failure of PEM-WEs has been related to the chemical degradation of the perfluorosulfonic acid (PFSA) based polymer electrolyte membrane, often observed as thinning of the membrane or as localized pinholes in the membrane. The concomitant increase in gas permeation ultimately leads to an unacceptably large, safety-critical  $\text{H}_2$  concentration in the  $\text{O}_2$  anode compartment, as the  $\text{H}_2$  oxidation activity of iridium based anode catalysts is very poor (contrary to the  $\text{O}_2$  reduction activity in the  $\text{H}_2$  anode). This is described in an early study by Stueckl et al., who showed that the failure of a dynamically operated 100 kW PEM-WE plant after only  $\approx 15,000$  h was mostly related to thinning of the PFSA membrane, caused by chemical degradation.<sup>12</sup> Here, however, it should be noted that the chemical durability of today's PFSA membranes is dramatically better

owing to stabilization of the polymer endgroups,<sup>13</sup> so that membrane thinning is likely less of an issue when using state-of-the-art PFSA membranes.<sup>14</sup> Another membrane related degradation effect is the contamination of the ionomeric membrane with cations,<sup>11,15-16</sup> typically introduced by improperly treated feed-water which is the major cause for PEM-WE failures in the field.<sup>16-17</sup> Sun et al. showed the operation of a 9-cell PEM-WE stack for 7800 h at constant current, and recorded a gradual decrease in performance that they attributed to cationic contamination, since the initial performance was mostly recovered by boiling the degraded MEA (membrane-electrode-assembly) in sulfuric acid.<sup>18</sup>

Apart from degradation of the membrane in the membrane-electrode-assembly via chemical degradation and cationic contamination, gradual passivation of the titanium porous transport layer (PTL) at the high potentials experienced by the anode electrode of an electrolyzer increases the internal ohmic resistance and, hence, leads to a decrease of performance. This was demonstrated by Rakousky et al. after operation at  $2 \text{ A cm}^{-2}_{\text{geo}}$  for 1000 h, where the high-frequency resistance (HFR) increased by  $26 \text{ m}\Omega \text{ cm}^{-2}_{\text{geo}}$  ( $\approx 20\%$ ) due to passivation of the Ti-PTL.<sup>19</sup> In addition, the authors observed a reduction of the anodic exchange current density, which they attribute to a contamination with titanium from either the anode catalyst itself (iridium oxide coated onto a titanium oxide support) or the anodic Ti-PTL.

With regards to the effect of dynamic PEM-WE operation, Rakousky et al. investigated the influence of different load profiles over 1000 h, namely constant current of 1 or  $2 \text{ A cm}^{-2}_{\text{geo}}$ , cycling between 1 and  $2 \text{ A cm}^{-2}_{\text{geo}}$ , or cycling between open-circuit voltage (OCV) and  $2 \text{ A cm}^{-2}_{\text{geo}}$ .<sup>20</sup> At a constant current of  $2 \text{ A cm}^{-2}_{\text{geo}}$  the authors observed an untypically high degradation rate ( $\approx 200 \mu\text{V h}^{-1}$ ) compared to that at a constant current of  $1 \text{ A cm}^{-2}_{\text{geo}}$  ( $< 1 \mu\text{V h}^{-1}$ ). When cycling between 1 and  $2 \text{ A cm}^{-2}_{\text{geo}}$  or between OCV and  $2 \text{ A cm}^{-2}_{\text{geo}}$ , the degradation rate was substantially lower than that at a constant current of  $2 \text{ A cm}^{-2}_{\text{geo}}$ , which the authors claim to be due to a not clearly defined reversible degradation effect.<sup>20</sup> Interestingly, comparing the degradation rates when cycling between OCV and  $2 \text{ A cm}^{-2}_{\text{geo}}$  at different interval times (10 min vs. 6 h per step), the degradation rate increased with the number of OCV periods over the 1000 h of test ( $\approx 16 \mu\text{V h}^{-1}$  for  $\approx 80$  OCV periods vs.  $\approx 50 \mu\text{V h}^{-1}$  for  $\approx 3000$  OCV periods over 1000 h). While the authors suggested that this might be due to cathode catalyst degradation, our data presented

<sup>z</sup>These authors contributed equally to this work.

\*Electrochemical Society Student Member.

\*\*Electrochemical Society Fellow.

<sup>†</sup>E-mail: alexandra.weiss@tum.de



below would suggest that it is related to the degradation of the anode catalyst.

To date, a detailed understanding of performance degrading phenomena associated with discontinuous operation, particularly with intermittent OCV periods, has not been established. In this work, we propose a dynamic accelerated stress test (AST) procedure, mimicking the variable power supply of renewable energy sources, where operation at low and high current densities ( $0.1$  and  $3 \text{ A cm}^{-2}_{\text{geo}}$ , respectively) alternate with idle periods, during which no current is supplied and the electrolyzer cell rests at the open circuit voltage. This test will be complemented by an experiment during which the cell voltage is not varying freely during the OCV periods but instead is potentiostated at  $1.3 \text{ V}$ , where the current density is on the order of  $1 \text{ mA cm}^{-2}_{\text{geo}}$  (i.e., significantly smaller than the  $100 \text{ mA cm}^{-2}_{\text{geo}}$ ). We will show that cycling into OCV leads to a significant performance loss, particularly at high current densities, compared to  $1.3 \text{ V}$  holds. The origin of this phenomenon will be examined via detailed electrochemical and physical characterization of the MEA before, during, and after the respective cycling test.

### Experimental

**Membrane electrode assembly (MEA) preparation and cell assembly.**—MEAs with an active area of  $5 \text{ cm}^2$  were prepared via the decal transfer method, where platinum supported on Vulcan XC72 carbon (45.8 wt.-% Pt/C, TEC10V50E from Tanaka, Japan) served as catalyst for the hydrogen evolution reaction (HER) at the cathode electrode and  $\text{IrO}_2$  supported on  $\text{TiO}_2$  ( $\text{IrO}_2/\text{TiO}_2$  with 75 wt.-% iridium, Elyst Ir75 0480 from Umicore, Germany) as catalyst for the oxygen evolution reaction (OER) at the anode electrode. De-ionized (DI) water ( $18 \text{ M}\Omega \text{ cm}$ ), 2-Propanol (purity  $\geq 99.9\%$  from Sigma Aldrich), and Nafion ionomer solution (20 wt.-% ionomer, D2021 from IonPower, USA) were used as solvents for the catalyst ink. The suspension was mixed for 24 h using a roller mill, where  $\text{ZrO}_2$  grinding balls (5 mm diameter) were added to achieve a homogenous suspension. The ink was coated onto a thin decal transfer substrate (PTFE,  $50 \mu\text{m}$  thick, from Angst+Pfister, Germany) using the Mayer rod technique. Subsequently,  $5 \text{ cm}^2$  decals were punched from the coating after drying and then hot-pressed onto a Nafion 212 membrane ( $50 \mu\text{m}$  thick, from Quintech, Germany) at  $155^\circ\text{C}$  for 3 minutes at a pressure of  $2.5 \text{ MPa}$ . By weighing the decals before and after hot-pressing, the actual weight of the electrodes was determined. Throughout the study, the loading was kept constant at  $0.2 \pm 0.1 \text{ mg}_{\text{Pt}} \text{ cm}^{-2}_{\text{geo}}$  for the hydrogen cathode and  $1.75 \pm 0.15 \text{ mg}_{\text{Ir}} \text{ cm}^{-2}_{\text{geo}}$  for the oxygen anode.

At the anode, sintered titanium (from Mott Corporation, USA) with a porosity of  $\approx 50\%$ , a thickness of  $280 \pm 10 \mu\text{m}$  and a pore size of  $10\text{--}50 \mu\text{m}$  (determined by SEM) was used as a porous transport layer (PTL), whereas a carbon fiber paper (TGP-H 120T from Toray, no MPL, 20 wt.-% PTFE) with a thickness of  $370 \pm 10 \mu\text{m}$  and pore sizes of  $20\text{--}50 \mu\text{m}$ <sup>21</sup> was used on the cathode. The MEA and PTLs were placed between the flow-fields of the electrolyzer cell and sealed with virgin PTFE gaskets. By choosing the right thickness of the gaskets, a compression of the carbon PTL by 25% was set, corresponding to a compressive contact pressure of  $\approx 1.7 \text{ MPa}$  at the MEA. Specific details about the cell hardware are reported elsewhere.<sup>22</sup>

**Physical characterization.**—After the electrochemical characterization and testing, a small piece of each MEA was embedded into room-temperature curing epoxy for scanning electron microscopy (SEM). Using SiC paper, the sample surface was polished in two steps (grade P320 and P1200) and afterwards polished using a  $9 \mu\text{m}$  diamond polishing agent (from Buehler, USA). The cross-sectional lamellae of the pristine and operated samples were prepared by focused ion beam milling (FIB, Zeiss NVision 40). Due to the porosity of the catalyst layer and the sensitive nature of the polymeric membrane, the area thinned for TEM analysis was kept to a minimum to keep the lamellae intact. The scanning transmission electron microscopy (STEM) was performed with a spherical aberration corrected TEM (ThermoScientific Titan Themis 60-300) equipped with a high

brightness gun source operated at  $200 \text{ kV}$ . The current was kept low to avoid possible electron beam induced damage which would cause collapse of the polymeric film. High-angle annular dark field-STEM (HAADF-STEM) images of the interface between the  $\text{IrO}_2/\text{TiO}_2$  anode catalyst layer and the Nafion membrane were acquired by collecting incoherently scattered electrons. Energy dispersive spectroscopy (STEM-EDS) elemental maps of iridium and oxygen were obtained by collecting characteristic X-ray signals via four silicon drift detectors located in close proximity to the sample at the TEM column.

**Contact resistance measurement.**—Contact resistance measurements were carried out with the test setup described by Bernt et al.<sup>22</sup> PTLs, along with an insulating Kapton foil ( $25 \mu\text{m}$ ) to ensure that the resistance is only measured along the PTL were sandwiched between two titanium flow-fields which, in turn, were sandwiched between and two copper plates. A pressure of  $\approx 1.7 \text{ MPa}$  was applied to this stack in order to simulate the contact pressure in the cell. By applying different currents via the copper plates and measuring the associated voltage drops across the flow-fields, the electronic resistance (essentially equating to the contact resistance) was quantified.

**Electronic resistance measurement of the anode electrode.**—Electronic conductivities of the  $\text{IrO}_2/\text{TiO}_2$  anode catalyst layers in the size of  $5 \text{ cm}^2_{\text{geo}}$  were determined by 4-point-probe in-plane conductivity measurements (Lucas/Signatone, pin distance  $1 \text{ mm}$ ) on the electrode coated onto the membrane by applying different potentials between  $0.1\text{--}0.5 \text{ V}$  and recording the corresponding current.

**Electrochemical characterization.**—All electrochemical measurements of the MEAs were performed on an automated test station from Greenlight Innovation, using a potentiostat equipped with a current booster (BioLogic VSP 300). The anode was supplied with  $5 \text{ mL}_{\text{H}_2\text{O}} \text{ min}^{-1}$  deionized (DI) water, which was pre-heated to  $80^\circ\text{C}$ . During the measurements, the cell temperature was kept constant at  $80^\circ\text{C}$ , and the product gas exiting from the anode side was diluted with nitrogen ( $200 \text{ nccm}$ ) to avoid the formation of an explosive gas mixture due to hydrogen permeation through the membrane into the anode compartment. During warm-up, the cathode is flushed with  $\text{N}_2$  for  $300 \text{ s}$  while  $5 \text{ mL}_{\text{H}_2\text{O}} \text{ min}^{-1}$  are constantly supplied to the anode side. After reaching the desired cell temperature of  $80^\circ\text{C}$ , the cell was conditioned at  $1 \text{ A cm}^{-2}_{\text{geo}}$  for  $30 \text{ min}$ . Subsequently, polarization curves were taken at ambient pressure ( $1 \text{ bar}_a$ ) and  $10 \text{ bar}_a$ , stepwise increasing the current density from  $0.01$  to  $4 \text{ A cm}^{-2}_{\text{geo}}$  and holding at each current for  $5 \text{ min}$  to ensure a stable cell voltage reading. Finally, the last  $10 \text{ s}$  of the cell voltage at each current density were averaged. Considering the first two polarization curves as part of the conditioning, they were not included in the analysis. For the load-cycling procedure, the flow of  $\text{H}_2\text{O}$  through the anode compartment and the cell temperature were kept constant also during the open-circuit voltage (OCV) or the  $1.3 \text{ V}$ -hold periods.

Additionally, AC impedance measurements were performed at the end of each current density step in a range from  $100 \text{ kHz}$  to  $1 \text{ Hz}$ , adjusting the amplitude of the current perturbation such that it was always  $<20\%$  of the applied current, except for the smallest current density of  $10 \text{ mA cm}^{-2}_{\text{geo}}$  where it was  $40\%$ . The high-frequency resistance (HFR) was determined from the high-frequency intercept with the real axis in a Nyquist plot. At the beginning-of-test (BoT) as well as during the test and at the end-of-test (EoT), cyclic voltammograms (CVs) of the anode electrode were recorded. For this, the test procedure was stopped either after the open-circuit voltage or the  $1.3 \text{ V}$ -hold period, and the cathode counter electrode was flushed with dry  $\text{H}_2$  at  $50 \text{ nccm}$  at ambient pressure to ensure a stable reference potential, while the anode electrode was continuously fed with  $5 \text{ mL}_{\text{H}_2\text{O}} \text{ min}^{-1}$  deionized water. The CVs were recorded in a potential range of  $0.05 \text{ V}\text{--}1.3 \text{ V}$  at  $50 \text{ mV s}^{-1}$  at  $80^\circ\text{C}$ ; showing the steady-state CVs ( $2^{\text{nd}}$  one recorded).



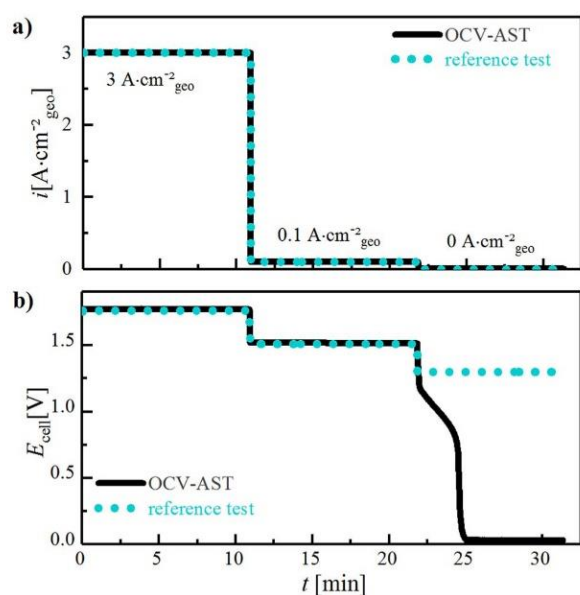


**Figure 1.** Test protocol for the accelerated stress test (AST) to mimic an intermittent power supply of a PEM-WE with periods of low and high current density followed by OCV (“OCV-AST”, black solid lines) and of a reference test avoiding OCV (“reference test”, blue dotted lines) by holding the potential at 1.3 V instead of OCV. a) Current profiles during the first cycle of the OCV-test; b) associated potential profiles recorded at 80°C with  $p_{\text{cathode}} = 10 \text{ bar}_a$  and  $p_{\text{anode}} = 1 \text{ bar}_a$ , while feeding  $5 \text{ mL H}_2\text{O min}^{-1}$  into the anode compartment. MEA specification:  $5 \text{ cm}^2$  active-area with  $\approx 1.75 \text{ mg}_{\text{Ir}} \text{ cm}^{-2}_{\text{geo}}$  anode and  $\approx 0.2 \text{ mg}_{\text{Pt}} \text{ cm}^{-2}_{\text{geo}}$  cathode loading using a Nafion 212 ( $\approx 50 \text{ }\mu\text{m}$  thick) membrane.

## Results and Discussion

**Degradation test protocols.**—In this section, we propose a test protocol to mimic transient operation of a PEM-WE. First a high ( $3 \text{ A cm}^{-2}_{\text{geo}}$ ) and then a low ( $0.1 \text{ A cm}^{-2}_{\text{geo}}$ ) current density are drawn from the cell, followed by a current interrupt during which the cell is left to rest at the OCV, simulating shut-off periods of a PEM-WE operated with intermittent renewable energy (denoted as “OCV-AST”). The duration of each interval was  $\approx 10 \text{ min}$ , and one cycle refers to the two current steps and the OCV period (black solid line in Figure 1a). In a second experiment, referred to as “reference test”, the OCV period at the end of each cycle was replaced by a potential hold at 1.3 V (blue dotted line in Figure 1a). During the entire operation (i.e., including the shut-off periods), the temperature was held at 80°C and  $5 \text{ mL min}^{-1}$  DI water was continuously fed into the anode compartment of the cell. During the OCV or 1.3 V-hold phase, the cathode pressure decreased by  $\approx 1 \text{ bar}_a$  (i.e., from  $10 \text{ bar}_a$  to  $\approx 9 \text{ bar}_a$ ) due to  $\text{H}_2$  permeating through the membrane into the anode compartment (the  $\text{H}_2$  partial pressure normalized permeation rate through a  $\approx 175 \text{ }\mu\text{m}$  thick Nafion 117 membrane in a PEM-WE at 80°C between 10 and  $30 \text{ bar}_a$  cathode pressure was found to be  $\approx 0.24 \text{ mA cm}^{-2}_{\text{geo}} \text{ bar}_{a(\text{H}_2)}^{-1}$ ,<sup>23</sup> which if scaled to a  $\approx 50 \text{ }\mu\text{m}$  thick Nafion 212 membrane equates to  $\approx 0.85 \text{ mA cm}^{-2}_{\text{geo}} \text{ bar}_{a(\text{H}_2)}^{-1}$  or  $\approx 5.9 \cdot 10^{-3} \text{ cm}_{s(\text{H}_2)}^3 \text{ cm}^{-2} \text{ bar}_{a(\text{H}_2)}^{-1} \text{ min}^{-1}$  (with  $\text{cm}_{s}^3$  referenced to  $1.103 \text{ bar}_a$  and  $25^\circ\text{C}$ )).

**Voltage and current response during the OCV-AST and the reference test.**—Figure 1b shows the cell voltage recorded during the different operation intervals in Figure 1a. During operation at constant current, the cell voltage remains essentially constant. Upon current interruption in the OCV-AST (black line), the potential drops immediately to  $\approx 1.2 \text{ V}$ , i.e., to the approximate thermodynamic cell voltage

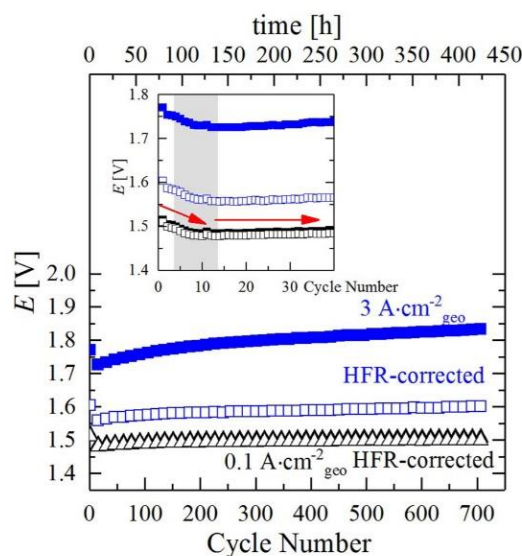


**Figure 2.** Evolution of the cell voltage and the HFR-corrected cell voltage at  $0.1 \text{ A cm}^{-2}_{\text{geo}}$  and  $3 \text{ A cm}^{-2}_{\text{geo}}$  during the OCV-AST at 80°C, cycling the cell according to the protocol shown in Figure 1 (black solid line) with  $p_{\text{cathode}} = 10 \text{ bar}_a$  and  $p_{\text{anode}} = 1 \text{ bar}_a$ , while feeding  $5 \text{ mL H}_2\text{O min}^{-1}$  into the anode compartment (same MEA specifications as in Figure 1). For better legibility, only every 15<sup>th</sup> point was plotted; the inset is a zoomed view of the initial 40 cycles including all data points.

for water electrolysis at 80°C. This is followed by a gradual decrease of the potential to  $\approx 0.8 \text{ V}$ , caused by the gradual enrichment of  $\text{H}_2$  in the anode compartment by permeation from the cathode compartment that is held at  $10 \text{ bar}_a$  (i.e., at a  $\text{H}_2$  partial pressure of  $9.5 \text{ bar}_a$ ), resulting in a  $\text{H}_2$  permeation flux of  $\approx 5.6 \cdot 10^{-2} \text{ cm}_{s(\text{H}_2)}^3 \text{ cm}^{-2} \text{ min}^{-1}$  (from the above quoted permeation rate). In this  $\text{H}_2$ -rich gas-phase at 80°C, the surface of the crystalline  $\text{IrO}_2$  on the  $\text{TiO}_2$  support undergoes a gradual partial reduction to a surface which is catalytically active for the hydrogen oxidation reaction (HOR).<sup>24</sup> Once its HOR activity is high enough (apparently at  $\approx 0.8 \text{ V}$ ), the equilibrium potential for the HOR at  $\approx 0 \text{ V}$  is being established very quickly (in less than 0.5 min), resulting in a drop of the cell voltage of the electrolyzer to  $\approx 0 \text{ V}$  vs. the reversible hydrogen electrode (RHE) potential (note that the platinum catalyzed cathode is still under a high  $\text{H}_2$  pressure, so that the  $\approx 0 \text{ V}$  cell voltage are clearly due to a drop of the anode potential to  $\approx 0 \text{ V}$  vs. RHE). When holding the cell voltage at 1.3 V instead in case of the reference test, the reduction of the  $\text{IrO}_2$  catalyst will be prevented (as will be proven later), however at the cost of applying a small bias current, as will be discussed in the last section of this work.

The evolution of the cell voltage as a function of the number of current/OCV cycles of the OCV-AST is shown in Figure 2. The cell voltage at both current densities initially decreases by  $\approx 50 \text{ mV}$  (inset of Figure 2) and above 10 cycles gradually increases, particularly at high current density. Since the HFR-corrected cell voltage also decreases during the first 10 cycles (cf. hollow blue and black symbols in Figure 2), the initially decreasing cell voltage must be due to an increase of the OER activity of the anode catalyst (note that the cathode overpotential would be  $< 10 \text{ mV}$  even if the loading of the Pt cathode catalyst would be reduced by an order of magnitude from the value of  $0.2 \text{ mg}_{\text{Pt}} \text{ cm}^{-2}_{\text{geo}}$  used in this work).<sup>25</sup> As was shown previously<sup>24</sup> and as will be further discussed below, this is indeed due to an increase in the OER activity of the  $\text{IrO}_2$  based anode catalyst after extended exposure to  $\text{H}_2$  during the OCV periods. The increase in cell voltage starting after 10 cycles is largely caused by an increase in the HFR, reflected by the fact that the HFR-corrected cell voltage at  $3 \text{ A cm}^{-2}_{\text{geo}}$  rises much less significantly than the cell voltage. The nevertheless



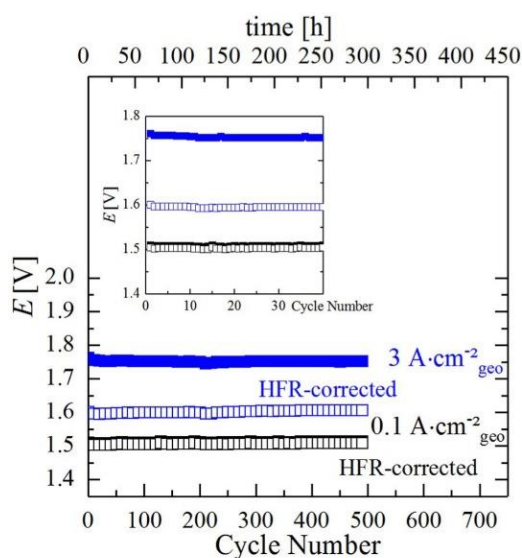


**Figure 3.** Evolution of the cell voltage and the HFR-free cell voltage at  $0.1 \text{ A cm}^{-2}_{\text{geo}}$  and  $3 \text{ A cm}^{-2}_{\text{geo}}$  during the reference test at  $80^\circ\text{C}$  with OCV periods replaced by  $1.3 \text{ V}$ -holds, cycling the cell according to the protocol shown in Figure 1 (blue dotted line) with  $p_{\text{cathode}} = 10 \text{ bar}_a$  and  $p_{\text{anode}} = 1 \text{ bar}_a$ , while feeding  $5 \text{ mL}_{\text{H}_2\text{O}} \text{ min}^{-1}$  into the anode compartment (same MEA specifications as in Figure 1). For better legibility, only every  $10^{\text{th}}$  point was plotted; the inset is a zoomed view of the initial 40 cycles including all data points.

noticeable increase of the HFR-corrected cell voltage upon extended cycling suggests the growth of a more complex mass transport resistance.

In the reference test, the potentiostatic control at  $1.3 \text{ V}$  during the shut-down period results in a constant cell as well as HFR-corrected potential at both currents over the entire cycling test (Figure 3). Interestingly, the substantial performance improvement observed over the first 10 cycles cannot be observed here, particularly not for the HFR-corrected data, as can be seen in the inset of Figure 3 ( $< 10 \text{ mV}$  vs.  $\approx 50 \text{ mV}$  in Figure 2). This suggests that the (partial) reduction of the anode catalyst does not occur at  $\geq 1.3 \text{ V}$ . The comparison of both experiments proves that the performance degradation during the first experiment (Figure 2) is directly related to the OCV period at the end of each cycle, during which  $\text{H}_2$  accumulates in the anode compartment and lowers the potential of the anode catalyst to  $\approx 0 \text{ V}$  vs. RHE (Figure 1b, blue dotted line). It further proves that the degradation observed during the OCV-AST (Figure 2) is not caused by experimental artefacts (e.g., ionic contamination of the feed-water). Apparently, avoiding temporary potential excursions of the anode catalyst to below  $1.3 \text{ V}$  during intermittent shut-down mitigates parasitic processes that lead to an increasing cell voltage, which, to a large extent but not completely, can be attributed to an increase in HFR. The current/power required to hold the potential at  $1.3 \text{ V}$  during shut-down periods will be discussed in the last section of this work.

In order to gain further insights into the observed performance decay during the OCV-AST, we examine polarization curves recorded at various stages of the OCV-AST and the reference test. Figure 4 shows ambient pressure polarization curves and the corresponding HFR values recorded over the course of the OCV-AST, namely at the beginning-of-test (BoT, green squares) and after 10 (blue circles), 200 (orange triangles), and 718 cycles (end-of-test or EoT; red diamonds). It is remarkable that the performance increases by  $\approx 45 \text{ mV}$  over the entire current density range after ten cycles (blue circles) compared to BoT (green squares), which can only be rationalized by an improved OER activity of the anode catalyst. However, upon further cycling, the ambient pressure cell voltage at each current density

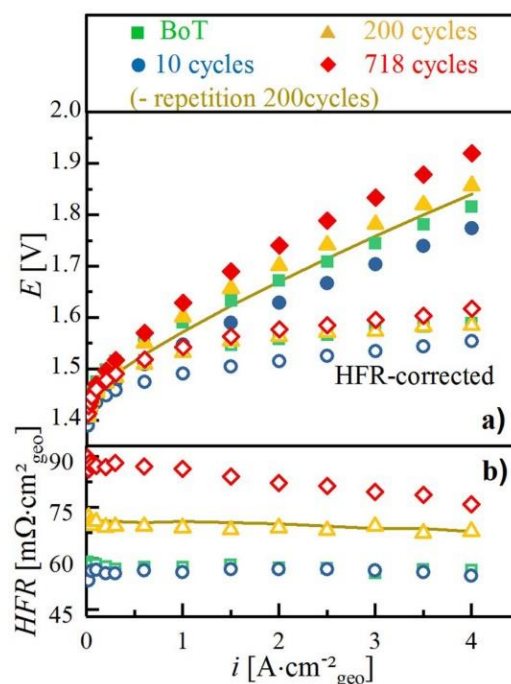


**Figure 4.** Ambient pressure PEM-WE performance data at  $80^\circ\text{C}$  recorded during the OCV-AST shown in Figure 2 a)  $E_{\text{cell}}$  vs.  $i$  performance (filled symbols) and HFR-free performance data (hollow symbols) with a cathode water-feed of  $5 \text{ mL}_{\text{H}_2\text{O}} \text{ min}^{-1}$ ; b) corresponding HFR values. The polarization curve and the HFR after 200 OCV-AST cycles for an independent repeated experiment are marked by the yellow lines.

increases continuously, consistent with the results presented above under differential pressure conditions ( $p_{\text{cathode}}/p_{\text{anode}} = 10/1 \text{ bar}_a$ , see Figure 2). This increase in cell voltage is accompanied by a substantial increase of the HFR (Figure 4b) by a factor of  $\approx 1.3$  after 200 cycles ( $\approx 71 \text{ m}\Omega \text{ cm}^2_{\text{geo}}$ ) and by a factor of  $\approx 1.6$  after 718 cycles ( $\approx 88 \text{ m}\Omega \text{ cm}^2_{\text{geo}}$ ) compared to its BoT value ( $\approx 56 \text{ m}\Omega \text{ cm}^2_{\text{geo}}$ ). Since the HFR represents the sum of the membrane ionic resistance and the electronic contact resistances at the PTL/electrode and PTL/flow field interface, one (or all) of these terms must be responsible for the performance degradation. A large fraction of the performance decrease between 10 cycles (blue circles) and EoT (red diamonds) can be ascribed to this dramatically increasing HFR, as indicated by the much smaller increase of the HFR-corrected voltage (open symbols in Figure 4a). However, the HFR increase alone cannot explain all of the performance losses over extended cycling, as the HFR-corrected voltage at each current density still increases between 10 cycles and EoT.

This analysis of the OCV-AST will be compared next to that of the reference test where OCV periods are replaced by  $1.3 \text{ V}$ -hold periods (Figure 5). Quite astoundingly, the cell voltage up to  $4 \text{ A cm}^{-2}_{\text{geo}}$  even slightly improves over 500 cycles (Figure 5a), which is related to the slightly decreasing HFR (Figure 5b), from  $\approx 54 \text{ m}\Omega \text{ cm}^2_{\text{geo}}$  initially (green squares) to  $\approx 50 \text{ m}\Omega \text{ cm}^2_{\text{geo}}$  after 500 cycles (red diamonds). The perfectly unchanged HFR-corrected cell voltage over 500 cycles signifies that the OER catalyst activity must remain unaltered. Considering the observations and conclusions from the polarization curves along with the development of the cell voltage over extended cycling, it is evident that the initial performance improvement observed after 10 cycles in the OCV-AST is not observed in the reference experiment, so that it must be linked directly to a change of the OER catalyst during the OCV periods. Quite clearly, the rather substantial performance degradation during OCV can be effectively prevented if the cell potential remains always at or above  $1.3 \text{ V}$ .



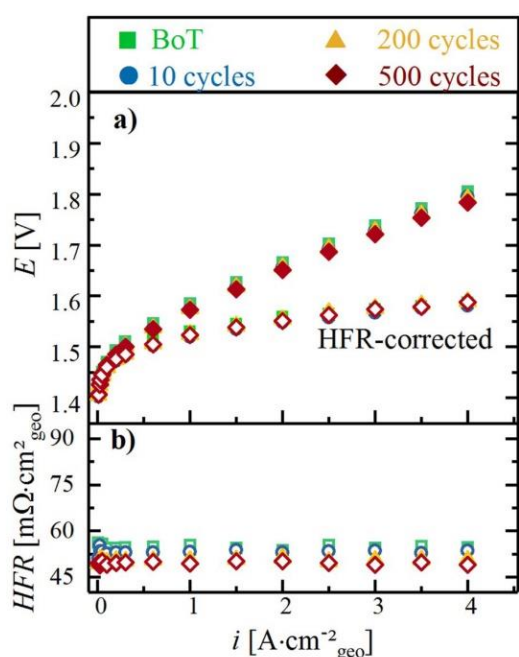


**Figure 5.** Ambient pressure PEM-WE performance data at 80°C recorded during the reference test shown in Figure 3. a)  $E_{cell}$  vs.  $i$  performance (filled symbols) and HFR-free performance data (hollow symbols) with a cathode water-feed of 5 mL<sub>H<sub>2</sub>O</sub> min<sup>-1</sup>; b) corresponding HFR values.

**Analysis of the effect of OCV periods on the OER catalyst.—**

This section will provide a detailed insight into the performance increase observed during the first ten cycles of the OCV-AST by taking a closer look at the OER kinetics. The Tafel slope, determined from the linear region (i.e., between 0.01 A cm<sup>-2</sup><sub>geo</sub> and 0.1 A cm<sup>-2</sup><sub>geo</sub>) of the ambient pressure HFR-corrected polarization curves recorded over the course of the OCV-AST (Figure 6a), decreases from 60 mV dec<sup>-1</sup> to 47 mV dec<sup>-1</sup> after the initial 10 cycles, clearly evidencing a change in the OER kinetics. Over further cycling, the Tafel slope increases slightly by  $\approx 3$  mV dec<sup>-1</sup> (50 mV dec<sup>-1</sup> after 200 cycles) and then stays constant until EoT (50 mV dec<sup>-1</sup> after 718 cycles). As one would expect, the initial Tafel slope obtained in the reference test is essentially identical with the initial value of the OCV-AST experiment (59 vs. 60 mV dec<sup>-1</sup>). However, contrary to the OCV-AST, it remained essentially constant, with a value of  $\approx 56$  mV dec<sup>-1</sup> (Figure 6b). This suggests that neither the iridium oxide surface nor the OER reaction mechanism seem to be affected during the reference experiment, while the substantial decrease of the Tafel slope in the first 10 cycles of the OCV-AST clearly suggests a change in the iridium oxide surface chemistry, induced by the OCV periods. In previous studies, we had observed a similar decrease of the Tafel slope upon in-situ reduction of the same IrO<sub>2</sub> catalyst under H<sub>2</sub> at 80°C for 15 h, accompanied by a  $\approx 40$  mV increase in OER activity and by the appearance of hydrogen underpotential deposition (H-UPD) features in the CV of the H<sub>2</sub>-exposed iridium oxide catalyst.<sup>24</sup> This was rationalized by the fact that thermally prepared, highly crystalline IrO<sub>2</sub> exhibits very different CV features than that of hydrous iridium oxide or metallic iridium.<sup>26</sup> Therefore, since the voltammetric response of the iridium oxide catalyst can provide valuable insights into the surface chemistry of the anode catalyst, we recorded the CVs of the anode catalyst before and during the OCV-AST and the reference test.

The BoT CV of the TiO<sub>2</sub> supported IrO<sub>2</sub> anode catalyst shows only capacitive currents but no well-defined features (region (1) & (2), green line Figure 7), which is characteristic of thermally treated, crystalline IrO<sub>2</sub>, and suggests that the surface of the iridium oxide corresponds

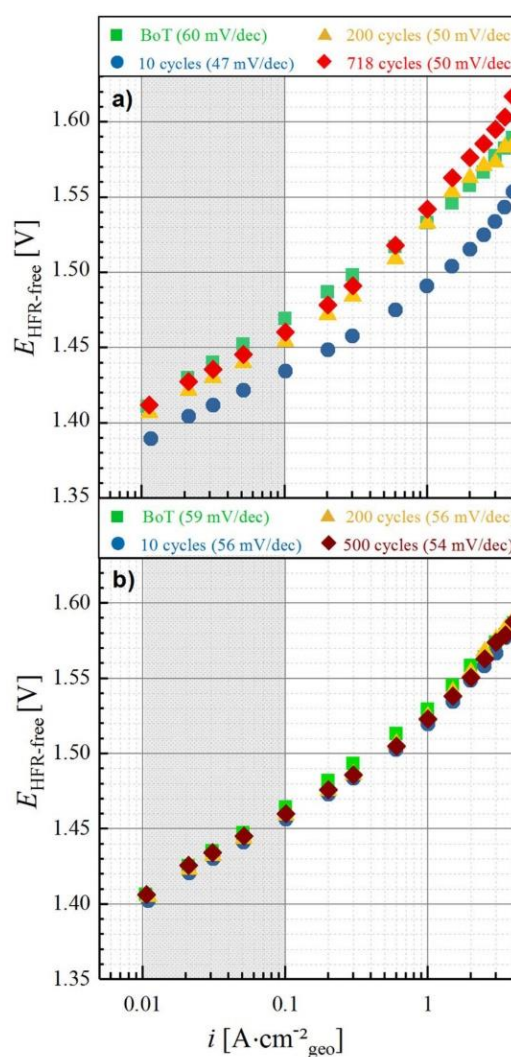


**Figure 6.** Tafel plots of  $E_{HFR-free}$  vs.  $i$  at ambient pressure and 80°C, obtained over the course of the cycling tests: a) for the OCV-AST (data from Figure 4); b) for the reference test where the OCV period was replaced by a potential hold at 1.3 V (data from Figure 5). Tafel slopes were determined between 0.01 A cm<sup>-2</sup><sub>geo</sub> and 0.1 A cm<sup>-2</sup><sub>geo</sub> (gray shaded region), and the values are given in the legend heading each of the two Tafel plots.

to that of crystalline IrO<sub>2</sub> rather than amorphous iridium oxide.<sup>26,27</sup> However, the CV changes significantly after the first 10 OCV periods of the OCV-AST (blue line): i) the capacitive currents are  $\approx 2$  times higher than at the beginning of test; ii) distinct H-UPD features can be observed at low potentials, characteristic of metallic iridium<sup>26,28,29</sup> (see region (1) in Figure 7); and, iii) the redox features observed in region (2) can be attributed to the transition between Ir(III)/Ir(IV).<sup>26</sup> The same change in CV features was reported for the same catalyst upon its exposure to pure H<sub>2</sub> at 80°C for 15 h.<sup>24</sup> Thus, this suggests a gradual reduction of the crystalline IrO<sub>2</sub> catalyst surface into a hydrous iridium oxide during the OCV-AST (i.e., during repeated polarization of the anode catalyst to  $\approx 0$  V vs. RHE), consistent with the latter's higher OER activity,<sup>24,30–32</sup> as demonstrated in Figure 6a. Quite clearly, since thermally prepared, crystalline IrO<sub>2</sub> is not stable below  $\leq 0.8$  V,<sup>24,33</sup> its surface is reduced to metallic iridium, which will be oxidized upon extended cycling to high potentials during the OCV-AST (i.e., up to an



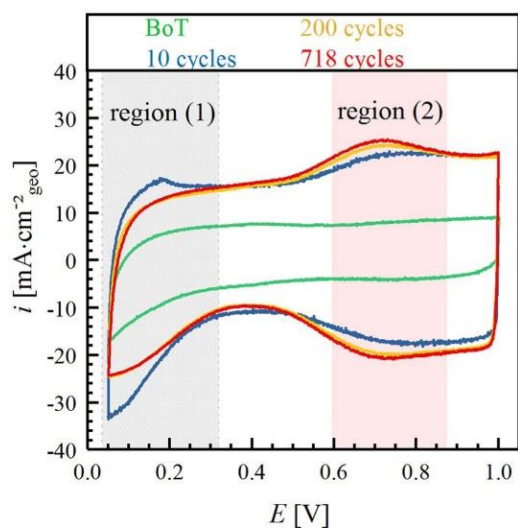


**Figure 7.** Cyclic voltammograms (CVs) recorded after different numbers of cycles of the OCV-AST (see Figure 2), recorded at 50 mV/s, 80°C, ambient pressure, and 5 mL<sub>H<sub>2</sub>O</sub> min<sup>-1</sup> (anode)/ 50 nccm H<sub>2</sub> (cathode).

anode potential of  $\approx 1.6$  V vs. RHE, as indicated by the HFR-corrected voltage at 3 A cm<sup>-2</sup> in Figure 2), forming hydrous iridium oxide.<sup>34</sup> The fact that these hydrous iridium oxide features are still present in the CVs recorded after 200 and 718 cycles (Figure 7, yellow and red lines) indicates an irreversible change of the iridium hydration state at the anode electrode surface with respect to that at the beginning of test, because it appears impossible to electrochemically form crystalline IrO<sub>2</sub>. Instead, the surface remains a hydrous iridium oxide (no significant changes from 200 to 718 cycles). However, the well-defined H-UPD features present after the 10<sup>th</sup> cycle disappear over the course of extended cycling, showing that the initially formed metallic iridium is indeed converted into hydrous iridium oxide.<sup>34</sup> Since the electronic conductivity of hydrous iridium oxide is reported to be lower than that of crystalline IrO<sub>2</sub>,<sup>30</sup> and since the long-time stability of hydrous iridium oxide in a PEM-WE is reported to be inferior to that of crystalline IrO<sub>2</sub>,<sup>31</sup> the transformation of the initially crystalline IrO<sub>2</sub> into hydrous iridium oxide may be the cause for the large degradation over the course of the OCV-AST (Figure 2) and thus would have important consequences for the operational requirements for a PEM-WE.

If our hypothesis was true that the performance degradation observed for the OCV-AST is due to a change of the surface chemistry of the iridium based anode catalyst, we would expect that the surface chemistry of the iridium catalyst after the reference test remains unchanged compared to its initial state, as no performance degradation is observed in this case (Figure 3). Indeed, the CVs recorded over the course of the reference test (Figure 8a) only exhibit marginal differences between the BoT (green line) and the EoT after 500 cycles (red line). This minor increase of the overall capacity, mostly occurring over the first 10 cycles, is either due to a small extent of surface roughening of the IrO<sub>2</sub> catalyst or perhaps more likely to a removal of (surface) impurities, as could be inferred from the slight decrease in HFR over cycling (Figure 5b). Nevertheless, the H-UPD as well as the characteristic hydrous iridium oxide features are absent in the reference test, so that their presence in the OCV-AST is clearly related to the repetitive polarization of the anode to  $\approx 0$  V vs. RHE during the OCV periods. Although the potential is cycled close to 0 V vs. RHE during the CV measurements, the time spent at low potentials is insufficient to form metallic iridium and hence, hydrous iridium oxide, which is why no change is expected. Summarizing our observations and analysis so far, the repetitive cycling of the anode catalyst during the OCV-AST between  $\approx 0$  V vs. RHE at OCV and  $\approx 1.6$  V vs. RHE

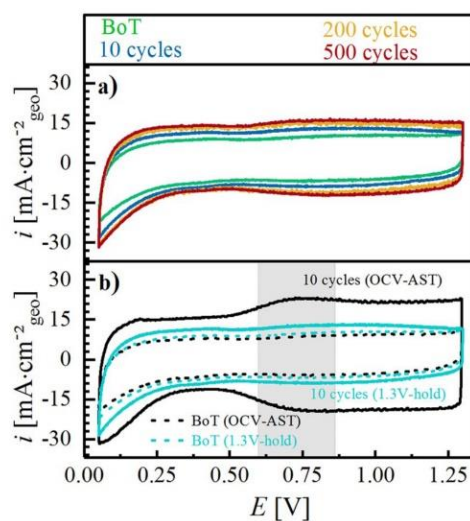


**Figure 8.** a) Cyclic voltammograms (CVs) recorded during the reference test, where the OCV periods are replaced by 1.3 V hold periods. b) Comparison between CVs recorded after 10 cycles for the OCV-AST (black line) and after 10 cycles of the reference test with 1.3 V-holds (blue line); the dotted lines represent the CVs recorded at BoT. CVs were recorded at 50 mV/s, 80°C, ambient pressure, and 5 mL<sub>H<sub>2</sub>O</sub> min<sup>-1</sup> (anode)/ 50 nccm H<sub>2</sub> (cathode).

at high current density leads to a transformation of the initially crystalline IrO<sub>2</sub> into hydrous iridium oxide, concomitant with a substantial decrease in performance and a large increase of the HFR (Figure 4). On the other hand, if the cell potential is controlled to  $\geq 1.3$  V during idle periods, the initial crystalline IrO<sub>2</sub> is retained over extended cycling, and neither a performance degradation nor an increase of the HFR is found (Figure 5).

#### Origin of the cell performance decrease during the OCV-AST.—

In this section, we will discuss possible reasons for the observed decrease in cell performance over the course of the OCV-AST, largely due to an increase of the HFR (Figure 4), contrary to the essentially constant performance and HFR when the OCV periods are replaced by potential holds at 1.3 V (Figure 5). Consequently, the increase of the HFR must be related to processes which take place during OCV periods when the anode potential was shown to decrease to  $\approx 0$  V vs. RHE or which are related to the recurring transition between high potentials (operation) and low potentials (OCV period). In general, an increase of the HFR can be ascribed to different processes occurring in the cell (see Figure 9), which will be discussed individually in the following.

At low potentials, not only can IrO<sub>2</sub> be reduced, but also parts of the cell can be corroded (e.g., flow-fields, PTL). If either of these processes were to result in the formation of metal cations (e.g., from metal impurities in titanium or cationic titanium species), these cations would be ion-exchanged into the membrane/ionomer phase and displace protons, which would not only lead to a reduction of the membrane/ionomer conductivity and to an increase of the HFR,<sup>35</sup> but it would also introduce additional mass transport resistance losses, particularly at high current densities, as described for cation-contaminated membranes in PEM fuel cells (① in Figure 9). The performance decrease and HFR increase over the course of the OCV-AST could in principle be also produced by the introduction of ionic contaminants into the feed water. However, in our test system, the deionized (DI) feed water was supplied through an ion-exchanger, and the resistivity measured between the ion-exchanger and the cell inlet was always  $> 15$  M $\Omega$ cm during the measurements. Moreover, the DI-water was not recycled during operation and therefore we can definitely exclude the presence of ionic contaminants. Moreover, ionic contamination of



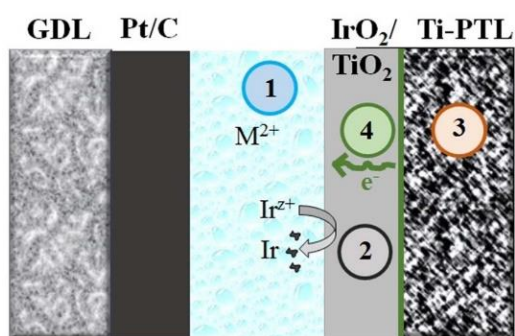


**Figure 9.** Scheme of a single cell, illustrating possible reasons for the observed HFR increase during the OCV-AST: 1) cationic contamination of the membrane; 2) dissolution of iridium from the anode catalyst and its redeposition in the membrane; 3) formation of an electronically insulating oxide film on the Ti-PTL surface; 4) additional resistance due to the low electronic conductivity of hydrous iridium oxide.

the feed water would be independent of the cell operating conditions and, hence, would have to be observed in both the OCV-AST and the reference test. If cationic contamination of the membrane from cell components were present, the HFR should be recovered upon ion-exchanging the aged MEA in 1 M  $\text{H}_2\text{SO}_4$  at  $80^\circ\text{C}$  for 2 h.<sup>18</sup> However, since the HFR after reassembling the cell with the acid treated MEA was still high ( $\approx 100 \text{ m}\Omega \text{ cm}^2_{\text{geo}}$ ) and almost identical to the one measured after the end of test ( $\approx 90 \text{ m}\Omega \text{ cm}^2_{\text{geo}}$ ), as shown in Figure 10, cationic contaminations can be ruled out as a reason for the observed performance loss. Dis- and reassembling of the MEA and PTL (which is considered incompressible) always bears the risk of a different alignment as well as the mechanical deformation of the catalyst or membrane and could be an explanation for the small discrepancy observed. However, both phenomena would most likely not be significant enough to mask the decrease in HFR due to the removal of ionic contaminations. Additionally, an experiment including a reference electrode placed in between two membranes which were subsequently laminated and processed into an MEA (unpublished data<sup>36</sup>)

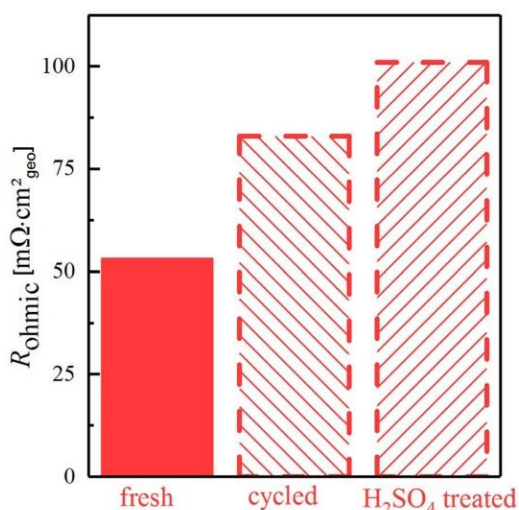


**Figure 10.** High frequency resistance of a fresh MEA at BoT, of a cycled MEA (500 OCV-AST cycles analogous to Figure 2), and of the cycled MEA cycled after 2 h in 1 M  $\text{H}_2\text{SO}_4$  at  $80^\circ\text{C}$ . The HFR was measured at OCV in the (re-assembled) electrolyzer cell at  $80^\circ\text{C}$  and ambient pressure, with a flow of  $5 \text{ mL}_{\text{H}_2\text{O}} \text{ min}^{-1}$  at the anode.

shows that the increase of the HFR during the OCV-AST can clearly be related to an increasing HFR on the anode side of the MEA. Cationic contamination, on the other hand, would lead to a lower ionic conductivity of the entire membrane and, hence, would result in an HFR increase measured between the reference electrode and the anode as well as between the reference electrode and the cathode. Thus, cationic contamination can clearly be eliminated as a possible cause of the performance decrease over the course of the OCV-AST.

Besides cationic contaminations, dissolution and re-precipitation of iridium within the membrane due to reaction with crossover hydrogen might cause an increase in HFR (② in Figure 9), if precipitated iridium were to form a barrier toward proton transport in the membrane. Geiger et al. reported that cycling iridium and thermally grown  $\text{IrO}_2$  films between 0.04 and 1.4 V vs. RHE in  $\text{H}_2\text{SO}_4$  at  $25^\circ\text{C}$  leads to the dissolution of iridium (quantified in a flow cell connected to an inductively coupled plasma mass spectrometer), whereby the dissolution rates for crystalline  $\text{IrO}_2$  were shown to be up to  $\approx 100$ -fold lower than those of iridium and hydrous iridium oxide.<sup>26,37,38</sup> This would predict that the repetitive transition of the HFR-corrected cell voltage (i.e., of the anode potential) between  $\approx 0 \text{ V}$  and  $\approx 1.6 \text{ V}$  during the OCV-AST should lead to the dissolution of iridium, which would either precipitate in the membrane and/or leave the cell with the water effluent. A similar effect involving the dissolution and the precipitation of the catalyst within the membrane due to reaction with crossover hydrogen was reported in the literature for platinum.<sup>39–41</sup> Grigoriev et al. used Pt as an OER catalyst at the anode of a PEM-WE, where they found it to dissolve and re-precipitate in the membrane during a long-term test (albeit at unrealistically high potentials exceeding 3 V vs. RHE).<sup>40</sup> On the other hand, in the case of fuel cells, voltage-cycling of the Pt-based cathode catalyst<sup>41</sup> or extended holds at OCV<sup>39</sup> lead to the precipitation of Pt in the membrane, appearing as a so-called “Pt-band”. The latter study also showed that the position of the Pt-band depends on the  $\text{H}_2/\text{O}_2$  partial pressure ratio,<sup>39</sup> from which one would predict that the deposition of dissolved iridium in a PEM-WE operated at the differential pressure conditions used in our OCV-AST ( $p_{\text{H}_2} = 9.5 \text{ bar}_a$ ,  $p_{\text{O}_2} = 0.5 \text{ bar}_a$ ) would have to occur very close to the anode/membrane interface.<sup>39</sup> To find out whether iridium is indeed being deposited within the membrane over the course of the OCV-AST, site specific TEM analysis were performed, where the membrane area close to the anode/membrane interface was closely inspected. HAADF-STEM images of the degraded MEA after EoT (718 OCV-AST cycles, Figures 11b and 11c) show a distribution of nanoparticles with particle size  $\leq 10 \text{ nm}$  (Figure 11d) for at least  $1 \mu\text{m}$  away from the interface, whereas a new MEA (Figure 11a) remains particle-free.

The STEM-EDS iridium map of a precipitated particle (Figure 11e) revealed that the particles are iridium-based with no obvious oxygen contribution as shown in the homogenous distribution of the oxygen EDS map (Figure 11f). Therefore, the precipitates are primarily composed of metallic iridium. Even though the amount of precipitated iridium is too small to cause the observed increase in HFR, the dissolution and re-precipitation results in a loss of active material in the anode electrode over time, which ultimately would lead to a lower OER activity due to a reduced electrochemically active surface area (ECSA). We believe that this effect is insignificant during the duration of the here shown experiment due to the high catalyst loadings used in this study, but would lead to a more significant performance decay for low Ir-loadings and longer test periods, which is the focus of our current studies.

Alternatively, the HFR could increase due to the formation of an electronically insulating surface film on the Ti-PTL (③ in Figure 9), leading to a higher contact resistance at the anode/PTL and/or the PTL/flow field interface. This was reported previously by Rakousky et al.<sup>19</sup> and can be easily verified by ex-situ measurements of the contact resistance between one PTL/flow-field interface for new or aged PTLs (cf. details in Experimental section).<sup>22</sup> Contact resistances measured ex-situ should be considered with caution, since temperature, contact pressure, and the exact nature of the interface (PTL/catalyst vs. PTL/flow field) during the measurement are different compared



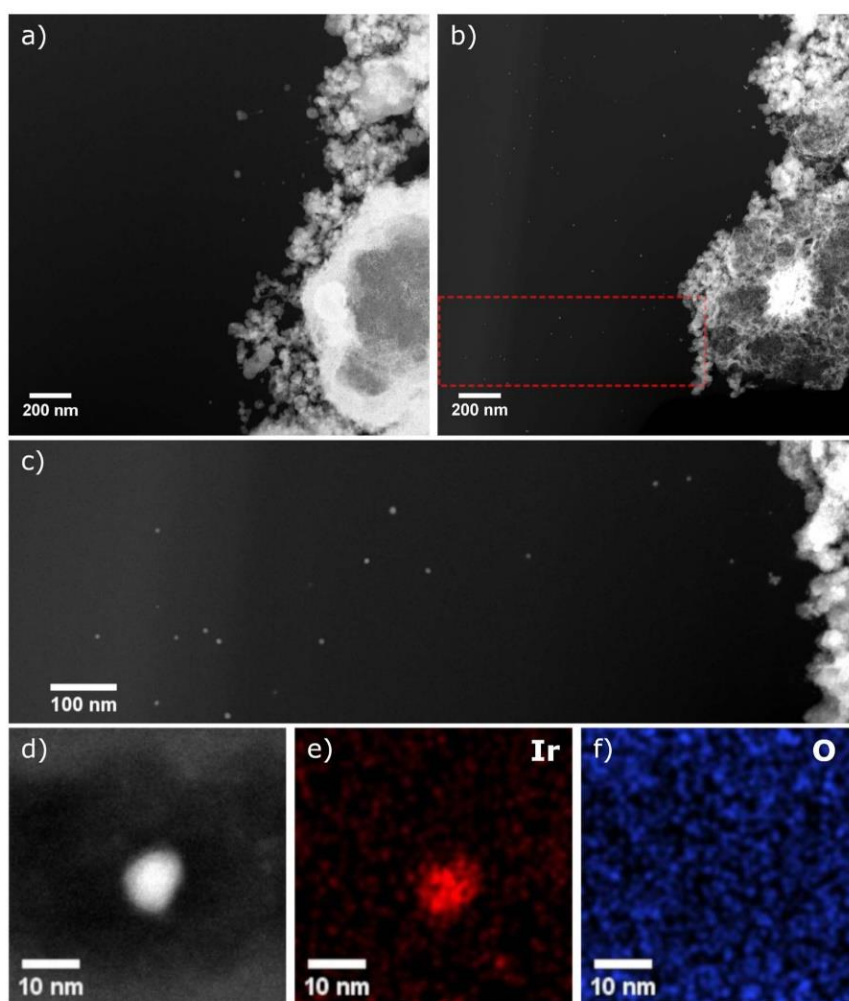


**Figure 11.** HAADF-STEM images of the interface between anode catalyst layer and membrane of (a) a new MEA and (b) an MEA after 718 cycles of the OCV-AST. (c) HAADF-STEM image of the interface of the MEA after 718 cycles of the OCV-AST (red dashed rectangular region in b). (d) HAADF-STEM image of a single particle precipitated at anode/membrane interface as well as the associated STEM-EDS elemental maps of (d) iridium and (e) oxygen.

to in-situ measurements. Nevertheless, they can be used to qualitatively judge the contribution of an additional contact resistance. For a simplified presentation, the contact resistances measured at EoT are normalized to the contact resistances measured at BoT.

The PTL/flow-field contact resistance for a PTL after 718 OCV-AST cycles measured ex-situ at  $\approx 1.7$  MPa (equivalent to the compression in the cell) is twice as high (black triangle in Figure 12) compared to BoT, while it even decreases slightly ( $-10\%$ ) after 500 cycles of the reference test with the 1.3 V-hold (black square in Figure 12). The observed decrease in contact resistance along with the HFR in case of the reference test, might be correlated to an improving alignment at the PTL/electrode interface during operation. In contrast to that, the observed increase in HFR along with the measured increase in contact resistance during the OCV-AST might be related to the passivation of the Ti-PTL. This was further investigated by repeating the OCV-AST with a Ti-PTL sputtered with a thin layer of gold, which is in the order of several micrometer (measured by SEM), on both sides, hoping that it would improve the contact resistance and serve as a protective coating.<sup>42</sup> Indeed, the contact resistance of the Au-sputtered PTL remained essentially constant after 135 OCV-AST cycles (black circle in Figure 12) and a slightly improved HFR at EoT

could be observed. This is in good agreement with the constant performance recorded during the OCV-AST when using a Au-sputtered PTL (data not shown) and thus, the recorded increase in HFR during the OCV-AST is correlated to the passivation of the Ti-PTL. However, the increase of the contact resistance over the OCV-AST ( $\approx 6 \text{ m}\Omega \text{ cm}^2_{\text{geo}}$ ) is much lower than the increase in HFR (see Figure 4) and would only account for a loss of  $\approx 20$  mV compared to the 117 mV cell voltage increase at  $3 \text{ A cm}^{-2}_{\text{geo}}$  (see Figure 2). In addition to the increasing contact resistance for a passivated Ti-PTL, the transition from the initially crystalline  $\text{IrO}_2$  to an amorphous, hydrous iridium oxide, which is known to exhibit lower conductivity,<sup>30</sup> can contribute to an increase in HFR. In this case, the observed HFR increase can be due to either an increase of the electronic through-plane resistance of the anode electrode and/or an increase of the contact resistance at the anode/PTL interface due to a lowering of the bulk conductivity of the anode catalyst as it transforms from a crystalline  $\text{IrO}_2$  to hydrous iridium oxide. Here it must be considered that the electronic through-plane resistance of an electrode does not add directly to the HFR due to coupling of ionic and electronic currents in the electrode, as was shown by a transmission-line analysis by Landesfeind et al.<sup>43</sup> For example, if the ionic and the electronic resistances in an electrode are equally large,



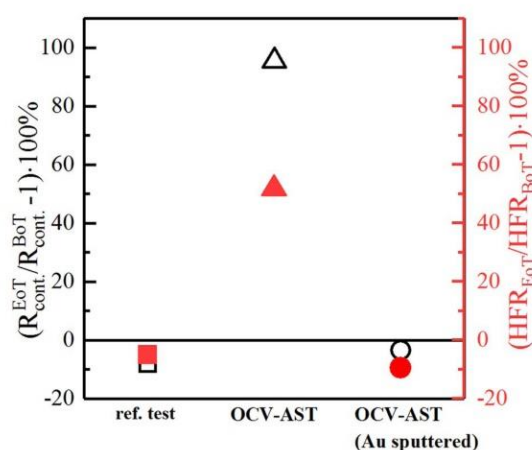


**Figure 12.** Percentage variation of the in-cell HFR (red; measured at  $0.01 \text{ A cm}^{-2}_{\text{geo}}$ ,  $80^\circ\text{C}$ , ambient pressure, with  $5 \text{ mL H}_2\text{O min}^{-1}$ ) and the ex-situ determined contact resistances between the titanium PTL and two Ti flow-fields (black; measured at 1.7 MPa compression) for various PTLs with respect to their BoT values. Left: after 500 cycles of the reference test with the 1.3 V-hold using an uncoated PTL (“ref. test”); middle: after 718 OCV-AST cycles with an uncoated PTL (“OCV-AST”); right: after 135 OCV-AST cycles with a gold-sputtered PTL (“OCV-AST (Au-sputtered)”).

only 50% of the electronic resistance are reflected in the HFR. For the anode used here,  $R_{\text{H}+\text{an}}$  ranges between  $14\text{--}30 \text{ m}\Omega \text{ cm}^2_{\text{geo}}$ , depending on the tortuosity of the electrode.<sup>22</sup> In order to explain an increase of  $\approx 26 \text{ m}\Omega \text{ cm}^2_{\text{geo}}$  over the course of the OCV-AST (i.e., the observed HFR increase minus the increase of the contact resistance between the aged PTL and the flow-field), the electronic through-plane resistance of the anode electrode would have to be roughly twice as high (i.e.,  $\approx 50 \text{ m}\Omega \text{ cm}^2_{\text{geo}}$ ). For a pristine  $\text{IrO}_2/\text{TiO}_2$  electrode, the electronic through-plane resistance is  $\approx 0.04 \text{ m}\Omega \text{ cm}^2_{\text{geo}}$  and for an MEA after 200 OCV-AST cycles it was determined to be  $\approx 0.08 \text{ m}\Omega \text{ cm}^2_{\text{geo}}$ . This clearly cannot explain the increase in HFR after 200 OCV-AST cycles of  $\approx 15 \text{ m}\Omega \text{ cm}^2_{\text{geo}}$ . Thus, the only viable explanation for the HFR increase during the OCV-AST is that the lower conductivity of hydrous iridium oxide in combination with a passivated Ti-PTL leads to an increase of the interfacial contact resistance between the PTL and the anode catalyst layer (a resistance that would not be detectable with the contact resistance measurements shown in Figure 12). Due to the low contact area between the electrode and the coarse PTL structure ( $10\text{--}50 \mu\text{m}$  pores) and the poor electronic conductivity of the passivated PTL surface (see Figure 12), even a comparably small change in the electronic conductivity of the catalyst could cause a significant increase of the contact resistance. Thus, the most likely reason for the increase of the HFR and the increase of the HFR-corrected cell voltage over the course of the OCV-AST (Figure 4) is the development of a contact resistance between hydrous iridium oxide and the titanium PTL.

In summary, the repetitive transition between  $\approx 1.6 \text{ V}$  at  $3 \text{ A cm}^{-2}_{\text{geo}}$  and  $\approx 0 \text{ V}$  vs. RHE at extended OCV periods during the OCV-AST leads to the transformation of crystalline  $\text{IrO}_2$  into a hydrous iridium oxide surface. These large voltage cycles cause the dissolution of iridium and its precipitation into the membrane near the anode/membrane interface, but the overall activity loss due to this mechanism is negligible for anodes with a high iridium loading. The vast majority of the performance loss is due to an increase of the HFR, whereby the above analysis shows that the most likely reason for its increase is a parasitic contact resistance developing between hydrous iridium oxide (formed during the OCV-AST) and the passivated titanium PTL.

**Current density and energy requirement for a 1.3 V-hold during idle periods.**—In this section, an operating strategy to avoid OCV

periods and the resulting degradation phenomena will be discussed in terms of a practical application of PEM electrolyzer systems. In the reference test shown in this study, a potential hold at 1.3 V was applied to avoid a potential drop during idle periods. The current density measured during these potential hold periods was typically very low with a value of  $\approx 1 \text{ mA cm}^{-2}_{\text{geo}}$  or below toward the end of the experiment. This translates into a power density of  $\approx 1.3 \text{ mW cm}^{-2}_{\text{geo}}$  required to hold the cell potential at 1.3 V, which is only 0.025% of the maximum power density of  $\approx 5.25 \text{ W cm}^{-2}_{\text{geo}}$  obtained at a current density of  $3 \text{ A cm}^{-2}_{\text{geo}}$  and a corresponding cell voltage of  $\approx 1.75 \text{ V}$ . Consequently, the amount of energy required to avoid OCV periods by a potential hold at 1.3 V would be negligible.

In a real system, however, this operating strategy might not be practical, since it would lead to an accumulation of hydrogen in the anode compartment of the electrolyzer due to hydrogen permeation through the membrane during the potential hold at 1.3 V. This accumulation of hydrogen cannot be prevented when operated at differential pressure ( $p_{\text{cathode}} = 10 \text{ bar}_a$ ,  $p_{\text{anode}} = 1 \text{ bar}_a$ ), even when a recombination catalyst in the membrane<sup>44</sup> or the flow field is used, since almost no oxygen, which would be required for a recombination with hydrogen to water, is produced at the very low current density of  $\approx 1 \text{ mA cm}^{-2}_{\text{geo}}$  or below. The amount of oxygen which needs to be evolved to allow a full recombination of hydrogen with oxygen can be estimated based on the permeation rate of hydrogen at the applied cathode pressure, in the present case  $p_{\text{cathode}} = 10 \text{ bar}_a$ . At a temperature of  $80^\circ\text{C}$  and in the presence of liquid water, a permeation rate of  $\approx 0.85 \text{ mA cm}^{-2}_{\text{geo}} \text{ bar}_a(\text{H}_2)^{-1}$  can be assumed (see also above).<sup>23</sup> For cathode pressures of  $10 \text{ bar}_a$  or  $30 \text{ bar}_a$ , this results in current densities of  $8.1 \text{ mA cm}^{-2}_{\text{geo}}$  or  $25.1 \text{ mA cm}^{-2}_{\text{geo}}$ , respectively, which would need to be applied to produce enough oxygen to achieve a hydrogen to oxygen stoichiometry of 2:1 and, consequently, to enable a full recombination of the permeating hydrogen. Taking the corresponding cell voltage values from Figure 5, this results in power densities of  $\approx 12 \text{ mW cm}^{-2}_{\text{geo}}$  at  $10 \text{ bar}_a$  and  $\approx 36 \text{ mW cm}^{-2}_{\text{geo}}$  at  $30 \text{ bar}_a$ , respectively. This means that only 0.2% (at  $10 \text{ bar}_a$ ) and 0.7% (at  $30 \text{ bar}_a$ ) of the maximum power would need to be applied during idle periods to prevent hydrogen accumulation on the anode. Assuming an electrolyzer system which is directly coupled to a fluctuating power source and cannot obtain energy from the grid, the required energy could be supplied by, e.g., coupling a battery to the electrolyzer.<sup>45</sup> In summary, this analysis shows that operating the electrolyzer at a small current density during idle periods ( $\ll 1\%$  of maximum power required) in combination with a recombination catalyst is a promising operating strategy to avoid OCV periods and the associated performance degradation as well as safety concerns due to hydrogen permeation.

## Conclusions

In this study, the impact of intermittent power supply on the performance and lifetime of a PEM water electrolyzer was investigated. An AST protocol was designed comprising periods of operation at two current densities ( $3 \text{ A cm}^{-2}_{\text{geo}}$  and  $0.1 \text{ A cm}^{-2}_{\text{geo}}$ ), alternating with idle periods where the cell is left at the OCV in order to simulate the discontinuous power output of renewable energy sources. An initial increase in performance was observed during the first 10 cycles ( $\approx 50 \text{ mV}$ ) while prolonged cycling led to a significant decrease in performance due to an increasing HFR ( $\approx 1.6$ -fold after 700 cycles).

The initial increase in performance is related to the OCV periods during which hydrogen crossover and accumulation leads to a decrease of the cell voltage close to the HOR potential ( $\approx 0 \text{ V}$ ), leading to a reduction of the surface of the thermal  $\text{IrO}_2$  anode catalyst (coated onto a  $\text{TiO}_2$  support) to metallic Ir. The subsequent oxidation of the catalyst during periods of operation leads to the transformation of the crystalline  $\text{IrO}_2$  to an amorphous iridium oxide, which was evidenced by a lower Tafel slope (consistent with an increased activity) and the evolution of the characteristic features of metallic Ir and amorphous iridium oxide in a CV. Amorphous iridium oxide is known to exhibit a higher activity compared to crystalline  $\text{IrO}_2$ , explaining the initial performance increase.



However, the repetitive transition between oxidizing conditions during operation and reducing conditions during OCV periods (i.e., between hydrous iridium oxide and metallic iridium) causes an enhanced dissolution of Ir, which was revealed by STEM imaging of the anode/membrane interface showing Ir nanoparticles deposited in the membrane. Even though the amount of precipitated Ir is too small to have a significant impact on performance, continuous dissolution will result in a loss of active material and ultimately in a lower OER activity.

The increasing HFR, which is the major reason for the performance loss during the OCV-AST, can be partially explained by an increasing contact resistance arising from passivation of the Ti-PTL during OCV/load cycles ( $\approx 20$  mV out of 117 mV at 3 A cm<sup>-2</sup><sub>geo</sub>). However, an additional contribution is hypothesized to be the formation of hydrous iridium oxide, which has a lower electronic conductivity. Due to the low contact area between the electrode and the coarse PTL structure (10–50  $\mu$ m pores) along with a poor electronic conductivity of the passivated PTL surface, even a relatively small reduction of the electronic conductivity of the catalyst could cause a significant increase of the interfacial contact resistance between catalyst layer and PTL, thus explaining the HFR increase.

Since a reference test where the OCV period was replaced by a potential hold at 1.3 V showed no degradation over 500 cycles, the performance loss can clearly be attributed to the OCV periods. Hence, avoiding OCV periods during operation of a PEM-WE is crucial to ensure long-term stability. Based on these findings, we suggest that applying a small current density ( $\ll 1\%$  of maximum power required) during idle periods in combination with a recombination catalyst is required for a dynamically operated PEM water electrolyzer to avoid degradation and mitigate safety concerns related to hydrogen crossover.

#### Acknowledgments

This work was funded by the Bavarian Ministry of Economic Affairs and Media, Energy and Technology through the project ZAE-ST (storage technologies) and by the German Ministry of Education and Research (funding number 03SFK2V0, Kopernikus-project P2X). We thank Matthias Singer for electrode preparation.

#### ORCID

A. Weiß  <https://orcid.org/0000-0001-7094-5016>  
 A. Siebel  <https://orcid.org/0000-0001-5773-3342>  
 M. Bernt  <https://orcid.org/0000-0001-8448-5532>

#### References

- M. Carmo, D. L. Fritz, J. Mergel, and D. Stolten, A Comprehensive Review on Pem Water Electrolysis, *International Journal of Hydrogen Energy*, **38**, 4901 (2013).
- F. Barbir, Pem Electrolysis for Production of Hydrogen from Renewable Energy Sources, *Solar Energy*, **78**, 661 (2005).
- K. E. Ayers, E. B. Anderson, K. Dreier, and K. W. Harrison, Fueling Vehicles with Sun and Water, *ECS Transactions*, **50**, 35 (2013).
- A. Butler and H. Spliethoff, Current Status of Water Electrolysis for Energy Storage, Grid Balancing and Sector Coupling Via Power-to-Gas and Power-to-Liquids: A Review, *Renewable and Sustainable Energy Reviews*, (2017).
- A. Mohammadi and M. Mehrpooya, A Comprehensive Review on Coupling Different Types of Electrolyzer to Renewable Energy Sources, *Energy*, (2018).
- R. Clarke, S. Giddey, F. Ciachini, S. Badwal, B. Paul, and J. Andrews, Direct Coupling of an Electrolyser to a Solar Pv System for Generating Hydrogen, *International Journal of Hydrogen Energy*, **34**, 2531 (2009).
- M. Little, M. Thomson, and D. Infield, Electrical Integration of Renewable Energy into Stand-Alone Power Supplies Incorporating Hydrogen Storage, *International Journal of Hydrogen Energy*, **32**, 1582 (2007).
- A. S. Aricò, S. Siracusano, N. Briguglio, V. Baglio, A. Di Blasi, and V. Antonucci, Polymer Electrolyte Membrane Water Electrolysis: Status of Technologies and Potential Applications in Combination with Renewable Power Sources, *Journal of Applied Electrochemistry*, **43**, 107 (2013).
- C. Schug, Operational Characteristics of High-Pressure, High-Efficiency Water-Hydrogen-Electrolysis, *International journal of hydrogen energy*, **23**, 1113 (1998).
- A. Bergen, L. Pitt, A. Rowe, P. Wild, and N. Djilali, Transient Electrolyser Response in a Renewable-Regenerative Energy System, *International Journal of Hydrogen Energy*, **34**, 64 (2009).
- U. Babic, M. Suermann, F. N. Büchi, L. Gubler, and T. J. Schmidt, Critical Review—Identifying Critical Gaps for Polymer Electrolyte Water Electrolysis Development, *Journal of The Electrochemical Society*, **164**, F387 (2017).
- S. Stucki, G. G. Scherer, S. Schlagowski, and E. Fischer, Pem Water Electrolyzers: Evidence for Membrane Failure in 100kw Demonstration Plants, *Journal of Applied Electrochemistry*, **28**, 1041 (1998).
- D. E. Curtin, R. D. Lousenberg, T. J. Henry, P. C. Tangeman, and M. E. Tisack, Advanced Materials for Improved Pemfc Performance and Life, *Journal of power Sources*, **131**, 41 (2004).
- C. K. Mittelsteadt, Pem Electrolysis: Ready for Impact. *ECS Transactions*, **69**, 205 (2015).
- S. Siracusano, N. Van Dijk, R. Backhouse, L. Merlo, V. Baglio, and A. Aricò, Degradation Issues of Pem Electrolysis Meas, *Renewable Energy*, **123**, 52 (2018).
- S. A. Grigoriev, D. G. Bessarabov, and V. N. Fateev, Degradation Mechanisms of Mea Characteristics During Water Electrolysis in Solid Polymer Electrolyte Cells, *Russian Journal of Electrochemistry*, **53**, 318 (2017).
- N. Danilovic, K. E. Ayers, C. Capuano, J. N. Renner, L. Wiles, and M. Pertoso, (Plenary) Challenges in Going from Laboratory to Megawatt Scale Pem Electrolysis, *ECS Transactions*, **75**, 395 (2016).
- S. Sun, Z. Shao, H. Yu, G. Li, and B. Yi, Investigations on Degradation of the Long-Term Proton Exchange Membrane Water Electrolysis Stack, *Journal of Power Sources*, **267**, 515 (2014).
- C. Rakousky, U. Reimer, K. Wippermann, M. Carmo, W. Lueke, and D. Stolten, An Analysis of Degradation Phenomena in Polymer Electrolyte Membrane Water Electrolysis, *Journal of Power Sources*, **326**, 120 (2016).
- C. Rakousky, U. Reimer, K. Wippermann, S. Kuhri, M. Carmo, W. Lueke, and D. Stolten, Polymer Electrolyte Membrane Water Electrolysis: Restraining Degradation in the Presence of Fluctuating Power. *Journal of Power Sources*, **342**, 38 (2017).
- M. F. Mathias, J. R., J. Fleming and W. Lehnert, *Diffusion Media Materials and Characterisation*, 2003; Vol. 3.
- M. Bernt and H. A. Gasteiger, Influence of Ionomer Content in IrO<sub>2</sub>/TiO<sub>2</sub> Electrodes on Pem Water Electrolyzer Performance, *Journal of The Electrochemical Society*, **163**, F3179 (2016).
- M. Bernt, J. Schröter, A. Weiß, A. Siebel, and H. A. Gasteiger, In *Analysis of Gas Permeation Phenomena in a Pem Water Electrolyzer Operated at High Pressure and Current Density*, Meeting Abstracts, The Electrochemical Society: 2018; pp 1598.
- P. J. Rheinländer, M. Bernt, Y. Incedag, and H. A. Gasteiger, Stability and Oer Activity of Irox in Pem Water Electrolysis, *Meeting Abstracts*, (2016), MA2016-02, 2427.
- M. Bernt, A. Siebel, and H. A. Gasteiger, Analysis of Voltage Losses in Pem Water Electrolyzers with Low Platinum Group Metal Loadings, *Journal of The Electrochemical Society*, **165**, F305 (2018).
- S. Geiger, O. Kasian, B. R. Shrestha, A. M. Mingers, K. J. J. Mayrhofer, and S. Cherevko, Activity and Stability of Electrochemically and Thermally Treated Iridium for the Oxygen Evolution Reaction, *Journal of The Electrochemical Society*, **163**, F3132 (2016).
- S. Ardizzone, A. Carugati, and S. Trasatti, Properties of Thermally Prepared Iridium Dioxide Electrodes, *Journal of Electroanalytical Chemistry and Interfacial Electrochemistry*, **126**, 287 (1981).
- R. Woods, Hydrogen Adsorption on Platinum, Iridium and Rhodium Electrodes at Reduced Temperatures and the Determination of Real Surface Area, *Journal of Electroanalytical Chemistry and Interfacial Electrochemistry*, **49**, 217 (1974).
- J. Durst, C. Simon, F. Hasché, and H. A. Gasteiger, Hydrogen Oxidation and Evolution Reaction Kinetics on Carbon Supported Pt, Ir, Rh, and Pd Electrocatalysts in Acidic Media, *Journal of The Electrochemical Society*, **162**, F190 (2015).
- E. Rastan, G. Hagen, and R. Tunold, Electrocatalysis in Water Electrolysis with Solid Polymer Electrolyte, *Electrochimica Acta*, **48**, 3945 (2003).
- S. Siracusano, V. Baglio, S. A. Grigoriev, L. Merlo, V. N. Fateev, and A. S. Aricò, The Influence of Iridium Chemical Oxidation State on the Performance and Durability of Oxygen Evolution Catalysts in Pem Electrolysis, *Journal of Power Sources*, **366**, 105 (2017).
- T. Reier, D. Teschner, T. Lunkenbein, A. Bergmann, S. Selve, R. Kraehnert, R. Schlögl, and P. Strasser, Electrocatalytic Oxygen Evolution on Iridium Oxide: Uncovering Catalyst-Substrate Interactions and Active Iridium Oxide Species, *Journal of The Electrochemical Society*, **161**, F876 (2014).
- M. Pourbaix, *Atlas of Electrochemical Equilibria in Aqueous Solutions*, 2nd. Eng. edn. ed.; NACE International Cebelcor Houston, Texas, USA 1974, p 373.
- P. G. Pickup and V. I. Birss, A Model for Anodic Hydrous Oxide Growth at Iridium, *Journal of Electroanalytical Chemistry and Interfacial Electrochemistry*, **220**, 83 (1987).
- T. Okada, Effect of Ionic Contaminants, *Handbook of fuel cells*, **3**, 627 (2003).
- A. Weiß, M. Bernt, A. Siebel, and H. A. Gasteiger, A Platinum Micro-Reference Electrode for Impedance Measurements in Polymer Electrolyte Membrane Water Electrolysis, *Manuscript in preparation*.
- S. Cherevko, S. Geiger, O. Kasian, A. Mingers, and K. J. J. Mayrhofer, Oxygen Evolution Activity and Stability of Iridium in Acidic Media. Part 1. – Metallic Iridium, *Journal of Electroanalytical Chemistry*, **773**, 69 (2016).
- S. Cherevko, S. Geiger, O. Kasian, A. Mingers, and K. J. J. Mayrhofer, Oxygen Evolution Activity and Stability of Iridium in Acidic Media. Part 2. – Electrochemically Grown Hydrous Iridium Oxide, *Journal of Electroanalytical Chemistry*, **774**, 102 (2016).

39. J. Zhang, B. A. Litterer, W. Gu, H. Liu, and H. A. Gasteiger, Effect of Hydrogen and Oxygen Partial Pressure on Pt Precipitation within the Membrane of Pemfcs, *Journal of The Electrochemical Society*, **154**, B1006 (2007).
40. S. A. Grigoriev, K. A. Dzhus, D. G. Bessarabov, and P. Millet, Failure of Pem Water Electrolysis Cells: Case Study Involving Anode Dissolution and Membrane Thinning, *International Journal of Hydrogen Energy*, **39**, 20440 (2014).
41. P. Ferreira, Y. Shao-Horn, D. Morgan, R. Makharia, S. Kocha, and H. Gasteiger, Instability of Pt/ C Electrocatalysts in Proton Exchange Membrane Fuel Cells a Mechanistic Investigation, *Journal of The Electrochemical Society*, **152**, A2256 (2005).
42. H.-Y. Jung, S.-Y. Huang, P. Ganesan, and B. N. Popov, Performance of Gold-Coated Titanium Bipolar Plates in Unitized Regenerative Fuel Cell Operation, *Journal of Power Sources*, **194**, 972 (2009).
43. J. Landesfeind, M. Ebner, A. Eldiven, V. Wood, and H. A. Gasteiger, Tortuosity of Battery Electrodes: Validation of Impedance-Derived Values and Critical Comparison with 3d Tomography, *Journal of The Electrochemical Society*, **165**, A469 (2018).
44. E. Price, Durability and Degradation Issues in Pem Electrolysis Cells and Its Components, *Johnson Matthey Technology Review*, **61**, 47 (2017).
45. B. Gillissen, H. Heinrichs, P. Stenzel, and J. Linssen, Hybridization Strategies of Power-to-Gas Systems and Battery Storage Using Renewable Energy, *International Journal of Hydrogen Energy*, **42**, 13554 (2017).



## 5.7 A Platinum Micro-Reference Electrode for Impedance Measurements in PEM Water Electrolysis

The last section deals with the article “A Platinum Micro-Reference Electrode for Impedance Measurements in PEM Water Electrolysis”, which was submitted to the *Journal of Electrochemical Society* in August 2021 and accepted for publication as an open access article under the terms of Creative Commons Attribution 4.0 License (CC BY) in November 2021. The study was presented by A.H.-W. at the 23<sup>rd</sup> European Fuel Cell Forum Conference in Luzern 2019.

The permanent web-link of the article is: <https://iopscience.iop.org/article/10.1149/1945-7111/ac3717/meta>

In the previous section 5.6, it was shown that during an OCV-AST the hydrogen crossover causes the cell potential to drop close to 0 V and also the formation of a hydrous iridium-oxide. Moreover, the decreasing performance was attributed to the formation of an additional interfacial resistance at the anode. In order to clearly prove that this is the main reason for the decaying performance, a Pt-wire reference electrode (Pt-WRE) is introduced within this study to record the individual impedance spectra of anode and cathode separately during operation. For this, a 50  $\mu\text{m}$  thick Pt-wire with an additional 9  $\mu\text{m}$  PTFE insulation is laminated in between two 50  $\mu\text{m}$  Nafion<sup>®</sup> membranes. SEM (scanning electron microscopy) images confirmed that the Pt-wire is placed centrally between the two electrodes. Polarization curves showed that the potential of the Pt-WRE depends on the relative permeation fluxes of hydrogen ( $\dot{N}_{\text{H}_2(x)}$ ) and oxygen ( $\dot{N}_{\text{O}_2(x)}$ ) at the location of the platinum wire. While it is close to the reversible potential of hydrogen ( $\approx 0 V_{\text{RHE}}$ ) at low current densities, it is close to the reversible potential of water at higher current densities. Since the Pt-WRE potential during operation shows a significant current density dependency, it is not possible to measure artefact-free individual electrode resolved impedance spectra during electrolyzer operation, since the Pt-WRE potential is shifted upon a variation in  $\text{H}_2$  and  $\text{O}_2$  partial pressures at the catalyst|membrane interface. At very low current densities (at/near the OCV), where the Pt-WRE potential is close to ( $\approx 0 V_{\text{RHE}}$ ), this effect is negligible and artefact-free individual electrode impedance spectra can be obtained.

Utilizing the reference electrode while applying the same OCV-AST as in section 5.6, it can be shown that, while the potential of the cathode remains close to the reversible hydrogen potential



during the OCV-period, the anode potential follows the cell potential and drops close to 0 V<sub>RHE</sub> within a couple of minutes. This confirms the permeation of hydrogen from the cathode into the anode compartment, which causes the formation of metallic iridium and thus the drop in potential. Recording individual half-cell spectra at 1.3 V at the end of each OCV-cycle further proved that the HFR of the anode increases simultaneously along with the HFR of the full-cell ( $\Delta\text{HFR} \approx 87 \mu\Omega\text{cm}^2_{\text{geo}}/\text{cycle}$ ), while the HFR of the cathode remained constant ( $\approx 0 \mu\Omega\text{cm}^2_{\text{geo}}/\text{cycle}$ ). Using a simplified transmission line model, where the charge transfer kinetics are assumed to be infinitely large, the anode spectra recorded at 1.3 V were fitted to extract the capacity as well as the proton sheet resistance. The constant HFR of the cathode along with the constant proton sheet resistance of the anode over cycling confirmed that cationic contamination could be excluded as one of the reasons for the increasing HFR. By utilizing the Pt-WRE during the OCV-AST, it was unequivocally proven that an additional contact resistance at the anode is causing the increasing HFR and the accompanied decrease in performance.

### **Authors contributions**

Fabrication of catalyst inks, membrane electrode assemblies, and electrochemical testing in a PEM-WE cell was performed by A.H.-W. Analysis of the experimental test results was done A.H.-W. A.H.-W. wrote the manuscript. All authors discussed the experimental results and revised the manuscript.

**OPEN ACCESS**

## A Platinum Micro-Reference Electrode for Impedance Measurements in a PEM Water Electrolysis Cell

To cite this article: Alexandra Hartig-Weiß *et al* 2021 *J. Electrochem. Soc.* **168** 114511

View the [article online](#) for updates and enhancements.



 The Electrochemical Society  
Advancing solid state & electrochemical science & technology

242nd ECS Meeting  
Oct 9 – 13, 2022 • Atlanta, GA, US

Abstract submission deadline: **April 8, 2022**

Connect. Engage. Champion. Empower. Accelerate.

**MOVE SCIENCE FORWARD**

 Submit your abstract



This content was downloaded from IP address 129.187.254.46 on 06/03/2022 at 16:18



## A Platinum Micro-Reference Electrode for Impedance Measurements in a PEM Water Electrolysis Cell

Alexandra Hartig-Weiß,<sup>1,\*</sup> Maximilian Bernt,<sup>1,2</sup> Armin Siebel,<sup>1</sup> and Hubert A. Gasteiger<sup>1,\*</sup>

<sup>1</sup>Chair of Technical Electrochemistry, Department of Chemistry and Catalysis Research Center, Technical University of Munich, 85748 Garching, Germany

<sup>2</sup>Bayerisches Zentrum für angewandte Energieforschung, 85748 Garching, Germany

We present a platinum wire micro-reference electrode (Pt-WRE) suitable for recording individual electrochemical impedance spectra of both the anode and the cathode in a proton exchange membrane water electrolyzer (PEM-WE). For this purpose, a thin, insulated Pt-wire reference electrode (Pt-WRE) was laminated centrally between two 50  $\mu\text{m}$  Nafion<sup>®</sup> membranes, whereby the potential of the Pt-WRE is determined by the ratio of the local H<sub>2</sub> and O<sub>2</sub> permeation fluxes at the tip of the Pt-WRE. Impedance analysis with the Pt-WRE allows determination of the proton sheet resistance of the anode, the anode catalyst layer capacitance, and the high-frequency resistance (HFR) of both electrodes individually, using a simple transmission-line model. This new diagnostic tool was used to analyze performance degradation during an accelerated stress test (AST), where low and high current densities were alternated with idle periods without current (i.e., at open circuit voltage (OCV)), mimicking the fluctuating operation of a PEM-WE with renewable energy. Our analysis revealed that the increasing HFR that was observed over the course of the OCV-AST, which is the main cause for the observed performance decrease, can unequivocally be assigned to an increasing contact resistance between the anode electrode and the porous transport layer.

© 2021 The Author(s). Published on behalf of The Electrochemical Society by IOP Publishing Limited. This is an open access article distributed under the terms of the Creative Commons Attribution 4.0 License (CC BY, <http://creativecommons.org/licenses/by/4.0/>), which permits unrestricted reuse of the work in any medium, provided the original work is properly cited. [DOI: 10.1149/1945-7111/ac3717]



Manuscript submitted August 31, 2021; revised manuscript received October 17, 2021. Published November 18, 2021.

In light of an increasing energy demand and the goal to drastically reduce CO<sub>2</sub> emissions, alternative energy carriers produced by renewable energies are a necessity to replace fossil fuels. However, since renewable energies such as wind and solar are inherently intermittent in their power output, an efficient energy carrier provided by a system capable of tolerating such a fluctuating operation is required. Gaseous hydrogen produced by electrochemical spitting of water in a proton exchange membrane water electrolyzer (PEM-WE) is one of the promising technologies that can meet all these requirements.<sup>1,2</sup> Even though PEM-WE durability over 50,000–100,000 h has been demonstrated for constant operation,<sup>3</sup> their durability when operated with renewable energy sources, where times of operation alternate with idle periods where no current is supplied,<sup>4,5</sup> is of greater relevance.

In a previous study by our group, an accelerated stress test (AST) was proposed, with repetitive cycles that consisted of periods of low and high current densities (0.1  $\text{Acm}^{-2}_{\text{geo}}$  and 3  $\text{Acm}^{-2}_{\text{geo}}$ ), mimicking times of operation, and of an idle period, where the cell was left at open circuit voltage (OCV); this OCV-AST was conducted at 80 °C, with 10 bar pressure on the hydrogen compartment and 1 bar pressure on the oxygen compartment, mimicking the differential pressure operation that would be used in applications where high pressure H<sub>2</sub> is the desired product.<sup>6</sup> Over the course of such an OCV-AST, the performance at 3  $\text{Acm}^{-2}_{\text{geo}}$  decreased significantly ( $\approx 100$  mV after 718 cycles), which was attributed to a substantial increase of the high-frequency resistance (HFR) by  $\approx 30$   $\text{m}\Omega\text{cm}^2$  over the 718 cycles. In contrast to that, the HFR remained constant when the cell was polarized at 1.3 V during the idle periods (requiring the supply of only  $\approx 1$   $\text{mAcm}^{-2}_{\text{geo}}$ , corresponding to  $<0.1\%$  of the power at 3  $\text{Acm}^{-2}_{\text{geo}}$ ), proving that the performance degradation is related to the OCV period where the electrolyzer cell voltage drops to near 0 V. By excluding other possible causes for the observed performance degradation, we attributed the increasing HFR to the build-up of a contact resistance at the interface between the anode catalyst layer and the titanium-based porous transport layer (PTL), due to the gradual passivation of

the titanium PTL in combination with a decrease of the electronic conductivity of the anode catalyst layer.<sup>6</sup> The latter is triggered by the OCV periods, during which the cell potential drops to  $\approx 0$  V due to crossover and accumulation of hydrogen in the anode electrode, thereby gradually reducing the initially crystalline IrO<sub>2</sub> phase of the anode catalyst and forming a hydrous iridium-oxide, which exhibits a lower electronic conductivity.<sup>6,7</sup> While all the observations made in our previous study support our hypothesis of a resistance at the anode||PTL interface being the cause for the observed performance decrease, this could not be proven unambiguously. Therefore, in the present study the processes occurring during the above described OCV-AST are reexamined using a membrane electrode assembly (MEA) into which a micro-reference electrode is incorporated, thereby allowing to record individual electrochemical impedance spectra of anode and cathode with which the origin of different voltage loss contributions can be identified.

Electrochemical impedance spectroscopy (EIS) is a powerful tool to characterize and quantify single performance losses, and there are several examples of reference electrodes being used to study electrochemical cells in the literature.<sup>8,9</sup> Depending on the design of the reference electrode, it can be used to track the half-cell potentials and/or to measure impedance of the individual half-cells. One prominent example often used in the literature to measure half-cell potentials in PEM fuel cells is the dynamic hydrogen electrode (DHE), where usually two thin Pt-wires are placed in close proximity to the active electrode area; by applying a small electrolysis current between the two wires, the potential of the wire where H<sub>2</sub> is being evolved is very close to the reversible hydrogen electrode potential (RHE) due to the fast kinetics for the hydrogen evolution reaction (HER) and can thus be used as a DHE reference electrode (i.e., 0 V vs DHE is only a few mV negative of 0 V vs RHE).<sup>10,11</sup> However, a proper positioning of the DHE reference electrode wire with respect to its distance from the active area of the working and counter electrodes is critical to avoid any potential shift that is caused by the non-linear potential profile in close proximity to the working and counter electrode areas.<sup>12,13</sup> A homogenous potential profile is established at a distance from the edge of the working/counter electrode that is larger than roughly three times the thickness of the ion conducting membrane.<sup>13</sup> Hence, the reference electrode should be placed at the appropriate distance ( $>3$ -times the thickness of the ion conducting membrane) from the active electrodes.

\*Electrochemical Society Fellow.  
\*E-mail: alexandra.weiss@tum.de



Moreover, a precise geometrical alignment of the working and counter electrode with respect to each other is essential, when seeking to record individual electrode impedance spectra. Adler et al. showed that even a small misalignment (e.g., if the working electrode is protruding beyond the adjacent counter electrode, or vice versa) can lead to erroneous half-cell impedance spectra when acquired with a reference electrode that is placed outside the working/counter electrode area; in this case, the magnitude of the individual electrode impedances are off by a factor of more than two if the counter and working electrodes are misaligned by more than the thickness of the membrane.<sup>12</sup> In summary, with a precise positioning of the DHE reference electrode, the DHE is a suitable tool to monitor half-cell potentials in electrochemical cells like PEM fuel cells or PEM-WEs, but individual electrode impedance spectra should be treated with caution, since a misalignment between the working and counter electrode that is much less than the thickness of the membrane (e.g., 50  $\mu\text{m}$  for a Nafion® 212 membrane) cannot be achieved during fabrication.

In a recently published study, Sorsa et al. used a carbon supported platinum catalyst to coat a ring-shaped Pt electrode on one side of a  $\approx 125 \mu\text{m}$  thick membrane while a disk-shaped electrolyzer electrode was coated on the other side such that the outer diameter of the disk electrode was smaller than the inner diameter of the concentrically placed ring electrode.<sup>9</sup> Laminating two such membranes together, with the ring electrodes facing each other and with a Pt wire placed in between, the Pt ring electrode could be used as pseudo reference electrode.<sup>9</sup> While also here the same artefacts due to the misalignment should occur, the authors used this method to measure the individual impedance contributions. They showed that the anode impedance spectra comprise two main processes, namely mass transport and charge transfer resistances. The interpretation of the cathode spectra, however, turned out to be more complicated due to the occurrence of an inductive loop at low frequencies. Ultimately, the authors concluded that the inductive loop is caused by carbon corrosion of the cathode catalyst layer. This, however, seems highly improbable, as the carbon support is known to be very stable at the potential of an electrolyzer cathode (i.e., at  $\approx 0 \text{ V}$  vs RHE), and it should be considered that the cathode impedance spectra could be flawed to electrode misalignment effects (based on the above discussion, misalignment on the order of 250  $\mu\text{m}$  would be expected to lead to such issues).

The artefacts due to a working/counter electrode misalignment can be avoided by placing the reference electrode within the active area of the electrodes. Such an approach was used by Brightman et al., where an external salt bridge containing a hydrogen reference electrode was used to record half-cell potentials during the operation of a PEM water electrolyzer.<sup>14</sup> In their approach, a Nafion® tube enclosed in a PTFE tube was inserted via a hole in the cathode diffusion media and brought in contact with the cathode catalyst layer of the MEA. While this allowed them to show that during electrolyzer operation the main contribution to the overpotential arises from the anode electrode (as expected due to the sluggish kinetics of the oxygen evolution reaction (OER) compared to the HER<sup>15</sup>), the ability of their approach to measure individual electrode impedance spectra was not evaluated.

Another way to avoid impedance artefacts due to electrode misalignment is to place a reference electrode in between the working and counter electrode rather than adjacent to it. This principle was used for studies with lithium-ion battery cells by Solchenbach et al.,<sup>8</sup> who placed an insulated 50  $\mu\text{m}$  diameter gold wire in between two  $\approx 200 \mu\text{m}$  thick separators that separated the anode and cathode electrode; after an initial lithiation of the gold wire, the gold wire reference electrode (Au-WRE) displayed a stable reference potential. With this configuration, artefact-free anode and cathode impedance spectra could be obtained,<sup>8</sup> which were later used to quantify the different impedance contributions in lithium-ion batteries.<sup>16,17</sup>

Therefore, in this study we developed a reference electrode, consisting of an insulated Pt-wire, which is laminated between two Nafion® 212 membranes and, thus, is centrally placed in the active area. The potential of the Pt-WRE is found to be controlled by the ratio of the permeation flux of  $\text{H}_2$  and  $\text{O}_2$  at the tip of the Pt-WRE that depends on the electrolyzer current density (similar to the potential of the Pt ring electrode used by Sorsa et al.<sup>9</sup>). While it thus only allows for a semi-quantitative determination of the electrolyzer anode and cathode potential, the Pt-WRE is sufficiently stable to serve as pseudo-reference electrode to record artefact-free anode impedance spectra under so-called blocking conditions, i.e., when the anode charge transfer resistance becomes very large. Under these conditions, the proton conduction resistance and the capacitance of the anode electrode as well as the contact resistance at the anode|PTL interface can be quantified. Monitoring these quantities over the course of the above described OCV-AST shows that it is indeed a build-up of a contact resistance at the anode|PTL interface rather than cationic contamination that leads to the observed performance degradation during this test.

## Experimental

**Membrane electrode assembly (MEA) preparation and cell assembly.**—Using the decal transfer method, MEAs with an active area of  $5 \text{ cm}^2$  were prepared, where  $\text{IrO}_2$  supported on  $\text{TiO}_2$  ( $\text{IrO}_2/\text{TiO}_2$  with 75 wt.-% iridium, Elyst Ir75 0480 from Umicore, Germany) served as the catalyst for the oxygen evolution reaction (OER) at the anode electrode and platinum supported on Vulcan XC72 carbon (45.8 wt.-% Pt/C, TEC10V50E from Tanaka, Japan) as the catalyst for the hydrogen evolution reaction (HER) at the cathode electrode. For ink preparation, de-ionized (DI) water (18  $\text{M}\Omega \text{ cm}$ ), 2-propanol (purity  $\geq 99.9\%$  from Sigma Aldrich), and Nafion® ionomer solution (20 wt.-% ionomer, D2021 from IonPower, USA) were added to the respective amount of catalyst powder. Using a roller mill, the catalyst ink was mixed together with  $\text{ZrO}_2$  grinding balls (5 mm diameter) for 24 h. Via the Mayer rod technique the ink was coated onto a thin decal transfer substrate (PTFE, 50  $\mu\text{m}$  thick, from Angst+Pfister, Germany); after drying at room temperature,  $5 \text{ cm}^2$  decals were punched from the coated decals. The actual weight of the electrodes was determined by weighing the decals before and after the electrode transfer step onto the membrane by hot-pressing. The following anode and cathode loadings/compositions were used in this study:  $0.3 \pm 0.1 \text{ mg}_{\text{Pt}} \text{ cm}^{-2}_{\text{geo}}$  for the cathode electrode with an ionomer to carbon weight ratio of 0.6/1  $\text{g}_{\text{ion}}/\text{g}_{\text{C}}$ , and  $2.0 \pm 0.1 \text{ mg}_{\text{Ir}} \text{ cm}^{-2}_{\text{geo}}$  for the anode electrode with an ionomer content of the electrode of 8 wt.-%.

A 50  $\mu\text{m}$  Pt-wire with a 9  $\mu\text{m}$  PTFE insulation (Goodfellow, Great Britain) was used as reference electrode. To ensure good electrical and ionic contact,  $\approx 1 \text{ cm}$  of the insulation was removed at both ends of the wire. One end of the wire was then placed centrally in between two Nafion® 212 membranes (50  $\mu\text{m}$  thick, from Quintech, Germany) and hot pressed together with the cathode and anode decals (see above) at 155  $^\circ\text{C}$  for 3 min at a pressure of 2.5 MPa. In order to protect the Pt-wire at the interface with the cell hardware, an additional layer of PP foil (40  $\mu\text{m}$  from Profol Germany,) was hot pressed at this spot.

Sintered titanium (from Mott Corporation, USA) with a porosity of  $\approx 50\%$  and a thickness of  $280 \pm 10 \mu\text{m}$  was used as a porous transport layer (PTL) on the anode, whereas a carbon fiber paper (TGP-H 120 from Toray, no MPL) with a thickness of  $370 \pm 10 \mu\text{m}$  was used on the cathode. The MEA and PTLs were placed between the flow-fields of the electrolyzer cell and sealed with virgin PTFE gaskets (from Reichelt, Germany). By choosing the right thickness of the gaskets, a compression of the carbon PTL by 25% was set, corresponding to a compressive force of  $\approx 1.7 \text{ MPa}$  at the MEA (note that at  $\approx 1.7 \text{ MPa}$ , the titanium PTL and the MEA are essentially incompressible). Specific details about the cell hardware are reported elsewhere.<sup>18</sup>



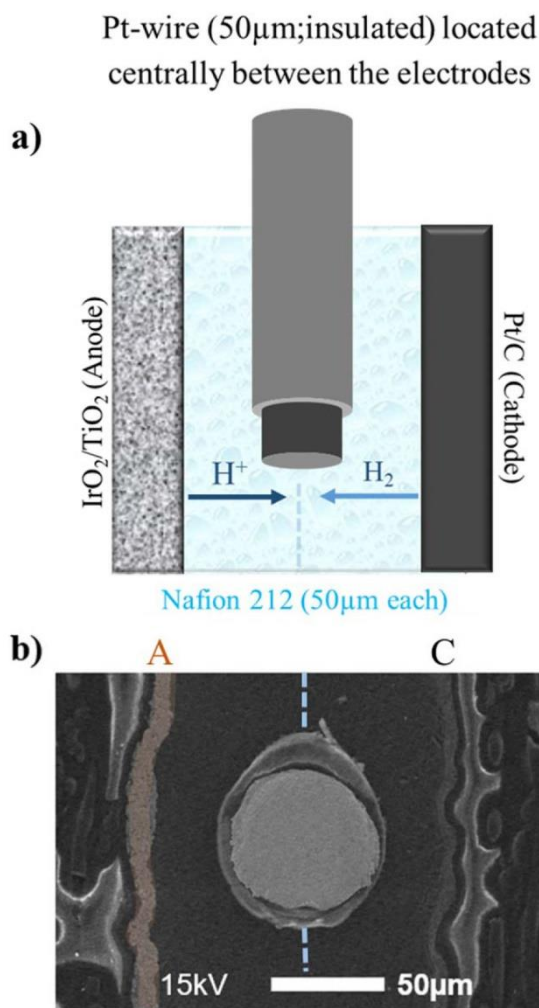


**Figure 1.** (a) Sketch of an MEA with a Pt-WRE, illustrating the placement of the Pt-wire and the prevailing environment at OCV with hydrogen being purged through the cathode compartment and water through the anode compartment. (b) Cross-sectional SEM image of an MEA including a 50  $\mu$ m Pt-WRE laminated between two 50  $\mu$ m Nafion® membranes.

**Electrochemical characterization.**—An automated test station from Greenlight Innovation with a potentiostat equipped with a current booster (BioLogic VSP 300) was used to perform all electrochemical measurements. The anode was supplied with 5 ml<sub>H<sub>2</sub>O</sub> min<sup>-1</sup> deionized (DI) water that was pre-heated to 80 °C. During the measurements, the cell temperature was kept constant at 80 °C, and the product gas exiting from the anode side was diluted with nitrogen (100 nccm) to avoid the formation of an explosive gas mixture due to hydrogen permeation through the membrane into the anode compartment. During warm-up, the cathode was flushed with N<sub>2</sub> for 300 s while supplying 5 ml<sub>H<sub>2</sub>O</sub> min<sup>-1</sup> to the anode compartment. After reaching the desired cell temperature of 80 °C, dry H<sub>2</sub> (50 nccm) at ambient pressure was supplied to the cathode in order to assess the functionality of the reference electrode. Since no current was applied and, hence, no oxygen is produced under these conditions, the potential of the Pt-WRE has to be 0 V on the reversible hydrogen electrode (RHE) potential scale, so that the potential between the H<sub>2</sub>-purged electrolyzer cathode and the

Pt-WRE must be 0 V, indicating proper electrical contact and isolation of the Pt-WRE. Afterwards, the cell was conditioned at 1 A cm<sup>-2</sup><sub>geo</sub> for 30 min. Subsequently, potential-controlled polarization curves were taken at ambient pressure (1 bar<sub>a</sub>) and 80 °C, stepwise increasing the cell potential from 1.3 to 1.9 V and holding at each potential for 15 min to ensure a stabilization of the electrolyzer current density. Finally, the last 10 s of both the cell voltage and current density were averaged for each point.

The OCV-AST was conducted at 80 °C with a cathode pressure of 10 bar<sub>a</sub> and ambient pressure at the anode. Each OCV-AST cycle consisted of 10 min holds at 3 A cm<sup>-2</sup><sub>geo</sub>, at 0.1 A cm<sup>-2</sup><sub>geo</sub>, and at OCV. After each OCV-hold, the potential was set to 1.3 V to perform impedance measurements in blocking conditions (see below). The flow of H<sub>2</sub>O through the anode compartment and the cell temperature were kept constant also during the OCV- or the 1.3 V-hold periods.

Impedance measurements (100 kHz to 1 Hz) were performed at the end of each potential step in the potentiostatic polarization curves, using 10 mV amplitude of the potential perturbation. In the case of the OCV-AST, impedance measurements (100 kHz to 1 Hz) were performed at the end of each current step, using a current perturbation amplitude that was set 500 mA for 3 A cm<sup>-2</sup><sub>geo</sub> and 60 mA for 0.1 A cm<sup>-2</sup><sub>geo</sub>. In addition, after each OCV-cycle, a potentiostatic impedance spectrum (100 kHz to 1 Hz) was acquired at 1.3 V, using 10 mV amplitude of the potential perturbation. During the impedance measurement at 1.3 V the temperature was kept at 80 °C and the pressure of the cathode was held at 10 bar<sub>a</sub>. The high-frequency resistance (HFR) was determined from the high-frequency intercept with the real axis in a Nyquist plot or by fitting a transmission line model to the anode impedance spectra as described in the section *Evaluation of the Impedance Spectra by Fitting a Transmission Line Model*. Using a Matlab based application (“EIS Breaker,” © J. Landesfeind), which is based on the fminsearch MATLAB function using a Nelder-Mead simplex algorithm and modulus weighing, the impedance spectra were fitted. The scaled difference between the measured data and fit vectors  $\left(\frac{|Z(f_i)| - |Z_{fit}(f_i)|}{|Z_{fit}(f_i)|}\right)$  at the same frequency  $f_i$  were used to calculate the residuals (in %).

At the beginning-of-test (BoT) and at the end-of-test (EoT) of the OCV-AST, cyclic voltammograms (CVs) of the anode electrode were recorded. For this, the test procedure was stopped after the 1.3 V-hold period, and the cathode counter electrode was flushed with dry H<sub>2</sub> at 50 nccm at ambient pressure to ensure a stable reference potential (i.e., the cathode served as counter and reference electrode in this case), while the anode electrode was continuously fed with 5 ml<sub>H<sub>2</sub>O</sub> min<sup>-1</sup> deionized water. The CVs were recorded in a potential range of 0.05 V–1.3 V at 50 mV s<sup>-1</sup> at 80 °C; shown are the steady-state CVs (2nd one recorded).

**Physical characterization.**—Using a JEOL JCM6000Plus NeoScope scanning electron microscope at an accelerating voltage of 15 kV, cross-sectional scanning electron microscopy (SEM) micrographs were obtained to depict the location of the Pt-wire reference electrode. The SEM samples were prepared by embedding the MEA in a room-temperature curing epoxy and drying over night at 80 °C. Afterwards, the sample surface was ground using a SiC paper in two steps (grade P320 and P1200, from Buehler, Germany) and subsequently polished on a microcloth using a 9  $\mu$ m diamond polishing agent.

## Results

**Implementation and validation of the Pt-wire reference electrode.**—By implementing an additional reference electrode—normally the cathode is serving as counter and reference electrode at the same time—it is possible to analyze both half-cells individually.<sup>8,11,14</sup> However, certain requirements must be met when the impedance of both half-cells is to be measured: i) the reference potential should be of a well-defined value for a true reference

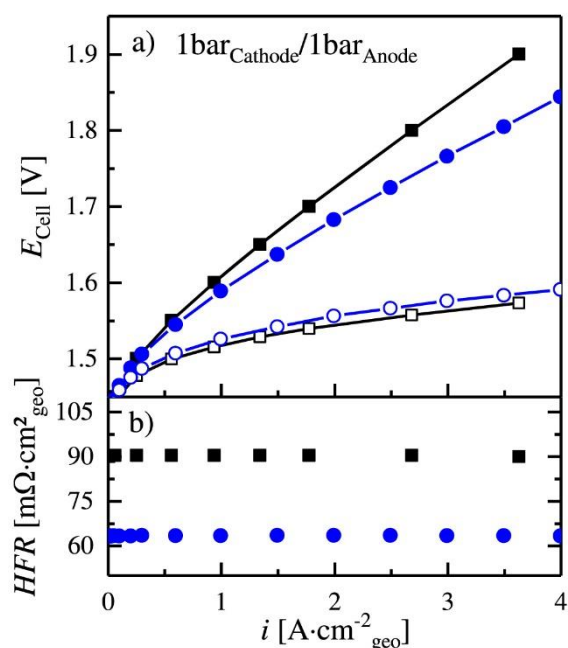


**Figure 2.** PEM-WE performance data at 80 °C and ambient pressure for an MEA including a Pt-WRE (100  $\mu\text{m}$  membrane, black squares) and an MEA with a single 50  $\mu\text{m}$  Nafion® membrane (blue circles): (a) cell voltage ( $E_{\text{cell}}$ ) vs current density ( $i$ ) performance (filled symbols) and HFR-corrected performance data (hollow symbols); (b) corresponding HFR values (extracted from the intercept in the Nyquist plot). MEA specifications: 5  $\text{cm}^2$  active-area with  $\approx 2 \text{ mg}_{\text{Ir}} \text{ cm}^{-2}_{\text{geo}}$  anode and  $\approx 0.3 \text{ mg}_{\text{Pt}} \text{ cm}^{-2}_{\text{geo}}$  cathode loading.

electrode; ii) however, even if the potential of the reference electrode is not well-defined (e.g., if it varies with the operating conditions), as long as its potential is stable over the course of an impedance measurement, it can be used as pseudo-reference electrode; iii) the reference electrode should be placed centrally between the two electrodes in order to avoid the edge effects that were discussed in the introduction section.<sup>8,19,20</sup> To address the last point, an approach already well established for lithium-ion battery cells<sup>8,16,17</sup> was adapted to the MEA of a PEM-WE. A 50  $\mu\text{m}$  thick Pt-wire was laminated between two 50  $\mu\text{m}$  Nafion® membranes that were coated with the respective anode or cathode catalyst layer; the tip of the Pt-wire was located at the center of each catalyst layer. As illustrated by the sketch in Fig. 1a and by the SEM cross-section of the MEA in Fig. 1b, the Pt-wire is located centrally between the two half-cell membranes, without bending towards either side of the MEA. A bending of the Pt-wire towards one of the electrodes can cause a disturbance of the impedance measurement due to an inhomogeneous current distribution or, in the worst case, a shortening of the cell.

The following experiments are aimed to verify that the Pt-WRE does not affect the overall electrolysis performance of the MEA. Figure 2a shows the performance curves measured at ambient pressure for the MEA with the Pt-WRE laminated between two 50  $\mu\text{m}$  Nafion® membranes used in this study (black squares) compared to an MEA with the same catalyst loadings but only a single 50  $\mu\text{m}$  Nafion® membrane without a Pt-WRE (blue circles). The cell voltage is higher for the MEA with the Pt-WRE, which can be attributed to its higher HFR (cf Fig. 2b), as would be expected due to its overall 2-fold higher membrane thickness. Consequently, the HFR-corrected cell voltages, compensating for the differences in membrane resistance are essentially identical for the MEA with the Pt-WRE (hollow black squares in Fig. 2a) and the MEA with the

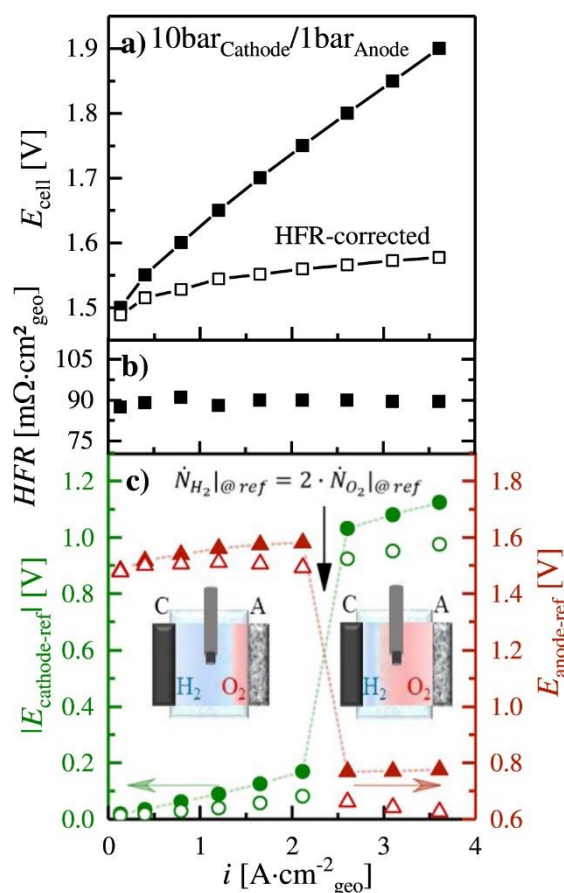


**Figure 3.** PEM-WE performance data at 80 °C recorded with the Pt-WRE MEA based on two 50  $\mu\text{m}$  Nafion® membranes (see Fig. 1) at a cathode pressure of 10 bar<sub>a</sub> and an anode pressure of 1 bar<sub>a</sub>: (a)  $E_{\text{cell}}$  vs  $i$  performance (filled symbols) and HFR-corrected performance data (hollow symbols); (b) corresponding HFR values (extracted from the high-frequency intercept with the real axis in the Nyquist plot). (c) Potential difference between the anode electrode and the Pt-WRE ( $|E_{\text{anode-ref}}|$ ; solid red triangles, plotted vs the right y-axis) and absolute potential difference between the cathode electrode and the Pt-WRE ( $|E_{\text{cathode-ref}}|$ ; solid green circles, plotted vs the left y-axis); the open circles and triangles represent a correction of these potentials by the ohmic potential drop through a single 50  $\mu\text{m}$  membrane (i.e., by  $i \times 40 \text{ m}\Omega\text{cm}^{-2}_{\text{geo}}$ ). The inset shows sketches depicting the prevalent local gas composition at the Pt-WRE tip at high (>2  $\text{Acm}^{-2}_{\text{geo}}$ , right sketch) and low current densities (<2  $\text{Acm}^{-2}_{\text{geo}}$ , left sketch). MEA specification: 5  $\text{cm}^2$  active-area with  $\approx 2 \text{ mg}_{\text{Ir}} \text{ cm}^{-2}_{\text{geo}}$  anode and  $\approx 0.3 \text{ mg}_{\text{Pt}} \text{ cm}^{-2}_{\text{geo}}$  cathode loading.

single 50  $\mu\text{m}$  membrane without the Pt-WRE (hollow blue circles; differing by only  $\approx 10 \text{ mV}$  at the highest current density). This proves that the Pt-wire does not negatively affect the cell performance. The HFR-corrected cell voltages in Fig. 2a are in excellent agreement with previous measurements by Bernt et al.<sup>18</sup> for Nafion® 212 based MEAs with the same catalysts and catalyst loadings.

As shown in Fig. 2b, the HFR for the MEA with the two 50  $\mu\text{m}$  Nafion® membranes and the Pt-WRE is  $\approx 90 \text{ m}\Omega\text{cm}^{-2}_{\text{geo}}$ . In general, the HFR is the sum of the electronic resistance ( $\approx 12 \text{ m}\Omega\text{cm}^{-2}_{\text{geo}}$  for the cell hardware used in this study<sup>18</sup>) and the membrane resistance, which based on various literature reports ranges between  $\approx 41\text{--}54 \text{ m}\Omega\text{cm}^{-2}_{\text{geo}}$  for a single 50  $\mu\text{m}$  Nafion® membrane at 80 °C.<sup>18</sup> Assuming the lower value, the resistance of two 50  $\mu\text{m}$  Nafion®



membranes should be  $\approx 82 \text{ m}\Omega\text{cm}^2_{\text{geo}}$ , predicting an overall HFR of  $\approx 94 \text{ m}\Omega\text{cm}^2_{\text{geo}}$ , which is in good agreement with the measured HFR, suggesting that the HFR is not affected by the presence of the Pt-WRE. It should be noted that the HFR of the MEA with the a single  $50 \mu\text{m}$  Nafion<sup>®</sup> membrane of  $\approx 62 \text{ m}\Omega\text{cm}^2_{\text{geo}}$  (see Fig. 2b) is somewhat higher than what we had observed previously for nominally identical MEAs ( $\approx 53\text{--}57 \text{ m}\Omega\text{cm}^2_{\text{geo}}$ <sup>6,18</sup>), which we believe is due to slight differences in cell compression that strongly affect the contact resistance between the PTLs and the flow fields.

Next we will examine whether the potential of the Pt-WRE is independent of the current density that is applied to the electrolyzer cell. Figure 3a shows the performance curve of the Pt-WRE MEA composed of two  $50 \mu\text{m}$  Nafion<sup>®</sup> membranes (i.e., with a total membrane thickness of  $100 \mu\text{m}$ ; see Fig. 1) measured at  $80^\circ\text{C}$  with  $10 \text{ bar}_a$  cathode and  $1 \text{ bar}_a$  anode pressure; the corresponding cell HFR values are shown in Fig. 3b. Again, while the cell voltage performance (black squares in Fig. 3a) is worse compared to that obtained with an otherwise identical MEA with a single  $50 \mu\text{m}$  Nafion<sup>®</sup> membrane that was reported by Bernt et al.,<sup>18</sup> the HFR-corrected performance (hollow squares in Fig. 3a) of both MEA types is essentially identical (e.g., at  $3 \text{ Acm}^{-2}_{\text{geo}}$  the cell voltage is  $\approx 1.56 \text{ V}$  in Fig. 3a vs  $\approx 1.55 \text{ V}$  in Ref. 18). This proves that the Pt-wire does not affect the cell performance, even when operated at differential pressure.

Figure 3c shows the half-cell potentials recorded during the polarization curve in Fig. 3a, namely the absolute value of the difference between the cathode and the Pt-WRE potential ( $|E_{\text{cathode-ref}}|$ ; solid green circles plotted vs the left y-axis) and the difference between the anode and the Pt-WRE potential ( $|E_{\text{anode-ref}}|$ ; solid red triangles plotted vs the right y-axis). It is most straightforward to first discuss the  $|E_{\text{cathode-ref}}|$  values as a function of current density. As was shown previously, the potential of an electrolyzer cathode at high Pt loadings of  $\approx 0.3 \text{ mgPt cm}^{-2}_{\text{geo}}$  is expected to remain within  $\leq 10 \text{ mV}$  vs RHE up to  $3 \text{ Acm}^{-2}_{\text{geo}}$  due to the fast HER kinetics<sup>18</sup> so that the cathode potential under the conditions in Fig. 3 can be considered essentially constant. At the same time, the potential of the Pt-WRE is a mixed potential resulting from the simultaneous electrochemical oxidation of  $\text{H}_2$  and the reduction of  $\text{O}_2$ , both of which are dissolved in the membrane phase. As a consequence, the potential of the Pt-WRE depends on the relative permeation fluxes of  $\text{H}_2$  ( $\dot{N}_{\text{H}_2(x)}$ ) and  $\text{O}_2$  ( $\dot{N}_{\text{O}_2(x)}$ ) at the location of the Pt-WRE, and Takaichi et al. showed that the potential of a membrane-embedded Pt-wire jumps from near  $0 \text{ V}_{\text{RHE}}$  to  $\approx 0.8\text{--}0.9 \text{ V}_{\text{RHE}}$  when  $\dot{N}_{\text{H}_2(x)} < 2 \times \dot{N}_{\text{O}_2(x)}$  at the location of the Pt-wire<sup>21</sup> (the same potential transition of a membrane-embedded Pt-wire was also observed by Liu and Zuckerbrod<sup>22</sup>). Since the permeability of  $\text{H}_2$  through a Nafion<sup>®</sup> membrane is  $\approx 2$  fold higher than the permeability of  $\text{O}_2$ ,<sup>22,23</sup> the potential of a Pt-wire embedded half-way through the thickness of a membrane (as is the case for our Pt-WRE) would be near the potential transition region when the partial pressures of  $\text{H}_2$  and  $\text{O}_2$  are equal; in this case, the molar flux of  $\text{H}_2$  at the Pt-WRE would be twice as high as the molar flux of  $\text{O}_2$ , allowing for the complete conversion of both of the dissolved gases to  $\text{H}_2\text{O}$ . On the other hand, for the differential pressure conditions used in Fig. 3 ( $p_{\text{anode}} = 1 \text{ bar}_a$  and  $p_{\text{cathode}} = 10 \text{ bar}_a$ ), the  $\text{H}_2$  partial pressure of  $p_{\text{H}_2} \approx 9.5 \text{ bar}$  ( $p_{\text{H}_2} = p_{\text{cathode}} - p_{\text{H}_2\text{O}}$ , with  $p_{\text{H}_2\text{O}} \approx 0.5 \text{ bar}$  at  $80^\circ\text{C}$ ) is nearly 20-fold higher than the  $\text{O}_2$  partial pressure of  $p_{\text{O}_2} \approx 0.5 \text{ bar}$ , so that the mixed potential of the Pt-WRE should be very close to  $0 \text{ V}_{\text{RHE}}$  (actually slightly positive of  $0 \text{ V}_{\text{RHE}}$  due to the mixed potential that derives from the reduction of  $\text{O}_2$  permeating from the anode to the Pt-WRE). Thus, based on these arguments, viz., the fast HER kinetics on Pt, the location of the Pt-WRE (see Fig. 1), and the well-known  $\text{H}_2$  and  $\text{O}_2$  permeabilities through Nafion<sup>®</sup>, the absolute value of the difference of the electrolyzer cathode and the Pt-WRE (i.e.,  $|E_{\text{cathode-ref}}|$ ) should be very close to  $0 \text{ mV}$ . This corresponds to a situation where residual dissolved gas at the Pt-WRE (i.e., after the stoichiometric reaction of  $\text{H}_2$  and  $\text{O}_2$  to

$\text{H}_2\text{O}$ ) would be  $\text{H}_2$ -rich, as depicted in the left-hand sketch in Fig. 3c. At low current densities  $|E_{\text{cathode-ref}}|$  is indeed very close to  $0 \text{ V}$ , as is shown in Fig. 3c (green circles).

However, as the current density increases,  $|E_{\text{cathode-ref}}|$  gradually increases and then exhibits a sudden potential increase to  $\approx 1 \text{ V}$  between  $\approx 2.1$  and  $\approx 2.6 \text{ Acm}^{-2}_{\text{geo}}$ , that previously has been observed to occur once  $\dot{N}_{\text{H}_2(x)}$  becomes  $< 2 \times \dot{N}_{\text{O}_2(x)}$ . This implies that  $\dot{N}_{\text{H}_2(x)}$  and  $\dot{N}_{\text{O}_2(x)}$  must be a function of current density. Based on previous measurements, the  $\text{H}_2$  permeation flux from cathode to anode in a PEM-WE operated at cathode/anode pressures of  $10/1.0 \text{ bar}_a$  remains essentially constant between  $0$  to  $2 \text{ Acm}^{-2}_{\text{geo}}$ .<sup>24</sup> On the other hand, the  $\text{O}_2$  permeation flux for an electrolyzer operated at cathode/anode pressures of  $1.0/1.0 \text{ bar}_a$  was reported by Trinke et al. to increase by  $\approx 20$ -fold when the current density increases from  $0$  to  $2 \text{ Acm}^{-2}_{\text{geo}}$ .<sup>25</sup> Thus, beyond this current density, where based on these literature reports  $\dot{N}_{\text{H}_2(x)}$  would become  $< 2 \times \dot{N}_{\text{O}_2(x)}$  (viz., at  $\approx 2 \text{ Acm}^{-2}_{\text{geo}}$ ), the expected residual dissolved gas at the location of the Pt-WRE would be  $\text{O}_2$ -rich (see right-hand sketch in Fig. 3c) and the Pt-WRE potential should increase to  $\approx 0.8\text{--}0.9 \text{ V}$  vs RHE.<sup>21,22</sup> This is actually in very good agreement with the observed rapid increase of  $|E_{\text{cathode-ref}}|$  near  $2 \text{ Acm}^{-2}_{\text{geo}}$  shown in Fig. 3c. Besides the large expected change in the  $\dot{N}_{\text{H}_2(x)}/\dot{N}_{\text{O}_2(x)}$  ratio and its effect on  $|E_{\text{cathode-ref}}|$ , a minor effect to consider is that the potential drop across the membrane segment between the cathode electrode and the Pt-WRE when drawing an electrolyzer current must also be considered, as it will add an additional ohmic potential drop, corresponding to the areal resistance of the  $50 \mu\text{m}$  Nafion<sup>®</sup> membrane ( $\approx 40 \text{ m}\Omega\text{cm}^2_{\text{geo}}$ , as discussed in the context of Fig. 2) multiplied by the electrolyzer current density. The  $|E_{\text{cathode-ref}}|$  values corrected by the ohmic potential drop are shown by the open green circles in Fig. 3c, amounting to  $\approx 0.92\text{--}0.98 \text{ V}$  at  $\approx 2.6\text{--}4.6 \text{ Acm}^{-2}_{\text{geo}}$ , consistent with the values reported for membrane-embedded Pt-wires at conditions where  $\dot{N}_{\text{H}_2(x)} < 2 \times \dot{N}_{\text{O}_2(x)}$ .<sup>21,22</sup>

In summary, prior to the transition region of the Pt-WRE potential, its potential corrected by the ohmic potential drop (open green circles) ranges between  $\approx 10\text{--}100 \text{ mV}_{\text{RHE}}$  and will thus allow a rough assignment of the cathode potential. It has to be noted, however, that the potential of the Pt-WRE is influenced by the oxygen crossover and thus the oxygen reduction, even before the transition point ( $\approx 2.1$  and  $\approx 2.6 \text{ Acm}^{-2}_{\text{geo}}$ ) occurs. Thus the observed increase in  $|E_{\text{cathode-ref}}|$  is most likely caused by a mixed potential of the Pt-WRE, that derives from the reduction of  $\text{O}_2$  permeating from the anode to the Pt-WRE as well as the oxidation of the hydrogen permeating from the the cathode to the Pt-WRE, rather than by the charge transfer kinetics of the HER on the cathode. Beyond the transition region, its ohmic potential drop corrected value is at  $\approx 0.9\text{--}1.0 \text{ V}_{\text{RHE}}$ . Owing to the significant current density dependence of the Pt-WRE potential during electrolyzer operation, artefact-free individual electrode resolved impedance spectra cannot be obtained during electrolyzer operation, as the variation of the  $\text{H}_2$  and  $\text{O}_2$  partial pressures at the catalyst||membrane interface during the impedance measurements leads to a simultaneous perturbation of the Pt-WRE, which in turn results in inductive loops of the individual impedance spectra,<sup>26</sup> similar to those observed by Sorsa et al.<sup>9</sup> However, at very low current densities (at/near the OCV), this effect is negligible and artefact-free individual electrode impedance spectra can be obtained, as will be shown later.

Figure 3c also shows the anode potentials referenced to the Pt-WRE ( $|E_{\text{anode-ref}}|$ ; solid red triangles plotted vs the right y-axis), and the same considerations apply: at low current densities, the anode potential can be determined by the Pt-WRE using the  $|E_{\text{anode-ref}}|$  values corrected by the ohmic potential drop (open red triangles), with an error that is increasing with current density and ranges between  $\approx 1.47\text{--}1.51 \text{ V}$ .

As a side note, it should be mentioned that the current density at which the potential transition region of the Pt-WRE occurs can



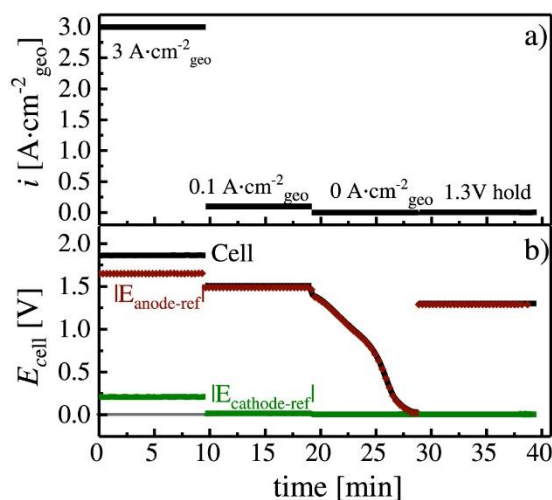


**Figure 4.** First cycle of the OCV-AST recorded with the Pt-WRE MEA based on two  $50\ \mu\text{m}$  Nafion<sup>®</sup> membranes (see Fig. 1), conducted at  $80\ ^\circ\text{C}$  with cathode/anode pressures of 10/1.0 bar<sub>a</sub> and with a continuous feed of  $5\ \text{ml}\ \text{H}_2\text{O}\ \text{min}^{-1}$  into the anode compartment. (a) Current profiles, with high and low current density periods followed by an idle period at OCV, mimicking electrolyzer operation with a fluctuating renewable energy source as well as a potential hold at 1.3 V to record an impedance spectrum. (b) Associated profiles of the cell voltage (black line) as well as of the half-cell potentials, described by the potential difference between the anode electrode and the Pt-WRE ( $|E_{\text{anode-ref}}|$ ; red triangles) and by the absolute potential difference between the cathode electrode and the Pt-WRE ( $|E_{\text{cathode-ref}}|$ ; green line). MEA specification:  $5\ \text{cm}^2$  active-area with  $\approx 2\ \text{mg}_{\text{Ir}}\ \text{cm}^{-2}_{\text{geo}}$  anode and  $\approx 0.3\ \text{mg}_{\text{Pt}}\ \text{cm}^{-2}_{\text{geo}}$  cathode loading.

provide a means to quantify the oxygen permeation rate at this current density, since at this point  $\dot{N}_{\text{H}_2(x)} = 2 \times \dot{N}_{\text{O}_2(x)}$ . Based on the results of Bernt et al., the hydrogen permeation flux through a  $50\ \mu\text{m}$  Nafion<sup>®</sup> 212 membrane at  $80\ ^\circ\text{C}$  and a cathode pressure of 10 bar<sub>a</sub> is  $\approx 0.54\ \frac{\text{mmol}}{\text{m}^2\text{s}}$  at a current density of  $\approx 2\ \text{Acm}^{-2}_{\text{geo}}$ .<sup>24</sup> As the potential transition region occurs at/near this current density, the corresponding oxygen permeation flux must be  $\approx 0.27\ \frac{\text{mmol}}{\text{m}^2\text{s}}$ . By applying different combinations of anode and cathode pressures and determining the current density at which the potential transition occurs, the oxygen permeation flux through the membrane can be determined if the  $\text{H}_2$  permeation flux is known (the latter is relatively easy to quantify).<sup>24</sup> However, this was beyond the scope of this work and will not be discussed further.

**Open circuit voltage—accelerated stress test (OCV-AST).**—In a previous study we proposed an accelerated degradation test protocol to determine whether cycles between load and OCV conditions would lead to MEA and/or OER catalyst degradation.<sup>6</sup> Figure 4a depicts one cycle of the OCV-AST test protocol, where current densities of  $3\ \text{Acm}^{-2}_{\text{geo}}$  and  $0.1\ \text{Acm}^{-2}_{\text{geo}}$  alternate with idle periods where no current is supplied and the cell is left at OCV, mimicking the operation of an electrolyzer with fluctuating renewable energy sources. Figure 4b shows the corresponding cell voltage of the electrolyzer as well as the half-cell potentials, plotted here for the very first cycle. The cell voltage (black line) remains essentially constant during operation and the cell voltages are in good agreement with the polarization curve at the respective current density that was shown in Fig. 3a. However, upon current interruption (i.e., during the OCV phase), the cell voltage gradually decreases to  $\approx 0\ \text{V}$  within  $\approx 10\ \text{min}$  which we attributed to an accumulation of hydrogen within the anode compartment via hydrogen permeation through the membrane from the cathode

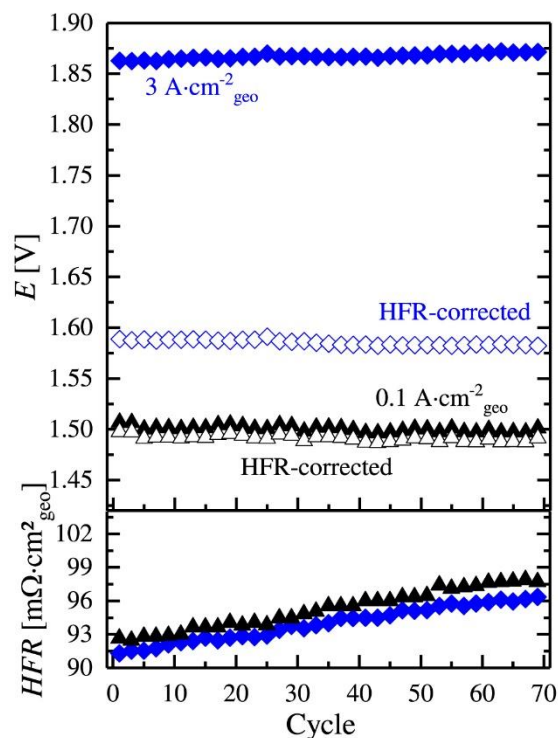


**Figure 5.** (a) Evolution of the cell voltage and the full-cell HFR-corrected cell voltage at  $0.1\ \text{Acm}^{-2}_{\text{geo}}$  and  $3\ \text{Acm}^{-2}_{\text{geo}}$  during the OCV-AST with the Pt-WRE MEA based on two  $50\ \mu\text{m}$  Nafion<sup>®</sup> membranes (see Fig. 1). The test was conducted at  $80\ ^\circ\text{C}$  with  $p_{\text{cathode}} = 10\ \text{bar}_a$  and  $p_{\text{anode}} = 1\ \text{bar}_a$ , cycling the cell with the protocol shown in Fig. 4a while feeding  $5\ \text{ml}\ \text{H}_2\text{O}\ \text{min}^{-1}$  into the anode compartment (same MEA specifications as in Fig. 4). (b) Corresponding full-cell HFR values. For better legibility, only every 2nd point was plotted.

compartment that was kept at a high  $\text{H}_2$  pressure ( $\approx 10\ \text{bar}_a$ ), concomitant with a lowering of the anode potential to  $\approx 0\ \text{V}$  vs RHE due to the reduction of  $\text{IrO}_2$  and the concomitant formation of metallic iridium, which is catalytically active towards the hydrogen oxidation reaction (HOR).<sup>6</sup>

To verify the above hypothesis, the OCV-AST was repeated with a Pt-WRE MEA with the same catalysts and catalyst loadings but with a thicker membrane (two  $50\ \mu\text{m}$  Nafion<sup>®</sup> membranes rather than one) in order to enable a determination of the cathode and anode half-cell potentials. Particularly at low current densities, the half-cell potentials can be determined quite accurately, since the Pt-WRE potential will be within  $\approx 10\text{--}20\ \text{mV}_{\text{RHE}}$  for  $< 0.4\ \text{Acm}^{-2}_{\text{geo}}$  (see green circles in Fig. 3c). Thus, at  $0.1$  and  $0\ \text{Acm}^{-2}_{\text{geo}}$  during the OCV-AST, the potential difference between the anode electrode and the Pt-WRE ( $|E_{\text{anode-ref}}|$ ; see triangles in Fig. 4b) as well as the absolute potential difference between the cathode electrode and the Pt-WRE ( $|E_{\text{cathode-ref}}|$ ; see green line) will represent the anode and cathode potentials vs RHE with an error of less than  $\approx 20\ \text{mV}$ . Based on this, Fig. 4b clearly shows that during the OCV period the cathode potential remains at  $\approx 0\ \text{V}_{\text{RHE}}$ , while the anode potential drops to  $\approx 1.3\ \text{V}_{\text{RHE}}$  right at the beginning of the OCV period (roughly corresponding to the reversible cell voltage under these conditions) and then gradually decreases to  $\approx 0\ \text{V}_{\text{RHE}}$  at the end of the OCV period. This gradual decrease in anode potential is attributed to the enrichment of hydrogen within the anode compartment via  $\text{H}_2$  permeation from the pressurized cathode compartment through the membrane to the anode compartment. As the cathode



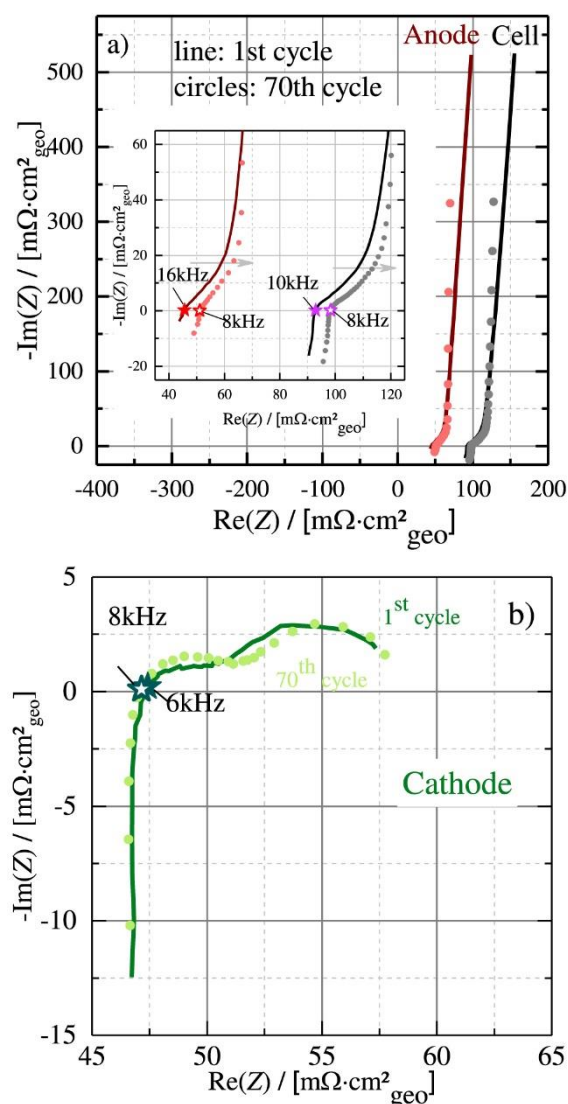


**Figure 6.** Electrochemical impedance spectra recorded at an electrolyzer voltage of 1.3 V and 80 °C (see Experimental section) over the course of the OCV-AST shown in Fig. 4, namely after the 1st (solid lines) and after the 70th (circles, plotting every 2nd data point for better visibility) OCV-AST cycle. (a) Full-cell impedance spectra (black line/circles) and anode impedance spectra taken with respect to the Pt-WRE (red line/circles); the inset is a magnification of the high-frequency regions of the spectra. (b) Cathode impedance spectra taken with respect to the Pt-WRE (green line/circles). The stars mark the real-axis high-frequency intercepts (and the corresponding frequencies) which are commonly used to determine the HFR (e.g., the full-cell HFR shown in Fig. 5b).

pressure is not released during the OCV period of our OCV-AST, a high  $H_2$  partial pressure of  $\approx 9.5$  bar in the cathode compartment will be maintained during the OCV period, resulting in a high  $H_2$  permeation rate of  $\approx 0.54$  mmol  $m^{-2}s^{-1}$ .<sup>24</sup> As a result, a hydrogen-rich gas-phase is developing at the anode side, causing a gradual reduction of the outermost surface of the  $IrO_2$  phase of the  $IrO_2/TiO_2$  OER catalyst to metallic iridium that is catalytically active for the hydrogen oxidation reaction (HOR).<sup>6,27–30</sup> Finally, once a sufficient

HOR activity is established, the anode voltage will drop rapidly close to the equilibrium potential for the HOR at  $\approx 0 V_{RHE}$ . This clearly confirms our previous hypothesis that the potential of the anode electrode decreases to  $\approx 0 V_{RHE}$  over the course of the OCV period of our OCV-AST.

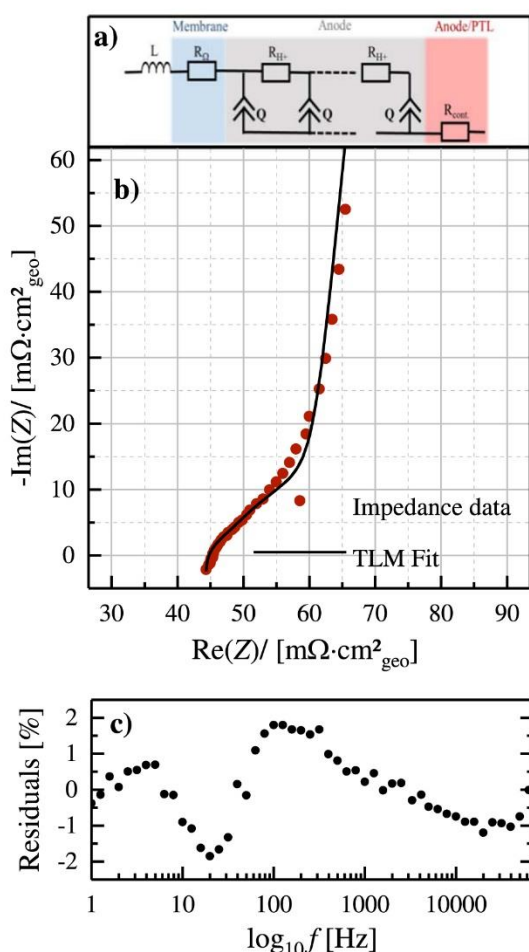
On a side note, it should be mentioned that based on Fig. 3 one would have expected that  $|E_{cathode-ref}|$  should be positive of 1 V at  $3 Acm^{-2}_{geo}$ , instead of the  $\approx 0.21$  V observed in Fig. 4b. This is due the fact that the potential of the Pt-WRE is extremely sensitive to pressure fluctuations at current densities that are close to the transition region of the Pt-WRE; as a consequence, even under nominally identical conditions, small variations in cathode/anode pressure shift the current density range in which the Pt-WRE potential transition occurs (found to be at  $\approx 2.1$ – $2.6 Acm^{-2}_{geo}$  in Fig. 3 and at  $>3 Acm^{-2}_{geo}$  in Fig. 4).

Figure 5a shows the cell voltage evolution over the first 70 cycles of the OCV-AST with the Pt-WRE MEA at the two different current densities of  $0.1 Acm^{-2}_{geo}$  (black triangles) and  $3 Acm^{-2}_{geo}$  (blue diamonds). Even after only 70 cycles, an increase in cell voltage of  $\approx 10$  mV can be observed, which is similar to that observed in our previous study,<sup>6</sup> although the absolute cell voltage ( $\approx 1.86$  V) is higher in the present study due to the larger membrane thickness (MEA based on two  $50 \mu m$  Nafion® membranes vs one  $50 \mu m$  Nafion® membrane, with identical catalysts and catalyst loadings). Compared to the performance at  $3 Acm^{-2}_{geo}$ , the cell performance at  $0.1 Acm^{-2}_{geo}$  (black triangles) remained essentially unchanged during the 70 OCV-AST cycles ( $\approx 1.5$  V). Here it must be noted that the initial increase in performance during the first 10 OCV-AST cycles that we had observed in our previous study (cf Fig. 2b from Weiß et al.<sup>6</sup>) was not observed in the present study, which we believe is due to the Pt-WRE functionality test at 80 °C prior to the OCV-AST, where hydrogen was purged through the cathode compartment while water was purged through the anode compartment without drawing any electrolysis current for some extended time. This exposure of the MEA to hydrogen in the absence of oxygen evolution leads to a hydrogen-rich environment in the anode compartment and a concomitant reduction of the crystalline  $IrO_2$  phase of the anode catalyst to a more OER active hydrous iridium-oxide phase, a process already occurring prior to initiating the OCV-AST.<sup>29,30</sup> As this pre-treatment was not used in our previous OCV-AST study,<sup>6</sup> the performance improvement associated with the formation of the more OER active hydrous iridium oxide instead occurred there over the first few cycles of the OCV-AST.

A closer look at the corresponding full-cell HFR (Fig. 5b) measured during the OCV-AST test reveals an increase of the full-cell HFR at both the high (blue diamonds;  $\Delta HFR \approx 5 m\Omega cm^2_{geo}$ ) and the low (black triangles;  $\Delta HFR \approx 5 m\Omega cm^2_{geo}$ ) current density. Once the cell voltage is corrected by the full-cell HFR (hollow symbols in Fig. 6a), an even slightly improving performance HFR-corrected cell performance at  $3 Acm^{-2}_{geo}$  can be observed over 70 cycles ( $\approx 10$  mV; hollow blue diamonds). This clearly shows that the decrease in cell voltage over the 70 OCV-AST cycles is caused by an increasing full-cell HFR, as was observed previously.<sup>6</sup>

#### Evaluation of the individual electrode impedance spectra.—

While artefact-free impedance spectra of individual electrodes cannot be obtained with the Pt-WRE during electrolyzer operation,<sup>26</sup> they can be acquired when the electrolyzer current is essentially zero. Therefore, we acquired impedance data at an electrolyzer cell voltage of 1.3 V, where the electrolyzer current is close to zero ( $\approx 1 mAcm^{-2}_{geo}$ , largely caused by the oxidation of part of the hydrogen permeation flux through the membrane). Based on the known OER kinetics of  $IrO_2/TiO_2$  that were shown to follow simple Tafel kinetics with a Tafel slope (TS) of  $\approx 50 mV dec^{-1}$ ,<sup>15,18</sup> the OER current density ( $i_{OER}$ ) at an electrolyzer cell voltage of 1.3 V is projected to be on the order of  $0.1 mAcm^2_{geo}$  (see Fig. 6 in Ref. 6). Using these values, the OER charge transfer resistance ( $R_{ct}$ ) can be estimated from Eq. 1, resulting in a value of  $\approx 220 \Omega cm^2_{geo}$  at



**Figure 7.** (a) Simplified transmission line model (TLM) to fit the anode impedance response under blocking conditions (i.e., at an electrolyzer cell voltage of 1.3 V) with the following circuit elements: i) an inductor ( $L$ ) to account for the inductive behavior of the system at high frequencies; ii) a resistor ( $R_{\Omega}$ ) to represent the proton conduction resistance of the membrane between the anode electrode and the Pt-WRE; iii) a constant phase element ( $Q$ ) to represent the capacitance of the anode electrode; iv) a resistor ( $R_{H^+}$ ) to represent the proton conduction resistance across the anode electrode; and, v) a resistor ( $R_{cont}$ ) to represent the contact resistance between the anode electrode and the titanium PTL. (b) Electrochemical impedance data of the anode (red circles; same data as shown in Fig. 6a (1st cycle, red line)) recorded at an electrolyzer voltage of 1.3 V (at 80 °C, and cathode/anode pressures of 10/1.0 bar<sub>a</sub>) and the fit of the impedance data (black line) obtained with the TLM shown in panel a. c) Residuals between the impedance data and the TLM fit as a function of frequency (see Experimental section).

an electrolyzer voltage of 1.3 V.

$$R_{ct} \equiv \frac{d\eta}{di_{OER}} = \frac{TS}{2.303 \cdot i_{OER}} \quad [1]$$

This very large estimated anodic  $R_{ct}$ -value implies that the anode impedance spectrum recorded at an electrolyzer voltage of 1.3 V should essentially resemble a spectrum recorded under blocking conditions. In this case, the full-cell impedance spectrum would also show the same features, if the overall cathode impedance is

sufficiently small,<sup>15,18</sup> as would be expected based on the fast HOR kinetics of the Pt/C based cathode electrode.

Figure 6a shows the full-cell impedance spectra after the 1st (black line) and after the 70th (black circles) OCV-AST cycle, indeed resembling an impedance spectrum that is governed by a blocking electrode response. A magnification of the high-frequency region of the spectra is shown in the inset of Fig. 6a, with the high-frequency intercepts with the real axis that correspond to the full-cell HFR-values shown in Fig. 5b being marked by the purple stars. Figure 6a and the inset also show the anode impedance spectra at 1.3 V recorded with the Pt-WRE after the 1st (red line) and after the 70th (red circles) OCV-AST cycle, exhibiting the expected blocking electrode response. The corresponding cathode impedance spectra are shown in Fig. 6b after the 1st (green line) and after the 70th (green circles) OCV-AST cycle, whereby the overall magnitude of the cathode impedance is very small compared to the anode and full-cell impedance. No apparent artefacts like inductive loops are observed for the anode and cathode impedance spectra acquired at 1.3 V by means of the Pt-WRE.

After the 1st OCV-AST cycle, the HFR of the anode ( $\approx 45 \text{ m}\Omega\text{cm}^2_{\text{geo}}$ ; see solid red star in the inset of Fig. 6a) and of the cathode ( $\approx 47 \text{ m}\Omega\text{cm}^2_{\text{geo}}$ ; see solid green star in Fig. 6b) sum up to  $\approx 92 \text{ m}\Omega\text{cm}^2_{\text{geo}}$ , which, within the error of measurement, agrees well with the full-cell HFR ( $\approx 93 \text{ m}\Omega\text{cm}^2_{\text{geo}}$ ; see solid purple star in the inset of Fig. 6a). Furthermore, the anode and cathode HFR-values are essentially identical, as would be expected for an equidistant placement of the Pt-WRE between the electrodes that was shown in Fig. 2.

In the following, we will first examine more closely the anode impedance spectra acquired with the Pt-WRE at an electrolyzer voltage of 1.3 V over the course of the OCV-AST. Owing to the high anode electrode charge transfer resistance at 1.3 V (see above), its impedance response resembles that of an electrode under blocking conditions, so that it can be fitted using a simple transmission line model (TLM). This allows for a determination of the proton conduction resistance of the anode electrode ( $R_{H^+}$ ) and its capacitance ( $C$ ), as was shown for PEM fuel cell cathodes<sup>31</sup> and for PME-WE anodes<sup>32</sup> using the hydrogen electrode as working and counter electrode as well as for lithium-ion battery electrodes using a micro-reference electrode.<sup>16,17</sup> Furthermore, the inductive response that is generally observed for electrochemical systems at high frequency can be modeled using an inductor element ( $L$ ), which then allows for a more precise estimation of the anode-HFR. Thus, for fitting the anode impedance spectra, the simplified transmission line model shown in Fig. 7a was used, consisting of an inductor ( $L$ ), the membrane resistance between the Pt-WRE and the anode electrode ( $R_{\Omega}$ ), a constant-phase element ( $Q$ , with its impedance defined as  $Z_Q = 1/[Q \cdot (j \cdot \omega)^{\alpha}]$ ), a resistor ( $R_{H^+}$ ) representing the proton conduction resistance of the anode electrode, and a resistor ( $R_{cont}$ ) representing the contact resistance between the anode PTL and the anode electrode.

Figure 7b shows the anode impedance spectrum recorded at a cell voltage of 1.3 V after the first OCV-AST cycle (red circles; same data as that shown in Fig. 6a) together with the TLM fit (black line). As shown in Fig. 7c, the agreement between the impedance data and the fit is quite good, with residuals of  $<2\%$  over the entire frequency range. The largest deviation between the data and the fit is observed in the 45 °—line region of the Nyquist plot that is governed by the through-plane proton conduction resistance of the electrode ( $R_{H^+}$ ). A deviation between the TLM fit and the impedance data in the 45 °—line region (see Fig. 7b) was recently observed for lithium-ion battery electrodes in the presence of a non-uniform binder gradient within the electrode that leads to an inhomogeneous ionic resistance distribution across the thickness of the electrode.<sup>33</sup> The deviation observed here would correspond to the case where the ionic resistance increases towards the interface of the anode electrode and the anode PTL interface (see Figs. 3 and 4a in Ref. 33). The same was also observed by Reshchenko and Kulikovskiy for PEM



fuel cell electrodes with an inhomogeneous ionomer distribution across the electrode.<sup>34</sup> While in such a case the apparent proton conduction resistance of the electrode would be lower than the true proton conduction resistance of the electrode, the rather small deviation observed in Figs. 7b and 7c is still negligible within the error of these measurements.

As mentioned before, extracting the high-frequency resistance from the high-frequency intercept of the impedance spectra with the real-axis in a Nyquist plot often results in an overestimation of the high-frequency resistance due to the inductive behavior at high frequencies. The differences in the high-frequency resistance values of the anode impedance spectra over the course of the OCV-AST, determined from either the high-frequency intercept with the real-axis ( $R_{\Omega(\text{intercept})}$ ) or from the TLM ( $R_{\Omega}$ , see Fig. 7a), are given in Table I.

This comparison shows that by using the high-frequency intercept of the impedance spectra with the real-axis in a Nyquist plot, the high-frequency resistance of the anode impedance spectra is overestimated by  $\approx 2 \text{ m}\Omega\text{cm}^2_{\text{geo}}$  compared to a simplified transmission line model, where the inductive branch at high frequencies is considered. The overall error, however, is  $<5\%$  (see Table I), so that the intercept can indeed be used as a good approximation of the high-frequency resistance.

Regarding the cathode impedance spectra shown in Fig. 6b, we already commented that the magnitude of the impedance is rather small compared to the full-cell and the anode impedance, except that the inductive response at high frequencies is similar in magnitude. Based on the well-known HOR kinetics of a Pt/C based electrode, a charge transfer resistance for a cathode loading of  $\approx 0.3 \text{ mg}_{\text{Pt}} \text{ cm}^{-2}_{\text{geo}}$ , on the order of only  $\approx 1 \text{ m}\Omega\text{cm}^2_{\text{geo}}$  would be expected (see appendix in Ref. 15). However, as shown by Kuhn et al., a detailed analysis of the cathode impedance response at the very small overall current density at 1.3 V would require considering the Tafel and the Volmer reaction steps of the hydrogen evolution/oxidation reactions in the impedance model,<sup>35</sup> in addition to the proton conduction resistance in the cathode electrode. Extracting meaningful proton conduction resistance values from such a model is not really possible, which is the reason why we did not pursue this approach. Instead, we only extracted the high-frequency resistance between the cathode electrode and the Pt-WRE from the intercept of the cathode impedance spectra at high frequencies with the real-axis of the Nyquist plot; based on the above analysis for the anode (summarized in Table I), we expect that the error induced by the inductive behavior at high frequencies will also be on the order of 5% or less for the cathode electrode.

Next we will examine the evolution of the impedance spectra acquired at a cell voltage of 1.3 V over the course of the OCV-AST shown in Fig. 5, where the full-cell HFR recorded at 0.1 and  $3.0 \text{ Acm}^{-2}_{\text{geo}}$  was observed to increase by  $\approx 5 \text{ m}\Omega\text{cm}^2_{\text{geo}}$  over 70 OCV-AST cycles. The full-cell impedance spectra recorded at a cell voltage of 1.3 V (see black lines/circles in the inset of Fig. 6a) show a similar, only slightly higher increase in the high-frequency intercept of  $\approx 6 \text{ m}\Omega\text{cm}^2_{\text{geo}}$  over the 70 cycles (this minor difference might be due to a slightly lower through-plane membrane hydration due to reduced osmotic drag at low current densities and thus a slightly lower cell compression). An identical increase of the high-frequency intercept is observed for the anode impedance spectra

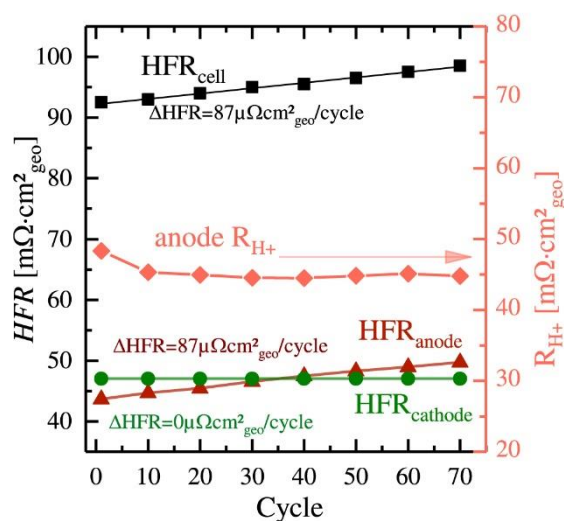


**Figure 8.** Evolution of the high-frequency resistances of the full-cell ( $\text{HFR}_{\text{cell}}$ , black squares), the anode ( $\text{HFR}_{\text{anode}}$ , red triangles), and the cathode ( $\text{HFR}_{\text{cathode}}$ , green circles) plotted vs the left y-axis, as well as of the proton conduction resistance of the anode ( $R_{\text{H}^+}$ , red diamonds, plotted vs the right y-axis), all determined at a cell voltage of 1.3 V, over the course of the OCV-AST shown in Fig. 4 (at  $80^\circ\text{C}$ , with cathode/anode pressures of 10/1.0 bar<sub>a</sub>). The half-cell impedances were obtained using the Pt-WRE (sandwiched between two  $50 \mu\text{m}$  Nafion<sup>®</sup> membranes (see Fig. 1); same MEA specifications as in Fig. 2).  $\text{HFR}_{\text{cell}}$  and  $\text{HFR}_{\text{cathode}}$  were determined by the intercept of the spectra at high frequencies with the real-axis in the Nyquist plot, while  $\text{HFR}_{\text{anode}}$  was extracted by fitting the impedance spectra with the TLM shown in Fig. 7a (in this case,  $\text{HFR}_{\text{anode}}$  corresponds to  $R_{\Omega}$  in Fig. 7a). For better legibility, the data of only every 10th cycle are plotted here; the equations given in the figure are linear regression fits of the change of the HFR with the number of cycles.

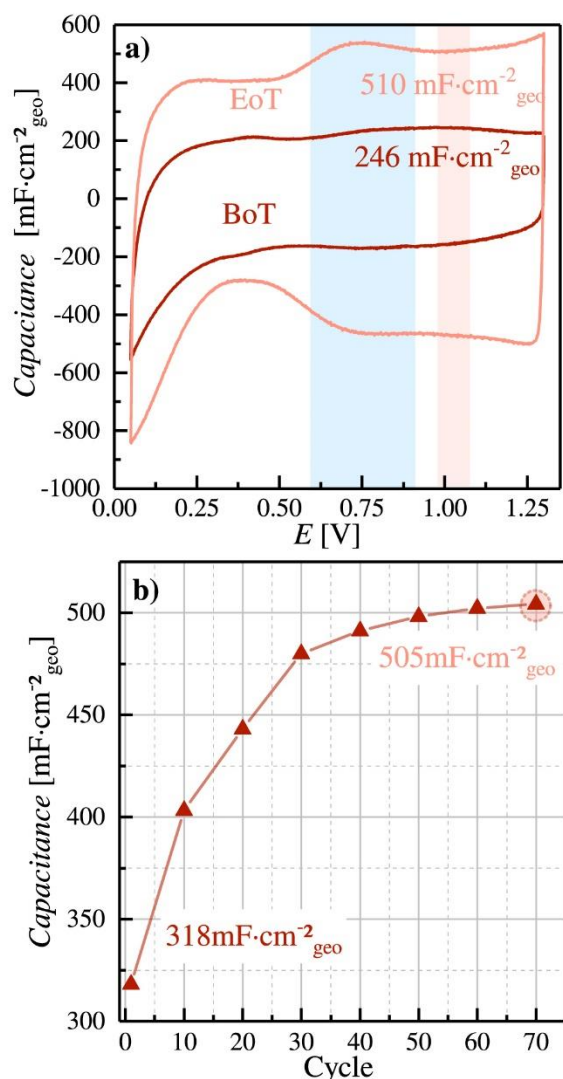
acquired at a cell voltage of 1.3 V (see red lines/circles in the inset of Fig. 6a), while the high-frequency intercept of the cathode impedance spectra (see Fig. 6b) remains constant over the 70 OCV-AST cycles.

Figure 8 shows the evolution of the high-frequency resistances of the full-cell ( $\text{HFR}_{\text{cell}}$ , black squares), the anode ( $\text{HFR}_{\text{anode}}$ , red triangles), and the cathode ( $\text{HFR}_{\text{cathode}}$ , green circles) acquired at a cell voltage of 1.3 V over the course of the OCV-AST (plotted vs the left-hand y-axis). The increase of the full-cell HFR per cycle amounts to  $\Delta\text{HFR}_{\text{cell}} = 87 \mu\Omega\text{cm}^2_{\text{geo}} \text{ cycle}^{-1}$  and is identical with that of the anode electrode ( $\Delta\text{HFR}_{\text{anode}} = 87 \mu\Omega\text{cm}^2_{\text{geo}} \text{ cycle}^{-1}$ ), while the cathode HFR is essentially zero ( $\Delta\text{HFR}_{\text{cathode}} = 0 \mu\Omega\text{cm}^2_{\text{geo}} \text{ cycle}^{-1}$ ). This clearly proves that the increase in the full-cell HFR during the OCV-AST can be ascribed solely to the anode side of the MEA.

Figure 8 also shows the proton conduction resistance of the anode electrode ( $R_{\text{H}^+}$ , red diamonds, plotted vs the right-hand y-axis) determined at a cell voltage of 1.3 V from the fit of the anode impedance spectra using the TLM shown in Fig. 7a. Clearly, the

**Table I.** Comparison of the high-frequency resistance values determined from the anode impedance spectra over the course of the OCV-AST shown in Fig. 4, either from the high-frequency intercept of the impedance spectra with the real-axis in the Nyquist plot ( $R_{\Omega(\text{intercept})}$ ) or from a fit to the TLM shown in Fig. 7a ( $R_{\Omega}$ ).

	1st cycle	10th cycle	20th cycle	40th cycle	60th cycle
$R_{\Omega(\text{intercept})} [\text{m}\Omega\text{cm}^2_{\text{geo}}]$	45.5	46.5	47.5	48.5	50.0
$R_{\Omega}$ from the TLM $[\text{m}\Omega\text{cm}^2_{\text{geo}}]$	43.6	44.6	45.4	47.4	48.9
$(R_{\Omega(\text{intercept})} - R_{\Omega})/R_{\Omega} [\%]$	+4.4%	+4.3%	+4.6%	+2.3%	+2.2%



**Figure 9.** (a) Cyclic voltammograms recorded at beginning-of-test (BoT, i.e., prior to the OCV-AST) and at end-of-test (EoT, i.e., after the 70 OCV-AST cycles shown in Fig. 5), recorded at 50 mV s<sup>-1</sup>, 80 °C, and ambient pressure, with 5 ml<sub>H<sub>2</sub>O</sub> min<sup>-1</sup> supplied to the anode and 50 ncm H<sub>2</sub> to the cathode. (b) Anode capacitance values extracted from the anode impedance spectra at 1.3 V<sub>cell</sub> over the course of the OCV-AST test, using the TLM shown in Fig. 7a.

proton conduction resistance of the anode remains almost constant over the course of the 70 OCV-AST cycles, decreasing slightly from initially  $\approx 48 \text{ m}\Omega\text{cm}^2_{\text{geo}}$  to  $\approx 45 \text{ m}\Omega\text{cm}^2_{\text{geo}}$  after 70 OCV-AST cycles. The absolute value of the anode  $R_{\text{H}^+}$  may be compared to the values estimated by Bernt et al.<sup>18</sup> for electrodes with the identical IrO<sub>2</sub>/TiO<sub>2</sub> anode catalyst and loadings as a function of ionomer content: interpolating their data to an ionomer content of 8 wt.%, the authors estimated the anode  $R_{\text{H}^+}$  to range between 23–49 m $\Omega\text{cm}^2_{\text{geo}}$ , which is consistent with the values shown in Fig. 8. Thus, by utilizing a Pt-WRE to determine the anode impedance spectra it was possible to extract the proton conduction resistance of the anode electrode in the cell. In previous works, the proton conduction resistance of the anode in a PEM-WE cell was determined from

full-cell impedance spectra measured under blocking conditions that were established by purging the cathode with H<sub>2</sub> and the anode with N<sub>2</sub>, assuming that the cathode does not contribute significantly to the full-cell impedance spectra.<sup>32,36</sup> That the latter assumption is correct under blocking conditions is shown by the comparably small magnitude of the cathode impedance compared to the anode impedance (see Figs. 7a and 7b). The use of the Pt-WRE, however, allows to deconvolute the ohmic resistance contributions from the anode and the cathode side of the MEA, clearly showing that the HFR only increases on the anode side. Possible unintended cationic contaminations of the ionomer phase in the membrane and the electrodes over the course of the OCV-AST can be excluded, as this would also have to lead to an increase of the cathode HFR, which clearly is not the case.

Besides the anode HFR and the anode proton conduction resistance, the use of the Pt-WRE also allows for an approximate quantification of the capacitance (C) of the anode electrode by fitting the TLM shown in Fig. 7a. While we use a constant phase element for the impedance fit, the  $\alpha$ -value in all fits was always  $>0.9$  so that the Q value of the constant phase element (in units of F·s<sup>(-1)</sup>) can be approximated with an actual capacitance (in units of F)). Figure 9b shows the development of the anode capacitance extracted from the anode impedance spectra acquired at a cell voltage of 1.3 V over the course of the OCV-AST. The anode capacitance of  $\approx 318 \text{ mFcm}^{-2}_{\text{geo}}$  prior to the OCV-AST initially increases rather rapidly with the number of OCV-AST cycles, and then gradually levels off to a value of  $\approx 505 \text{ mFcm}^{-2}_{\text{geo}}$  after 70 OCV-AST cycles. This increase of the anode capacitance clearly points towards a change of surface chemistry of the anode catalyst, consistent with the differences in the cyclic voltammetric features of the anode electrode (see Fig. 9a) when taken at the beginning-of-test (BoT, i.e., prior to the OCV-AST) and at the end-of-test (EoT, i.e., after 70 OCV-AST cycles). This shows that over the course of the OCV-AST, the originally crystalline IrO<sub>2</sub> phase of the IrO<sub>2</sub>/TiO<sub>2</sub> anode catalyst with the typical CV observed at BoT (dark red CV in Fig. 9a) gradually converts into a hydrous iridium-oxide (light red CV in Fig. 10a) due to the exposure of the catalyst to hydrogen during the OCV periods.<sup>29,30</sup> The hydrous iridium-oxide exhibits the characteristic Ir(III)/Ir(IV) redox-features at  $\approx 0.75 \text{ V}$ ,<sup>37,38</sup> and also has a significantly higher capacitance, e.g.,  $\approx 510 \text{ mFcm}^{-2}_{\text{geo}}$  at 1.0 V compared to  $\approx 250 \text{ mFcm}^{-2}_{\text{geo}}$  for crystalline IrO<sub>2</sub> (see Fig. 9a). These findings are consistent with the irreversible transition of crystalline IrO<sub>2</sub> to a hydrous iridium-oxide observed in our previous OCV-AST study.<sup>6</sup> The capacitance values determined from the anode impedance spectra at 1.3 V (Fig. 9b) are in reasonably good agreement with those obtained by the CVs at 1.0 V (Fig. 9a). This confirms that the use of the Pt-WRE electrode indeed enables the determination of the anode capacitance from the anode impedance data.

In summary, the application of a Pt-WRE allows for the determination of the individual HFR as well as the anode proton conduction resistance of the anode and its capacitance under OCV conditions. During operation, however, the water distribution and content within the cell can change with current densities, as will the proton conduction resistance and the high frequency resistances of both anode and cathode. Moreover, the surface chemistry of the iridium might change at higher currents, which would lead to a concomitant change in capacitance. Hence, the values obtained at 1.3 V can be taken as indication for any changes observed over the course of the OCV-AST, but cannot be used to quantitatively capture individual performance loss contributions during operation.

**Origin of the increasing HFR over the course of an OCV-AST.**—The main cause for a decreasing performance during an OCV-AST was found to be an increasing HFR, which in principle can result either from a higher proton transport resistance of the membrane due to cationic contaminants and/or an additional electronic resistance. In this section, we will review and discuss the different reasons for an increasing HFR, which are illustrated in



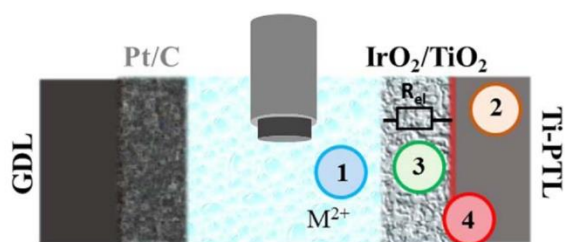


**Figure 10.** Scheme of an MEA with a Pt-WRE, illustrating possible reasons for the observed HFR increase during the OCV-AST: 1) cationic contamination of the membrane; 2) formation of an electronically insulating oxide film on the Ti-PTL surface; 3) additional resistance due to the low electronic conductivity of hydrous iridium-oxide; 4) additional interfacial resistance at the interface of the anode electrode and the titanium PTL due to passivation of Ti-PTL in combination with the lower electronic conductivity of the anode catalyst.

Fig. 10. One common failure mechanism for PEM water electrolyzers is a decreasing performance due to ion-exchanging the protons of the sulfuric acid groups of the ionomer membrane by cationic contaminants (⊙ in Fig. 10), often introduced by insufficiently cleaned feed water.<sup>39–42</sup> Since the deionized (DI) feed water quality was recorded and monitored continuously over the course of the OCV-AST and since the resistivity of the feed water was always maintained at  $\geq 15 \text{ M}\Omega\text{cm}$ , an introduction of cationic contaminants via the feed water was considered highly unlikely; alternatively, cationic contaminants could also result from the corrosion of cell hardware components, but post-mortem analysis of the membrane seemed to exclude also that possibility.<sup>6</sup> The observation in the present study that the cathode HFR ( $\text{HFR}_{\text{cathode}}$ , see Fig. 8) remains constant over the 70 OCV-AST cycles while the anode HFR ( $\text{HFR}_{\text{anode}}$ ) and the full-cell HFR ( $\text{HFR}_{\text{cell}}$ ) increase by the same rate now allows to unequivocally exclude any cationic contaminant effects: in case of cationic contamination, both sides of the membrane would be affected and, therefore, the  $\text{HFR}_{\text{cathode}}$  would have to increase as well, especially since cations would be driven to the cathode side of the cell. The constant proton conduction resistance of the anode (red diamonds in Fig. 8) further proves that cationic contaminants are not the cause of the increasing full-cell HFR.

An increasing HFR due to the passivation of the Ti-PTL during operation and the accompanied increasing contact resistance at the anode (⊙ in Fig. 10)<sup>43</sup> was already investigated in our previous OCV-AST study by contact resistance ( $R_{\text{cont}}$ ) measurements between the PTL and the flow field performed ex situ.<sup>6,18</sup> It was shown, that an increasing contact resistance indeed contributes to the increasing HFR, but this can only partially explain the overall increase. Moreover it is known that a hydrous iridium-oxide exhibits a lower electronic conductivity compared to crystalline  $\text{IrO}_2$ <sup>7</sup> and that if the electronic resistance of the catalyst layer is not significantly smaller than the ionic resistance (1/100) this would be reflected in the HFR.<sup>44</sup> Therefore, a decreasing electronic through-plane resistance of the catalyst layer might be responsible for the observed increase in HFR during cycling (⊙ in Fig. 10). The formation of a hydrous iridium-oxide was proven by both an increasing anode capacitance during cycling as well as by the formation of the typical Ir(III)/Ir(IV) redox features (Fig. 9). Additionally, in-plane resistance measurements showed that the electronic in-plane resistance of the  $\text{IrO}_2$  is indeed lower at BoT ( $\approx 0.04 \text{ m}\Omega\text{cm}^2_{\text{geo}}$ ) compared to the in-plane resistance determined at EoT upon the formation of a hydrous iridium-oxide ( $\approx 0.08 \text{ m}\Omega\text{cm}^2_{\text{geo}}$ ).<sup>6</sup> Since this electronic resistance is still small compared to the ionic resistance, it would not lead to an increase of the full-cell or anode HFR. Hence, the only feasible explanation, as already concluded in the previous study,<sup>6</sup> is an interfacial resistance

at the interface of the anode electrode and the Ti-PTL (⊙ in Fig. 10), due to a decreased electronic conductivity of the hydrous iridium-oxide catalyst layer in combination with the increased contact resistance due to the passivation of the Ti-PTL. Due to the coarse structure of the Ti-PTL (10–50  $\mu\text{m}$  pores)<sup>15</sup> and the resulting small contact area between the Ti-PTL and anode electrode, even a small change in conductivity might lead to a significant increase in contact resistance.<sup>6</sup>

## Conclusions

In this study a Pt wire micro-reference electrode (Pt-WRE) was applied in between the electrodes of a membrane electrode assembly (MEA) for a PEM water electrolyzer (PEM-WE) by laminating an insulated 50  $\mu\text{m}$  Pt-wire between two 50  $\mu\text{m}$  Nafion<sup>®</sup> membranes, with the aim to measure the individual electrode potentials and impedances. By comparing the performance of an MEA with the Pt-WRE to previous data recorded for an MEA without a Pt-WRE, it could be shown that the Pt-WRE does not affect MEA performance. Since the potential at the Pt-WRE depends on the ratio of the local permeation rates of  $\text{O}_2$  and  $\text{H}_2$  through the membrane, it changes with different operating pressures and current densities. However, for the applied anode and cathode pressures of 1.0 and 10 bar<sub>a</sub>, the potential of the Pt-WRE is close to the reversible hydrogen potential (i.e., at  $\approx 0 \text{ V}_{\text{RHE}}$ ) and can be used to determine the individual half-cell potentials of anode and cathode separately at low current densities (e.g., during OCV and potential holds at an electrolyzer voltage of 1.3 V). Even though it is not possible to obtain artefact-free anode or cathode impedance spectra while drawing significant electrolyzer currents due to the changing Pt-WRE potential, artefact-free electrode impedances can be obtained at OCV or at a 1.3 V potential hold.

The Pt-WRE was used to study the degradation observed in our previously proposed OCV-AST, where periods of high and low current densities (3  $\text{Acm}^{-2}_{\text{geo}}$  and 0.1  $\text{Acm}^{-2}_{\text{geo}}$ ) alternate with idle periods (OCV), mimicking electrolyzer operation with a fluctuating power supply. This allowed to prove that the anode potential drops close to the reversible hydrogen potential during the OCV-period, whereas the cathode potential remains at  $\approx 0 \text{ V}_{\text{RHE}}$ . Over the course of 70 OCV-AST cycles, the electrolyzer performance decreased by  $\approx 10 \text{ mV}$  at 3  $\text{Acm}^{-2}_{\text{geo}}$ , which can be mostly ascribed to an increase in full-cell HFR ( $\Delta\text{HFR}_{\text{cell}} \approx 5 \text{ m}\Omega\text{cm}^2_{\text{geo}}$ ).

The Pt-WRE was used to measure anode impedance spectra at an electrolyzer voltage of 1.3 V, where the charge transfer resistance of the OER is very large and the anode impedance can be described by a simplified transmission line model (TLM). During the OCV-AST, the cathode HFR (measured between the Pt-WRE and the cathode flow field) remained constant ( $\approx 47 \text{ m}\Omega\text{cm}^2_{\text{geo}}$ ), whereas the full-cell HFR and the anode HFR (measured between the Pt-WRE and the anode flow field) both increased by  $\approx 6 \text{ m}\Omega\text{cm}^2_{\text{geo}}$  over the course of 70 OCV-cycles. Thus the increasing full-cell HFR and the accompanied decrease in electrolyzer performance is related to an increasing HFR at the anode side. Since the cathode HFR and the anode proton conduction resistance remained constant over the course of the OCV-AST, an increase of the HFR due to cationic contaminants can be ruled out. Ultimately, the decreasing performance can be ascribed to an increasing contact resistance between the Ti-PTL in combination with a lower conductivity of the  $\text{IrO}_2$ -based anode catalyst due to the formation of a hydrous iridium-oxide during the OCV-periods. The formation of a hydrous iridium-oxide could be proven by both the increasing anode capacitance extracted from the anode impedance spectra via a transmission line model fit and by the development of the characteristic Ir(III)/Ir(IV) redox-features observed in the recorded CVs at the end-of-test.

In summary, the implementation of a Pt-WRE allows for a detailed electrode resolved impedance analysis of both anode and cathode, and thus enables the extraction of meaningful physical-chemical parameters such as anode and cathode HFR, the anode proton conduction resistance, and the anode capacitance.



### Acknowledgments

This work was funded by the German Ministry of Education and Research (funding number 03SF2V0, Kopernikus project P2X). We thank Dr. Johannes Landesfeind, Anna T.S. Freiberg, Dr. Daniel Pritzl, Robert Morasch, and Dr. Bharat Suthar for the fruitful and helpful scientific discussions.

### ORCID

Alexandra Hartig-Weiß  <https://orcid.org/0000-0001-7094-5016>  
Maximilian Bernt  <https://orcid.org/0000-0001-8448-5532>

Armin Siebel  <https://orcid.org/0000-0001-5773-3342>

Hubert A. Gasteiger  <https://orcid.org/0000-0001-8199-8703>

### References

1. F. Barbir, "PEM electrolysis for production of hydrogen from renewable energy sources." *Sol. Energy*, **78**, 661 (2005).
2. A. Buttler and H. Spliethoff, "Current status of water electrolysis for energy storage, grid balancing and sector coupling via power-to-gas and power-to-liquids: a review." *Renew. Sustain. Energy Rev.*, **82**, 2440 (2017).
3. K. E. Ayers, E. B. Anderson, K. Dreier, and K. W. Harrison, "Fueling vehicles with sun and water." *ECS Trans.*, **50**, 35 (2013).
4. A. S. Aricò, S. Siracusano, N. Briguglio, V. Baglio, A. Di Blasi, and V. Antonucci, "Polymer electrolyte membrane water electrolysis: status of technologies and potential applications in combination with renewable power sources." *J. Appl. Electrochem.*, **43**, 107 (2013).
5. R. Clarke, S. Giddey, F. Ciacchi, S. Badwal, B. Paul, and J. Andrews, "Direct coupling of an electrolyser to a solar PV system for generating hydrogen." *Int. J. Hydrogen Energy*, **34**, 2531 (2009).
6. A. Weiß, A. Siebel, M. Bernt, T.-H. Shen, V. Tileli, and H. A. Gasteiger, "Impact of intermittent operation on lifetime and performance of a PEM water electrolyzer." *J. Electrochem. Soc.*, **166**, F487 (2019).
7. E. Rasten, G. Hagen, and R. Tunold, "Electrocatalysis in water electrolysis with solid polymer electrolyte." *Electrochim. Acta*, **48**, 3945 (2003).
8. S. Solchenbach, D. Pritzl, E. J. Y. Kong, J. Landesfeind, H. A. Gasteiger, and A. Gold, "Micro-reference electrode for impedance and potential measurements in lithium ion batteries." *J. Electrochem. Soc.*, **163**, A2265 (2016).
9. O. Sorsa, J. Nieminen, P. Kauranen, and T. Kallio, "Stable reference electrode in polymer electrolyte membrane electrolyzer for three-electrode measurements." *J. Electrochem. Soc.*, **166**, F1326 (2019).
10. Z. Siroma, R. Kakitubo, N. Fujiwara, T. Ioroi, S.-I. Yamazaki, and K. Yasuda, "Compact dynamic hydrogen electrode unit as a reference electrode for PEMFCs." *J. Power Sources*, **156**, 284 (2006).
11. G. Li and P. G. Pickup, "Measurement of single electrode potentials and impedances in hydrogen and direct methanol pem fuel cells." *Electrochim. Acta*, **49**, 4119 (2004).
12. S. B. Adler, "Reference electrode placement in thin solid electrolytes." *J. Electrochem. Soc.*, **149**, E166 (2002).
13. S. Adler, B. Henderson, M. Wilson, D. Taylor, and R. E. Richards, "Reference electrode placement and seals in electrochemical oxygen generators." *Solid State Ionics*, **134**, 35 (2000).
14. E. Brightman, J. Dodwell, N. van Dijk, and G. Hinds, "In situ characterisation of PEM water electrolyzers using a novel reference electrode." *Electrochem. Commun.*, **52**, 1 (2015).
15. M. Bernt, A. Siebel, and H. A. Gasteiger, "Analysis of voltage losses in pem water electrolyzers with low platinum group metal loadings." *J. Electrochem. Soc.*, **165**, F305 (2018).
16. J. Landesfeind, D. Pritzl, and H. A. Gasteiger, "An analysis protocol for three-electrode li-ion battery impedance spectra: part I. analysis of a high-voltage positive electrode." *J. Electrochem. Soc.*, **164**, A1773 (2017).
17. D. Pritzl, J. Landesfeind, S. Solchenbach, and H. A. Gasteiger, "An analysis protocol for three-electrode li-ion battery impedance spectra: part II. analysis of a graphite anode cycled Vs LnmO." *J. Electrochem. Soc.*, **165**, A2145 (2018).
18. M. Bernt and H. A. Gasteiger, "Influence of ionomer content in IrO<sub>2</sub>/TiO<sub>2</sub> electrodes on PEM water electrolyzer performance." *J. Electrochem. Soc.*, **163**, F3179 (2016).
19. G. Inzelt, A. Lewenstam, and F. Scholz, *Handbook of Reference Electrodes* (Springer, Berlin) (2013).
20. M. Ender, A. Weber, and I.-T. Ellen, "Analysis of three-electrode setups for ac-impedance measurements on lithium-ion cells by FEM simulations." *J. Electrochem. Soc.*, **159**, A128 (2011).
21. S. Takaichi, H. Uchida, and M. Watanabe, "Distribution profile of hydrogen and oxygen permeating in polymer electrolyte membrane measured by mixed potential." *Electrochem. Commun.*, **9**, 1975 (2007).
22. W. Liu and D. Zuckerbrod, "In situ detection of hydrogen peroxide in PEM fuel cells." *J. Electrochem. Soc.*, **152**, A1165 (2005).
23. J. Zhang, B. A. Litterer, W. Gu, H. Liu, and H. A. Gasteiger, "Effect of hydrogen and oxygen partial pressure on Pt precipitation within the membrane of PEMFCs." *J. Electrochem. Soc.*, **154**, B1006 (2007).
24. M. Bernt, J. Schröter, M. Möckl, and H. Gasteiger, "Analysis of gas permeation phenomena in a PEM water electrolyzer operated at high pressure and high current density." *J. Electrochem. Soc.*, **167**, 124502 (2020).
25. P. Trinke, B. Bensmann, and R. Hanke-Rauschenbach, "Experimental evidence of increasing oxygen crossover with increasing current density during PEM water electrolysis." *Electrochem. Commun.*, **82**, 98 (2017).
26. A. Hartig-Weiß, *Current Challenges in Stability Assessment of Oxygen Evolution Reaction Catalysts for PEM Water Electrolyzer PhD Thesis (submitted)*, Technical University of Munich (2021).
27. P. J. Rheinländer, M. Bernt, Y. Incedag, and H. A. Gasteiger, "Stability and OER activity of IrO<sub>x</sub> in PEM water electrolysis." *Meeting Abstracts*, **38**, 2427 (2016), MA-022016.
28. G. Papakonstantinou and K. Sundmacher, "H<sub>2</sub> Permeation through N117 and Its consumption by IrO<sub>x</sub> in PEM water electrolyzers." *Electrochem. Commun.*, **108**, 106578 (2019).
29. M. F. Tovini, A. M. Damjanovic, H. A. El-Sayed, J. Speder, C. Eickes, J.-P. Suchsland, A. Ghielmi, and H. Gasteiger, "Degradation mechanism of an IrO<sub>2</sub> anode co-catalyst for cell voltage reversal mitigation under transient operation conditions of a PEM fuel cell." *J. Electrochem. Soc.*, **168**, 064521 (2021).
30. P. J. Rheinländer and J. Durst, "Transformation of the oer-active IrO<sub>2</sub> species under transient operation conditions in PEM water electrolysis." *J. Electrochem. Soc.*, **168**, 024511 (2021).
31. Y. Liu, M. W. Murphy, D. R. Baker, W. Gu, C. Ji, J. Jorne, and H. A. Gasteiger, "Proton conduction and oxygen reduction kinetics in pem fuel cell cathodes: effects of ionomer-to-carbon ratio and relative humidity." *J. Electrochem. Soc.*, **156**, B970 (2009).
32. U. Babic, E. Nilsson, A. Pátru, T. J. Schmidt, and L. Gubler, "Proton transport in catalyst layers of a polymer electrolyte water electrolyzer: effect of the anode catalyst loading." *J. Electrochem. Soc.*, **166**, F214 (2019).
33. R. Morasch, J. Landesfeind, B. Suthar, and H. A. Gasteiger, "Detection of binder gradients using impedance spectroscopy and their influence on the tortuosity of li-ion battery graphite electrodes." *J. Electrochem. Soc.*, **165**, A3459 (2018).
34. T. Reshetenko and A. Kulikovskiy, "Impedance spectroscopy study of the PEM fuel cell cathode with nonuniform nafion loading." *J. Electrochem. Soc.*, **164**, E3016 (2017).
35. H. Kuhn, B. Andreaus, A. Wokaun, and G. Scherer, "Electrochemical impedance spectroscopy applied to polymer electrolyte fuel cells with a pseudo reference electrode arrangement." *Electrochim. Acta*, **51**, 1622 (2006).
36. U. Babic, T. J. Schmidt, and L. Gubler, "Communication—Contribution of catalyst layer proton transport resistance to voltage loss in polymer electrolyte water electrolyzers." *J. Electrochem. Soc.*, **165**, J3016 (2018).
37. S. Geiger, O. Kasian, B. R. Shrestha, A. M. Mingers, K. J. J. Mayrhofer, and S. Cherevkov, "Activity and stability of electrochemically and thermally treated iridium for the oxygen evolution reaction." *J. Electrochem. Soc.*, **163**, F3132 (2016).
38. S. Ardizzone, A. Carugati, and S. Trasatti, "Properties of thermally prepared iridium dioxide electrodes." *J. Electroanal. Chem. Interfacial Electrochem.*, **126**, 287 (1981).
39. N. Danilovic, K. E. Ayers, C. Capuano, J. N. Renner, L. Wiles, and M. Pertoso, "(Plenary) challenges in going from laboratory to megawatt scale PEM electrolysis." *ECS Trans.*, **75**, 395 (2016).
40. S. A. Grigoriev, D. G. Bessarabov, and V. N. Fateev, "Degradation mechanisms of MEA characteristics during water electrolysis in solid polymer electrolyte cells." *Russ. J. Electrochem.*, **53**, 318 (2017).
41. U. Babic, M. Suermann, F. N. Büchi, L. Gubler, and T. J. Schmidt, "Critical review—identifying critical gaps for polymer electrolyte water electrolysis development." *J. Electrochem. Soc.*, **164**, F387 (2017).
42. S. Siracusano, N. Van Dijk, R. Backhouse, L. Merlo, V. Baglio, and A. Aricò, "Degradation issues of PEM electrolysis MEAs." *Renewable Energy*, **123**, 52 (2018).
43. C. Rakousky, U. Reimer, K. Wippermann, M. Carmo, W. Lueke, and D. Stolten, "An analysis of degradation phenomena in polymer electrolyte membrane water electrolysis." *J. Power Sources*, **326**, 120 (2016).
44. J. Landesfeind, M. Ebner, A. Eldiven, V. Wood, and H. A. Gasteiger, "Tortuosity of battery electrodes: validation of impedance-derived values and critical comparison with 3d tomography." *J. Electrochem. Soc.*, **165**, A469 (2018).

## 6 Conclusion

Hydrogen produced via the electrochemical splitting of water in a PEM water electrolyzer is a promising method to reduce the overall greenhouse gas emission and to promote the application of renewable energies. Although the PEM-WE system is already technically advanced, there are still some hurdles that have to be overcome in order to enable the application of PEM-WE systems on the GW-scale (see chapter 5.1). Within this thesis, some of these challenges are addressed and highlighted. In Figure 6.1 an overview of the scope of this thesis is given.

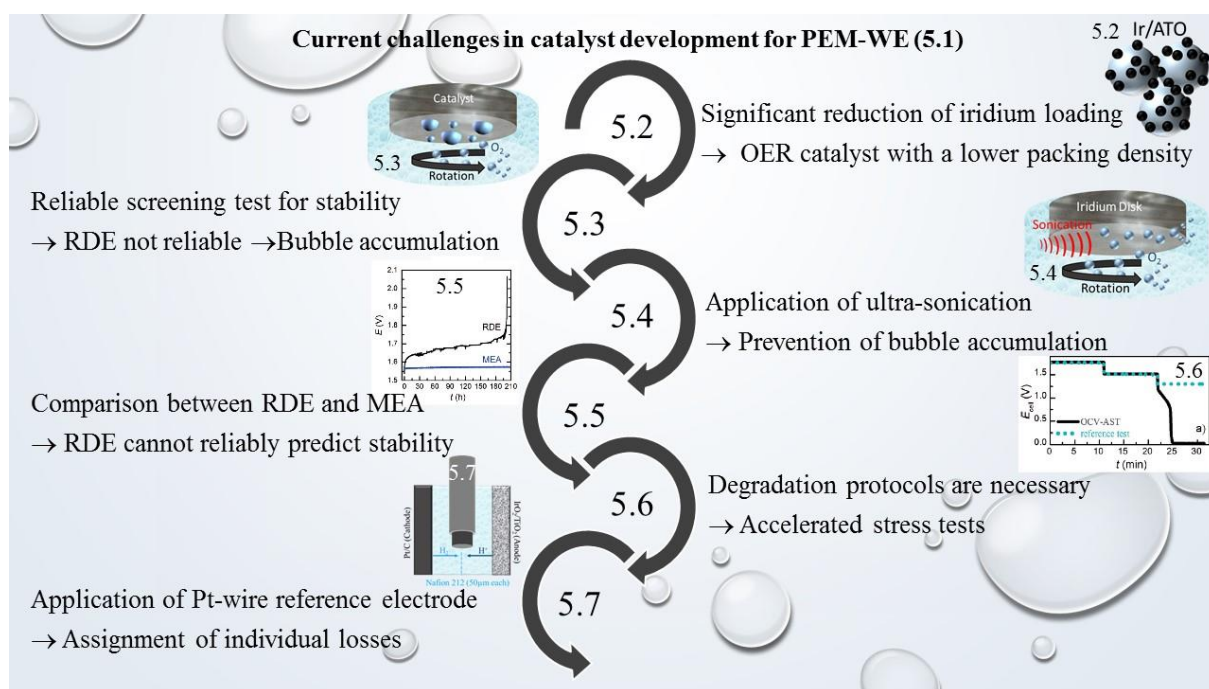


**Figure 6.1** Scheme illustrating the single challenges tackled within this thesis

Due to the harsh environment (low pH, high overpotentials and high oxygen concentration), the choice of catalyst material is limited to the platinum group metals (PGM). While today the catalyst costs only account for  $\approx 5\%$  of the overall systems costs in a kW-range system,<sup>140</sup> this share will rise significantly when aiming for GW-scale systems due to the drop in manufacturing costs in contrast to bare material costs. In addition to that, the availability of iridium is limited and in order to enable a GW-scale application, a reduction in iridium loading from today's  $1 - 2 \text{ mg}_{\text{Ir}}\text{cm}^{-2}_{\text{geo}}$  to  $\approx 0.05 \text{ mg}_{\text{Ir}}\text{cm}^{-2}_{\text{geo}}$  is required (see chapter 5.1).<sup>65, 134</sup> While a study by Bernt et al. showed that the activity of commercially available catalysts would be sufficiently high, the high iridium packing density ( $\approx 2.3 \text{ mg}_{\text{Ir}}\text{cm}^{-3}$ ) averts the fabrication of low loadings, since it leads to an inhomogeneous catalyst layer.<sup>65</sup> Hence, the development of OER catalysts exhibiting a lower iridium packing density is required.

One approach would be the dispersion of iridium nanoparticles on electrically conductive support materials, an approach similar to the Pt/C catalysts used in PEM-FCs. In chapter 5.2, iridium nano-particles ( $\approx 2$  nm) are deposited on a highly conductive oxide support (antimony doped tin oxide – ATO). The high electrical conductivity of the ATO ( $2 \text{ Scm}^{-1}$ ) in combination with its high surface area ( $50 \text{ m}^2\text{g}^{-1}$ ) enables a high catalyst dispersion and a strong metal-support interaction (SMSI). Comparing the activity determined at  $1.5 V_{\text{RHE}}$ , measured within a three-electrode RDE setup, the synthesized Ir/ATO (11 wt.-%;  $\approx 185 \text{ Ag}_{\text{Ir}}^{-1}$ ) outperformed two commercially available catalysts (Ir-black:  $\approx 48 \text{ Ag}_{\text{Ir}}^{-1}$  and  $\text{IrO}_2/\text{TiO}_2$ :  $\approx 5 \text{ Ag}_{\text{Ir}}^{-1}$ ). Also at more system relevant temperatures ( $80^\circ\text{C}$ ), the Ir/ATO (11 wt.-%;  $\approx 1100 \text{ Ag}_{\text{Ir}}^{-1}$ ) catalysts showed a significantly higher activity compared to Ir-black ( $\approx 190 \text{ Ag}_{\text{Ir}}^{-1}$ ) and  $\text{IrO}_2/\text{TiO}_2$  ( $\approx 45 \text{ Ag}_{\text{Ir}}^{-1}$ ). Hence, this catalyst design approach presents one possibility to significantly reduce the iridium loading, while still maintaining a homogenous and sufficiently thick catalyst layer.

Besides the activity, the stability of newly developed OER catalysts is decisive for their large-scale use. Rotating disk electrode measurements as well as flow-channel configurations are often used to obtain the activity and long-term stability of OER catalysts, since only a small quantity of catalyst is needed. The stability obtained in RDE measurements, however, differs significantly from the lifetimes assessed in a PEM-WE (see chapter 5.1). Commonly, a constant current (e.g.,  $10 \text{ mAcm}^{-2}_{\text{disk}}$ ) is applied during an RDE measurement to obtain the stability of an OER catalyst and the observed gradual increase in potential is ascribed to catalyst deactivation/degradation. Ultimately, the experiments terminate with a sudden jump in potential, which is associated with a full degradation of the catalyst. In chapter 5.3, the stability protocol is closely analyzed and clear evidence is provided that the gradual loss in performance is mainly due to the shielding of active sites by oxygen bubbles that accumulate within the catalyst layer. Due to the partial shielding of active sites, parts of the catalyst layer are ionically isolated and the potentials at the remaining active sites increases in order to maintain the applied current. Ultimately, this results in a sudden jump in potential ( $>2 \text{ V}$ ), which was so far associated with full catalyst degradation. However, holding the electrode for an extended period of time ( $\approx 30$  min) at OCV under argon, the catalyst activity and surface area (based on CVs) can be partially recovered. Hence, the observed increase in potential during a constant current RDE measurement cannot be used reliably to predict the long-term stability of an OER catalysts since it is greatly influenced by the accumulation of oxygen bubbles within the catalyst layer. If one were able to ensure an oxygen bubble-free catalyst layer during the measurement, one should be able to assess the long-term catalyst stability using an RDE setup.



One approach would be the application of ultra-sonication to efficiently remove the produced oxygen. In chapter 5.4, a constant current ( $10 \text{ mAcm}^{-2}_{\text{disk}}$ ) measurement is performed using an Ir-disk, where additional ultra-sonication is applied. While the potential significantly increases ( $\approx 100 \text{ mV}$  within 450 s) and is almost independent of the applied electrode rotation rate, the application of ultra-sonication not only led to a significantly lower initial potential ( $\approx 50 \text{ mV}$ ) but also to a stable performance over the recorded 450 s. While the lower initial potential shows that the accumulation of oxygen bubbles occurs immediately when a constant current is applied, the stable performance proves that additional ultra-sonication efficiently prevents the accumulation of oxygen bubbles. However, OER catalysts are commonly in nano-particulate form, and ultra-sonication would lead to the physical detachment of the catalyst layer during operation and thus cannot be used to perform stability tests using an RDE setup.

These previous studies already provide evidence that an RDE configuration cannot be used to reliably predict the lifetime of OER catalysts. Additionally, a comprehensive comparison of the commonly used stability protocols (constant current or constant potential hold as well as potential cycling) performed in the RDE and MEA configuration given in chapter 5.5 shows that while each stability test led to a significant decrease in performance when using the RDE setup, the performance remained stable within the MEA configuration. Although the results suggest that the accumulation of oxygen bubbles also occurs in an MEA, it occurs to a much lesser extent compared to an RDE, hence resulting in orders of magnitude longer lifetimes (hours in the RDE vs ten thousands of hours in the MEA configuration). The study clearly shows that an RDE configuration cannot be used to predict the lifetime of an OER catalyst, and MEA measurements in a PEM-WE are required. Nevertheless, to assess the long-term stability of newly developed catalysts one cannot measure thousands of hours before any conclusion can be drawn, and thus the development of accelerated stress tests is a necessity.

In chapter 5.6, an AST-protocol mimicking a fluctuation power supply is presented, where the cell is cycled between high ( $3 \text{ Acm}^{-2}_{\text{geo}}$ ) and low current densities ( $0.1 \text{ Acm}^{-2}_{\text{geo}}$ ) with a subsequent idle period (OCV-period), where the cell potential drops to  $\approx 0 \text{ V}$  due to the hydrogen crossover. After an initial improvement ( $\approx 50 \text{ mV}$ ), the performance decreases over the course of cycling, which was found to be related to an increasing HFR. The initial gain in performance is associated with the formation of metallic iridium during the OCV-period and its subsequent oxidation to hydrous iridium oxide upon resuming operation. Although the formation of a hydrous iridium oxide seems to be beneficial due to its higher activity toward the OER, it also exhibits a lower electrical conductivity compared to a crystalline  $\text{IrO}_2$ . The

lower conductivity of the formed hydrous iridium oxide in combination with a higher contact resistance due to the passivation of the Ti-PTL at high potentials leads to an additional interfacial contact resistance at the electrode||PTL interface, and thus a higher HFR. In a reference study, where the cell was polarized at 1.3 V during the idle period, the performance remained stable over the course of cycling because the formation of a hydrous iridium oxide was prevented.

Since an unambiguous determination of the interfacial resistance is not trivial, the application of a Pt-wire reference electrode (Pt-WRE) is introduced in chapter 5.7, which allows the separation of the individual half-cell impedance spectra.<sup>141</sup> For this a 50  $\mu\text{m}$  thick Pt-wire, with a 9  $\mu\text{m}$  PTFE insulation is centrally laminated between two 50  $\mu\text{m}$  Nafion<sup>®</sup> membranes. The potential of the Pt-wire is determined by the relative permeation fluxes of hydrogen and oxygen at the location of the wire, resulting in a reference potential close to the reversible potential of hydrogen ( $\leq 25$  mV) at low current densities ( $\leq 0.5$   $\text{Acm}^{-2}_{\text{geo}}$ ) and a reference potential ( $\geq 1$  V) close to the thermodynamic potential of water splitting ( $\approx 1.18$  V) at higher current densities ( $2$   $\text{Acm}^{-2}_{\text{geo}}$ ). Due to observed change in reference potential with current density, the Pt-WRE can only be used to track the half-cell potentials at low current densities (near/at OCV). Applying the same OCV-AST cycling protocol as in chapter 5.6, it is shown that, while the HFR of the cathode remains constant during cycling, the HFR of the anode increases simultaneously along with HFR of the full-cell. This clearly proves that an additional resistance at the anode is responsible for the observed increasing HFR during OCV-AST cycling.

In summary, while the development of highly active OER catalysts that exhibit a low iridium packing density is one necessity, the elaboration of reliable screening tools, especially regarding the long-term stability, is essential to speed up catalyst development. Within the present work some of the challenges are tackled, which have to be overcome in order to enable an economically viable and widespread application of PEM-WE in the GW-scale.

# Bibliography

1. Wetterdienst, D.  
[https://www.dwd.de/DE/klimaumwelt/aktuelle\\_meldungen/200910/fakten\\_zum\\_klimawandel.html?nn=344870](https://www.dwd.de/DE/klimaumwelt/aktuelle_meldungen/200910/fakten_zum_klimawandel.html?nn=344870) (accessed 01.12.2020).
2. Umweltbundesamt  
<https://www.umweltbundesamt.de/themen/klima-energie/klimawandel/zu-erwartende-klimaaenderungen-bis-2100> (accessed 14.02.2021).
3. Umweltbundesamt Indikator: Emission Von Treibhausgasen.  
<https://www.umweltbundesamt.de/indikator-emission-von-treibhausgasen#die-wichtigsten-fakten> (accessed 14.02.2021).
4. United Nations Framework Convention on Climate Change.  
<https://unfccc.int/process-and-meetings/the-paris-agreement/the-paris-agreement> (accessed 24.11.2020).
5. Bundesministerium Für Wirtschaft Und Energie (BMWi);  
*Die Nationale Wasserstoffstrategie* June 2020.
6. Umweltbundesamt Erneuerbare Energien in Zahlen.  
<https://www.umweltbundesamt.de/themen/klima-energie/erneuerbare-energien/erneuerbare-energien-in-zahlen#ueberblick> (accessed 24.11.2020).
7. Bareiß, K.; de la Rua, C.; Möckl, M.; Hamacher, T., Life Cycle Assessment of Hydrogen from Proton Exchange Membrane Water Electrolysis in Future Energy Systems. *Applied Energy* **2019**, *237*, 862-872.
8. Buttler, A.; Spliethoff, H., Current Status of Water Electrolysis for Energy Storage, Grid Balancing and Sector Coupling Via Power-to-Gas and Power-to-Liquids: A Review. *Renewable and Sustainable Energy Reviews* **2018**, *82*, 2440-2454.
9. Siemens  
<https://assets.new.siemens.com/siemens/assets/public/1524040818.abae9c1e48d6d239c06d88e565a25040ed2078dc.ct-ree-18-047-db-silyzer-300-db-de-en-rz.pdf> (accessed 01.12.2020).
10. H-Tec Systems. <https://www.h-tec.com/produkte/elektrolyseur-me-4501400/> (accessed 01.12.2020).
11. Babic, U.; Suermann, M.; Büchi, F. N.; Gubler, L.; Schmidt, T. J., Critical Review—Identifying Critical Gaps for Polymer Electrolyte Water Electrolysis Development. *Journal of The Electrochemical Society* **2017**, *164*, F387-F399.
12. Böhm, D.; Beetz, M.; Schuster, M.; Peters, K.; Hufnagel, A. G.; Döblinger, M.; Böller, B.; Bein, T.; Fattakhova-Rohlfing, D., Efficient Oer Catalyst with Low Ir Volume Density Obtained by Homogeneous Deposition of Iridium Oxide Nanoparticles on Macroporous Antimony-Doped Tin Oxide Support. *Advanced Functional Materials* **2019**, *30*.
13. Geiger, S.; Kasian, O.; Shrestha, B. R.; Mingers, A. M.; Mayrhofer, K. J. J.; Cherevko, S., Activity and Stability of Electrochemically and Thermally Treated Iridium for the Oxygen Evolution Reaction. *Journal of The Electrochemical Society* **2016**, *163*, F3132-F3138.
14. Cherevko, S.; Geiger, S.; Kasian, O.; Mingers, A.; Mayrhofer, K. J. J., Oxygen Evolution Activity and Stability of Iridium in Acidic Media. Part 1. – Metallic Iridium. *Journal of Electroanalytical Chemistry* **2016**, *773*, 69-78.
15. Cherevko, S.; Geiger, S.; Kasian, O.; Mingers, A.; Mayrhofer, K. J. J., Oxygen Evolution Activity and Stability of Iridium in Acidic Media. Part 2. – Electrochemically

- Grown Hydrrous Iridium Oxide. *Journal of Electroanalytical Chemistry* **2016**, 774, 102-110.
16. Oh, H.-S.; Nong, H. N.; Reier, T.; Gliech, M.; Strasser, P., Oxide-Supported Ir Nanodendrites with High Activity and Durability for the Oxygen Evolution Reaction in Acid PEM Water Electrolyzers. *Chemical Science* **2015**, 6, 3321-3328.
  17. Geiger, S. Stability Investigations of Iridium-Based Catalysts Towards Acidic Water Splitting. PhD Thesis Bochum, Ruhr-Universität Bochum, 2017.
  18. Ayers, K. E.; Anderson, E. B.; Capuano, C.; Carter, B.; Dalton, L.; Hanlon, G.; Manco, J.; Niedzwiecki, M., Research Advances Towards Low Cost, High Efficiency PEM Electrolysis. *ECS transactions* **2010**, 33, 3-15.
  19. Medina, P.; Santarelli, M., Analysis of Water Transport in a High Pressure PEM Electrolyzer. *International Journal of Hydrogen Energy* **2010**, 35, 5173-5186.
  20. Carmo, M.; Fritz, D. L.; Mergel, J.; Stolten, D., A Comprehensive Review on PEM Water Electrolysis. *International Journal of Hydrogen Energy* **2013**, 38, 4901-4934.
  21. McBride, B. J.; Zehe, M. J.; Gordon, S., *Nasa Glenn Coefficients for Calculating Thermodynamic Properties of Individual Species*; National Aeronautics and Space Administration, John H. Glenn Research Center, 2002.
  22. Bratsch, S. G., Standard Electrode Potentials and Temperature Coefficients in Water at 298.15 K. *Journal of Physical and Chemical Reference Data* **1989**, 18, 1-21.
  23. Neyerlin, K. C.; Gu, W.; Jorne, J.; Gasteiger, H. A., Study of the Exchange Current Density for the Hydrogen Oxidation and Evolution Reactions. *Journal of The Electrochemical Society* **2007**, 154, B631-B635.
  24. Sheng, W.; Gasteiger, H. A.; Shao-Horn, Y., Hydrogen Oxidation and Evolution Reaction Kinetics on Platinum: Acid Vs Alkaline Electrolytes. *Journal of The Electrochemical Society* **2010**, 157, B1529-B1536.
  25. Gasteiger, H.; Yan, S., Dependence of PEM Fuel Cell Performance on Catalyst Loading. *Journal of Power Sources* **2004**, 127, 162-171.
  26. Neyerlin, K. C.; Gu, W.; Jorne, J.; Gasteiger, H. A., Determination of Catalyst Unique Parameters for the Oxygen Reduction Reaction in a PEMFC. *Journal of The Electrochemical Society* **2006**, 153, A1955-A1963.
  27. Bernt, M.; Gasteiger, H. A., Influence of Ionomer Content in IrO<sub>2</sub>/TiO<sub>2</sub> Electrodes on PEM Water Electrolyzer Performance. *Journal of The Electrochemical Society* **2016**, 163, F3179-F3189.
  28. Matsumoto, Y.; Sato, E., Electrocatalytic Properties of Transition Metal Oxides for Oxygen Evolution Reaction. *Materials Chemistry and Physics* **1986**, 14, 397-426.
  29. Reier, T.; Teschner, D.; Lunkenbein, T.; Bergmann, A.; Selve, S.; Kraehnert, R.; Schlögl, R.; Strasser, P., Electrocatalytic Oxygen Evolution on Iridium Oxide: Uncovering Catalyst-Substrate Interactions and Active Iridium Oxide Species. *Journal of The Electrochemical Society* **2014**, 161, F876-F882.
  30. Cherevko, S.; Reier, T.; Zeradjanin, A. R.; Pawolek, Z.; Strasser, P.; Mayrhofer, K. J. J., Stability of Nanostructured Iridium Oxide Electrocatalysts During Oxygen Evolution Reaction in Acidic Environment. *Electrochemistry Communications* **2014**, 48, 81-85.
  31. Reier, T.; Oezaslan, M.; Strasser, P., Electrocatalytic Oxygen Evolution Reaction (OER) on Ru, Ir, and Pt Catalysts: A Comparative Study of Nanoparticles and Bulk Materials. *ACS Catalysis* **2012**, 2, 1765-1772.
  32. Hu, J.-M.; Zhang, J.-Q.; Cao, C.-N., Oxygen Evolution Reaction on IrO<sub>2</sub>-Based Dsa® Type Electrodes: Kinetics Analysis of Tafel Lines and EIS. *International Journal of Hydrogen Energy* **2004**, 29, 791-797.
  33. Bessarabov, D.; Wang, H.; Li, H.; Zhao, N., *PEM Electrolysis for Hydrogen Production: Principles and Applications*; CRC press, 2016.



34. Springer, T. E.; Zawodzinski, T.; Gottesfeld, S., Polymer Electrolyte Fuel Cell Model. *Journal of the Electrochemical Society* **1991**, *138*, 2334-2342.
35. Ito, H.; Maeda, T.; Nakano, A.; Takenaka, H., Properties of Nafion Membranes under PEM Water Electrolysis Conditions. *International Journal of Hydrogen Energy* **2011**, *36*, 10527-10540.
36. Okada, T., Effect of Ionic Contaminants. In *Handbook of Fuel Cells-Fundamentals, Technology and Applications* Vielstich, W.; Gasteiger, H. A.; Lamm, A., Eds. John Wiley & Sons, Ltd.: 2003; Vol. 3, pp 627-646.
37. Büchi, F. N.; Scherer, G. G., Investigation of the Transversal Water Profile in Nafion Membranes in Polymer Electrolyte Fuel Cells. *Journal of the Electrochemical Society* **2001**, *148*, A183-A188.
38. Hwang, G. S.; Parkinson, D. Y.; Kusoglu, A.; MacDowell, A. A.; Weber, A. Z., Understanding Water Uptake and Transport in Nafion Using X-Ray Microtomography. *ACS Macro Letters* **2013**, *2*, 288-291.
39. Zawodzinski, T. A.; Derouin, C.; Radzinski, S.; Sherman, R. J.; Smith, V. T.; Springer, T. E.; Gottesfeld, S., Water Uptake by and Transport through Nafion® 117 Membranes. *Journal of the Electrochemical Society* **1993**, *140*, 1041-1047.
40. Liu, Y.; Murphy, M. W.; Baker, D. R.; Gu, W.; Ji, C.; Jorne, J.; Gasteiger, H. A., Proton Conduction and Oxygen Reduction Kinetics in PEM Fuel Cell Cathodes: Effects of Ionomer-to-Carbon Ratio and Relative Humidity. *Journal of The Electrochemical Society* **2009**, *156*, B970-B980.
41. Store, F. C. <https://www.fuelcellstore.com/spec-sheets/chemours-nafion-211-212-spec-sheet.pdf> (accessed 27.11.2019).
42. Doyle, M.; Rajendran, G., Perfluorinated Membranes In *Handbook of Fuel Cells-Fundamentals, Technology and Applications*, Vielstich, W.; Gasteiger, H. A.; Lamm, A., Eds. John Wiley & Sons, Ltd.: 2003; Vol. 3, pp 351-395.
43. Thompson, E. L.; Jorne, J.; Gu, W.; Gasteiger, H. A., PEM Fuel Cell Operation at -20° C. II. Ice Formation Dynamics, Current Distribution, and Voltage Losses within Electrodes. *Journal of the Electrochemical Society* **2008**, *155*, B887.
44. Gu, W.; Baker, D. R.; Y.Liu; Gasteiger, H. A., Proton Exchange Membrane Fuel Cell (PEMFC) Down-the-Channel Performance In *Handbook of Fuel Cells- Fundamentals, Technology and Applications*, Vielstich, W.; Yokokawa, H.; Gasteiger, H. A., Eds. John Wiley & Sons, Ltd.: 2009; Vol. 6, pp 631-657.
45. Liu, Y.; Ji, C.; Gu, W.; Jorne, J.; Gasteiger, H. A., Effects of Catalyst Carbon Support on Proton Conduction and Cathode Performance in PEM Fuel Cells. *Journal of The Electrochemical Society* **2011**, *158*, B614-B621.
46. Neyerlin, K.; Gu, W.; Jorne, J.; Clark, A.; Gasteiger, H. A., Cathode Catalyst Utilization for the ORR in a PEMFC Analytical Model and Experimental Validation. *Journal of The Electrochemical Society* **2007**, *154*, B279-B287.
47. Babic, U.; Nilsson, E.; Pătru, A.; Schmidt, T. J.; Gubler, L., Proton Transport in Catalyst Layers of a Polymer Electrolyte Water Electrolyzer: Effect of the Anode Catalyst Loading. *Journal of The Electrochemical Society* **2019**, *166*, F214-F220.
48. Liu, Y.; Murphy, M.; Baker, D.; Gu, W.; Ji, C.; Jorne, J.; Gasteiger, H. A., Determination of Electrode Sheet Resistance in Cathode Catalyst Layer by Ac Impedance. *ECS Transactions* **2007**, *11*, 473-484.
49. Marangio, F.; Santarelli, M.; Cali, M., Theoretical Model and Experimental Analysis of a High Pressure PEM Water Electrolyser for Hydrogen Production. *International Journal of Hydrogen Energy* **2009**, *34*, 1143-1158.
50. Lvovich, V. F., *Impedance Spectroscopy: Applications to Electrochemical and Dielectric Phenomena*; John Wiley & Sons, 2012, p Chapter 1; p.1-21.

51. Lasia, A., Electrochemical Impedance Spectroscopy and Its Applications. In *Modern Aspects of Electrochemistry*, Springer: 2002; pp Chapter 2; p.7-66.
52. Makharia, R.; Mathias, M. F.; Baker, D. R., Measurement of Catalyst Layer Electrolyte Resistance in PEFCs Using Electrochemical Impedance Spectroscopy. *Journal of The Electrochemical Society* **2005**, *152*, A970-A977.
53. Landesfeind, J.; Pritzl, D.; Gasteiger, H. A., An Analysis Protocol for Three-Electrode Li-Ion Battery Impedance Spectra: Part I. Analysis of a High-Voltage Positive Electrode. *Journal of The Electrochemical Society* **2017**, *164*, A1773-A1783.
54. Solchenbach, S.; Pritzl, D.; Kong, E. J. Y.; Landesfeind, J.; Gasteiger, H. A., A Gold Micro-Reference Electrode for Impedance and Potential Measurements in Lithium Ion Batteries. *Journal of The Electrochemical Society* **2016**, *163*, A2265-A2272.
55. Sorsa, O.; Nieminen, J.; Kauranen, P.; Kallio, T., Stable Reference Electrode in Polymer Electrolyte Membrane Electrolyser for Three-Electrode Measurements. *Journal of The Electrochemical Society* **2019**, *166*, F1326-F1336.
56. Mittelstaedt, C. K., Pem Electrolysis: Ready for Impact. *ECS Transactions* **2015**, *69*, 205.
57. Mittelstaedt, C.; Willey, J.; Stone, R.; Riffle, J.; Rowlett, J.; Daryaei, A.; McGrath, J., High Temperature, High Pressure Electrolysis. 2015.
58. Garbe, S.; Futter, J.; Schmidt, T. J.; Gubler, L., Insight into Elevated Temperature and Thin Membrane Application for High Efficiency in Polymer Electrolyte Water Electrolysis. *Electrochimica Acta* **2021**, *377*, 138046.
59. Trinke, P.; Bensmann, B.; Hanke-Rauschenbach, R., Experimental Evidence of Increasing Oxygen Crossover with Increasing Current Density During PEM Water Electrolysis. *Electrochemistry Communications* **2017**, *82*, 98-102.
60. Bernt, M.; Schröter, J.; Möckl, M.; Gasteiger, H., Analysis of Gas Permeation Phenomena in a PEM Water Electrolyzer Operated at High Pressure and High Current Density. *Journal of the Electrochemical Society* **2020**, *167*.
61. Watanabe, M.; Uchida, H.; Seki, Y.; Emori, M.; Stonehart, P., Self-Humidifying Polymer Electrolyte Membranes for Fuel Cells. *Journal of The Electrochemical Society* **1996**, *143*, 3847-3852.
62. Onda, K.; Murakami, T.; Hikosaka, T.; Kobayashi, M.; Notu, R.; Ito, K., Performance Analysis of Polymer-Electrolyte Water Electrolysis Cell at a Small-Unit Test Cell and Performance Prediction of Large Stacked Cell. *Journal of The Electrochemical Society* **2002**, *149*, A1069-A1078.
63. Durst, J.; Simon, C.; Hasché, F.; Gasteiger, H. A., Hydrogen Oxidation and Evolution Reaction Kinetics on Carbon Supported Pt, Ir, Rh, and Pd Electrocatalysts in Acidic Media. *Journal of The Electrochemical Society* **2015**, *162*, F190-F203.
64. Wilson, M. S.; Gottesfeld, S., Thin-Film Catalyst Layers for Polymer Electrolyte Fuel Cell Electrodes. *Journal of Applied Electrochemistry* **1992**, *22*, 1-7.
65. Bernt, M.; Siebel, A.; Gasteiger, H. A., Analysis of Voltage Losses in PEM Water Electrolyzers with Low Platinum Group Metal Loadings. *Journal of The Electrochemical Society* **2018**, *165*, F305-F314.
66. Fabbri, E.; Haberer, A.; Waltar, K.; Kötz, R.; Schmidt, T. J., Developments and Perspectives of Oxide-Based Catalysts for the Oxygen Evolution Reaction. *Catalysis Science & Technology* **2014**, *4*, 3800-3821.
67. Cherevko, S.; Zeradjanin, A. R.; Topalov, A. A.; Kulyk, N.; Katsounaros, I.; Mayrhofer, K. J., Dissolution of Noble Metals During Oxygen Evolution in Acidic Media. *ChemCatChem* **2014**, *6*, 2219-2223.
68. Tunold, R.; Marshall, A. T.; Rasten, E.; Tsyppkin, M.; Owe, L.-E.; Sunde, S., Materials for Electrocatalysis of Oxygen Evolution Process in PEM Water Electrolysis Cells. *ECS Transactions* **2010**, *25*, 103-117.

69. Owe, L.-E.; Tsytkin, M.; Wallwork, K. S.; Haverkamp, R. G.; Sunde, S., Iridium–Ruthenium Single Phase Mixed Oxides for Oxygen Evolution: Composition Dependence of Electrocatalytic Activity. *Electrochimica Acta* **2012**, *70*, 158-164.
70. Roller, J. M.; Josefina Arellano-Jiménez, M.; Jain, R.; Yu, H.; Barry Carter, C.; Maric, R., Oxygen Evolution During Water Electrolysis from Thin Films Using Bimetallic Oxides of Ir-Pt and Ir-Ru. *Journal of The Electrochemical Society* **2013**, *160*, F716-F730.
71. Kasian, O.; Geiger, S.; Stock, P.; Polymeros, G.; Breitbach, B.; Savan, A.; Ludwig, A.; Cherevko, S.; Mayrhofer, K. J. J., On the Origin of the Improved Ruthenium Stability in RuO<sub>2</sub>–IrO<sub>2</sub> Mixed Oxides. *Journal of The Electrochemical Society* **2016**, *163*, F3099-F3104.
72. Siracusano, S.; Baglio, V.; D’Urso, C.; Antonucci, V.; Aricò, A., Preparation and Characterization of Titanium Suboxides as Conductive Supports of IrO<sub>2</sub> Electrocatalysts for Application in Spe Electrolysers. *Electrochimica Acta* **2009**, *54*, 6292-6299.
73. Rakousky, C.; Reimer, U.; Wippermann, K.; Carmo, M.; Lueke, W.; Stolten, D., An Analysis of Degradation Phenomena in Polymer Electrolyte Membrane Water Electrolysis. *Journal of Power Sources* **2016**, *326*, 120-128.
74. Lettenmeier, P.; Kolb, S.; Burggraf, F.; Gago, A. S.; Friedrich, K. A., Towards Developing a Backing Layer for Proton Exchange Membrane Electrolyzers. *Journal of Power Sources* **2016**, *311*, 153-158.
75. Rakousky, C.; Keeley, G. P.; Wippermann, K.; Carmo, M.; Stolten, D., The Stability Challenge on the Pathway to High-Current-Density Polymer Electrolyte Membrane Water Electrolyzers. *Electrochimica Acta* **2018**, *278*, 324-331.
76. Schuler, T.; De Bruycker, R.; Schmidt, T. J.; Büchi, F. N., Polymer Electrolyte Water Electrolysis: Correlating Porous Transport Layer Structural Properties and Performance: Part I. Tomographic Analysis of Morphology and Topology. *Journal of The Electrochemical Society* **2019**, *166*, F270-F281.
77. Schuler, T.; Schmidt, T. J.; Büchi, F. N., Polymer Electrolyte Water Electrolysis: Correlating Performance and Porous Transport Layer Structure: Part II. Electrochemical Performance Analysis. *Journal of The Electrochemical Society* **2019**, *166*, F555-F565.
78. H2Gen, A. Areva H2gen Wasserstoff Generatoren - Technische Spezifikationen [https://www.avevah2gen.com/Wp-Content/Uploads/2019/10/Areva\\_H2gen\\_Fiche\\_Energy\\_V5-Uk.Pdf](https://www.avevah2gen.com/Wp-Content/Uploads/2019/10/Areva_H2gen_Fiche_Energy_V5-Uk.Pdf) (accessed 21.12.2019).
79. ITM-Power HGas2SP - Technical Data Sheet <https://www.itm-power.com/Images/Products/Hgas2sp.Pdf>. (accessed 21.12.2019).
80. Skulimowska, A.; Dupont, M.; Zaton, M.; Sunde, S.; Merlo, L.; Jones, D. J.; Rozière, J., Proton Exchange Membrane Water Electrolysis with Short-Side-Chain Aquivion® Membrane and IrO<sub>2</sub> Anode Catalyst. *International Journal of Hydrogen Energy* **2014**, *39*, 6307-6316.
81. Europe, H. <https://hydrogeneurope.eu/Refueling-Stations>. (accessed 21.12.2019).
82. Grigoriev, S.; Porembskiy, V.; Korobtsev, S.; Fateev, V.; Auprêtre, F.; Millet, P., High-Pressure PEM Water Electrolysis and Corresponding Safety Issues. *International Journal of Hydrogen Energy* **2011**, *36*, 2721-2728.
83. Grigoriev, S.; Millet, P.; Korobtsev, S.; Porembskiy, V.; Pepic, M.; Etievant, C.; Puyenchet, C.; Fateev, V., Hydrogen Safety Aspects Related to High-Pressure Polymer Electrolyte Membrane Water Electrolysis. *International Journal of Hydrogen Energy* **2009**, *34*, 5986-5991.
84. Suermann, M.; Schmidt, T. J.; Büchi, F. N., Cell Performance Determining Parameters in High Pressure Water Electrolysis. *Electrochimica Acta* **2016**, *211*, 989-997.

85. Janssen, H.; Bringmann, J.; Emonts, B.; Schröder, V., Safety-Related Studies on Hydrogen Production in High-Pressure Electrolysers. *International Journal of Hydrogen Energy* **2004**, *29*, 759-770.
86. Price, E., Durability and Degradation Issues in PEM Electrolysis Cells and Its Components. *Johnson Matthey's International Journal of Research Exploring Science and Technology in Industrial Applications* **2017**, *61*, 47-51.
87. Siracusano, S.; Van Dijk, N.; Backhouse, R.; Merlo, L.; Baglio, V.; Aricò, A., Degradation Issues of PEM Electrolysis MEAs. *Renewable Energy* **2018**, *123*, 52-57.
88. Danilovic, N.; Ayers, K. E.; Capuano, C.; Renner, J. N.; Wiles, L.; Pertoso, M., (Plenary) Challenges in Going from Laboratory to Megawatt Scale PEM Electrolysis. *ECS Transactions* **2016**, *75*, 395-402.
89. Grigoriev, S. A.; Bessarabov, D. G.; Fateev, V. N., Degradation Mechanisms of MEA Characteristics During Water Electrolysis in Solid Polymer Electrolyte Cells. *Russian Journal of Electrochemistry* **2017**, *53*, 318-323.
90. Mo, J.; Steen III, S. M.; Zhang, F.-Y.; Toops, T. J.; Brady, M. P.; Green Jr, J. B., Electrochemical Investigation of Stainless Steel Corrosion in a Proton Exchange Membrane Electrolyzer Cell. *International Journal of Hydrogen Energy* **2015**, *40*, 12506-12511.
91. Sun, S.; Shao, Z.; Yu, H.; Li, G.; Yi, B., Investigations on Degradation of the Long-Term Proton Exchange Membrane Water Electrolysis Stack. *Journal of Power Sources* **2014**, *267*, 515-520.
92. Lettenmeier, P.; Wang, R.; Abouatallah, R.; Saruhan, B.; Freitag, O.; Gazdzicki, P.; Morawietz, T.; Hiesgen, R.; Gago, A.; Friedrich, K., Low-Cost and Durable Bipolar Plates for Proton Exchange Membrane Electrolyzers. *Scientific Reports* **2017**, *7*, 44035.
93. Babic, U.; Zlobinski, M.; Schmidt, T. J.; Boillat, P.; Gubler, L., CO<sub>2</sub>-Assisted Regeneration of a Polymer Electrolyte Water Electrolyzer Contaminated with Metal Ion Impurities. *Journal of The Electrochemical Society* **2019**, *166*, F610-F619.
94. Laconti, A.; Liu, H.; Mittelsteadt, C.; McDonald, R., Polymer Electrolyte Membrane Degradation Mechanisms in Fuel Cells - Findings over the Past 30 Years and Comparison with Electrolyzers. *ECS Transactions* **2006**, *1*, 199-219.
95. Curtin, D. E.; Lousenberg, R. D.; Henry, T. J.; Tangeman, P. C.; Tisack, M. E., Advanced Materials for Improved PEMFC Performance and Life. *Journal of Power Sources* **2004**, *131*, 41-48.
96. Chen, C.; Fuller, T. F., The Effect of Humidity on the Degradation of Nafion® Membrane. *Polymer Degradation and Stability* **2009**, *94*, 1436-1447.
97. Madden, T.; Perry, M.; Protsailo, L.; Gummalla, M.; Burlatsky, S.; Cipollini, N.; Motupally, S.; Jarvi, T., Proton Exchange Membrane Fuel Cell Degradation: Mechanisms and Recent Progress. In *Handbook of Fuel Cells-, Volume 5 & 6, Advances in Electrocatalysis, Materials, Diagnostics and Durability* Vielstich, W.; Gasteiger, H. A.; Lamm, A., Eds. John Wiley & Sons, Ltd.: 2009; Vol. 6, pp 861-879.
98. Vengatesan, S.; Fowler, M. W.; Yuan, X.-Z.; Wang, H., Diagnosis of MEA Degradation under Accelerated Relative Humidity Cycling. *Journal of Power Sources* **2011**, *196*, 5045-5052.
99. Cherevko, S., Stability and Dissolution of Electrocatalysts: Building the Bridge between Model and "Real World" Systems. *Current Opinion in Electrochemistry* **2018**, *8*, 118-125.
100. Pourbaix, M., *Atlas of Electrochemical Equilibria in Aqueous Solutions* 2nd. Eng. edn. ed.; NACE International Cebelcor Houston, Texas, USA 1974, p 373-377.
101. Kasian, O.; Grote, J. P.; Geiger, S.; Cherevko, S.; Mayrhofer, K. J., The Common Intermediates of Oxygen Evolution and Dissolution Reactions During Water Electrolysis on Iridium. *Angewandte Chemie International Edition* **2018**, *57*, 2488-2491.



102. Wagner, C., Theorie Der Alterung Von Niederschlägen Durch Umlösen (Ostwald-Reifung). *Zeitschrift für Elektrochemie, Berichte der Bunsengesellschaft für physikalische Chemie* **1961**, *65*, 581-591.
103. Darling, R. M.; Meyers, J. P., Kinetic Model of Platinum Dissolution in PEMFCs. *Journal of the Electrochemical Society* **2003**, *150*, A1523-A1527.
104. Zhang, J.; Litteer, B. A.; Gu, W.; Liu, H.; Gasteiger, H. A., Effect of Hydrogen and Oxygen Partial Pressure on Pt Precipitation within the Membrane of PEMFCs. *Journal of The Electrochemical Society* **2007**, *154*, B1006-B1011.
105. Mittermeier, T.; Weiß, A.; Hasché, F.; Hübner, G.; Gasteiger, H. A., PEM Fuel Cell Start-up/Shut-Down Losses Vs Temperature for Non-Graphitized and Graphitized Cathode Carbon Supports. *Journal of The Electrochemical Society* **2017**, *164*, F127-F137.
106. Borup, R. L.; Papadias, D. D.; Mukundan, R.; Spornjak, D.; Langlois, D. A.; Ahluwalia, R.; More, K. L.; Grot, S., Carbon Corrosion in PEM Fuel Cells During Drive Cycle Operation. *Ecs Transactions* **2015**, *69*, 1029-1038.
107. Meyers, J. P.; Darling, R. M., Model of Carbon Corrosion in PEM Fuel Cells. *Journal of the Electrochemical Society* **2006**, *153*, A1432-A1442.
108. Jung, H.-Y.; Huang, S.-Y.; Ganesan, P.; Popov, B. N., Performance of Gold-Coated Titanium Bipolar Plates in Unitized Regenerative Fuel Cell Operation. *Journal of Power Sources* **2009**, *194*, 972-975.
109. James, B. *Cost Projections of PEM Fuel Cell Systems for Automobiles and Medium-Duty Vehicles*; Department of Energy April 25, 2018
110. Infomine <https://www.infomine.com/investment/metal-prices/platinum/> (accessed 06.06.2020).
111. Mayyas, A. T.; Ruth, M. F.; Pivovar, B. S.; Bender, G.; Wipke, K. B. *Manufacturing Cost Analysis for Proton Exchange Membrane Water Electrolyzers*; National Renewable Energy Lab.(NREL), Golden, CO (United States): 2019.
112. NOW Studie Indwedeindustrialisierung Der Wasserelektrolyse Indeutschland: Chancenundherausforderungen Fürnächhaltigen Wasserstoff Für Verkehr, Stromundwärme; Nationale Organisation Wasserstoff- und Brennstoffzellentechnologie: [https://www.now-gmbh.de/content/service/3-publikationen/1-nip-wasserstoff-und-brennstoffzellentechnologie/indwede-studie\\_v04.1.pdf](https://www.now-gmbh.de/content/service/3-publikationen/1-nip-wasserstoff-und-brennstoffzellentechnologie/indwede-studie_v04.1.pdf), 2018.
113. BMWI Bundesministerium Für Wirtschaft Und Energie <https://www.bmwi.de/Redaktion/De/Infografiken/Energie/Energiedaten/Energiegewinnung-Und-Energieverbrauch/Energiedaten-Energiegewinnung-Verbrauch-03.html>. (accessed 30.12.2019).
114. Geiger, S.; Kasian, O.; Mingers, A. M.; Nicley, S. S.; Haenen, K.; Mayrhofer, K. J. J.; Cherevko, S., Catalyst Stability Benchmarking for the Oxygen Evolution Reaction: The Importance of Backing Electrode Material and Dissolution in Accelerated Aging Studies. *ChemSusChem* **2017**, *10*, 4140-4143.
115. El-Sayed, H. A.; Weiß, A.; Olbrich, L. F.; Putro, G. P.; Gasteiger, H. A., Oer Catalyst Stability Investigation Using Rde Technique: A Stability Measure or an Artifact? *Journal of The Electrochemical Society* **2019**, *166*, F458-F464.
116. Bernt, M. P. Analysis of Voltage Losses and Degradation Phenomena in PEM Water Electrolyzers. PhD Thesis, Technische Universität München, 2019.
117. Li, G.; Pickup, P. G., Measurement of Single Electrode Potentials and Impedances in Hydrogen and Direct Methanol PEM Fuel Cells. *Electrochimica Acta* **2004**, *49*, 4119-4126.
118. Adler, S. B., Reference Electrode Placement in Thin Solid Electrolytes. *Journal of The Electrochemical Society* **2002**, *149*, E166-E172.

119. Adler, S.; Henderson, B.; Wilson, M.; Taylor, D.; Richards, R. E., Reference Electrode Placement and Seals in Electrochemical Oxygen Generators. *Solid State Ionics* **2000**, *134*, 35-42.
120. Pritzl, D.; Landesfeind, J.; Solchenbach, S.; Gasteiger, H. A., An Analysis Protocol for Three-Electrode Li-Ion Battery Impedance Spectra: Part II. Analysis of a Graphite Anode Cycled Vs. LNMO. *Journal of The Electrochemical Society* **2018**, *165*, A2145-A2153.
121. Rozain, C.; Millet, P., Electrochemical Characterization of Polymer Electrolyte Membrane Water Electrolysis Cells. *Electrochimica Acta* **2014**, *131*, 160-167.
122. Dedigama, I.; Angeli, P.; Ayers, K.; Robinson, J.; Shearing, P.; Tsaoulidis, D.; Brett, D., In Situ Diagnostic Techniques for Characterisation of Polymer Electrolyte Membrane Water Electrolysers—Flow Visualisation and Electrochemical Impedance Spectroscopy. *international Journal of Hydrogen Energy* **2014**, *39*, 4468-4482.
123. Durst, J.; Siebel, A.; Simon, C.; Hasche, F.; Herranz, J.; Gasteiger, H., New Insights into the Electrochemical Hydrogen Oxidation and Evolution Reaction Mechanism. *Energy & Environmental Science* **2014**, *7*, 2255-2260.
124. Inzelt, G.; Lewenstam, A.; Scholz, F., *Handbook of Reference Electrodes*; Springer, 2013.
125. Kocha, S., Principles of MEA Preparation, | Handbook of Fuel Cells: Fundamentals Technology and Applications. Volume 3: Fuel Cell Technology and Applications. Chichester: W. Vielstich, A. Lamm, HA Gasteiger, John Wiley & Sons Inc: 2003; pp 538-565.
126. Simon, C.; Hasché, F.; Gasteiger, H. A., Influence of the Gas Diffusion Layer Compression on the Oxygen Transport in PEM Fuel Cells at High Water Saturation Levels. *Journal of The Electrochemical Society* **2017**, *164*, F591-F599.
127. Ferrell, R. T.; Himmelblau, D. M., Diffusion Coefficients of Nitrogen and Oxygen in Water. *Journal of Chemical and Engineering Data* **1967**, *12*, 111-115.
128. Schalenbach, M.; Hoefner, T.; Paciok, P.; Carmo, M.; Lueke, W.; Stolten, D., Gas Permeation through Nafion. Part 1: Measurements. *The Journal of Physical Chemistry C* **2015**, *119*, 25145-25155.
129. Kuhn, H.; Andraus, B.; Wokaun, A.; Scherer, G., Electrochemical Impedance Spectroscopy Applied to Polymer Electrolyte Fuel Cells with a Pseudo Reference Electrode Arrangement. *Electrochimica Acta* **2006**, *51*, 1622-1628.
130. Kuhn, H.; Wokaun, A.; Scherer, G., Exploring Single Electrode Reactions in Polymer Electrolyte Fuel Cells. *Electrochimica Acta* **2007**, *52*, 2322-2327.
131. Schneider, I. A.; Bayer, M. H.; Boillat, P.; Wokaun, A.; Scherer, G. G., Formation of Low Frequency Inductive Loops in Polymer Electrolyte Fuel Cell (PEFC) Impedance Spectra under Sub-Saturated Conditions. *ECS Transactions* **2007**, *11*, 461-472.
132. Pivac, I.; Barbir, F., Inductive Phenomena at Low Frequencies in Impedance Spectra of Proton Exchange Membrane Fuel Cells—a Review. *Journal of Power Sources* **2016**, *326*, 112-119.
133. Lefebvre, M. C.; Martin, R. B.; Pickup, P. G., Characterization of Ionic Conductivity Profiles within Proton Exchange Membrane Fuel Cell Gas Diffusion Electrodes by Impedance Spectroscopy. *Electrochemical and Solid-State Letters* **1999**, *2*, 259-261.
134. Bernt, M.; Hartig-Weiß, A.; Tovini, M. F.; El-Sayed, H. A.; Schramm, C.; Schröter, J.; Gebauer, C.; Gasteiger, H. A., Current Challenges in Catalyst Development for PEM Water Electrolyzers. *Chemie Ingenieur Technik* **2020**, *92*, 31-39.
135. Hartig-Weiss, A.; Miller, M.; Beyer, H.; Schmitt, A.; Siebel, A.; Freiberg, A. T.; Gasteiger, H. A.; El-Sayed, H. A., Iridium Oxide Catalyst Supported on Antimony-Doped Tin Oxide for High Oxygen Evolution Reaction Activity in Acidic Media. *ACS Applied Nano Materials* **2020**, *3*, 2185-2196.

136. Hartig-Weiss, A.; Tovini, M. F.; Gasteiger, H. A.; El-Sayed, H. A., OER Catalyst Durability Tests Using the Rotating Disk Electrode Technique: The Reason Why This Leads to Erroneous Conclusions. *ACS Applied Energy Materials* **2020**.
137. Tan, X.; Shen, J.; Semagina, N.; Secanell, M., Decoupling Structure-Sensitive Deactivation Mechanisms of Ir/Irox Electrocatalysts toward Oxygen Evolution Reaction. *Journal of Catalysis* **2019**, *371*, 57-70.
138. Tang-Kong, R.; Chidsey, C. E.; McIntyre, P. C., Reversible Decay of Oxygen Evolution Activity of Iridium Catalysts. *Journal of The Electrochemical Society* **2019**, *166*, H712.
139. Tovini, M. F.; Hartig-Weiss, A.; Gasteiger, H.; El-Sayed, H. A., The Discrepancy in Oxygen Evolution Reaction Catalyst Lifetime Explained: RDE Vs MEA Dynamicity within the Catalyst Layer Matters. *Journal of the Electrochemical Society* **2021**, *168*.
140. Bertuccioli, L.; Chan, A.; Hart, D.; Lehner, F.; Madden, B.; Standen, E., Study on Development of Water Electrolysis in the EU. *Fuel cells and hydrogen joint undertaking* **2014**.
141. Hartig-Weiß, A.; Bernt, M.; Siebel, A.; Gasteiger, H.A., A Platinum Micro-Reference Electrode for Impedance Measurements in a PEM Water Electrolysis Cell. *Journal of The Electrochemical Society* **2021**, *168*, 114511